Utilisation of biomass-derived gaseous fuels using solid-oxide fuel cells

by
Kleitos Panagi

A submission presented in partial fulfilment of the requirements of

University of South Wales / Prifysgol De Cymru

for the degree of Doctor of Philosophy

January 2021

Abstract

Solid oxide fuel cells (SOFCs) are highly efficient electrochemical energy conversion devices that can potentially reduce greenhouse gas emissions and revolutionize our energy infrastructures. This research investigates and demonstrates novel and highly efficient methods of utilising renewable biomass-derived gases using SOFC technology with commercially available anode (ASC) and electrolyte supported (ESC) button cells. The utilisation of biohydrogen and biohythane mixtures have been investigated in fuel cell, electrolysis and co-electrolysis modes. Cell electrical performance was characterised using potentiostatic techniques and fuel processing was characterised using online quadrupole mass spectroscopy.

Biologically produced mixtures of H_2 and CO_2 (biohydrogen) from processes such as dark fermentation or photo-fermentation are versatile feedstocks which can potentially be utilised in SOFC devices. In this work, solid oxide electrolysis of biohydrogen has been investigated for the first time and is compared directly with fuel cell mode utilisation in both ASC and ESC supported cells. The effects of fuel variability on SOC overpotentials and outputs have been established and it is shown that cell performance for ESC and ASC is not significantly affected provided the fuel composition stays within 40-60 vol% H_2. The effects of fuel variability are affiliated to the presence of the revere water-gas shift (RWGS) reaction, which takes place simultaneously alongside electrochemical processes. The ASC demonstrated better performance in fuel cell mode with more power being produced compared to an ESC, although ASC was more sensitive to fuel variability. QMS measurements indicated H_2O and CO production took place in-situ via the RWGS reaction. Electrical power production in fuel cell mode was predominantly through H_2 oxidation, whilst CO was converted in the WGS reaction to regenerate CO_2 but did not contribute to electrical power production. In electrolysis mode,

CO was produced simultaneously through electrochemical CO_2 reduction and the RWGS reaction, H_2O is electrochemically reduced to regenerate H_2. Different operating conditions such as temperature have been studied and shown to have an effect on the performance and outputs of the cell.

Co-production of energy and useful chemicals using was demonstrated through investigations into the utilisation of biohythane ($CH_4/CO_2/H_2$ - 60/30/10 vol%) produced from an optimised two-stage anaerobic digestion (AD) process. The gain in energy yield from two-stage AD was supplemented with additional gains in SOFC efficiency due to the presence of H_2 in biohythane, giving up to 77% increased electrical energy yields from biomass overall compared with utilisation of biogas from single-stage AD in SOFCs. The results revealed that biohythane production rather than biogas is a highly advantageous route to energy production from biomass. Furthermore, the effects of fuel variability on the electrical performance and fuel processing of the cell operating on biohythane mixtures at different operating temperatures were studied. When H_2/CO_2 is blended with CH_4 to make biohythane, the SOFC efficiency is significantly increased, high SOFC durability is achieved, and there are considerable savings in CH_4 consumption. Enhanced electrical performance was due to the additional presence of H_2 and promotion of CH_4 dry reforming, the reverse Boudouard and reverse water-gas shift reactions. These processes alleviated carbon deposition and promoted electrochemical oxidation of H_2 as the primary power production pathway. Substituting 50 vol% CH_4 with 25/75 vol% H_2/CO_2 was shown to increase cell power output by 81.6% at 0.8 V compared with pure CH_4. This corresponded to a 3.4-fold increase in the overall energy conversion efficiency and a 72% decrease in CH_4 consumption. A 260 h durability test demonstrated very high cell durability when operating on a typical 60/30/10 vol% $CH_4/CO_2/H_2$ biohythane mixture under high fuel utilisation due to inhibition of carbon deposition. A significant outcome of this work suggests that decarbonising gas grids by substituting natural gas with renewably produced

H_2/CO_2 mixtures and utilising in SOFC technology gives considerable gains in energy conversion efficiency and carbon emissions savings.

Co-electrolysis of biohythane using ASCs was investigated and compared with biohydrogen and biogas (CH_4/CO_2 60/40 vol%) mixtures, operated with three different co-oxidants (steam, steam/CO_2 and CO_2). The overall performance and the composition of the output gases have been shown to be very sensitive to the co-oxidant used and by adding H_2 to biogas feedstocks improves the overall performance of the cell compared with H_2-free biogas.

Acknowledgements

I would like to express my sincere gratitude to my supervisor, Dr. Christian Laycock for giving me the opportunity to do this research project and providing invaluable guidance, support and encouragement throughout this research. I also need to thank Prof. Alan Guwy and Dr. James Reed for their diverse expertise, insightful input and valuable feedback.

I would like to thank my future wife Chrystalla, my parents Sotiris and Thekla and the rest of my family for their constant love and support.

Contents

List of Figures

List of Tables

List of Reactions

Equation Number	Reaction Name	Reaction	Enthalpy (kJ/mol)
Eq. 1	Electrochemical oxidation of hydrogen	$H_2 + O^{2-} \rightleftharpoons H_2O + 2e^-$	**-286**
Eq. 2	Oxygen reduction	$2e^- + ½O_2 \rightleftharpoons O^{2-}$	
Eq. 3	Electrochemical H_2 oxidation	$H_2 + ½O_2 \rightarrow H_2O$	**-286**
Eq. 4	Steam reforming of CH_4	$CH_4 + H_2O \rightleftharpoons CO + 3H_2$	**205**
Eq. 5	Sulphur poisoning	$Ni + H_2S \leftrightarrow Ni–S + H_2$	
Eq. 6	Methane cracking	$CH_4 \rightleftharpoons 2H_2 + C$	**74.9**
Eq. 7	Revere boudouard	$2CO \rightleftharpoons CO_2 + C$	**-172.4**
Eq. 8	Reduction of CO	$H_2O + C \rightleftharpoons CO + H_2$	**131.3**
Eq. 9	Electrochemical reduction of H_2O	$H_2O + 2e^- \rightarrow H_2 + O^{2-}$	**241.8**
Eq. 10	Electrochemical reduction of CO_2	$CO_2 + 2e^- \rightarrow CO + O^{2-}$	**283.0**
Eq. 11	Oxygen ion formation	$2O^{2-} \rightarrow O_2 + 4e^-$	
Eq. 12	Water gas shift reaction	$H_2O + CO \rightleftharpoons H_2 + CO_2$	**-41**
Eq. 13	Methanation reaction	$CO + 3H_2 \rightleftharpoons CH_4 + H_2O$	**35.7**
Eq. 14	Reverse steam reforming	$2CO + 2H_2 \rightleftharpoons CH_4 + CO_2$	**-205**
Eq. 15	Reverse dry reforming of CH_4	$CO_2 + 4H_2 \rightleftharpoons CH_4 + 2H_2O$	**-247**
Eq. 16	Reverse water gas shift reaction	$H_2 + CO_2 \rightleftharpoons H_2O + CO$	**41**
Eq. 17	Dry reforming of CH_4	$CH_4 + CO_2 \rightleftharpoons 2H_2 + 2CO$	**+247**
Eq. 18	Electrochemical CO oxidation	$CO + O^{2-} \rightleftharpoons CO_2 + 2e^-$	**-283**
Eq. 19	Partial oxidation of methane	$CH_4 + O^{2-} \rightleftharpoons 2H_2 + CO + 2e^-$	**-35.7**
Eq. 20	Total oxidation of methane	$CH_4 + 4O^{2-} \rightleftharpoons 2H_2O + CO_2 + 8e^-$	**-890.3**
Eq. 21	Electrolysis of steam	$H_2O + 2e^- \rightleftharpoons H_2 + O^{2-}$	**241.8**
Eq. 22	Electrolysis of CO_2	$CO_2 + 6e^- \rightleftharpoons CO + 3O^{2-}$	**283**

Chapter 1: Introduction

1.1. Context of Research

Due to the increasing trends and consequences of climate change and air pollution, it is essential to become more efficient and resourceful in the production and utilisation of energy and materials. The world has already warmed by 1 °C above pre-industrial levels and is continuing to do so at a concerning rate due to over-dependence on fossil feedstocks, Carnot-limited processes and inefficient waste management techniques [1]. Greenhouse gas and air pollutant emissions are global public health issues that are affecting the availability of soil, food and water supplies [2]. Fossil fuels provide almost 90% of global energy demand and are the main source of greenhouse gases and harmful atmospheric pollutants [3]. Most fuels and feedstocks are currently utilised in inefficient and dirty combustion technologies and processes.

Alleviation of these issues will require innovative deployment of efficient and clean energy technologies combined with optimal management of waste and renewable resources. Aiming to reduce environmental problems, fuel cells have received increased academic and industrial attention [4, 5] in recent decades because they can produce electrical energy, heat and useful chemicals with considerably greater efficiency compared with conventional combustion technologies [6-8]. This research investigates novel and highly efficient methods of utilising renewable biomass-derived gas mixtures via conversion into energy and useful chemicals using state-of-the-art solid oxide fuel cell (SOFC) technology.

1.2. Fuel Cell Operating Principles and Technology

A fuel cell is an electrochemical energy conversion device, which produces electrical power directly from a chemical fuel and therefore avoids Carnot limitations [9, 10]. Fig. 1.1 illustrates the basic operating principle of a general H_2-O_2 fuel cell (Eq. 1). A typical fuel cell consist of two electrodes (anode and cathode) and an electrolyte, through which ions are conducted [11].

Oxygen is reduced to oxygen ions (Eq. 2) at the cathode, which are transferred through the electrolyte to react with the fuel at the triple phase boundary (TPB) where fuel gases (H_2) meet (Eq. 3). Fuel and air are stored externally and supplied to the fuel cell to produce electricity and heat. As long fuel and air are supplied, electricity will be generated; unlike a battery, a fuel cell is not consumed when it produces electrical power [12].

$$H_2 + O^{2-} \rightleftharpoons H_2O + 2e^- \quad \text{(Eq. 1)}$$

$$2e^- + \tfrac{1}{2}O_2 \rightleftharpoons O^{2-} \quad \text{(Eq. 2)}$$

$$H_2 + \tfrac{1}{2}O_2 \rightarrow H_2O \quad \text{(Eq. 3)}$$

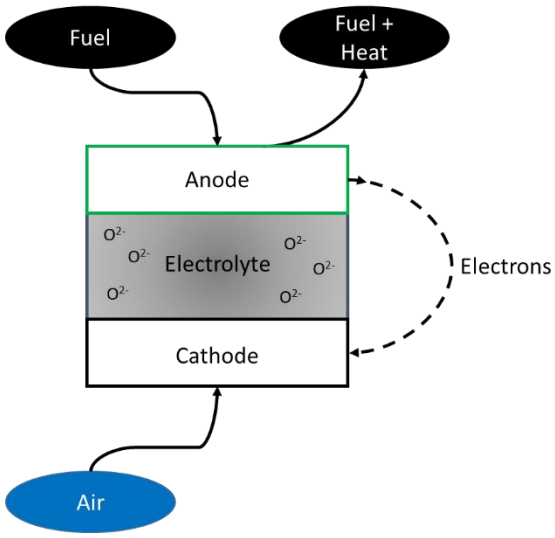

Figure 1.1: Schematic diagram showing the operating principle of a general H_2-O_2 fuel cell.

Fuel cells are known for highly efficient electrical power production [11] and most fuel cells are able to utilise a wide range of fuels and feedstocks including complex gas mixtures [7, 13]. The high electrical efficiency of these devices potentially enables fossil fuel and energy consumption to be decreased, as well as reductions in greenhouse gas and harmful air pollutant emissions [14]. Fuel cells have no moving parts and therefore operate quietly and do not suffer mechanical

reliability issues. They have a modular and scalable design, which enables power and capacity to be scaled independently. Because fuel cells require a fuel for operation, they have better energy densities than batteries and can reduce demand on electricity grids. Although fuel cells are expensive to manufacture and the fuel mixtures containing hydrogen are highly flammable and difficult to store.

The high operating temperature enables deployment of systems in combined heat and power (CHP) applications [15-17]. Fuel cells are frequently used because of higher electrical efficiency for CHP applications and grid connections ranging from 10 kW to 100 MW with efficiencies exceeding 80% and reducing CO_2 emissions by more than 60% [18, 19]. These systems are used in residential sites for electricity and heating, for auxiliary power, data processing centres, hospitals and industrial units [20-22]. Fuel cells can be used in the transportation sector to eventually replace diesel engines as hydrogen fuel cells offer lower carbon and lower pollution emissions [23, 24] but fuel economy and system efficiency must be further studied and developed to be compatible with internal combustion engines (ICE) [25-27]. Fuel cells can be used for portable applications for portable power generators and in electronic devices usually in the range between 5 – 500 W [28-31].

Fuel cells can be characterised by the type of electrolyte material used, which determines a range of characteristics including the operating temperature range, component chemistry, fuel flexibility and performance [32, 33] in (see Table 1.1). Although PAFCs, AFCs and MCFCs have been commercially deployed [34-38], they each have specific disadvantages, which significantly limit their applicability and therefore commercial potential. Most fuel cell research and development focusses on PEMFCs and SOFCs, which are perceived as having much greater performance and commercial potential in future [39-42].

Table 1.1: Description of major fuel cell types

	PEMFC	PAFC	AFC	MCFC	SOFC
Electrolyte	Polymer Membrane	Liquid H_3PO_4	Liquid KOH	Molten Carbonate	Ceramic
Electrodes	Carbon based	Carbon based	Carbon based	Stainless steel based	Ceramic based
Charge Carrier	H^+	H^+	OH^-	CO_3^{2-}	O^{2-}
Operating Temperature	80 °C	200 °C	60 – 220 °C	650 - 1500 °C	500 – 1000 °C
Catalyst	Platinum	Platinum	Platinum	Nickel	Perovskites and Nickel (ceramic)
Fuel Compatibility	H_2	H_2	H_2	H_2, CH_4	H_2, CH_4, CO, NH_3
Major Contaminants	CO, NH_3 and sulphides	CO, siloxane and sulphides	CO_2	Sulphides and halides	Sulphides
Applications	Transportation, stationary and portable applications	Stationary applications	Portable applications	Stationary applications	Transportation, stationary and portable applications

Polymer Electrolyte Membrane Fuel Cells (PEMFCs) use a hydrated organic polymer-based membrane as the electrolyte. Both electrodes are composed of a carbon-based gas-diffusion layer with a platinum electrocatalyst. The operating temperature is relatively low (< 100 °C), and therefore expensive precious metal-based electrodes are essential. PEMFCs require very pure H_2 as the fuel and air as the oxidant, with extensive fuel processing required to ensure the hydrogen is very pure (99.9999 vol%). This is because Pt is easily poisoned by trace levels of carbon monoxide, gaseous sulfur and halogens. PEMFCs have the highest power density of any fuel cell type, have quick start-up times due to the low temperatures and a compact design. They are therefore suited to a wide range of applications including transportation, portable and stationary applications such as the balancing of intermittent renewable energy resources. The disadvantages of PEMFC include very high costs (mainly due to platinum), the low temperatures which make water and thermal management challenging, expensive fuel purity

requirements, lack of fuel flexibility and platinum catalyst poisoning [43, 44]. They are not suitable for CHP applications, the utilisation of complex fuel mixtures or those composed of hydrocarbons or ammonia.

1.3. Operating Principles of Solid Oxide Fuel Cells

SOFCs are a type of high temperature (>750 °C) fuel cell made with a ceramic electrolyte material which conducts oxygen ions (O^{2-}) between the electrodes. The operating principle of an SOFC is shown in Fig. 1.2. Fuel (H_2) is delivered to the anode where it is electrochemically oxidised to H_2O through reaction with oxygen ions coming from the electrolyte. This process releases electrons which are conducted externally around the electrolyte to the cathode. A reduction reaction takes place at the cathode (Eq. 2) where oxygen is delivered to the cathode (usually in the form of air) and reduced to oxygen ions through combination with the incoming electrons. The oxygen ions are conducted through the electrolyte to the anode where they react again with H_2 completing the process [6, 45].

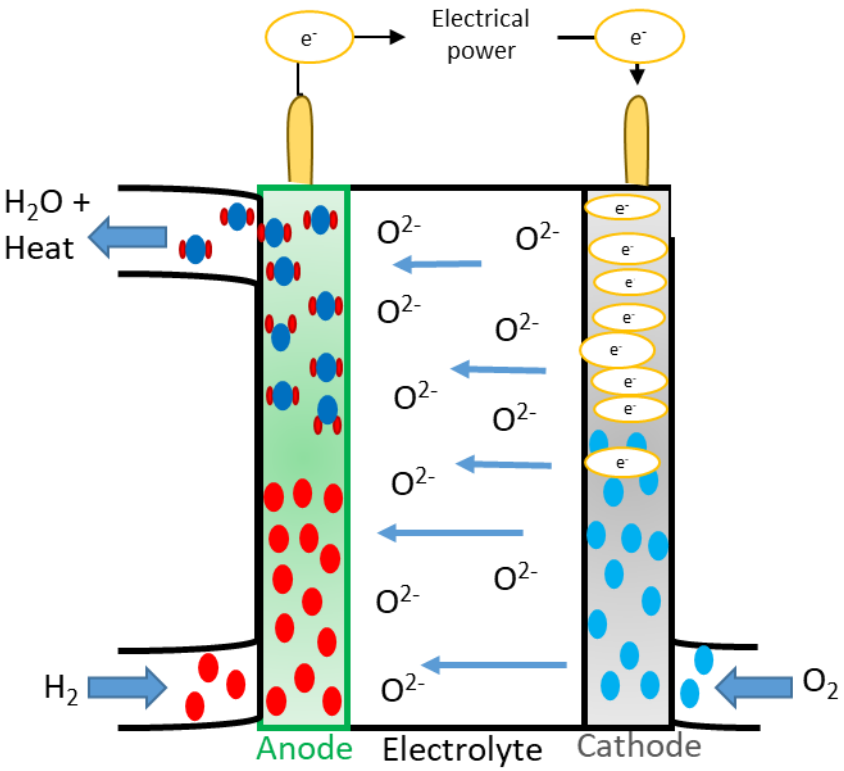

Figure 1.2: Schematic diagram showing solid oxide fuel cell operation

There are three types of SOFC based on their operating temperature, high temperature SOFCs (HT-SOFCs), which operate approximately > 750 °C and have the best performance, can tolerate small quantities of impurities in the fuel but have significant materials issues and therefore the poorest durability [46-49] due to materials issues. Hence, there is interest in intermediate temperature SOFCs (IT-SOFCs), which operate in the region ~ 500-750 °C and low temperature SOFCs (LT-SOFCs), which operate at less than 500 °C. The lower operating temperature helps to reduce materials degradation, increasing durability but at the expense of performance [50-54]. This research is focussed on the characterisation of HT-SOFCs.

HT-SOFCs have electrical efficiencies of up to 60% and combined electrical and thermal efficiencies of up to 90% [11]. They are relatively compact and scalable compared with other high temperature fuel cells, can be sized between 1 kW and 1 MW and can be deployed in CHP applications [15, 16]. Due to the high operating temperatures and oxidation of the fuel with oxygen ions, they are able to utilise a wide range of fuels and feedstocks, including complex gas mixtures and those composed of carbon monoxide [55-57], hydrocarbons [58-61] and ammonia [62-65] . SOFCs have also demonstrated to operate on natural gas [66-68], biogas [69-73], hythane [74-78] and biohydrogen [79-81]. SOFCs have high efficiency when operating on pure H_2 due to the small size and simplicity of the hydrogen molecule, which is more readily electrochemically oxidised. Most commercially available SOFCs are designed to operate on CH_4-based fuels so that they can be connected to natural gas grids, thereby increasing their commercialisation prospects [66, 82]. They are equipped with a dedicated fuel processing unit in which hydrocarbons are catalytically converted into synthesis gas (H_2/CO) via steam reforming (Eq. 4) prior to delivery onto the fuel electrodes [83, 84].

$$CH_4 + H_2O \rightleftharpoons CO + H_2 \qquad \text{(Eq. 4)}$$

The reforming reactions take place directly on the anode (internally) in SOFCs or externally using catalytic pre-reformer. It is a key requirement of the fuel processing unit to remove sulphur from gas streams, because sulphur poisons the anode by converting Ni to Ni-sulphide

(Eq. 5) that forms dense metal sulphide particles on the anode surface [85, 86] causing a reduction in TPBs and cell degradation.

$$Ni + H_2S \leftrightarrow Ni–S + H_2 \quad \text{(Eq. 5)}$$

Steam reforming assists with stack cooling since steam reforming is highly endothermic, and alleviates issues caused by hydrocarbon cracking and carbon deposition [87, 88]. Carbon deposition is a very significant problem because it reduces the performance and durability and generate local thermal stress leading to cell cracks and delamination. Carbon deposition largely occurs due to methane cracking (Eq. 6), reduction of CO (Eq. 7) alternatively the addition of steam can remove carbon deposition (Eq. 8).

$$CH_4 \rightleftharpoons 2H_2 + C \quad \text{(Eq. 6)}$$

$$2CO \rightleftharpoons CO_2 + C \quad \text{(Eq. 7)}$$

$$H_2O + C \rightleftharpoons CO + H_2 \quad \text{(Eq. 8)}$$

1.3.1. Electrolysis Mode

Like all fuel cells, solid oxide cells are able to operate in reverse to perform electrolysis. Solid oxide electrolysis cells (SOECs) consume water, heat and electrical power to yield separate pure hydrogen and oxygen gas streams [89-92]. The operating principles of solid oxide electrolysis are the reverse of SOFCs. Steam and carbon dioxide can be supplied to the anode where the electrochemical reductions of H_2O (Eq. 9) and CO_2 (Eq. 10) take place at the TPB.

$$H_2O + 2e^- \rightarrow H_2 + O^{2-} \quad \text{(Eq. 9)}$$

$$CO_2 + 2e^- \rightarrow CO + O^{2-} \quad \text{(Eq. 10)}$$

At the oxygen electrode, the oxygen ions travel through the electrolyte to the fuel electrode releasing electrons forming oxygen molecules (Eq. 11).

$$2O^{2-} \rightarrow O_2 + 4e^- \quad \text{(Eq. 11)}$$

In steam electrolysis, a small amount of H_2 (5-10%) needs to be added in order to prevent oxidation of the anode. Steam and carbon dioxide can be electrolysed separately or they can be co-electrolysed where both H_2O and CO_2 are supplied to the cell simultaneously and directly converted to H_2, CO and O_2. In addition to the above overall reactions (Eqs. 9-11) the water gas-shift reaction (WGS) (Eq. 12), methanation reaction (Eq. 13) and the reverse steam reforming reaction (Eqs. 14 and 15) can occur at the fuel electrode [93-96].

$$CO + H_2O \rightleftharpoons H_2 + CO_2 \quad \text{(Eq. 12)}$$

$$CO + 3H_2 \rightleftharpoons CH_4 + H_2O \quad \text{(Eq. 13)}$$

$$2CO + 2H_2 \rightleftharpoons CH_4 + CO_2 \quad \text{(Eq. 14)}$$

$$CO_2 + 4H_2 \rightleftharpoons CH_4 + 2H_2O \quad \text{(Eq. 15)}$$

Hence SOECs can utilise CO_2 to yield CO [97-100]. It is also possible for SOECs to utilise mixtures of H_2O and CO_2 to yield synthesis gas (H_2 + CO), which is known as co-electrolysis [101-105]. The cell resistance for CO_2 electrolysis is higher compared to H_2O electrolysis therefore the performance of SOEC is worse when CO_2 is utilised [97, 99, 101, 105, 106]. This potentially creates opportunities for disposal and conversion of industrial waste gas mixtures containing H_2O and CO_2. Synthesis gas (syngas) mixtures are already produced on a large scale for the manufacture of important commodity chemicals include methanol, ammonia, acetic acid and liquid fuels through Fischer-Tropch (F-T) processes. SOECs offer an alternative route towards CO_2 emissions reduction because they are fuel flexible and suitable for integration with many industrial resources in a variety of scenarios [107-112].

1.3.1.1. Utilisation of fuels in SOECs

The need to decrease CO_2 emissions and the rapid increase of interest for suitable synthetic fuels led to SOEC investigations. A lot of research is focused on co-electrolysis pathways where is suggested that the performance of H_2O electrolysis and H_2O/CO_2 co-electrolysis are similar [113, 114]. On the other hand, results from Graves *et al.* and Shi *et al.* show that H_2O electrolysis and CO_2 electrolysis both occurred in co-electrolysis due to the RWGS reaction and

CO_2 electrolysis producing CO [101, 115]. Conversion of pure CO_2 is kinetically slower due to slower conversion kinetics compared to electrolysis of pure H_2O and co-electrolysis of H_2O/CO_2. Also, pure CO_2 electrolysis can result to nickel oxidation on the Ni/YSZ fuel electrode causing degradation of the cell performance [116, 117]. Therefore, co-electrolysis of H_2O/CO_2 for CO_2 conversion to useful chemicals is more efficient [118]. The requirement of the RWGS reaction is not needed in co-electrolysis because CO_2 reduction takes place during co-electrolysis to form CO therefore the RWGS reaction is attributing to the CO production [105, 119]. Based on literature there are different synthetic routes that can take place for syngas production, where CO is produced by the RWGS reaction and H_2 is mostly produced by steam electrolysis [95].

Co-electrolysis with SOFC technology has previously been shown as an effective method to convert carbon dioxide, steam and mixtures thereof into syngas (H_2 + CO), which can be processed further to produce higher hydrocarbon fuels via F-T synthesis [120]. This type of process avoids the use of carbon capture and storage, which is proving to be a highly complex and expensive technology [121, 122]. Co-electrolysis also enables storage of electrical energy in the form of chemical energy, which can be readily used for power production. In addition, co-electrolysis can be integrated with various renewable and industrial waste resources [123-125] and can therefore contribute simultaneously to CO_2 reduction pathways, mitigation of industrial carbon emissions and energy storage.

Alternatively, it is possible to co-electrolyse renewable feedstocks using H_2O and CO_2 in SOCs for syngas production. Many studies have shown that fuel-assisted SOECs can reduce the operating potential and the electrical power consumption, increasing the efficiency of the cell [126, 127]. It has been demonstrated that addition of hydrogen to H_2O/CO_2 mixtures significantly improves the performance of SOECs by preventing oxidation of the Ni/YSZ anode [128]. Martinez-Frias *et al*. showed that natural-gas assisted cells displayed a voltage reduction when compared to conventional steam electrolysers and also improved the efficiency [129]. Another study by Wang *et al.* showed that the electrochemical potential required for co-

electrolysis ca be decreased by the addition of reducing gases such as CH_4 and CO in the anode [130, 131]. In addition, methane can assist co-electrolysis because it creates a reducing atmosphere at the anode, which decreases the oxygen partial pressure between the electrodes.

However, methane assisted co-electrolysis is a very complex process because methane conversion is a slow process and there are many catalytic and electrochemical reactions that can take place [128]. Another concern is carbon deposition, which is well-known to take place easily when CH_4 is present due to cracking. Carbon deposition is strongly affected by the operating temperature and steam-to-carbon ratio [74-77]. Studies have shown that carbon deposition could be suppressed and even eliminated in the methane fuelled SOECs by decreasing the operating temperatures, increasing current densities and by the presence of steam [71].

1.4. Fuel Cell Characterisation

In a chemical reaction, the Gibbs free energy changes with temperature, with the reactant pressure and concentration. When a change is applied to the amount of chemical species (such as the concentration) in a fuel cell, there is also a change in the free energy of the system, which leads to changes of the voltage of a fuel cell. Therefore, Gibbs free energy of a reaction can be stated as:

$$\Delta G = \Delta G^0 + RT \ln (a_{products} / a_{reactants})$$

where,

ΔG = Gibbs free energy of the reaction in equilibrium state
ΔG^0 = Gibbs free energy of the at standard conditions
R = ideal gas constant
T = temperature
a = activity of reactants or product species

Due to the electrochemical reactions taking place in a fuel cell and electrons being transferred during the reaction the Gibbs free energy can be stated as:

$\Delta G = -nFE^0$

To calculate the voltage with different reactant/product variations the theoretical reversible potential (E_{rev}) of a fuel cell can be calculated by using the Nernst equation:

$E_{rev} = E^o - (RT / nF) \ln (\Pi a^{vi} \text{ products} / \Pi a^{vi} \text{ reactants})$

where,

E^o = Ideal potential

R = universal gas constant

T = temperature (K)

n = number of electrons transferred in the cell reaction

F = Faraday's constant

Π = activity of species

vi = stoichiometric coefficient

The activity of each species must be raised by its corresponding stoichiometric coefficient. For example, if a reaction involves 2H, the activity of hydrogen must be raised to the power of 2. Relevantly, only chemical species that are in fact participating as reactants or products in the electrochemical reaction appear in the Nernst equation and the activities or partial pressures of unreactive, inert, or diluent species (such as He) are not included. The Nernst plots calculations have been included (see appendix A) going through the calculations in detail.

The actual voltage of a fuel cell is lower than the theoretical Nernst value due to activation (η_{act}), ohmic (η_{ohmic}) and concentration (η_{conc}) losses. The actual voltage of a fuel cell can be calculated by subtracting the various losses:

$$V = E_{rev} - \eta_{act} - \eta_{ohmic} - \eta_{conc}$$

Fuel cell performance is characterised by measuring the open circuit potential (OCP), the current-voltage (I-V) curve and the electrochemical impedance spectra (EIS). I-V curves shows the relationship between the voltage and current output of a cell (Fig 1.3). The size of the cell determines the amount of electrical current produced, voltage is plotted against current density, which is the amount of electrical current produced per unit of electrochemically active area. This enables the performance of different sized fuel cells to be compared. Temperature and fuel

composition can affect the performance of a fuel cell resulting in changes of the I-V curve from three main irreversibilities: (1) activation losses: caused by the slowness of the reactions taking place on the surface of the electrodes. Energy is required to carry out the electrochemical reactions, reduction of oxygen at the cathode and oxidation of the fuel gases at the anode causing reduced electrochemical potential. Therefore a fraction of the voltage produced is lost in driving the chemical reaction that transports the electrons to or from the electrode [132]. Activation losses can be minimised by increasing the reaction surface area and the operating temperature [133-135]. (2) Ohmic losses: caused by the resistance to the flow of electrons through the materials of the electrodes and interconnections and the resistance to the flow of ions through the electrolyte [132]. Ohmic losses can be minimised using high conductivity electrodes and by making the electrolyte thinner [136-138]. (3) Concentration losses: caused by the change in concentration of the reactants at the surface of the electrodes as the fuel is used. The decline of concentration is due to the failure to transport enough reactants caused by slow diffusion to the electrode surface which is also called ‘mass transport losses’ [132].

A power density curve can be produced (from the data of an i-V curve) by multiplying the voltage at each point on the i-V curve by the corresponding current density. Fig. 1.3 shows combined i-V and power density curves. The current supplied by the fuel cell is directly proportional to the amount of fuel consumed [6].

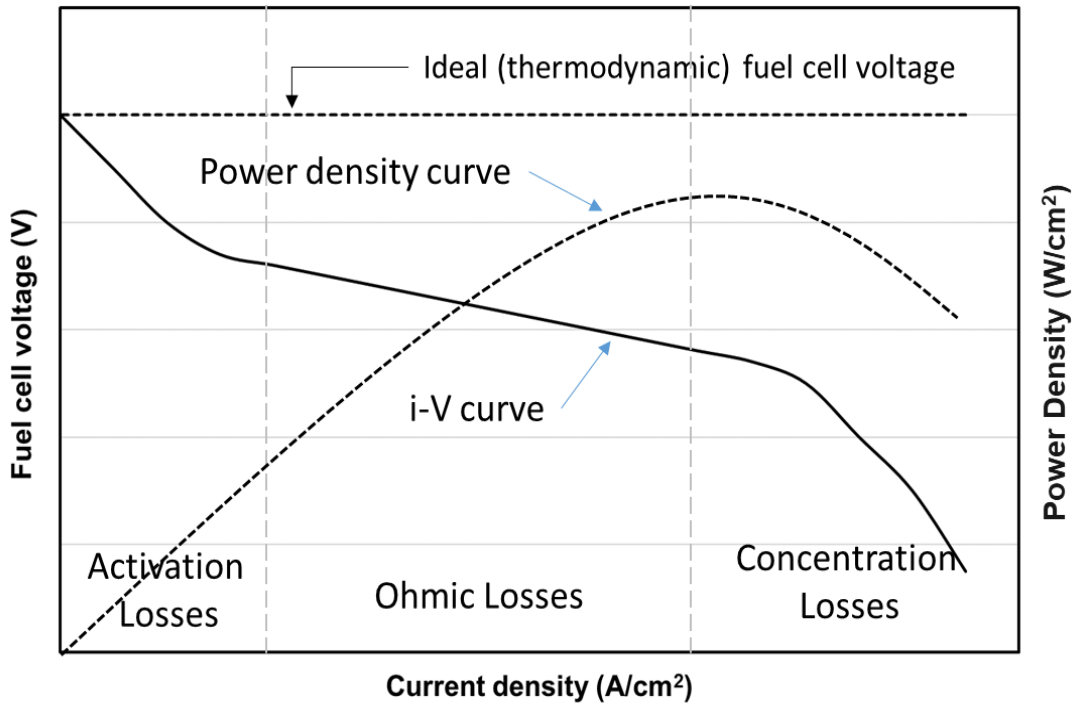

Figure 1.3: Fuel cell i-V curve and thermodynamically predicted fuel cell voltage. The corresponding fuel cell power curve is plotted on the secondary axis.

EIS is another technique for distinguishing the different losses, by measuring the ability of a system to impede the flow of electrical current. Impedance (Z) is the ratio between time dependent voltage (V(t)) and a time depended current (i(t)):

$Z = V(t) / i(t)$

The impedance data plots are known as Nyquist plots where the real (Z_{real}) and imaginary ($-Z_{imag}$) components are plotted (Fig. 1.4). Nyquist plots are made by many different frequencies and describe the impedance performance of a system over various orders of magnitude of frequency [6]. The Nyquist plot (Fig. 1.4) shows two arcs, where the size of each arc can be attributed to fuel cell losses. The first x-axis intercept denoted by Z_{Ω} corresponds to ohmic losses, the second x-axis intercept (first arc) denoted by Z_{fA} corresponds to anode activation losses and the third x-axis intercept (second arc) denoted by Z_{fC} corresponds to cathode activation losses. The size of each arc corresponds to the relative losses in a fuel cell.

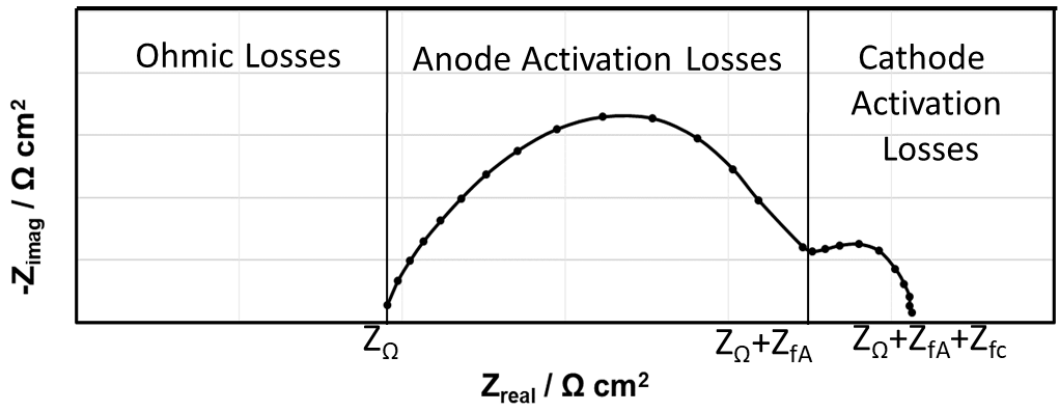

Figure 1.4: Electrochemical impedance spectra of a fuel cell

To examine further the losses taking place in a fuel cell impedance spectrum, an equivalent circuit model was designed. The model was designed with an inductance (L), a resistor (R) and capacitor (C) describing the behaviour of ohmic conduction processes and electrochemical reaction kinetics.

For ohmic losses the equivalent circuit representation is a resistor where,

$Z_{\Omega} = R_o$

Fig. 1.5 shows a Nyquist plot with two semicircles. The real-axis intercept corresponds to the ohmic resistance of the fuel cell model (R_o). The diameter of the high frequency arc (R_1) corresponds to the anode activation kinetics and the diameter of the low frequency arc (R_2) corresponds to the cathode activation kinetics. From the R_1 and R_2 values the kinetics of the anode and cathode can be calculated (C_1 and C_2) from the maximum point of each semicircle in the Nyquist plot. At the centre of each semicircle the value of 'ω' can be determined and by using the following equation (C_1 and C_2) can be determined:

$\omega = 1 / R_1C_1$

Therefore, by identifying the values of R and ω the capacitance value (C) can be calculated using the above equation.

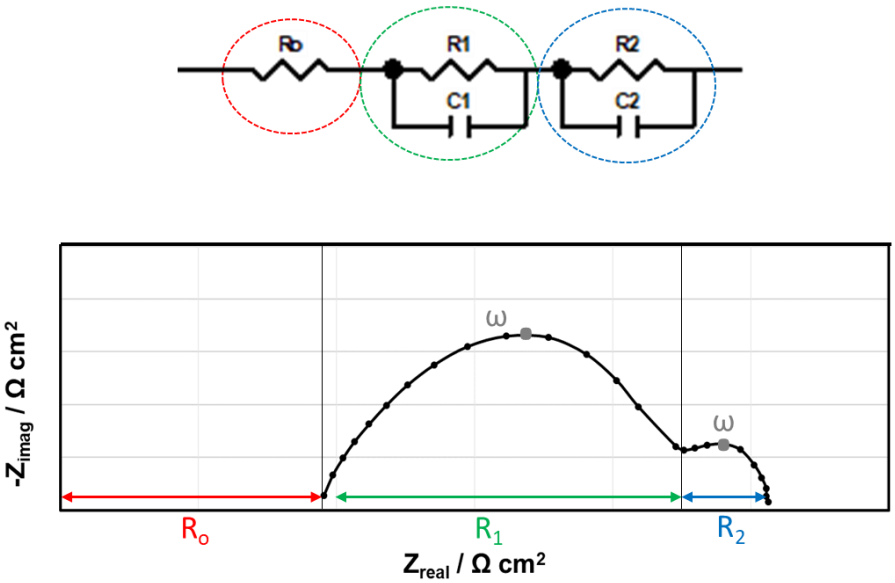

Figure 1.5: Circuit diagram and Nyquist plot for a fuel cell impedance model. The equivalent circuit for this fuel cell consists of an ohmic resistor to simulate the ohmic losses and two parallel RC elements to model the anode and cathode activation kinetics.

The spectrum can be well fitted with a more detailed equivalent circuit consisting of four RC parallel couples in series. Four processes are identified for the cell in the form of RC units and correspond to cathode polarization losses (RC-unit 1), RC-unit 2 is used to describe the electrochemical anode polarization losses and two RC-units (3 and 4) are used to describe gas diffusion and conversion at the anode. The circuit used to analyse the impedance spectra contains four units plus a serial contribution and an inductance contribution that mainly comes from current leads. To gain quantitative insights into the EIS data, the equivalent circuit in Fig. 1.6 was adopted for data fitting in ZView software (Scribner) [139]. One set of fitting results with percentage errors is shown alongside impedance spectra. Further work needs to be done to produce a more accurate model that reflects and describes the losses in greater detail.

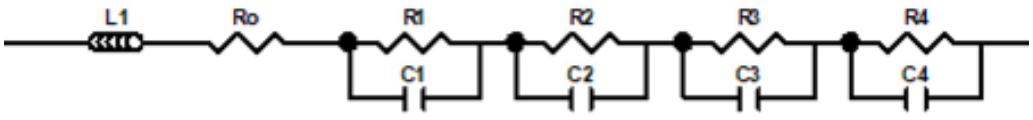

Figure 1.6: Detailed circuit diagram for a fuel cell impedance model. The equivalent circuit for this fuel cell consists an inductor (L1), of an ohmic resistor to simulate the ohmic losses (Ro), and four parallel RC elements to model the anode and cathode activation kinetics.

1.5. SOFC Materials

SOFC have great potential to reach the future demand for efficient and clean energy but development of SOFC technology into commercial products is challenging. SOFC materials should be widely available, cost effective, and easy to manufacture. Materials should be environmentally benign to produce, handle and dispose. Materials should also have a long operating lifetime (high durability).

1.5.1. Electrolyte Materials

The electrolyte is responsible for the transport of oxygen ions between the cathode and the anode. The ideal properties of an electrolyte are: (1) high oxygen ion conductivity to minimise ohmic losses, (2) negligible porosity to prevent fuel and oxidant gases from mixing (gas crossover) and therefore ensure that the fuel cell reactions (Eqs. 2 and 3) occur separately [140], (3) low electronic conductivity to prevent loss of current, (4) good mechanical strength, (5) high stability in both oxidizing and reducing environments, (6) excellent thermal and chemical stability at high temperatures, (7) similar thermal expansion coefficients to other components to prevent cracking/delamination of components and (8) chemical compatibility with other components.

The most widely used electrolyte material for high temperature (> 750 °C) SOFCs is yttria-stabilized zirconia (YSZ) [141], the structure of which is depicted in Fig. 1.7. Doping zirconia (ZrO_2) with yttria (Y_2O_3) stabilises the crystal structure into the cubic fluorite phase across all temperatures up to the melting point of 2,680 °C. The oxidation state of zirconium is 4^+, whilst yttrium has an oxidation state of 3^+. Therefore, doping zirconia with yttria creates a charge imbalance, which is compensated for by the creation of oxide ion vacancies. Oxide ions are conducted through the YSZ lattice by moving from one oxide ion vacancy to another. Increasing the number of oxide ion vacancies and stabilisation of the crystal structure into the cubic fluorite phase enhances oxygen ion conductivity, since oxygen ions are relatively big and the extra space made available reduces the activation energy associated with oxide ion hopping between vacancies. Increasing the quantity of yttria in YSZ to 8 mol% increases the number of

oxygen ion vacancies present, increasing the oxide ion conductivity of the material. However, when more than 8 mol% yttria is added, the yttrium ions themselves fill the oxide ion vacancies, causing the oxygen ion conductivity to decrease. In addition, the material starts to become very brittle, decreasing mechanical strength and ease of handling. Optimum oxide ion conduction is achieved at 8 mol% yttria (8-YSZ), which is the most widely used electrolyte material for high temperature SOFCs. YSZ is the most widely used material because whilst not perfect it meets many of the requirements, but the biggest challenge is reducing the high operating temperatures whilst keeping the high ionic conductivity of YSZ [142-144].

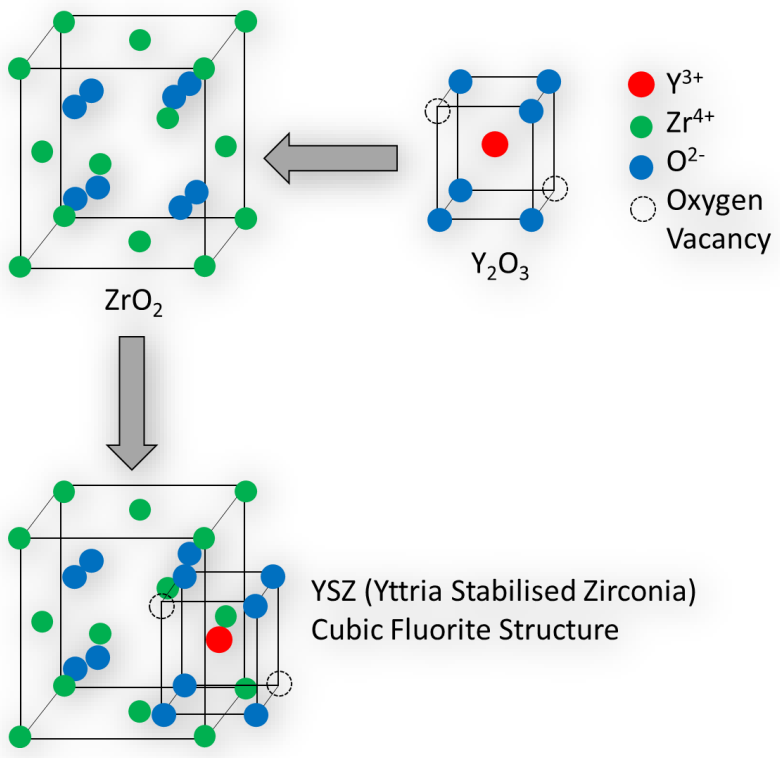

Figure 1.7: The crystal structure of cubic fluorite YSZ adopted from [145].

Alternative electrolyte materials have been investigated that can provide better conductivity than YSZ with interest also aiming in lowering the operating temperature because YSZ only works at high temperatures. Alternative electrolytes are being considered such as scandium doped zirconia which is more conductive than YSZ allowing fuel cell operation at lower temperatures [146-148]. Scandia-stabilised zirconia ($Sc_2O_3ZrO_2$) is another potential

replacement because it possesses highest ionic conductivity compared to YSZ allowing lower operating temperatures [149] and also it has higher mechanical strength compared to YSZ, therefore it can be manufactured as a much thinner electrolyte than YSZ, decreasing ohmic losses. These advantages have led many groups to study SSZ [150-153].

Doped ceria is another potential candidate material that has significantly higher oxygen ion conductivity than YSZ and is the most suited and the main material used to intermediate temperature (550-650 °C) SOFCs. At temperatures more than 600 °C, CGO is partially reduced and the formation of Ce^{3+} ions produce electron holes, which make ceria electronically conductive. Ionic conductivity is reliant on the type and concentration of the dopant ions with samaria (Sm) SDC and gadolinia (Gd) GDC giving the highest values of conductivity [154-156]. GDC offers higher conductivity at lower temperatures compared to YSZ but has disadvantages relating to electrical conductivity and mechanical instability [157].

Doped-perovskite materials are also used as electrolyte materials with the generic formula (ABO_3) where A and B are metal atoms such as zirconium, cerium or barium. Due to the two different metal cation sites accessible for substitutions lanthanum gallate ($LaGaO_3$) has emerged as the most promising candidate due to it high oxygen ionic conductivity by substituting some of the lanthanum with strontium, calcium or barium. By substituting, some of the gallium with Mg^{2+} (LSGM) can increase the conductivity even further [158, 159]. LSGM have higher ionic conductivity than YSZ but not as high as GDC. $LaGaO_3$ materials are generally more expensive and more difficult to fabricate [160, 161].

1.5.2. Anode Materials

SOFC anodes must be stable under reducing conditions and have high catalytic activity towards electrochemical fuel oxidation. An anode material must have high ionic conductivity, high porosity and high electronic conductivity to enable enhanced interaction between oxide ions, free electrons and gaseous fuel. In addition, electronic conductivity is required to transport the electrons generated from the electrode reaction to the external circuit. Materials used for SOFC anodes must be refractory to tolerate high temperatures over long operation times. In addition,

chemical and physical stability are required also must have similar thermal expansion coefficient and be chemically compatible with other components [162].

The most widely used anode material is Ni-YSZ, which is composed of a porous YSZ structure on which particles of nickel have been dispersed. The metallic nickel has high catalytically activity towards the electrochemical reactions and has excellent electronic conductivity. The YSZ creates a structural framework which enhances the number of TPB sites. It also enables oxygen ion conductivity and helps to match the thermal expansion coefficient of the anode with that of the electrolyte, whilst acting as an inhibitor for the coarsening (at high temperatures nickel particles can experience sintering in which they agglomerate to form bigger particles, causing a loss of TPB area [163-165]) of the Ni-phase [6]. Even at high temperatures, Ni-YSZ anodes are chemically stable under reducing atmospheres and the thermal expansion coefficient is similar to that of an YSZ electrolyte avoiding tensions that could lead in delamination or in cracking. The performance of the anode is impacted significantly by the Ni/YSZ ratio, which must be above 30 wt% Ni in order to ensure sufficient electrical conductivity. In general, many Ni/YSZ anodes have a Ni content of ~ 60 wt% in order to achieve a balance of desirable properties. Like all nickel catalysts, Ni/YSZ is also extremely active towards catalytic hydrocarbon conversion, enabling SOFCs to run on carbon-based fuels (section 1.3).

Although Ni-YSZ anodes are widely used, they have several disadvantages such as low tolerance to sulphur impurities because H_2S can strongly be absorbed (section 1.3) on Ni-active sites causing a significant drop in the rate of electrochemical reaction occurring at TPBs [166, 167]. In addition, Ni-YSZ anodes have a tendency when operated with hydrocarbons fuels to form carbon deposits on the Ni particles blocking the electrochemical reactions causing deterioration in cell performance. To avoid carbon deposition steam can be supplied in the fuel stream to suppressing carbon formation. Another disadvantage is the oxidation reduction intolerance. Ni-YSZ anodes must be reduced to from NiO to Ni but if the anode is exposed to air at high temperatures can result the Ni to re-oxidise causing the anode's structure and strength to minimise. Therefore, anodes must be kept at reducing conditions during operation.

Ceria-based materials are being investigated as suitable candidates for SOFC anodes due to their ability to supress carbon deposition which enables the direct use of hydrocarbons fuels [168-170]. Doped-ceria is good electrocatalyst (like Ni) for methane oxidation [171] and is less susceptible to carbon deposition [172] because doped-ceria is a good electron conductor which extends the active area that the electrochemical reaction can occur and good oxygen ion conductor in reducing environments [173]. The higher the dopant concentrations for ceria anodes the better ($Ce_{0.6}Gd_{0.4}O_{1.8}$, GDC40). The performance of ceria based anodes can be considerably enhanced by the addition of Ni, Co, Pt, Rh, Pd or Ru [174-176]. Another approach to enhance the electrochemical performance is by using nanoparticles which increase considerably the density of reaction sites [177, 178].

Perovskite oxides are another potential candidate for SOFC anodes due to their ability to supress carbon deposition. LSCV ($La_{0.8}Sr_{0.2}Cr_{0.9}V_{0.03}O_3$) is a perovskite material typically mixed with YSZ providing improved stability and thermal expansion. LSCV-YSZ anodes showed electrochemical performance similar to Ni/YSZ but with greater resistance to carbon deposition but don't provide improved catalytic activity for methane reforming.

1.5.3. Cathode Materials

Cathodes must provide high electrical and ionic conductivity, good stability under oxidising conditions, high activity towards the electrochemical reduction of oxygen and good chemical and thermal compatibility with other cell components. Generally, cathodes used in SOFCs are ceramic-based because metallic electron conductors are not stable in high temperature oxidising environments. Lanthanum strontium manganite ($La_{0.5}Sr_{0.5}MnO_3$ - LSM) is the most widely used material in high temperature SOFCs. It is usually applied as a composite with YSZ (50/50 wt% LSM/YSZ) in order to improve compatibility with the electrolyte and enhance the TPB area.

LSM can reduce oxygen due to the divalent Sr^{2+} dopant at the B-site, which it shares with the La^{3+} cation. Doping with Sr^{2+} makes LSM a p-type semiconductor, allowing Mn^{3+} to access the Mn^{4+} oxidation state. Under oxidising conditions, the Mn^{3+} cations are oxidised to Mn^{4+} resulting in the production of O^{2-} ions and electrons coming from the anode reduce the Mn^{4+}

back to Mn^{3+} and the cycle repeats again. Despite having suitable electronic and ionic conductivity and been studied and used frequently in SOFC cathodes LSM is inadequate for operating in lower temperatures. Therefore, there is interest in lanthanum strontium cobalt ferrite (LSCF) which is been investigated as an alternative because it can operate in lower temperatures (700 – 800 °C).

1.6. SOFC Membrane Electrode Assembly

The Membrane Electrode Assembly (MEA) is the assembly of the anode, cathode and electrode, which are the three key components of a fuel cell. The MEA can be manufactured in three different designs: Electrolyte-Supported Cell (ESC), Cathode-Supported Cell (CSC) and Anode-Supported Cell (ASC). The differences between these designs are illustrated in Fig. 1.8.

ESCs have a thicker electrolyte layer than ASC and CSC. The electrolyte provides mechanical strength to the cell, making ESCs the most robust MEA design. However, the thicker electrolyte layer means that ESCs have the poorest electrical performance and generally operate at a higher temperature to ensure good conduction of oxide ions. ESCs generally have increased ohmic losses compared with other MEA designs. The anode layer is also much thinner which limits ESCs to operation on H_2 only. Their performance on CH_4 and other carbon-based fuels is low and therefore the fuel flexibility of ESCs is limited, however, due to the thick and strong electrolyte layer, ESCs can be made using less expensive materials and manufacturing techniques.

CSCs and ASCs have a thicker cathode and anode layer respectively, which provide the mechanical support. Both designs have a thinner electrolyte which allows the cell to operate at lower temperatures and generally gives much higher electrical performance. The thinner electrolyte layer reduces the resistance towards oxide ion conduction and therefore significantly decreases the ohmic losses. The mechanical robustness of CSCs and ASCs are not as good as ESCs, with cracking or delamination much more likely. ASCs are widely used due to the thick anode layer, which enables much more efficient conversion of a wide range of fuels including methane and other hydrocarbon-based fuels as well as ammonia. Due to the thin structure of the

electrolyte, ASCs and CSCs are not as mechanically robust as ESCs and they are also much more expensive (£0.022 per square centimetre for an ESC and £0.035 per square centimetre for an ASC [23]). However, ASCs generally have the highest performance and fuel flexibility of all MEAs. The thickness of SOFC MEA is shown in Fig. 1.8. In order to maintain mechanical stability, a thick anode is used as support for the thin electrolyte. ASCs use the same electrode and electrolyte materials as the ESCs. Compared with ESCs, ASCs can deliver higher power outputs and can be operated at lower temperatures due to the use of a thick anode and the cell stability can be enhanced

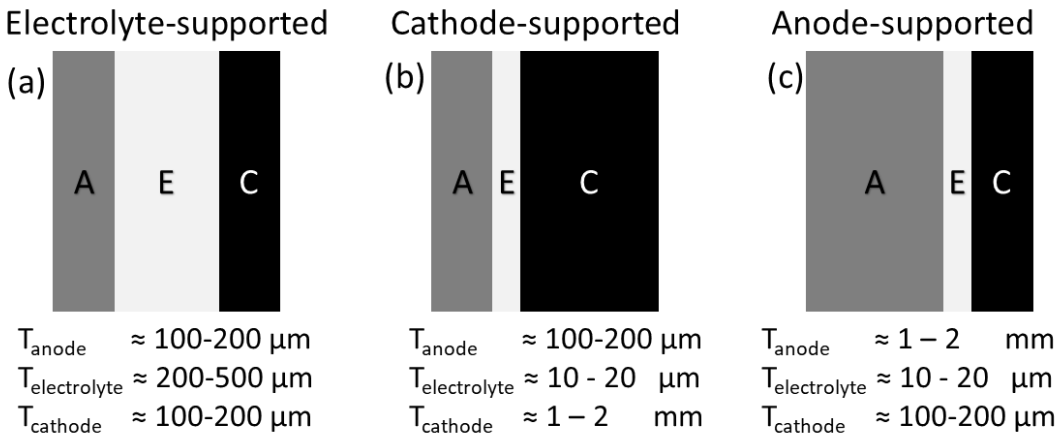

Figure 1.8: SOFC MEA thickness: (a) electrolyte supported cell, (b) cathode supported cell and (c) anode supported cell (adopted from [6]).

1.7. Aims of the PhD

The first objective of the project was to design and construct a SOFC testing system. The aim of the research was to investigate the performance of SOFC with biomass-derived fuels.

Aims of research:

1. Investigate the utilisation of biohydrogen and biohythane in SOFC technology and explore the implications for decarbonisation of natural gas grids

2. Characterise the use of electrolyte-supported cells and anode-supported cells in fuel cell mode and electrolysis modes of operation including co-electrolysis with H_2O and CO_2
3. Establish the effects of fuel variability and operating temperature on SOFC performance and outputs
4. Characterise fuel conversion mechanisms and SOFC outputs using combined electrochemical techniques and online mass spectrometry

1.8. Overview of Thesis

Chapter-2 includes a literature review on utilisation of biomass-derived fuels in SOFCs. This chapter reviews how biomass is utilized in different ways to enable production of useful feedstocks from organic waste focusing on different fuel mixtures yielded from biomass and how they can be upgraded and cleaned for injection into the natural gas grid and decarbonisation. The chapter also analyses the utilisation of biogas, biohydrogen, biohythane and other biomass-derived fuels in SOFC.

Chapter-3 includes material specifications for the electrolyte and anode supported SOFC used in this work. Experimental methods are included explaining how the cell was mounted, how electrical connections were made and how fuel delivery and output gas recovery was achieved. In addition, the cell heating and conditioning is described. Lastly, electrochemical measurements and anode output gas analysis via a quadrupole mass spectrum (QMS) are explained.

Chapter-4 shows how biologically produced mixtures of H_2 and CO_2 can potentially be utilised in an electrolyte and an anode supported cell. This chapter investigates solid oxide electrolysis of biohydrogen for the first time and is compared directly with fuel cell mode utilisation. The performance and fuel processing of SOFCs utilising biohydrogen have been characterised at different operating temperatures and the effects of fuel variability on SOFC overpotentials and outputs have been established. A direct comparison of an ESC and an ASC operating on biohydrogen both in fuel cell and electrolysis mode was also investigated.

Chapter-5 describes a novel and highly efficient method of utilising renewable and industrial waste gases with co-production of energy and useful chemicals using SOFCs. This chapter shows, the gain in energy yield from two-stage AD to be supplemented with additional gains in SOFC efficiency, resulting in an increased electrical energy yield from biomass overall compared with utilisation of biogas from single-stage AD in SOFCs. In addition, this chapter investigates the effects of biohythane fuel variability on the performance and fuel processing of the cell. A long term biohythane durability test was also carried out.

Chapter-6 explores the co-electrolysis of biohythane with various co-oxidants H_2O (steam), H_2/CO_2 (50/50 vol%) and CO_2 using an ASC for high quality syngas production. In addition, biohythane was compared with other-biomass derived fuels to investigate fuel processing and syngas production. Furthermore, biohythane fuel variability was examined and SOEC overpotentials and outputs have been established.

Chapter-7 includes a summary of the thesis, implications of research, future work and closing remarks.

Chapter 2: Literature Review

2.1. Overview of biomass-derived fuels

The need to increase the share of power production from renewable and low-carbon resources has led to increased use of biomass [179-184]. Biomass can be utilised in different ways, with anaerobic digestion (AD) being one of the most widely used and efficient technologies [185-187]. AD is an established and widely deployed technology that enables the production of useful feedstocks from food and organic wastes [188].The process involves bacterial digestion of organic substrates in the absence of oxygen [189], yielding a nutrient-rich digestate and a biogas mixture and trace levels of contaminant gases [190]. The digestate can potentially be utilised as fertiliser, whilst the biogas can be used as a fuel which, provided the initial waste is sourced and managed sustainably, is a renewable and low-carbon resource [191].

AD takes place in four steps: (1) hydrolysis, (2) acidogenesis, (3) acetogenesis, and (4) methanogenesis [192]. In the first two steps, the waste substrate is converted into H_2 and CO_2 (biohydrogen) and a liquid phase rich in short-chain C1-C5 carboxylic acids and alcohols [123]. In step three, the H_2 and CO_2 are converted into carboxylic acids, which are converted in step four by CH_4-producing bacteria into CH_4/CO_2 (biogas) and a nutrient-rich digestate [193]. AD is a complex process where each step requires different populations of bacteria [186]. Conventionally, AD is carried out as a single stage process, where all four steps are conducted within a single reactor vessel.

Biogas can be upgraded and cleaned to yield biomethane for injection into natural gas grids [3, 194], thereby helping to achieve decarbonisation. Decarbonising natural gas grids is of great importance since they provide significant amounts of energy for heating, electricity production and manufacturing all over the world [195, 196]. The greenhouse gas emissions resulting from natural gas consumption are considerable due to fugitive CH_4 emissions and the CO_2 emitted

upon oxidation [197, 198]. Decarbonisation of natural gas grids is urgently required due to the lack of progress in heat decarbonisation and the increasing demand on electricity grids.

However, gas upgrading has been well studied for biogas to biomethane processes [199-202] and a comparison of established gas upgrading technologies is shown in Table 2.1. Each of these technologies requires electrical energy and in some cases heat energy, whilst most also have a consumables demand and do not operate effectively under partial load. The use of a gas upgrading technology represents a capital and operational cost to the consumer. Furthermore, there is an inevitable loss of fuel, which decreases the net energy gain and causes fugitive fuel emissions.

Table 2.1: Comparison of biogas upgrading technologies. Information and values applicable for production of biomethane from biogas [199-202].

Parameter	**Water scrubbing**	**Organic physical scrubbing**	**Amine scrubbing**	**Pressure swing absorption**	**Membrane separation**
Electrical energy demand / kWh m^{-3}	0.40-0.50	0.45-0.70	0.25-0.35	0.40-0.50	0.25-0.45
Operating temperature / °C	-	70-80	120-160	-	-
Consumables demand	Antifouling and drying agents	Organic solvents	Amine-based solvents	Activated carbon	-
Partial load range	50-100%	50-100%	50-100%	85-100%	50-100%
Typical capital costs / €$(m^3\ h^{-1})^{-1}$	3.5-10.0	3.5-9.5	3.-9.5	3.7-10.0	3.5-7.6
Typical operational costs / € m^{-3}	0.09-0.14	0.09-0.14	0.11-0.14	0.09-0.13	0.07-0.16
Methane recovery	98%	96%	>99%	98%	80-99.5%

SOFCs have been shown to operate with a high efficiency on biogas and related fuels without the need to remove CO_2. Previously published work is reviewed in the following sections. Their ability to operate on fuel mixtures composed of CH_4, CO_2 and H_2 makes SOFCs compatible with efforts to decarbonise natural gas grids via addition of pure H_2, biomass-derived gas mixtures as well as biomethane [78].

2.1.1. Biogas

Biogas mainly consists with CH_4 (50-80 vol%) and CO_2 (30-50 vol%) and depending on the biomass source, biogas also contains variable levels of impurities such as H_2S, NH_3, siloxanes and tars [203-205]. The increasing usage and production of biogas has led to a significant amount of previous research into biogas utilisation in SOFCs [206-209]. The utilisation of biogas mixtures [3, 69, 87, 88, 194, 210-212] have shown that carbon deposition [213-215] caused by excessive methane decomposition and sulphur poisoning [216-218] are the main degradation issues with this fuel mixture making the utilisation of biogas in SOCs challenging [219-223].

To address carbon deposition when operating on pure CH_4 the addition of steam or CO_2 is usually required [224]. Many studies indicate therefore that it is not necessary to remove CO_2 from biogas and that SOFC performance is considerably improved by keeping CO_2 present [225-227]. Further studies from Lanzini *et al.* [228] and Johnson *et al.* [229] suggested the addition of more CO_2 in the biogas mixture had a beneficial effect on carbon formation, decreasing the cell degradation.

Laycock *et al.* [230] indicated that direct electrochemical conversion of CH_4 not contributing significantly to electrical power production, with fuel utilisation proceeding via CO_2 reforming of CH_4 and subsequent electrochemical oxidation of H_2 and CO, further demonstrating the benefit of keeping CO_2 present. The presence of CO_2 also inhibits carbon formation, prolonging cell degradation processes [84]. In addition, CO_2 reforming of CH_4 is highly endothermic and

therefore assists with stack cooling. Studies indicate the optimum CH_4 content of biogas to be in the range 30-45 vol% [84, 231]. Biogas mixtures containing 45 vol% CH_4 have yielded the highest SOFC performance, although 30 vol% CH_4 ensures complete prevention of carbon deposition.

2.1.2. Biohydrogen

Mixtures of H_2 and CO_2 can be produced from numerous processes including dark fermentation, photo-fermentation, indirect biophotolysis and bioelectrochemical techniques [232-235]. These techniques limit AD to steps 1 and 2 only (see section 2.1). H_2/CO_2 mixtures produced from these types of processes are widely known as 'biohydrogen' and typically have a 50/50 vol% H_2/CO_2 content (see Table 2.2). Like biogas, they are variable mixtures and contain trace levels of sulfur, nitrogen-, and carbon-based contaminants [80, 236]. Crucially, they avoid the need to handle methane, which is a very potent greenhouse gas.

Table 2.2: Typical composition of gases from biohydrogen production processes [80].

Component	Biohydrogen
Hydrogen	35-50 vol%
Carbon dioxide	50-55 vol%
Nitrogen	3-8 vol%
Carbon Monoxide	<0.001 vol%
Methane	<0.01 vol%
Sulfur-containing compounds	<200 ppm
FigOther impurities	<2 vol%

Biohydrogen mixtures can potentially be utilised in various technologies including internal combustion devices and fuel cell technology [79-81, 199, 200, 236-239]. Combustion engines

and low temperature fuel cells require prior removal of CO_2 due to the very strict fuel composition requirements of these devices. Utilisation of biohydrogen in SOFC technology removes the need to upgrade the fuel mixture because SOFC devices are fuel flexible and have no strict requirements for CO_2 removal. Desulfurisation of biohydrogen would still be necessary but would not require an energy intensive or complex gas upgrading system. In fact, the significant presence of H_2 in biohydrogen is likely to increase the sulfur tolerance of SOFCs in comparison with operation on a carbon-based fuel such as natural gas or biogas [80, 81, 240]. The absence of methane in biohydrogen has been shown to make SOFCs less prone towards carbon deposition, which is a significant problem for operation on methane-based fuel mixtures [69-72, 80, 212, 241-243].

Utilisation of biohydrogen in SOFCs has been demonstrated in fuel cell mode with comparable performance to that observed when operating on pure H_2 [238]. Biohydrogen is more versatile than biogas and can also potentially be very efficiently electrolysed in SOFCs to yield useful mixtures of synthesis gas (H_2 + CO). Conversion of biohydrogen in a reversible SOFC device therefore also gives energy production and storage flexibility, since electrical power or synthesis gas can be produced as required using a single SOFC device with combined efficiencies over 90% [16, 244], reducing investment costs and payback times. However, significant technological development is required in order to reduce the capital costs of SOFC devices [89, 91, 100, 101, 116, 140, 245-248].

Previous work into the utilisation of biohydrogen in SOFC devices has focussed on fuel cell mode operation to yield electrical power and heat [79-81, 236-238]. Leone *et al.* [80, 81] have shown that conversion of biohydrogen is closely related to the Reverse Water Gas Shift (RWGS) reaction (Eq. 16):

$$H_2 + CO_2 \rightleftharpoons H_2O + CO \qquad \text{(Eq. 16)}$$

A computational study by Razbani *et al.* [237] illustrated the importance of the RWGS reaction to the performance and cooling requirements of SOFCs running on biohydrogen. The RWGS reaction is kinetically fast and thermodynamically favourable over nickel catalysts at SOFC

operating temperatures [249-252]. It causes the presence of H_2 to decrease and CO to increase, and therefore has a negative effect on the open circuit potential (OCP) of SOFCs. The RWGS reaction is mildly endothermic ($\Delta H = +41$ kJ mol^{-1}) and therefore reduces stack cooling requirements in comparison with pure H_2 or H_2/ N_2 mixtures; however, stack cooling requirements are increased in comparison with biogas utilisation in SOFCs, where fuel conversion proceeds simultaneously with the highly endothermic CO_2 ($\Delta H = +247$ kJ mol^{-1}) or steam reforming ($\Delta H = + 205$ kJ mol^{-1}) reactions [69-72, 212, 241-243, 248]. Nevertheless, the overall performance and durability of SOFCs is better for biohydrogen due to the absence of methane, which causes significant problems relating to carbon deposition for SOFCs running on biogas mixtures [236].

A separate study by Razbani *et al.* [79] investigated the effects of various SOFC operating parameters on biohydrogen utilisation. It was shown that increasing the operating temperature increases the overall cell performance due to increased activation and ohmic efficiencies, as well as a shift in the RWGS equilibrium. In addition, investigations into fuel variability show that cell performance is generally increased with increasing H_2 content of the fuel due to decreased activation losses, better heat distribution across the cell from the fuel cell reactions and the reduced cooling effects of the RWGS reaction at high temperatures.

2.1.3. Biohythane

AD processes where all four stages are carried out in one reactor is referred to as single-stage fermentation [253]. However, it is possible to achieve further energetic gains from biomass by carrying out steps one and two in a separate reactor to stages three and four [124, 125, 254-257].

This is two-stage fermentation and enables each of the stages to be optimised separately to give an energy yield that is up to 46% greater compared with single-stage AD [232]. The first reactor yields biohydrogen (H_2/CO_2) and the second reactor gives biogas (CH_4/CO_2) these are then combined to produce a gaseous mixture typically composed of 60/30/10 vol% $CH_4/CO_2/H_2$ referred to as biohythane [124]. Two-stage fermentation therefore yields a gaseous feedstock which contains an additional presence of H_2 with a higher calorific value, gives lower

greenhouse gas emissions. Furthermore, the additional presence of H_2 makes biohythane easier and more beneficial to utilize than conventional methane-rich biogas [258] [256, 259].

There has been very little previous research undertaken into the utilisation of biohythane or $CH_4/CO_2/H_2$ mixtures in SOFCs. The main body of work has been carried out by Chen *et al*. [77], who studied these mixtures in the context of recirculating anode exhaust gases as a means of improving the fuel utilisation efficiency of methane-fuelled SOFCs. The study established the effects of fuel variability and investigated the performance of SOFCs operating on 30/60/10 vol% and 15/60/25 vol% $CH_4/CO_2/H_2$ mixtures. As such, this study investigated $CH_4/CO_2/H_2$ mixtures with higher CO_2 and lower CH_4 contents than are typically found in biohythane mixtures. It was found that fuel utilisation partly proceeds via CO_2 reforming of CH_4 (Eq. 17) and the RWGS reaction (Eq. 16).

$$CH_4 + CO_2 \rightleftharpoons 2H_2 + 2CO \qquad \text{(Eq. 17)}$$

The high content of CO_2 limited carbon formation reactions and carbon deposition was not reported to be a significant problem for the mixtures studied. However, thermodynamic calculations indicated that for higher CH_4 contents like biohythane, carbon deposition is likely to be a problem.

The substitution of natural gas with H_2 as a potential way to decarbonise natural gas grids, although they mainly focus on the addition of H_2 to CH_4 for the purposes of suppressing carbon deposition caused by methane cracking. Nikooyeh *et al.* [74] studied carbon deposition on Ni/YSZ composite powders exposed to various CH_4/H_2 mixtures with H_2/CH_4 ratios in the range 0-1.5. Temperature programmed oxidation measurements clearly indicated that carbon deposition was suppressed significantly as the H_2 content of the mixture was increased. In addition, carbon deposition under CH_4/H_2 mixtures was found to be less damaging to the microstructure of the cell compared with pure CH_4.

Escudero *et al*. [75] studied the effect of changing the CH_4/H_2 ratio on the performance and stability of an SOFC with a bimetallic Mo-Ni/CeO_2 anode material. It was found that increasing

the CH_4 presence decreased the current output of the cell and destabilised the OCP. Impedance spectra and I-V curves indicated the current output decreased due to the increased robustness and size of the CH_4 molecule, whilst the OCP instability suggested the occurrence of carbon deposition on the anode. Avoidance of carbon deposition could be achieved by using high current densities and it was noted by the authors that according to thermodynamic predictions, increasing the current density initially partially oxidises the carbon to CO at low and intermediate current densities before totally oxidising to CO_2 at high current densities, resulting in stable operation. The effect of increasing the operating temperature on the OCP was also established in this study, revealing that under high H_2 contents ($\leq$ 20 vol% CH_4), increasing the temperature caused the OCP to decrease, in accordance with Nernst predictions. Under higher CH_4 contents however, increasing the temperature slightly increased the OCP due to the presence of partial oxidation of CH_4.

Almutairi *et al.* [76] investigated a 100 W SOFC system operating on H_2 containing up to 20 vol% CH_4. In agreement with previous research, increasing the CH_4 content increased the OCP and the activation overpotentials, overall resulting in better cell performance. However, the performance degraded during long-term tests as a result of carbon deposition, which accumulated within the pores of the anode, preventing electrochemical conversion and fuel diffusion. Removal of carbon was found to be difficult and complex.

2.1.4. Other related fuel mixtures

Other mixtures containing CH_4, H_2 and CO_2 include gasifier exhaust gas mixtures, which have a typical (but variable) composition of 50/15/20/12/3 vol% N_2-H_2-CO-CO_2-CH_4 [44]. Under some conditions, CO is an important electrochemical reactant which makes a significant contribution to electrical power production and in some cases gives better performance than H_2. CO_2 decreased the OCP of the cell but not the overall cell performance and under some conditions increased the power density of the cell due to the RWGS reaction. Finally, CH_4 does not negatively impact on the performance of the cell, although due to being present in very low

concentrations, it is not clear whether CH_4 makes a contribution to electrical power production directly, indirectly or at all.

Chapter 3: Materials and Experimental Methods

3.1. Button Solid Oxide Fuel Cells

Measurements with electrolyte-supported cells were acquired using FCM NextCell-2.0 (SKU: 213205) cells. These cells were composed of a 150 μm thick scandium-stabilised zirconia electrolyte, a 50 μm NiO-GDC/NiO-YSZ (yttria-stabilized zirconia) anode and a 50 μm LSM/LSM-GDC cathode (where LSM is Lanthanum Strontium Manganite and GDC is Gadolinia-doped Ceria).

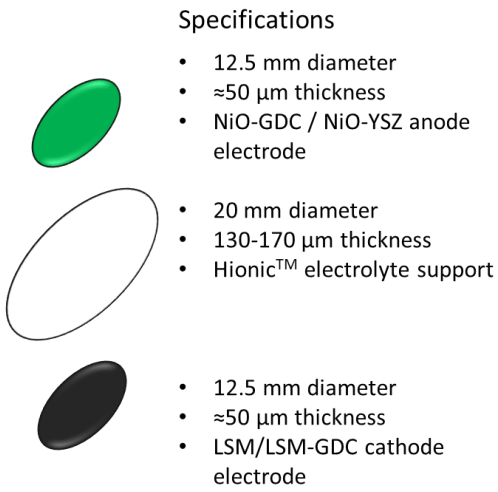

Figure 3.1: Specifications of the electrolyte-supported fuel cell adopted from [260] .

Measurements with anode-supported cells were acquired using two commercially available cells. The first cell was the FCM ASC-2.0 (SKU: 213308) which was composed of a 3 μm 8-yttria-stablised zirconia (8-YSZ) electrolyte layer, a 3 μm GDC barrier layer, a 400 μm NiO-YSZ anode and a 12 μm lanthanum strontium chromite (LSC) cathode. The diameter of the anode and electrolyte layers was 20 mm and the diameter of the cathode was 12.5 mm. The second one was the Fiaxell 2R-Cell™ button cell which was composed of a NiO anode (thickness 0.2-1.0 mm), an yttria-stabilised zirconia (8-YSZ) electrolyte (thickness 5-20 μm)

and a 60/40 vol% LSCF/GDC (Lanthanum Strontium Cobalt Ferrite, Gadolinia-doped Ceria) composite cathode (thickness 2.5 μm).

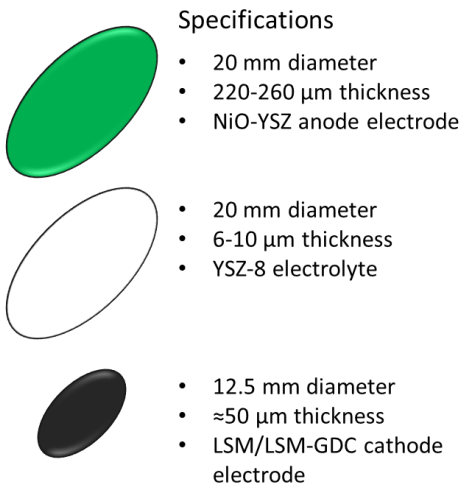

Figure 3.2: Specifications of the anode-supported fuel cell adopted from [260].

3.2. Cell Mounting and Connections

Cells were tested using a Fiaxell Open Flanges SOFC test set-up [261] (see Fig. 3.3). This system enabled testing of planar cells of any shape and size up to 5 × 5 cm and involved pressing the cell in between two Inconel steel flanges (made with Inconel 600 and 601), were fuel and oxidant gases supplied separately. Fuel was supplied via the diffuser (see Fig. 3.4) which was firstly inserted into the fuel inlet tube of the anode flange. The diffuser also had a nickel rod attached to make electrical connection to the cell. This was insulated from the cathode-side components by being positioned within a ceramic tube. Fuel was supplied to the anode of the cell to the centre of the cell from the two and the output gases were recovered via the two peripheral tubes as shown in Fig. 3.3.

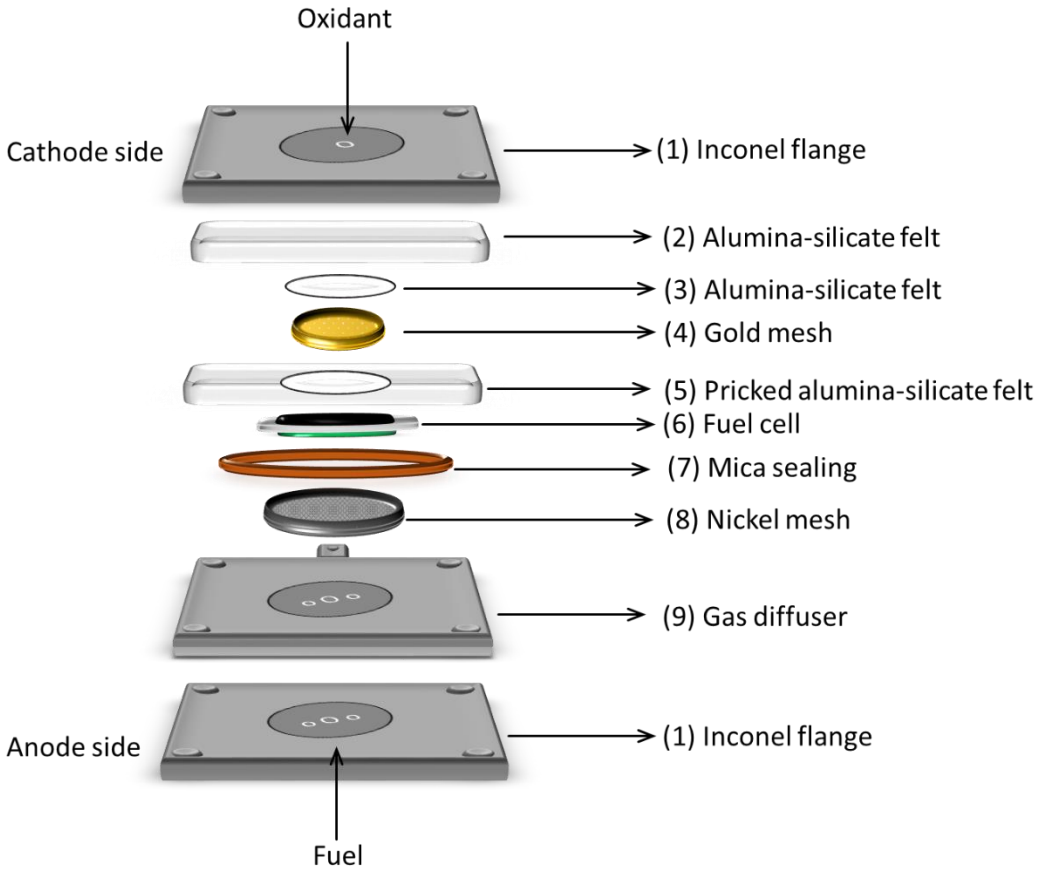

Figure 3.3: Cell mounting schematic setup displaying gas tight seals and insulation between the flanges of the setup.

To mount the cell, a piece of nickel foam (0.5 mm width) was secured with silica-free glue on the diffuser with the dimension of the cell (see Fig. 3.3, no. 8). A piece of deformable mica (0.5 mm width see Fig. 3.3 no. 7) with a hole-punched in the middle the size of the nickel foam was centred around the nickel foam. Then the mica was placed on the diffuser such that the nickel foam was in the hole punch of the mica. The cell was then placed on top of the nickel foam with the anode in contact with the nickel foam and was held in place with a small piece of silica free scotch tape. A sheet of alumina-silica felt (5 x 5 cm Fig. 3.3 no. 5) with a hole in the centre of the felt to allow contact between the gold mesh and cathode of the cell was placed on top of the cell. Then the gold mesh with gold wires was placed on top of the cathode of the cell (Fig. 3.3 no. 4) and on top of that the remaining alumina silicate felt (Fig. 3.3 no. 3) followed by a second

sheet of alumina-silicate felt was placed over the top of everything, covering and electrically insulating the gold mesh and wires (Fig. 3.3 no. 2).

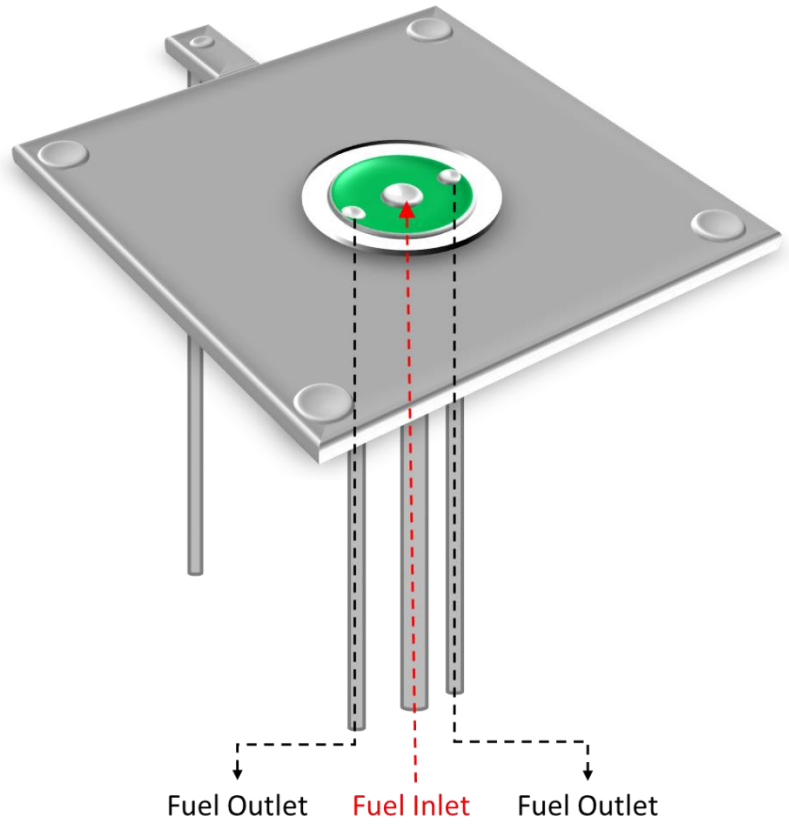

Figure 3.4: Gas diffuser used in fuel cell testing with fuel inlet and outlet ports

The flanges were tightened using four external springs and screws, which applied pressure to the flanges uniformly. The springs were compressed to 26-27 mm (measured with calipers), generating a pressure of 18 kg/turn[1] needed to create a gas tight seal. The precise temperature of the cell was measured using a type-K thermocouple, which was positioned in a dedicated tube near to the cell on top of the alumina felt. The thermocouple was connected to a temperature display and used to monitor the precise temperature at the cell. The flanges were then spring loaded, completing the cell mounting procedure.

[1]For one turn of wingnut: 0.8mm * 2.8 kg/mm = 2.24 kg per spring. With 4 springs the total pressure per turn is: 2.24 *4 ≈ 9 kg/turn

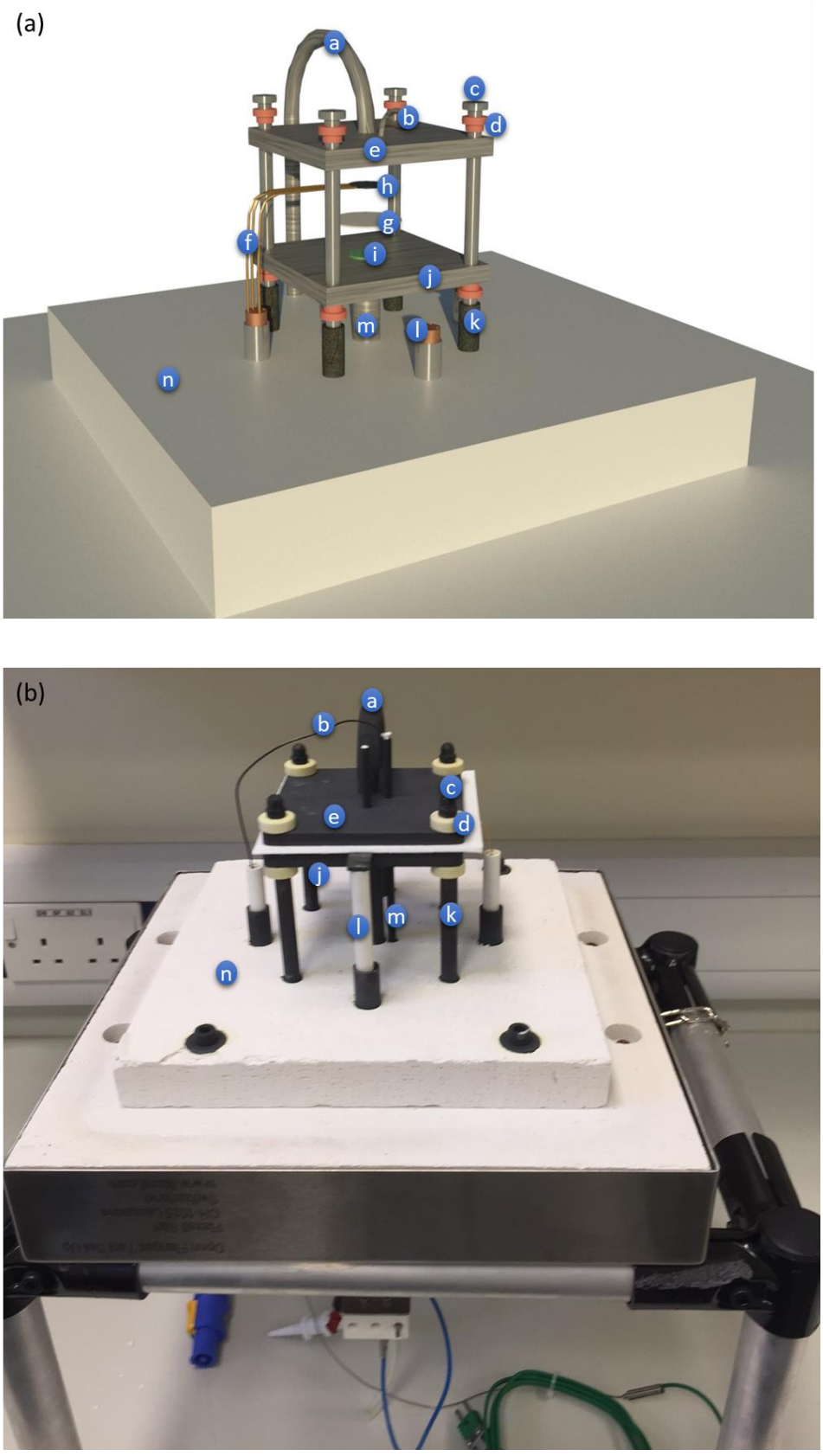

Figure 3.5: (a) Schematic and (b) open flanges head with fuel diffuser and thermocouple holder: (a) air feeding tube, (b) thermocouple, (c) spring loaded rod, (d) feed through bush, (e) Inconel upper flange, (f) gold mesh, (g) fuel cell electrolyte, (h) fuel cell cathode, (i) fuel cell anode, (j) Inconel bottom flange, (k) spring loaded steel tube, (l) 4 bores insulator ceramic tube, (m) fuel feeding tube and (n) ceramic insulation plates

Once mounted, the underside of the test set-up (containing the flanges) was placed inside a chamber furnace (Toploader Squadro SQ11 equipped with a Bentrup TC505 temperature controller), which was used to heat the cell to the required temperature. Silicone tubes were connected for the air inlet and stainless-steel tubes for the fuel outlet gases. For the fuel inlet, connections were achieved using 14 mm Swagelok fittings. Two 8 mm Swagelok fittings were used for the outlet gases. The current collection and voltage sensing wires were connected to a potentiostat (Ivium Technologies IviumStat.h), enabling electrochemical measurements to be carried out. The anode potential was measured by fixing the wire from the terminal plug to the 3 mm nickel rod using a crocodile clip. The anodic current flowed in the diffuser rod and was collected from a metallic clip. The cathodic current flowed through the two gold wires that were connected to the gold mesh and the current was collected using two terminal plugs.

3.3. Fuel delivery and output gas recovery

Fuel and air were delivered to the cell using the system shown in Fig. 3.6. Gases were handled using Nylon (RS PRO air hose NLF series/415-0389) tubing 6 mm × 8 mm (ID × OD). Air (Air Liquide, 99.99%) was supplied to the cathode connection using a rotameter. Fuel gas mixtures were supplied to the anode using a Bronkhorst Flow-SMS digital mass flow controller system, which enabled laminar flow delivery of gaseous mixtures containing H_2 (Air Liquide, 99.99%), CO_2 (Air Liquide, 99.99%), He (Air Liquide, 99.99%) CH_4 (Air Liquide, 99.99%), N_2 (Air Liquide, 99.99%) and Air (Air Liquide, 99.99 %). For details on how the mass flow controllers were laminated, see Appendix B. Product gases from the anode were collected continuously and fed into the QMS (Cyionics Ltd. and MKS Cirrus 2) fitted with a residual gas analyser, enabling continuous measurement of the product gas composition. It was necessary to remove H_2O present in the output gases using a silica gel desiccant in order to prevent flooding of the QMS capillary inlet line. The presence of H_2O in the output gases was therefore not measured. For details on how the QMS sensitivities were calculated and used for data correction, see Appendix C.

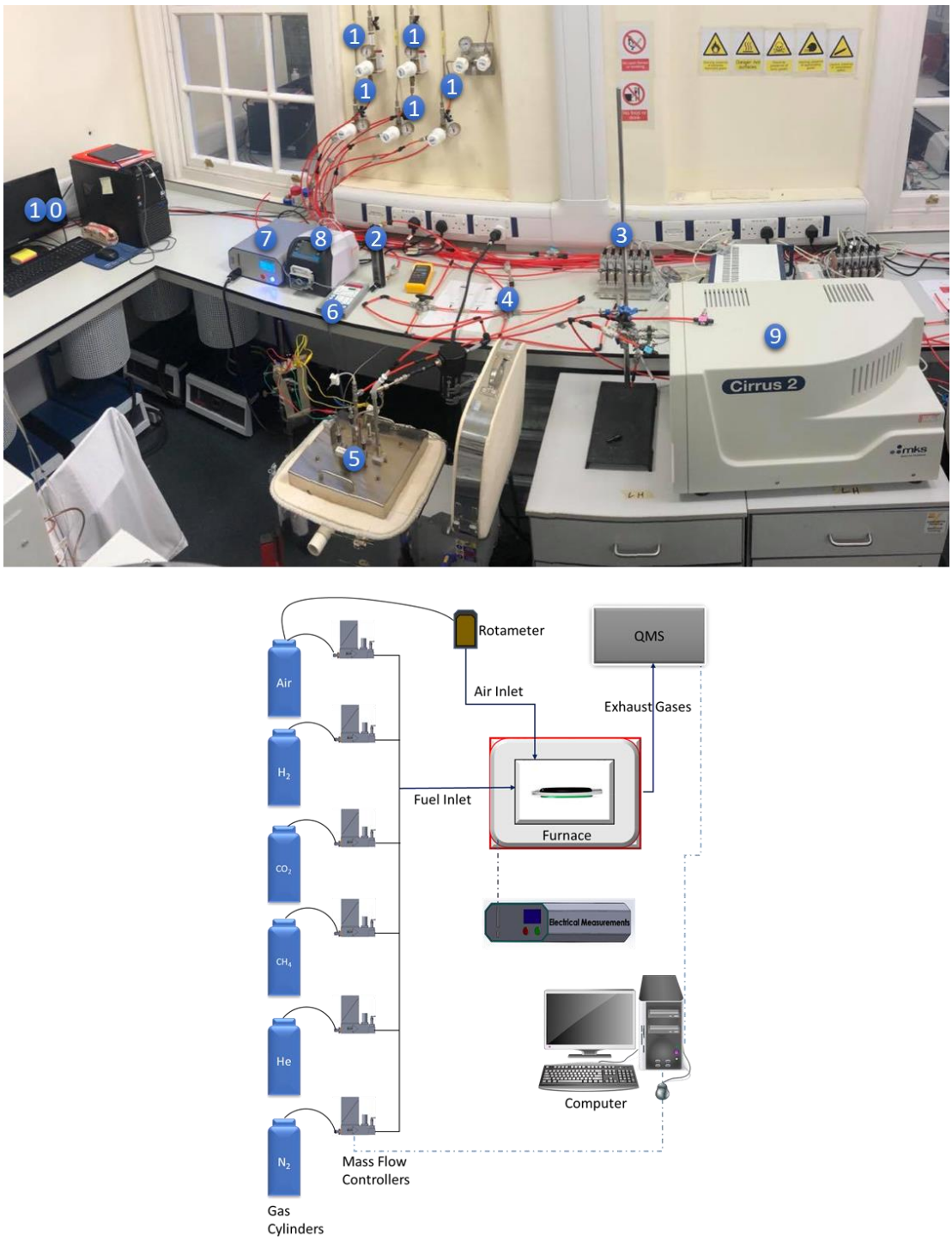

Figure 3.6: (a) SOFC test set-up, (1) fuel lines, (2) air rotameter, (3) mass-flow controllers, (4) fuel/air delivery and recovery system, (5) SOFC furnace, (6) furnace temperature controller, (7) Iviumstat for electrical measurements, (8) peristaltic pump, (9) QMS, (10) computer and (b) schematic representation

For co-electrolysis measurements, the fuel mixtures were mixed with steam using an integrated ceramic cartridge containing alumina fibers (99.9 % Al_2O_3 cartridge in a 4 mm Ø 99.9 % Al_2O_3

tube) that provided a constant steam flow rate directly in the fuel feeding inlet. Deionized water was delivered through the cartridge using a peristaltic pump (Lead fluid BT101L intelligent peristaltic pump) at the required flow rate. The cartridge was resistively heated from the chamber furnace, enabling a constant steam flux to be delivered to the anode as required.

3.4. Cell heating and conditioning

When starting an experiment, the fuel delivery lines were firstly purged with 30 cm^3 min^{-1} of an inert gas (helium or nitrogen) for 30 minutes in order to displace oxygen. The chamber furnace was then set to heat at 120 °C h^{-1} up to 400 °C, followed by a second heating ramp of 200 °C h^{-1} up to the desired temperature. This heating programme was in accordance with manufacturer recommendations and ensured good sealing between the cell and components. During heating, air was supplied at 100 cm^3 min^{-1} to the cathode to burn off the tape and adhesive used during cell mounting. When the cell reached the required temperature, the spring-loaded pressure of the flanges was checked and corrected as required. This was necessary because heating caused slight compression of the sheets and felts.

After reaching the desired temperature, 5 vol% H_2 was introduced into the fuel inlet mixture in order to reduce the anode. Reduction was monitored by observing the OCP of the cell. When the OCP had stabilised, the H_2 content was increased to 10 vol% until the OCP had re-stabilised. This procedure was repeated until the gas stream consisted of 100 vol% H_2. The OCP observed under pure H_2 was typically 1.10 – 1.14 V depending on the temperature, indicating negligible gas crossover and current loss. Finally, a voltage of 0.8 V was applied to the cell for a few hours in order to condition the electrolyte.

3.5. Electrochemical measurements

When collecting electrochemical measurements, the fuel mixtures were supplied to the anode at a flow rate of 30 cm^3 min^{-1}, and air was supplied to the cathode at 50 cm^3 min^{-1}. When changing the cell conditions such as temperature or fuel composition, the OCP of the cell was left to stabilise for 10-20 minutes before taking any measurements. For fuel mixtures containing CH_4,

air was added at a CH_4/air ratio of 5:1 by volume in order to prevent any interference to data caused by intolerable carbon deposition. In order to ensure the total flow rate of gases remained constant for different fuel compositions, an appropriate flow of He was added to the mixture to give a total flow rate of 36 cm^3 min^{-1}.

I-V curves were measured over the range OCP - 0.1 V in fuel cell mode, and in electrolysis and co-electrolysis mode were measured in the range OCP – 2.0 V. All I-V curves were measured potentiostatically at a scan rate of 500 mV s^{-1}. Electrochemical impedance spectroscopy (EIS) measurements were taken potentiostatically over the frequency range of 0.1 kHz - 100 MHz using a voltage amplitude of 10 mV. EIS measurements were carried out at the OCP, in fuel cell mode at 0.1 V below the OCP, and in electrolysis mode at 0.1 V above the OCP.

3.6. Anode output gas analysis using QMS

The composition of the output gases leaving the anode was measured using a MKS Cirrus 2 QMS. The spectrometer was primarily set to measure the intensities of m/z = 2 (H_2), 4 (He), 15 (CH_4), 28 (CO), 32 (O_2) and 44 (CO_2). The sensitivity of the spectrometer towards each of the gases was measured and used for data correction (see Appendix D), so that the data presented in this work represents the relative partial pressures of the output gases leaving the cell. Helium (m/z = 4) was used as the carrier gas. When taking QMS measurements, fuel gases were delivered at a total flow rate of 8 cm^3 min^{-1}. Air was added into the mixture at a CH_4/air ratio of 5:1 to prevent any carbon deposition at the anode. The gases were then diluted in an appropriate flow rate of helium to give a total gas flow rate to the cell of 20 cm^3 min^{-1}.

Chapter 4: Utilisation of H_2/CO_2 mixture in SOFC technology

4.1. Introduction

Whilst previous studies into biohydrogen utilisation in SOCs have focussed on fuel cell mode characterisation running on biohydrogen predominantly using computational and electrochemical techniques, the following experimental investigations characterise biohydrogen utilisation in SOCs using a combination of electrochemical techniques (see Chapter 2) and QMS, which have enabled the performance and fuel processing to be investigated in significantly greater detail than has been achieved previously. In addition, solid oxide electrolysis of biohydrogen has been investigated for the first time and is compared directly with fuel cell mode performance and products. Finally, the effects of fuel variability on SOC performance and products have been established.

4.2. Utilisation of biohydrogen in electrolyte supported cells

4.2.1. Effect of fuel composition on OCP

The effect of H_2/CO_2 composition on the OCP of the cell is shown in Fig. 4.1a alongside the theoretical Nernst potential which decreased linearly as the H_2/CO_2 composition was varied from 100/0 – 10/90 vol%. Under pure H_2, the experimentally measured OCP agreed closely with the Nernst potential, indicating the cell was well sealed with minimal gas crossover and current loss. Adding CO_2 to the fuel mixture immediately caused the OCP to deviate sharply away from the Nernst potential in a manner consistent with previously reported theoretical and experimental trends [79-81, 236-238]. The OCP decreased non-linearly as the CO_2 content was increased to approx. 20 vol%. From 20-60 vol% CO_2, the OCP decreased almost linearly and in parallel with the Nernst potential before again decreasing non-linearly as the CO_2 content was increased above 60 vol%.

The deviation of the OCP away from the theoretical Nernst potential is explained by the presence of the RWGS reaction (3.1), which was observed by analysis of the product gases leaving the anode as shown in Fig. 4.1b. At 75/25 vol% H_2/CO_2, the levels of H_2 and CO_2 leaving the anode were less than 0.75 au and 0.25 au respectively, and CO was detected. The signal intensities of masses 15 and 31 were measured to check for the presence of CH_4 and CH_3OH respectively but none were found, suggesting the presence of other reactions such as methanation were not significant and implying the presence of the RWGS reaction. Fig. 4.1b shows the presence of CO did not change significantly as the CO_2 content of the input gases was increased from 25 - 60 vol%, indicating the H_2/CO_2 composition did not have a significant effect on the equilibrium of the RWGS reaction over this range. This explains the linear decrease of OCP observed over this range in Fig. 4.1a; the equilibrium of the RWGS reaction was not changed and therefore the OCP varied linearly and in parallel with the theoretical Nernst potential due to a proportional dilution of the gases in CO_2. The sharp deviation of the OCP away from the Nernst potential at 0 - 25 vol% CO_2 indicates that the equilibrium of the RWGS reaction was strongly influenced by the H_2/CO_2 composition over this range. Adding CO_2 did not therefore cause a simple dilution of H_2 in CO_2; some of the H_2 was also converted in the RWGS reaction, significantly affecting the OCP of the cell. The effect of changing composition as a function of temperature have been calculated with H_2 and CO_2 being converted into product gases (H_2, CO, H_2O and CO_2) to predict the product gas composition at different and CO_2/H_2 mixtures at different temperatures (Appendix E).

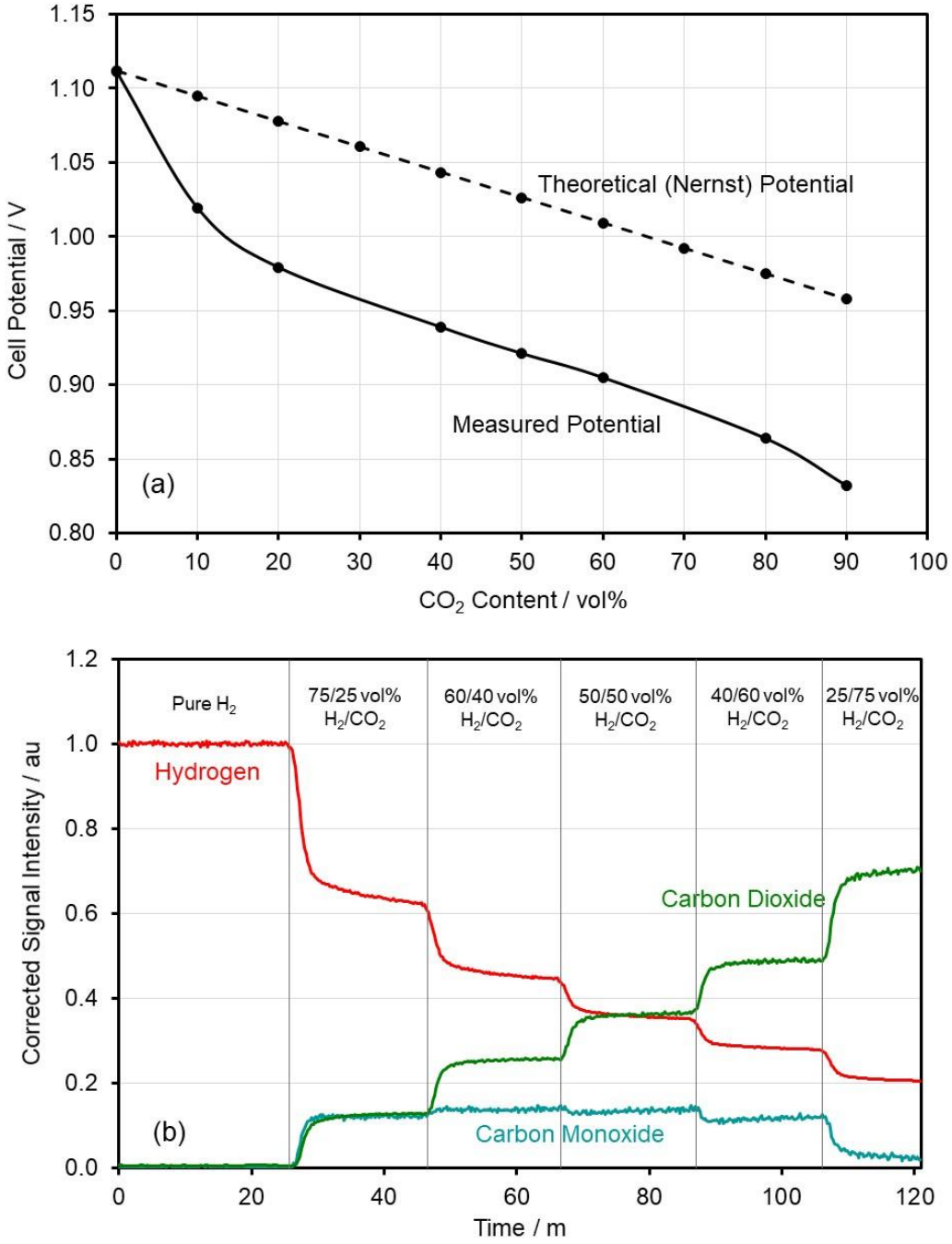

Figure 4.1: The effect of H_2/CO_2 fuel composition on: (a) the OCP of the ESC, and (b) the composition of the output gases leaving the anode at OCP. The temperature of the ESC was 800 °C.

The non-linear decrease of OCP at ≥ 60 vol% CO_2 is explained by both the increased dilution of gases in CO_2 and the shifting equilibrium of the RWGS reaction. Fig. 4.1b shows the CO presence decreased significantly above 60 vol% CO_2, indicating a decreased presence of the RWGS reaction. The decreased presence of H_2, CO and H_2O, coupled with increased dilution in

CO_2, caused the OCP to decrease non-linearly and to further deviate away from the Nernst potential under high CO_2 concentrations.

4.2.2. Utilisation of 50/50 vol% H_2/CO_2

Fig. 4.2 shows the effect of decreasing the operating voltage on the products of the ESC when running on 50/50 vol% H_2/CO_2 in fuel cell mode. In agreement with Fig. 4.1, some of the initial H_2 and CO_2 were converted in the RWGS reaction to give an OCP of 0.92 V. Across all operating voltages, there was CO present in the output gases which was not present in the input gases, indicating that the RWGS reaction took place simultaneously with electrochemical processes on the anode. As the cell voltage was progressively decreased, the electrical current produced increased, with a maximum current of approx. 1235 mA cm^{-2} produced at 0.1 V.

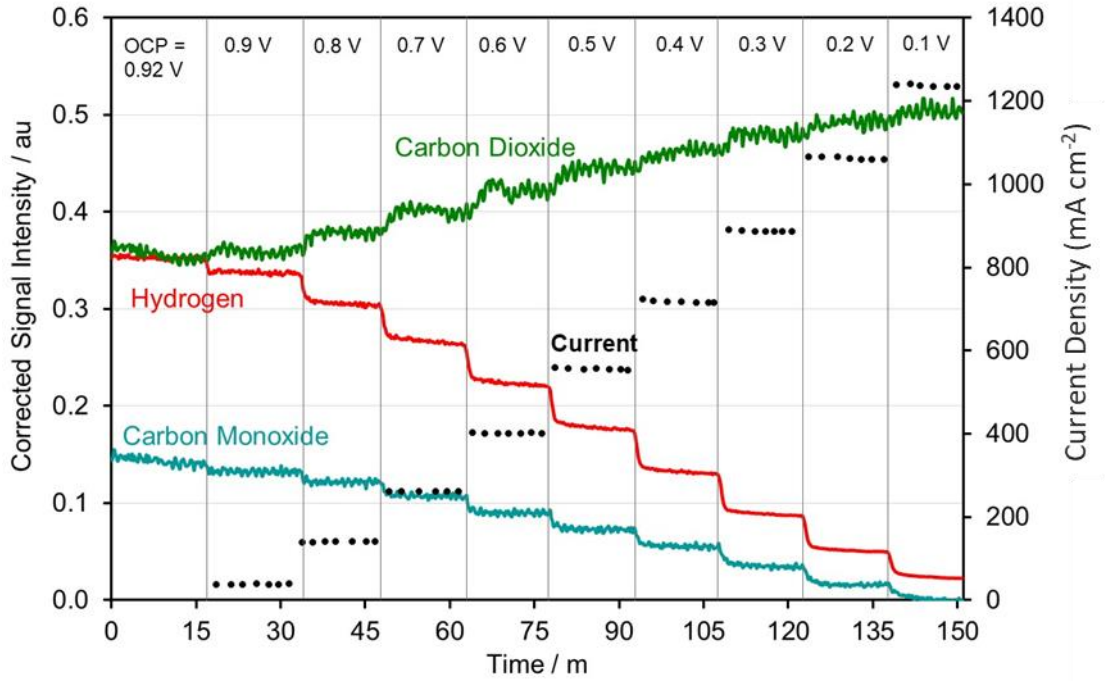

Figure 4.2: The effect of operating voltage on the gaseous and current outputs of the ESC running on 50/50 vol% H_2/CO_2 in fuel cell mode at 800 °C. The figure plots the output gases on the primary vertical axis, and the corresponding current density on the secondary vertical axis.

It has previously been reported that provided the ratio of H_2 to CO is greater than 1, the electrochemical oxidation of H_2 on Ni-based SOC anodes is predominant and the rate of electrochemical CO oxidation is negligible [262-267]. Since the condition $H_2/CO > 1$ is satisfied

across all the cell potentials studied in Fig. 4.2, the conversion of CO and subsequent CO_2 re-generation through the direct electrochemical oxidation of CO was not likely to be significant. The current generated by the cell was therefore more likely to be produced mainly from the electrochemical oxidation of H_2.

The observed conversion of CO and subsequent regeneration of CO_2 was more likely due to a shift in equilibrium of the RWGS reaction imposed by the electrochemical oxidation of H_2 (Eq. 1), which caused the partial pressure of H_2 to decrease and the partial pressure of H_2O to increase:

$$H_2 + O^{2-} \rightleftharpoons H_2O + 2e^- \quad \text{(Eq. 1)}$$

As the potential of the cell was decreased therefore, the rate of electrochemical H_2 oxidation increased and the equilibrium of the RWGS reaction was shifted increasingly towards the WGS reaction (Eq. 12):

$$H_2O + CO \rightleftharpoons H_2 + CO_2 \quad \text{(Eq. 12)}$$

The main pathway of CO_2 regeneration was therefore likely to be through the electrochemical oxidation of H_2 (Eq. 1) followed by the WGS reaction (Eq. 12).

Fig. 4.2 also illustrates that the electrical and gaseous products of SOFCs running on H_2/CO_2 mixtures varied significantly depending on the operating potential of the cell. The presence of CO in the output gases underlines the importance of ensuring high fuel utilisation efficiencies when running SOCs on H_2/CO_2 mixtures. Fig. 4.2 therefore indicates that due to the presence of the RWGS reaction, poor fuel utilisation efficiencies will lead to emissions of CO.

Fig. 4.3 shows the effect of operating potential on the products of the ESC running on 50/50 vol% H_2/CO_2 in electrolysis mode. As the operating potential was increased, the partial pressure of CO_2 decreased, and the H_2 and CO increased. The synthesis gas production rate increased from approx. 12 $cm^3\ min^{-1}\ cm^{-2}$ at the OCP, to approx. 21 $cm^3\ min^{-1}\ cm^{-2}$ at 1.8 V. At the OCP, H_2-rich synthesis gas mixtures with a H_2/CO ratio of approximately 2.3 by volume

were produced, whilst at the highest voltage studied (1.8 V) the H_2/CO ratio decreased to approx. 1.2 by volume.

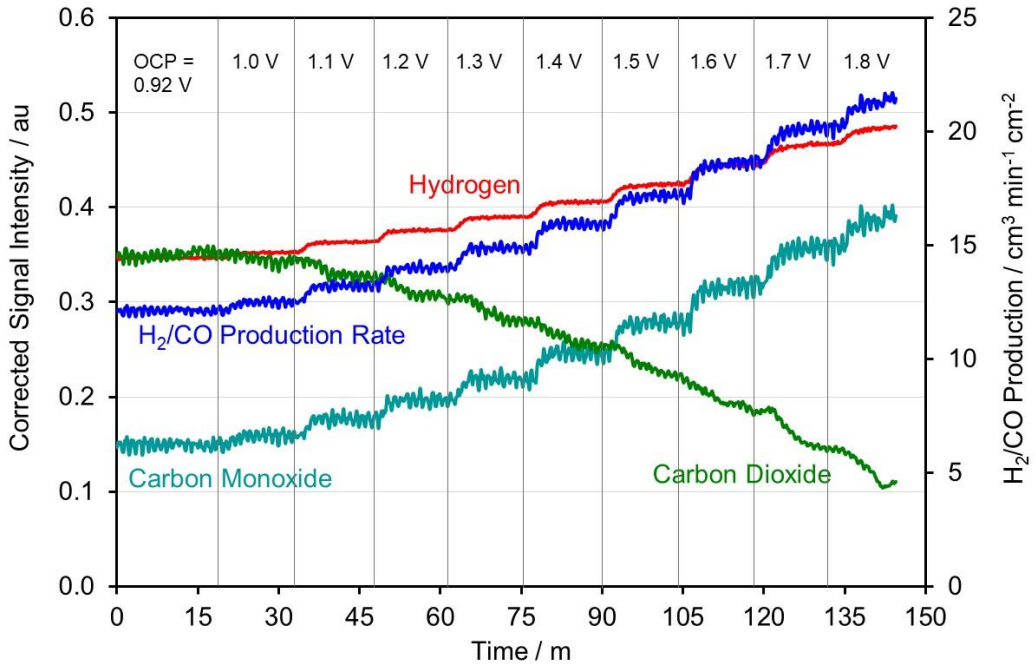

Figure 4.3: The effect of operating voltage on the gaseous products of the ESC running on 50/50 vol% H_2/CO_2 in electrolysis mode at 800 °C. The figure plots the output gases from the anode on the primary vertical axis, and the corresponding total synthesis gas production (H_2 + CO) on the secondary vertical axis.

The observed decrease of the H_2/CO ratio is significant, because it indicates the rate of CO production increased relative to H_2 production as the cell voltage was increased. It is widely accepted that the rate of CO production through electrochemical CO_2 reduction (Eq. 10) is much slower than H_2 production through electrochemical H_2O reduction (Eq. 9) [89, 91, 100, 101, 116, 140, 245-248, 262-267] :

$$H_2O + 2e^- \rightleftharpoons H_2 + O^{2-} \qquad \text{(Eq. 9)}$$

$$CO_2 + 2e^- \rightleftharpoons CO + O^{2-} \qquad \text{(Eq. 10)}$$

It is therefore unlikely that such a significant decrease of the H_2/CO ratio can be explained by an increase in the rate of electrochemical CO_2 reduction alone, and it is probable that CO production also took place through electrochemical reduction of H_2O followed by the RWGS

reaction. Electrochemical reduction of H_2O causes the presence of H_2O to decrease and the H_2 to increase, and is likely therefore to have shifted the equilibrium of the RWGS reaction towards the production of CO. This is the reverse effect to that observed in fuel cell mode, where electrochemical oxidation of H_2 (which decreased the presence of H_2 and increased the presence of H_2O) shifted the RWGS equilibrium towards the conversion of CO. The presence of H_2O at the OCP was likely to be the same as that of CO (they have a 1:1 stoichiometry in the RWGS reaction), with a corrected signal intensity of approximately 0.15 au. Taking into account the stoichiometries of electrochemical H_2O reduction and the RWGS reaction, the maximum possible CO production through this reaction pathway would give a corrected signal intensity for CO of 0.30 au. At the highest voltage studied (1.8 V), the corrected signal intensity of CO was approximately 0.38 au and therefore it can be inferred that CO production must have taken place through the RWGS reaction and electrochemical reduction of CO_2 simultaneously.

This work shows that the RWGS reaction significantly influences the OCP of SOC devices running on H_2/CO_2 mixtures and results in the *in-situ* production of CO and H_2O on the anode. The equilibrium of the RWGS reaction is dependent on the operating voltage of the cell; at lower voltages, the equilibrium is shifted towards the WGS direction, whilst at higher voltages the equilibrium is shifted towards the RWGS reaction.

4.2.3. Effects of fuel variability in fuel cell mode

The I-V and power curves in Fig. 4.4 show that the current and power produced in fuel cell mode were very sensitive to changes in the fuel composition, with significantly more current and power produced as the H_2 content of the fuel was increased. All I-V curves decreased non-linearly at high voltages, indicating the presence of activation losses. The I-V curves were almost parallel across the fuel composition range 100 - 40 vol% H_2, suggesting similar activation losses for each fuel composition. Concentration losses were clearly observed for mixtures containing 20 vol% H_2 or less, where a non-linear decrease of voltage was observed below 0.5 V. However, the I-V curves clearly indicate that the efficiencies and electrical power

output are not significantly affected by fuel variability provided the biohydrogen composition stays within the range 40-60 vol% H_2, particularly at high operating voltages.

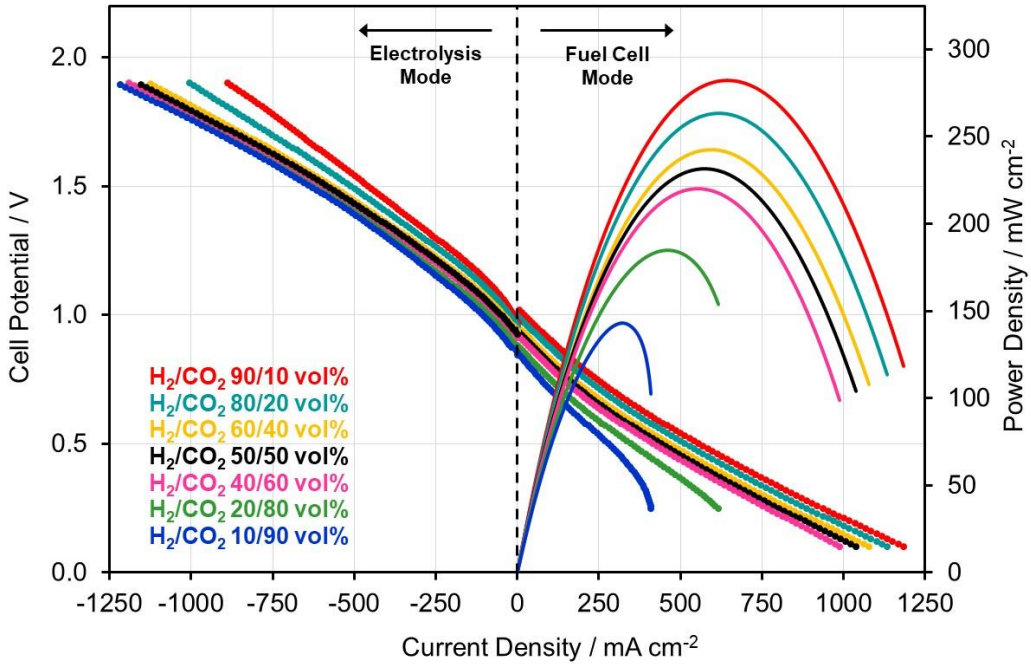

Figure 4.4: The effect of H_2/CO_2 composition on the I-V curve of the ESC running in fuel cell mode and electrolysis mode at 800 °C. The corresponding fuel cell power curves are plotted on the secondary axis.

The electrochemical impedance spectra shown in Fig. 4.5, which were collected with the cell running on different H_2/CO_2 mixtures, were composed of two polarisation arcs. Zhan *et al*. have previously assigned the low frequency arc to gas diffusion losses and the high frequency arc to charge transfer and surface diffusion losses [268]. The widths of the arcs were measured and are shown in Table 4.1. In fuel cell mode, the width of the high frequency arc did not respond significantly to changes in the fuel composition across the entire fuel composition range studied, indicating that charge transfer and surface diffusion losses, whilst being relatively significant (approx. 0.52 Ω cm^2), were not sensitive to the composition of the fuel. This is also further evidence that electrical power production was through electrochemical oxidation of H_2 only. The electrochemical oxidation of CO has previously been reported to cause a much higher activation overpotential compared with H_2 oxidation [262-267] .

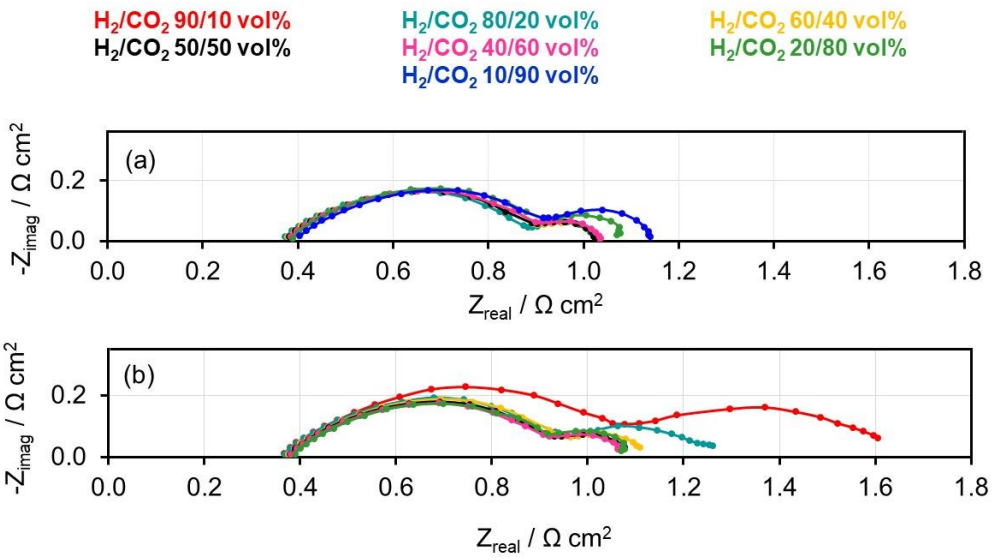

Figure 4.5: The effect of H_2/CO_2 composition on the electrochemical impedance spectra of the ESC at 800 °C. Measurements were taken at 0.1-100000 Hz: (a) OCP - 0.1 V (fuel cell mode), and (b) OCP + 0.1 V (electrolysis mode).

Table 4.1: Widths of the high and low frequency arcs in the electrochemical impedance spectra presented in Fig. 4.5.

H_2/CO_2 vol%	**OCP-0.1 V (Fuel cell mode)**		**OCP+0.1 V (Electrolysis Mode)**	
	High Frequency Arc Width / Ω cm^2	Low Frequency Arc Width / Ω cm^2	High Frequency Arc Width / Ω cm^2	Low Frequency Arc Width / Ω cm^2
90/10	0.5179	0.1316	0.7105	0.5290
80/20	0.5248	0.1245	0.5880	0.3039
60/40	0.5217	0.1214	0.5887	0.1444
50/50	0.5269	0.1240	0.5514	0.1460
40/60	0.5276	0.1530	0.5392	0.1415
20/80	0.5121	0.2255	0.5276	0.1530

Fig. 4.6a shows the experimental data set and the fitting results plotted together for H_2/CO_2 80/20 vol% mixture and Fig. 4.6b show the equivalent circuit model which provides the fitting values for each component and the errors associated. Although, to be brief, only one set of fitting results are shown here, all the other fittings are to the same level of precision. An obvious mismatch between the two curves can be found at the high frequency end. The experimental curve deviated from the fitting curve by titling slightly further towards the imaginary axis and

this is attributed to the imperfections of the working electrode surface. Although an analogous performance can be seen between the two curves at the low frequency end.

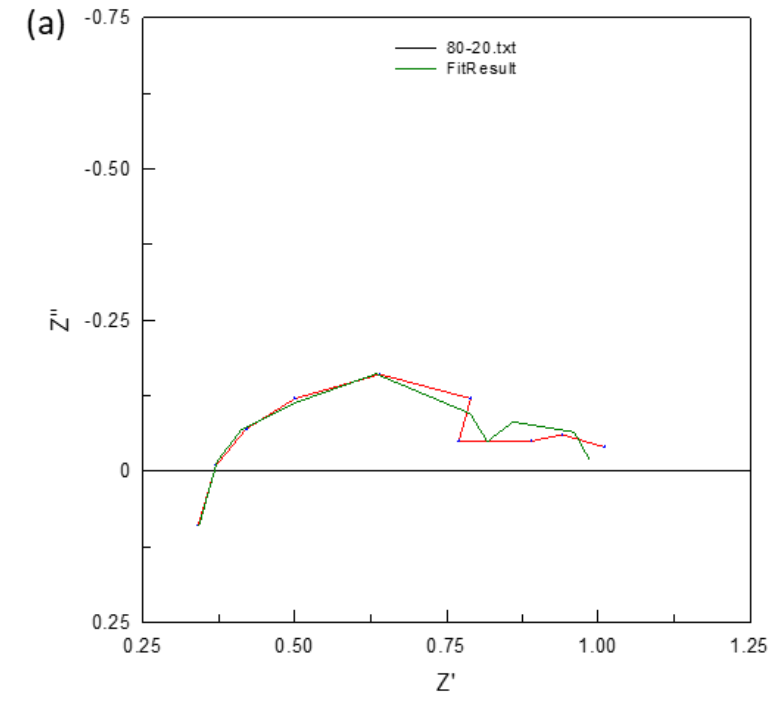

(b)

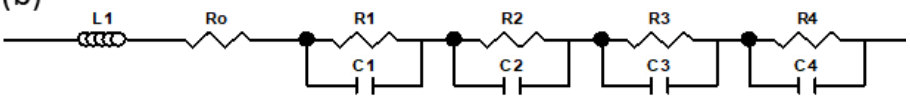

Element	Freedom	Value	Error	Error %
L1	Free(+)	2.8167E-07	3.8885E-08	13.805
Ro	Free(+)	0.33643	0.016305	4.8465
R1	Free(+)	0.17218	0.026315	15.283
C1	Free(+)	0.39777	0.14018	35.241
R2	Free(+)	0.136	0.0343	25.221
C2	Free(+)	0.00065999	0.00029413	44.566
R3	Free(+)	0.28913	0.037293	12.898
C3	Free(+)	0.0027947	0.00087919	31.459
R4	Free(+)	0.053678	0.022389	41.71
C4	Free(+)	0.00014595	0.00012317	84.392

Figure 4.6: (a) Equivalent Circuit fitting to experiment data 80/20 vol% H_2/CO_2 and (b) equivalent circuit model and fitting results.

Fig. 4.7 indicates that in fuel cell mode, the presence of CO varied significantly across different fuel mixtures due to the shifting equilibrium of the RWGS reaction. Therefore, if the cell was

utilising CO for power production, greater variation in the activation overpotential with fuel composition would be expected. The activation overpotentials were comparable across all compositions, indicating electrical current production by the cell was predominantly through the electrochemical oxidation of H_2.

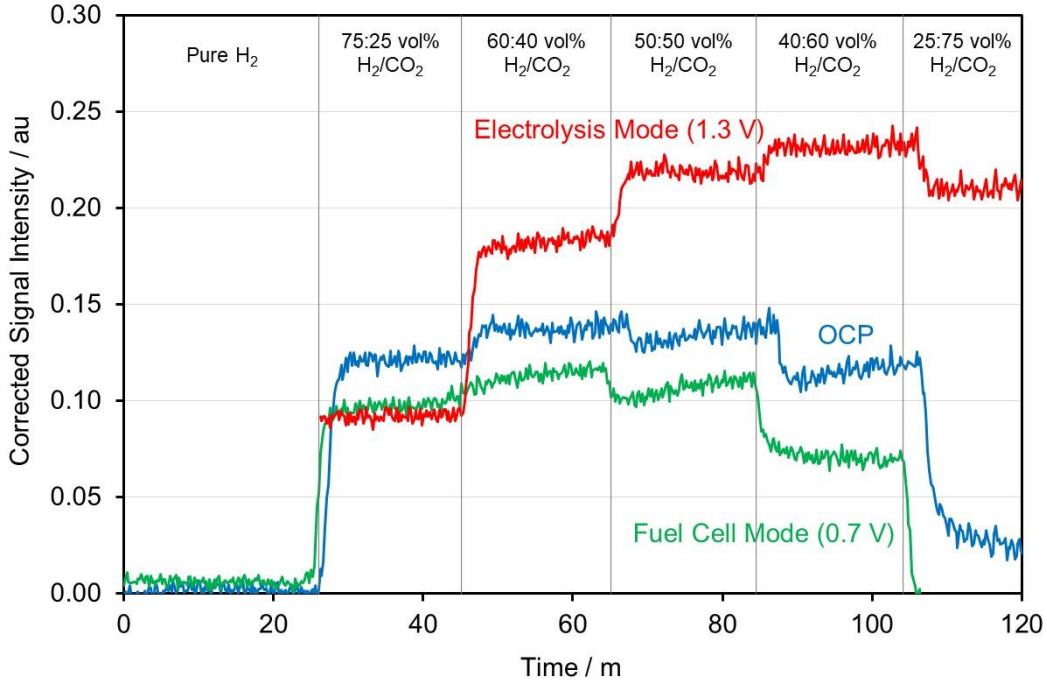

Figure 4.7: Comparison of CO partial pressure in the anode output gases of the ESC when running on different fuel mixtures at 800 °C. Data are shown for the ESC when at OCP and when operating in fuel cell and electrolysis mode. The operating voltages are indicated on the figure.

The low frequency arc width also did not vary significantly in fuel cell mode for fuel mixtures in the range 50-90 vol% H_2, indicating that gas diffusion losses were not sensitive to the fuel composition in this range. For mixtures containing 50-90 vol% H_2 therefore, it was only the OCP losses that were sensitive to fuel variability as shown in Fig. 4.1. Decreasing the H_2 content from 50-20 vol% increased the low frequency arc width more significantly from 0.1240-0.2255 Ω cm^2 respectively, indicating that losses due to diffusion of H_2 through the anode were more important and sensitive to the fuel composition as the H_2 content was decreased below 50 vol%.

4.2.4. Effects of fuel variability in electrolysis mode

The I-V curves collected in electrolysis mode (see Fig. 4.4) show that activation losses were present in electrolysis mode, with a non-linear increase of voltage observed at 0.9 – 1.2 V that was more pronounced than the activation losses observed in fuel cell mode. In addition, there was no non-linear behaviour observed at high voltages, indicating that unlike fuel cell mode, concentration losses were not observed to be significant in electrolysis mode. As was the case in fuel cell mode, the I-V curve was not affected by fuel variability provided the biohydrogen composition stayed within the range 40-60 vol% H_2.

The electrochemical impedance spectra collected in electrolysis mode (see Fig. 4.5b) generally have wider polarisation arcs than fuel cell mode, indicating that the ESC had poorer kinetic performance in electrolysis mode. Table 4.1 shows the high frequency arc widths were generally greater than in fuel cell mode, indicating increased charge transfer and surface diffusion losses. In addition, the width of the high frequency polarisation arc was sensitive to the fuel composition and decreased from 0.7105 - 0.5276 Ω cm^2 as the CO_2 content was increased. This contrasts with fuel cell mode, where activation overpotentials were not sensitive to fuel variability.

The low frequency polarisation arc widths were greater in electrolysis mode. CO_2 and H_2O are bigger in size than H_2 and CO and therefore caused greater gas diffusion overpotentials. The width of the low frequency arc and therefore the gas diffusion losses remained approximately constant across the range 40-80 vol% CO_2. When the CO_2 content was decreased below 40 vol% however, the arc width increased from 0.1444 - 0.5290 Ω cm^2, indicating that gas diffusion losses were very sensitive to fuel variability in this range.

Fig. 4.7 shows that CO production increased in electrolysis mode as the CO_2 content of the fuel was increased from 25 - 60 vol%. This was due to the activation and gas diffusion losses, which both decreased over this fuel range, as indicated by the decreasing widths of the high (activation) and low (diffusion) frequency arc widths of the impedance spectra (see Table 4.1). Fig. 4.7 shows the increase of CO production was particularly prevalent as the fuel mixture was

changed from 75/25 - 60/40 vol% H_2/CO_2. The impedance data in Table 4.1 show the high frequency arc widths for 80/20 vol% and 60/40 vol% H_2/CO_2 mixtures were very similar (~ 0.588 Ω cm^2), whilst the low frequency arc width decreased significantly from 0.3039 Ω cm^2 to 0.1444 Ω cm^2. This indicates that the large increase of CO production observed from 75/25 - 60/40 vol% H_2/CO_2 was mainly due to improved diffusion of CO_2.

The behaviour of CO production in Fig. 4.7 and the impedance data in Table 4.1 are also further evidence that CO production occurred simultaneously through the RWGS reaction and electrochemical reduction of CO_2. Table 4.1 indicates that the activation and gas diffusion potentials continued to decrease (the arc widths decrease) as the CO_2 content was increased to 80 vol%, suggesting that CO production should have continued to increase as the CO_2 content was increased. This was not the case above 60 vol% CO_2 where a clear decrease in CO production was observed. The CO production at OCP shown in Fig. 4.7 (which was entirely due to the RWGS reaction) decreased when the CO_2 content was greater than 60 vol% due to a shift in the equilibrium of the RWGS reaction. The observed decrease of CO above 60 vol% CO_2 in electrolysis mode therefore indicates that CO production could not entirely have been due to electrochemical reduction of CO_2, and that the RWGS reaction was also a significant reaction pathway of CO production.

Fig. 4.8 shows the variation in the quantity and composition of the synthesis gas produced as the fuel composition was changed. It is clear that fuel variability significantly influenced the composition and quantity of syngas produced by the cell in electrolysis mode. Increasing the CO_2 content from 25 - 75 vol% decreased the total production of synthesis gas from 20 - 9 cm^3 min^{-1} cm^{-2}. The H_2/CO ratio of the synthesis gas also decreased significantly from approximately 7.9 - 0.7, although the variation was less over the range 40 - 60 vol% CO_2. The sharp decrease of H_2/CO ratio observed as the fuel mixture was changed from 25 - 40 vol% CO_2 was due to the decrease of CO_2 gas diffusion overpotential (see Table 4.1) as described earlier. The H_2/CO ratio continued to decrease from 40-60 vol% CO_2 due to a mixture of increased CO production and direct displacement of H_2 with CO_2 in the initial fuel mixture. Despite a loss of

CO production above 60 vol% CO_2 (see Fig. 4.7), the H_2/CO ratio again decreased due to direct displacement of H_2 with CO_2.

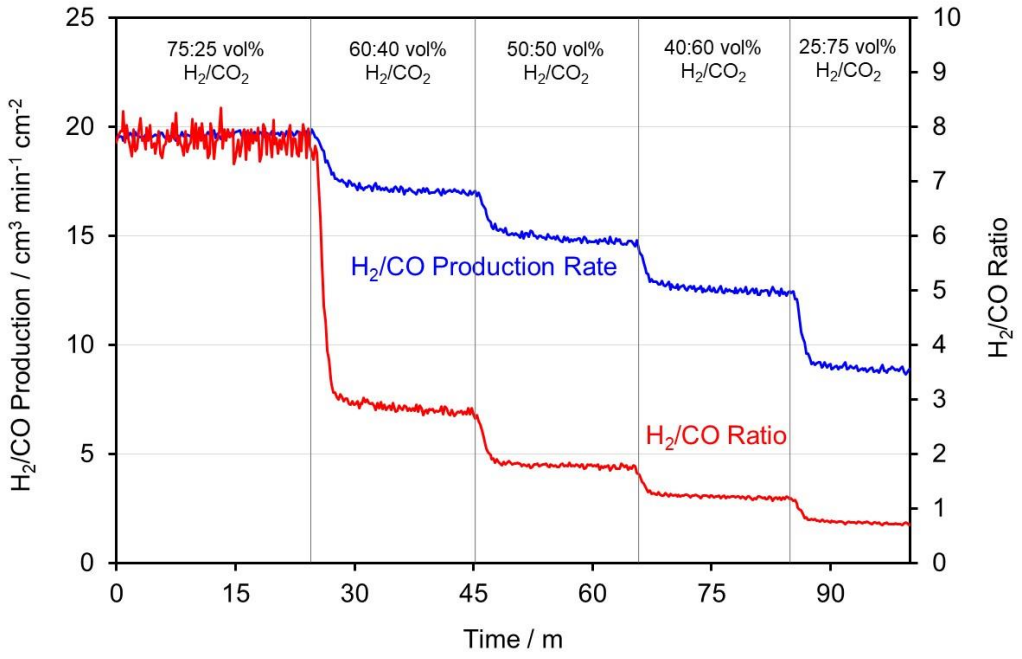

Figure 4.8: The effect of H_2/CO_2 composition on the products of the ESC running in electrolysis mode at 800 °C. The operating voltage of the cell was 1.3 V. The figure shows the synthesis gas production (H_2 + CO) on the primary vertical axis and the composition of the synthesis gas (H_2/CO ratio) on the secondary vertical axis.

Since synthesis gas is composed of CO and H_2, the decrease of H_2/CO production rate as the CO_2 content increased was partly due to direct displacement of H_2 with CO_2 in the initial fuel mixture. Even though the CO production increased as the CO_2 content was increased up to 60 vol% (see Fig. 4.7) therefore, CO was not produced at a fast enough rate to give an overall increase of H_2/CO production rate. The drop in H_2/CO production was more pronounced as the CO_2 content was increased from 60 – 75 vol%, which was likely due to the loss of CO produced from the RWGS reaction (see Fig. 4.7) as described earlier. Therefore, even though the OCP and the activation and gas diffusion overpotentials were improved as the CO_2 partial pressure was increased, the displacement of H_2 with CO_2 in the initial fuel mixture and the loss of the RWGS reaction caused the overall synthesis gas production rate to decrease, highlighting the importance of the RWGS reaction in the production of CO.

4.2.5. The influence of SOFC operating temperature on biohydrogen fuel variability effects

In order to determine the effect of operating temperature on the utilisation of biohydrogen in SOFCs, the measurements described in earlier sections were repeated at 850 °C. Fig. 4.9a shows the effect of fuel composition on the output gases of the OCP at 850 °C and largely indicates similar behaviour to 800 °C in Fig. 4.1b. The H_2 decreased and the presence of CO did not change significantly as the CO_2 content of the input gases was increased from 25 - 60 vol%. Fig. 4.9b shows the behaviour of the OCP at 850 °C. At all fuel compositions, the OCP was lower compared with 800 °C, in agreement with Nernst behaviour. The key difference at 850 °C was the conversion of H_2 and CO_2 at all fuel compositions was higher and faster compared with 800 °C. This was particularly true for CO_2, of which up to 15 vol% greater conversion was observed across all fuel compositions studied (see Fig. 4.9c). Increasing the temperature promoted the RWGS reaction, which is endothermic and would also take place at a faster rate due to the greater thermal energy available. It is clear that increasing the temperature increased the production of CO across all fuel compositions studied. This was particularly the case at 25/75 vol% H_2/CO_2, where the conversion of H_2 and CO_2 was much higher compared with that observed at 800 °C.

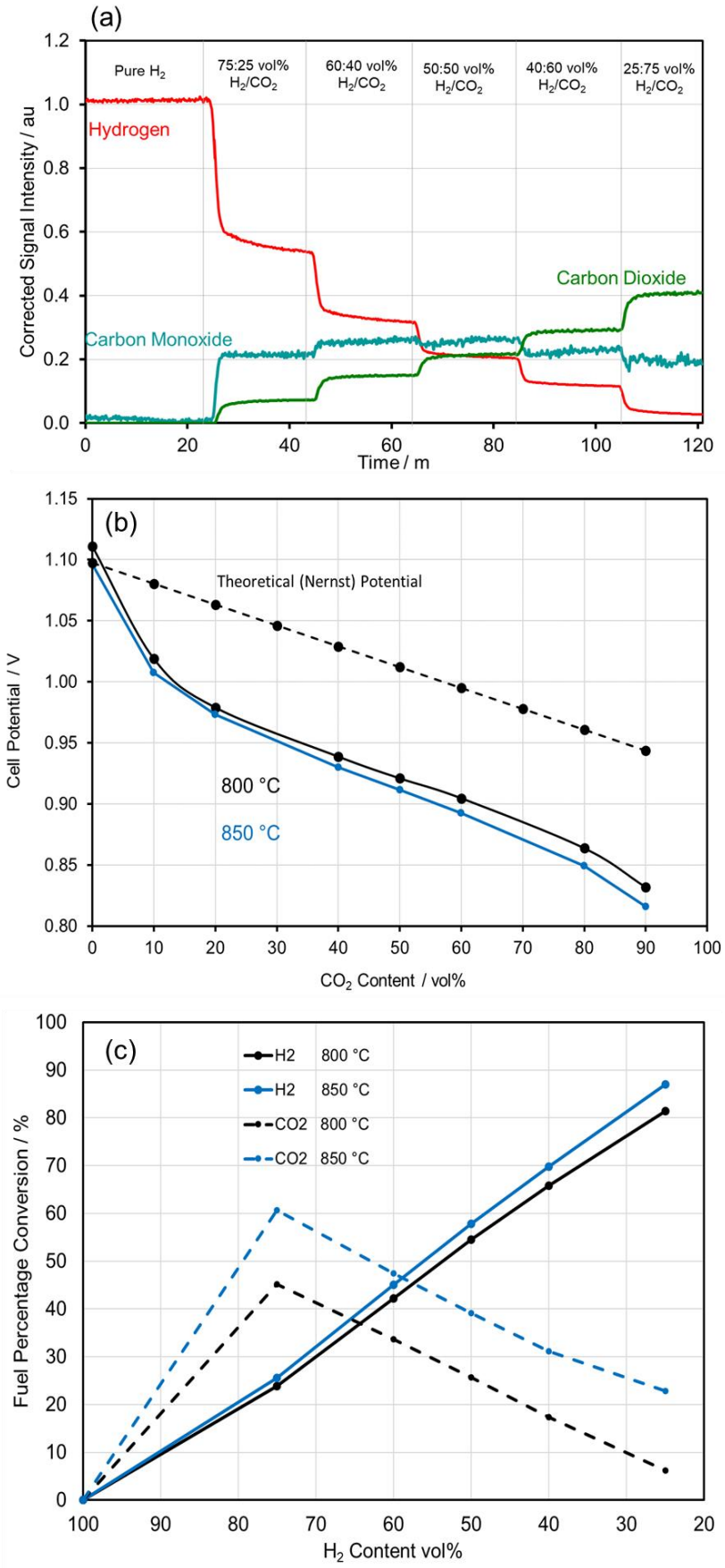

Figure 4.9: The effect of temperature on: (a) the composition of the output gases leaving the anode at OCP at 850 °C (b) the OCP and (c) on the fuel percentage conversion at 800 °C and 850 °C.

Fig. 4.10a shows the effect of fuel variability on the I-V and power curves of the cell in fuel cell and electrolysis mode. The shapes of the curves in fuel cell and electrolysis mode were very sensitive to changes in the fuel composition. In general, the behaviour was largely consistent with that observed at 800 °C. In fuel cell mode, significantly more current and power were produced as the H_2 content of the fuel was increased. Compared with 800 °C, the activation losses were lower due to the faster kinetics of fuel conversion and the ohmic losses were lower due to more efficient oxygen ion conduction through the electrolyte. The concentration losses were greater due to the more efficient fuel conversion but overall, the performance of the cell was improved greatly at 850 °C.

In electrolysis mode, for fuel compositions with H_2 content (90 - 80 vol%) the I-V curves increased non-linearly between 1.0-1.4 V, indicating the presence of activation losses. The I-V curves were almost parallel across the fuel composition range 60 - 10 vol% H_2, suggesting that for these fuel compositions the activation losses decrease. The I-V curves indicate that for fuel composition in the range 60-10 vol% H_2 the efficiencies and the performance are not significantly affected by fuel variability. At high current densities, there is a point of inflexion in the I-V curve indicating the resistance decreased. This is attributed to local heating effects under high current densities.

Fig. 4.10b shows the effect of temperature on the I-V and power curves of the cell when utilising a 50/50 vol% H_2/CO_2 mixture. In fuel cell mode, the I-V curve at 850 °C decreased linearly at high voltages compared with a non-linear decrease observed at 800 °C 1.0 – 0.7 V, indicating the activation losses were much lower at 850 °C. It is also apparent that the linear decrease in the mid-voltage range has a shallower gradient at 850 °C, indicating the increased temperature also improved the ohmic losses. There were no concentration losses apparent in the I-V curves. As a result, increasing the temperature increased the power across all operating voltages. The I-V curves in electrolysis mode show much the same behaviour as fuel cell mode. Activation losses were significantly decreased at 850 °C compared with 800 °C, and the linear decrease in the mid-current region had a shallower gradient, indicating decreased ohmic losses.

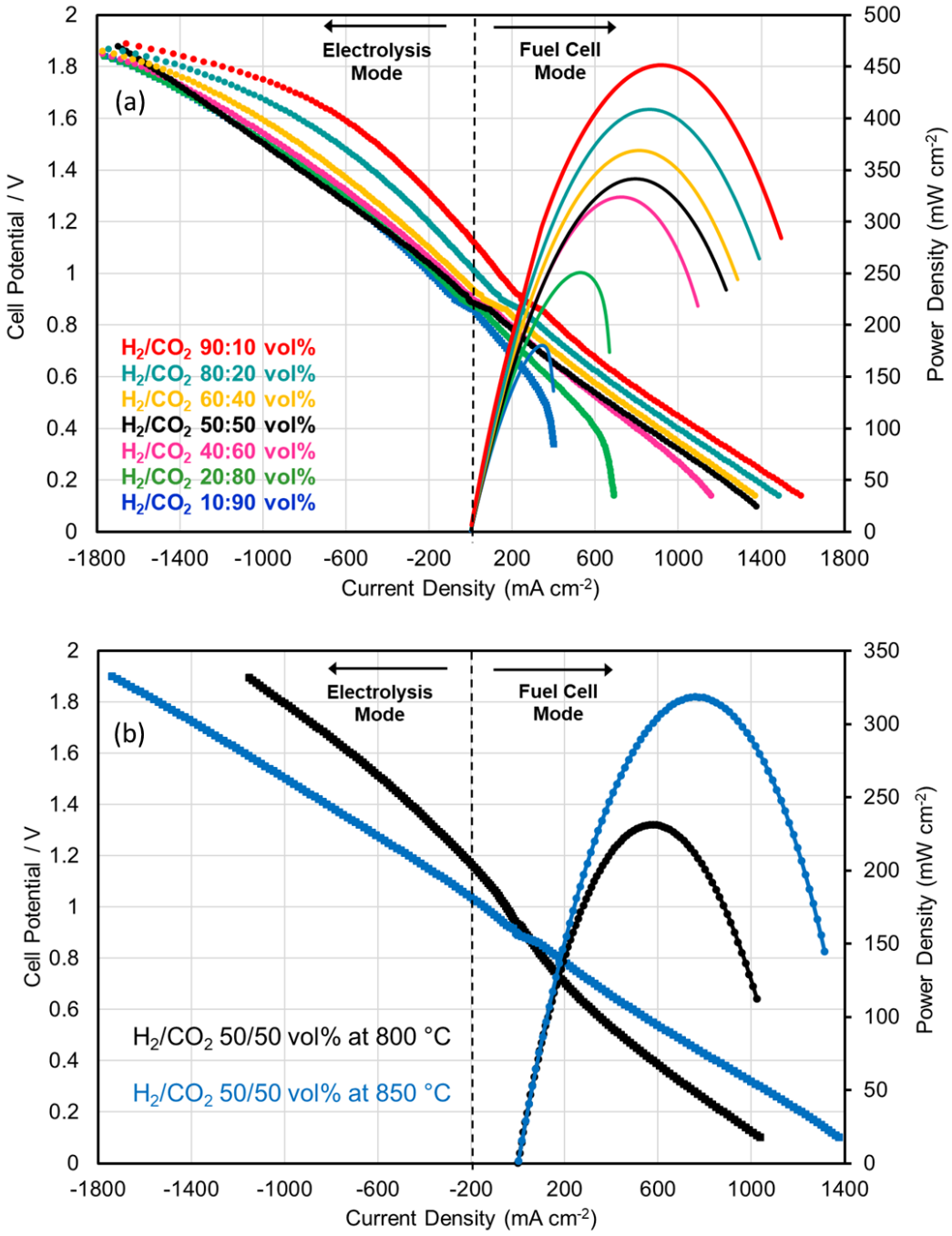

Figure 4.10: The effect of: (a) fuel variability on the I-V and power curves of the ESC and (b) on 50/50 vol% H_2/CO_2 composition on the I-V curve of the ESC running in fuel cell mode and electrolysis mode. The corresponding fuel cell power curves are plotted on the secondary axis.

The electrochemical impedance spectra shown in Fig. 4.11, which present the effect of fuel variability of H_2/CO_2 mixtures at 850 °C. The widths of the arcs were measured and are shown

in Table 4.2. Fig. 4.11 shows the width of the high and low frequency arcs that followed an identical pattern as the high and low frequency arcs at 800 °C.

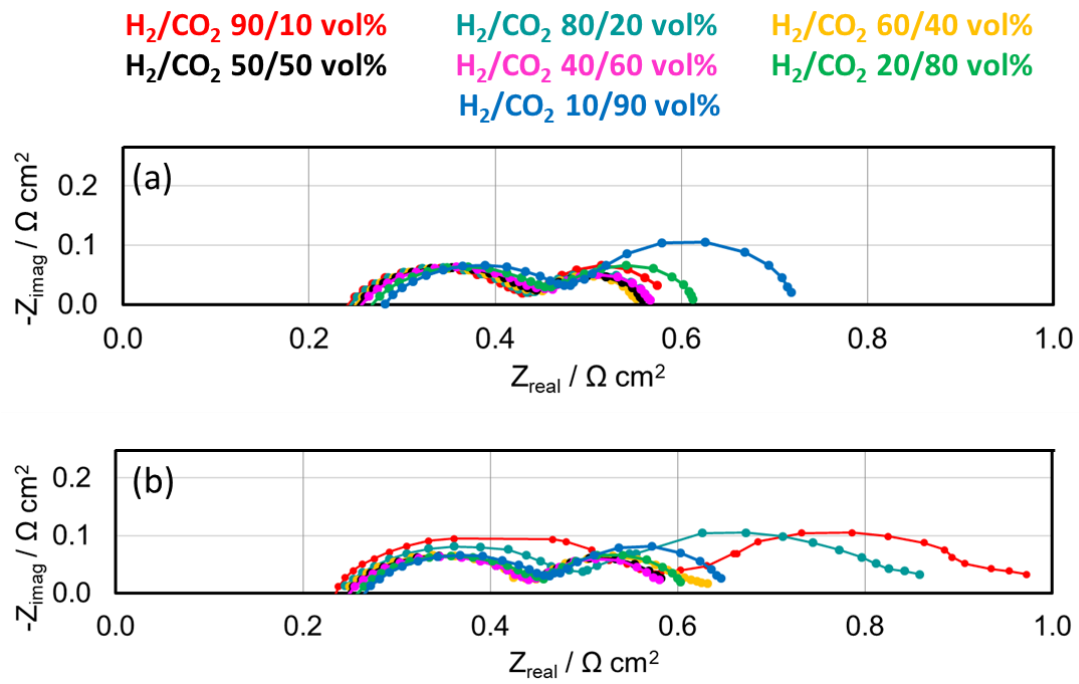

Figure 4.11: The effect of H_2/CO_2 composition on the electrochemical impedance spectra of the ESC at 850 °C. Measurements were taken at 0.1-100000 Hz: (a) OCP - 0.1 V (fuel cell mode), and (b) OCP + 0.1 V (electrolysis mode).

Table 4.2: Widths of the high and low frequency arcs in the electrochemical impedance spectra presented in Fig. 4.11.

H_2/CO_2 vol%	**OCP-0.1 V (Fuel cell mode)**		**OCP+0.1 V (Electrolysis Mode)**	
	High Frequency Arc Width / Ω cm^2	Low Frequency Arc Width / Ω cm^2	High Frequency Arc Width / Ω cm^2	Low Frequency Arc Width / Ω cm^2
90/10	0.1879	0.1454	0.3895	0.3449
80/20	0.1903	0.1264	0.2531	0.3601
60/40	0.1910	0.1001	0.1990	0.1833
50/50	0.1918	0.1144	0.2027	0.1331
40/60	0.1978	0.1131	0.1922	0.1396
20/80	0.1990	0.1519	0.2001	0.1460
10/90	0.1996	0.2372	0.2023	0.1828

Fig. 4.12 shows the effect of temperature on the EIS of the cell when utilising a 50/50 vol% H_2/CO_2 mixture. The impedance data show that the activation, concentration and ohmic losses improved as the temperature was increased (see Table 4.3).

Fig.4.12a shows the width of the high frequency arc in fuel cell mode decreased significantly (approx. 0.33 Ω cm^2) indicating the activation losses were substantially decreased at higher temperature, in agreement with the I-V curves. Therefore, the decrease of the high frequency arc at higher temperature signified that charge transfer and surface diffusion losses are sensitive to temperature. The low frequency arc width was also decreased but to a much lesser extent at higher temperature in fuel cell mode (approx. 0.01 Ω cm^2) indicating that gas diffusion losses had a much smaller effect on the diffusion of reactants through the anode. The ohmic losses were also significantly decreased (approx. 0.13 Ω cm^2), as indicated by the high frequency arc horizontal axis intercept at higher temperature indicating more efficient oxygen ion conduction through the electrolyte.

Fig. 4.12b and Table.4.3 shows the width of high and low frequency arcs in electrolysis mode. The high frequency arc decreased (approx. 0.35 Ω cm^2), the low frequency arc decreased (approx. 0.01 Ω cm^2) and the ohmic losses decreased (approx. 0.13 Ω cm^2) at higher temperature indicating that the activation, concentration and ohmic losses improved as the temperature was increased.

The impedance data shows that the fundamental kinetic performance of the cell was similar in both fuel cell and electrolysis mode.

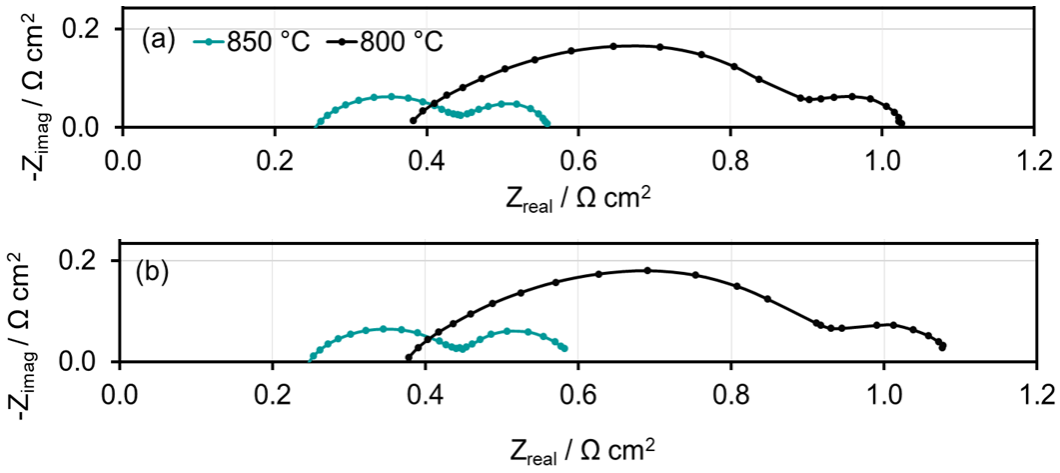

Figure 4.12: The effect of temperature on 50/50 vol% H_2/CO_2 composition on the electrochemical impedance spectra. Measurements were taken at 0.1-100000 Hz: (a) OCP - 0.1 V (fuel cell mode), and (b) OCP + 0.1 V (electrolysis mode).

Table 4.3: Widths of the ohmic losses, high and low frequency arcs in the electrochemical impedance spectra presented in Fig. 4.12.

Temperature	**OCP-0.1 V (Fuel cell mode)**			**OCP+0.1 V (Electrolysis Mode)**		
	Ohmic Losses	High Frequency Arc Width / Ω cm^2	Low Frequency Arc Width / Ω cm^2	Ohmic Losses	High Frequency Arc Width / Ω cm^2	Low Frequency Arc Width / Ω cm^2
800 °C	0.3819	0.5217	0.1214	0.3716	0.5514	0.1460
850 °C	0.2523	0.1918	0.1144	0.2464	0.2027	0.1331

Fig. 4.13a shows the experimental data set and the fitting results plotted together for H_2/CO_2 50/50 vol% mixture at 800 °C and Fig. 4.13b show the equivalent circuit model which provides the fitting values for each component and the errors associated. Although, to be brief, only one set of fitting results are shown here, all the other fittings are to the same level of precision. An obvious mismatch between the two curves can be found at the high frequency end. The experimental curve deviated from the fitting curve by titling slightly further towards the imaginary axis and this is attributed to the imperfections of the working electrode surface. Although an analogous performance can be seen between the two curves at the low frequency end.

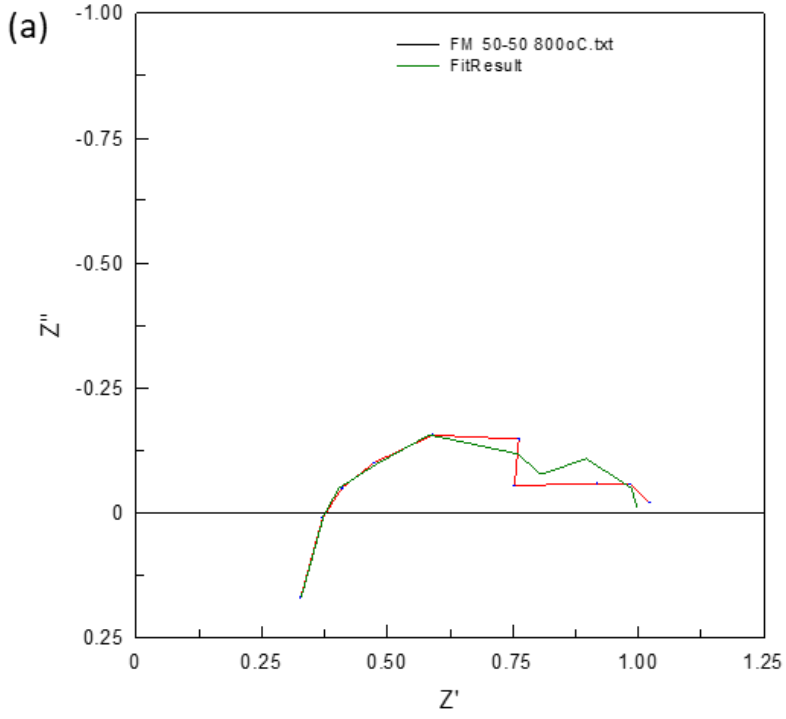

(b)

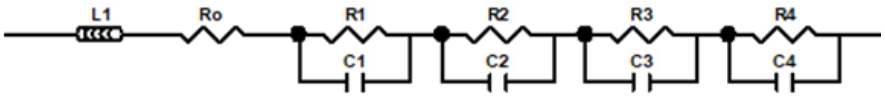

Element	Freedom	Value	Error	Error %
L1	Free(+)	5.1128E-07	6.184E-08	12.095
Ro	Free(+)	0.31334	0.030834	9.8404
R1	Free(+)	0.20053	0.029591	14.756
C1	Free(+)	0.20077	0.071783	35.754
R2	Free(+)	0.11077	0.031685	28.604
C2	Free(+)	0.00085396	0.00038978	45.644
R3	Free(+)	0.30017	0.034935	11.638
C3	Free(+)	0.0032635	0.00094639	28.999
R4	Free(+)	0.073053	0.028524	39.046
C4	Free(+)	6.8691E-05	7.3338E-05	106.77

Figure 4.13: (a) Equivalent Circuit fitting to experiment data 80/20 vol% H_2/CO_2 and (b) equivalent circuit model and fitting results.

4.3. Utilisation of Biohydrogen in an Anode Supported Cell

The following section describes experiments that were undertaken to investigate how fuel variability and temperature influenced the utilisation of biohydrogen in an anode supported cell (ASC). As described in Chapter 1, ASCs have greater performance than ESCs because they

have a much thinner electrolyte (giving reduced ohmic losses) and a much thicker anode layer, which generally decreases activation losses significantly, and makes lower temperature operation and the utilisation of carbon-based fuels like CH_4 feasible.

4.3.1. OCP Measurements

The effect of H_2/CO_2 composition on the OCP of an ASC is shown in Fig. 4.14 alongside the theoretical Nernst potential. Under pure H_2, the experimentally measured OCP (1.14 V) agreed closely with the Nernst potential, indicating the cell was well sealed with minimal gas crossover and current loss. Adding CO_2 to the fuel mixture immediately caused the OCP to deviate sharply away from the Nernst potential in a manner consistent with previous results. The OCP decreased non-linearly as the CO_2 content was increased to approx. 20 vol%. From 20-60 vol% CO_2, the OCP decreased almost linearly and in parallel with the Nernst potential before again decreasing non-linearly as the CO_2 content was increased above 60 vol%. The behaviour of the ASC was generally very similar but with higher OCP values to the behaviour observed for the ESC.

The deviation of the OCP away from the theoretical Nernst potential is explained by the presence of the RWGS reaction (4.1), which was observed by analysis of the product gases leaving the anode as shown in Fig. 4.14b. At 75/25 vol% H_2/CO_2, the levels of H_2 and CO_2 leaving the anode were less than 0.75 au and 0.25 au respectively, and CO was detected. Fig. 4.14b shows the presence of CO did not change significantly as the CO_2 content of the input gases was increased from 25 - 60 vol%, indicating the H_2/CO_2 composition did not have a significant effect on the equilibrium of the RWGS reaction over this range. This explains the linear decrease of OCP observed over this range in Fig. 4.14a; the equilibrium of the RWGS reaction was not changed and therefore the OCP varied linearly and in parallel with the theoretical Nernst potential due to a proportional dilution of the gases in CO_2. The sharp deviation of the OCP away from the Nernst potential at 0 - 25 vol% CO_2 indicates that the equilibrium of the RWGS reaction was strongly influenced by the H_2/CO_2 composition over this range. Adding CO_2 did not therefore cause a simple dilution of H_2 in CO_2; some of the H_2 was

also converted in the RWGS reaction, significantly affecting the OCP of the cell. The non-linear decrease of OCP at ≥ 60 vol% CO_2 is explained by both the increased dilution of gases in CO_2 and the shifting equilibrium of the RWGS reaction. Fig. 4.14b shows the CO presence decreased significantly above 60 vol% CO_2, indicating a decreased presence of the RWGS reaction. The decreased presence of H_2, CO and H_2O, coupled with increased dilution in CO_2, caused the OCP to decrease non-linearly and to further deviate away from the Nernst potential under high CO_2 concentrations.

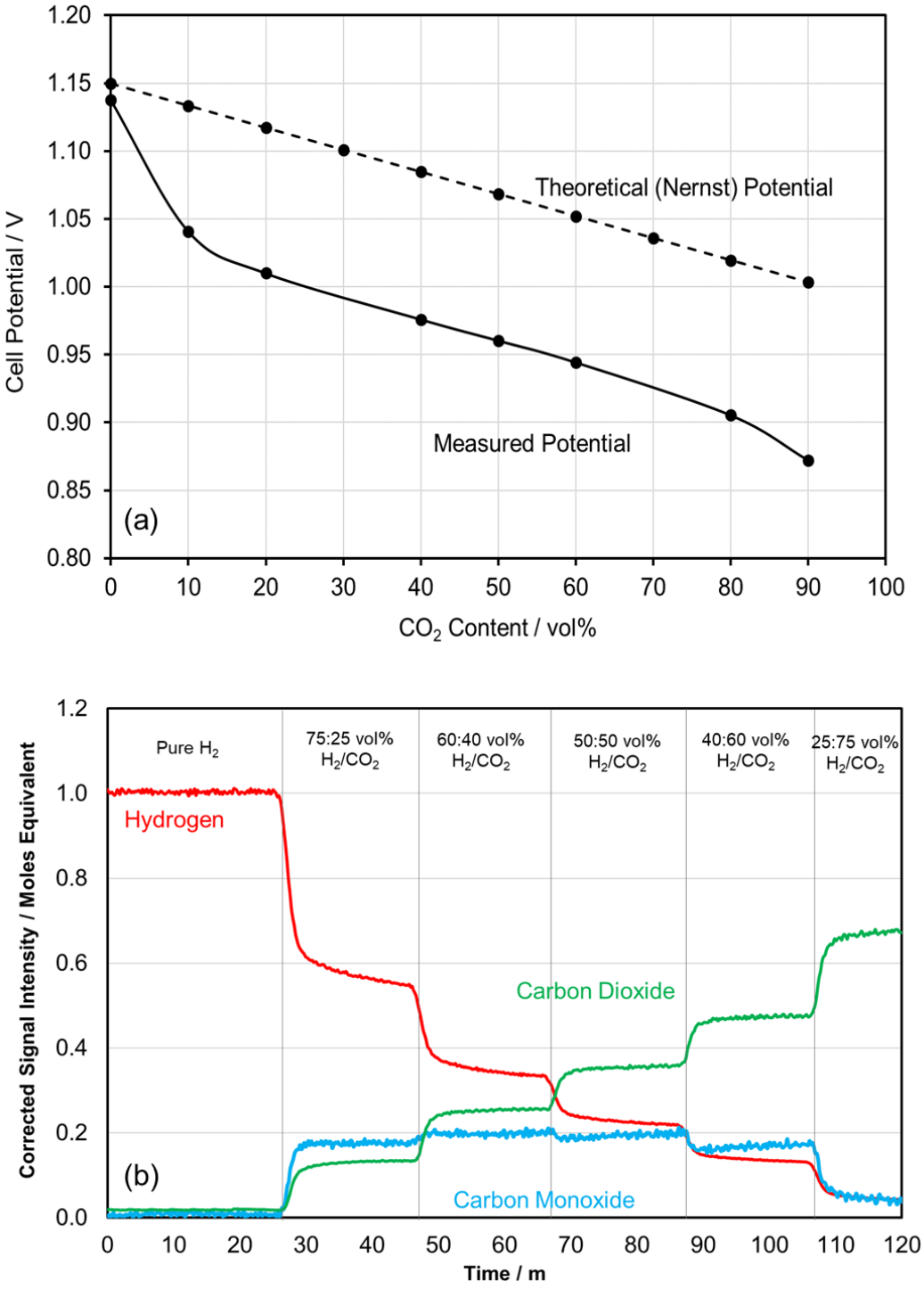

Figure 4.14: The effect of $H_2/CO2$ fuel composition on: (a) the OCP of the ASC, and (b) the composition of the output gases leaving the anode at OCP. The temperature of the ASC was 750 °C.

Fig. 4.15 shows the effect of H_2/CO_2 composition on the OCP of the ASC at different temperatures over the range 750-850 °C. Across most fuel compositions, as the temperature was increased from 750 °C to 850 °C the OCP decreased by approx. 0.02-0.03 V, in agreement with

Nernst predictions. The addition of CO_2 to the fuel mixture caused the OCP to deviate in a similar manner for all temperatures. Therefore, increasing the temperature did not appear to have a significant effect on the equilibrium of the RWGS reaction, particularly when the hydrogen content was high. A small effect was observed under higher CO_2 content mixtures, where increasing the temperature caused the OCP to decrease to a larger extent. Over this fuel range, increasing the temperature caused more H_2 to convert in the RWGS reaction, decreasing the presence of H_2 in the anode causing the OCP to decrease more prevalently. Therefore, in the case of the ASC the performance is significantly decreased as the temperature is increasing. When pure H_2 was used the OCP decreased by 0.020 V as the temperature increased from 800 °C to 850 °C for the ASC and in the case of ESC the OCP decreased by 0.015 V as the temperature increased. For the ASC at 50/50 vol% H_2/CO_2 the OCP decreased by 0.026 V when the temperature increased from 800 °C to 850 °C whereas in the ESC the OCP decreased by 0.009 V. The OCP decreased more for the ASC (0.037 V) as the H_2 content decreased to 10/90 vol% H_2/CO_2 whereas for the ESC (0.016 V). This pattern was observed for all fuel compositions where the ASC performance is significantly decreased more that ESC at higher operating temperatures. This can be explained by the decrease of the oxidation reaction or carbon deposition for the ASC. At lower temperatures, the ASC demonstrates better performance than the ESC but as the temperature increases, the performance of the ASC is decreasing more than the ESC under this fuel composition.

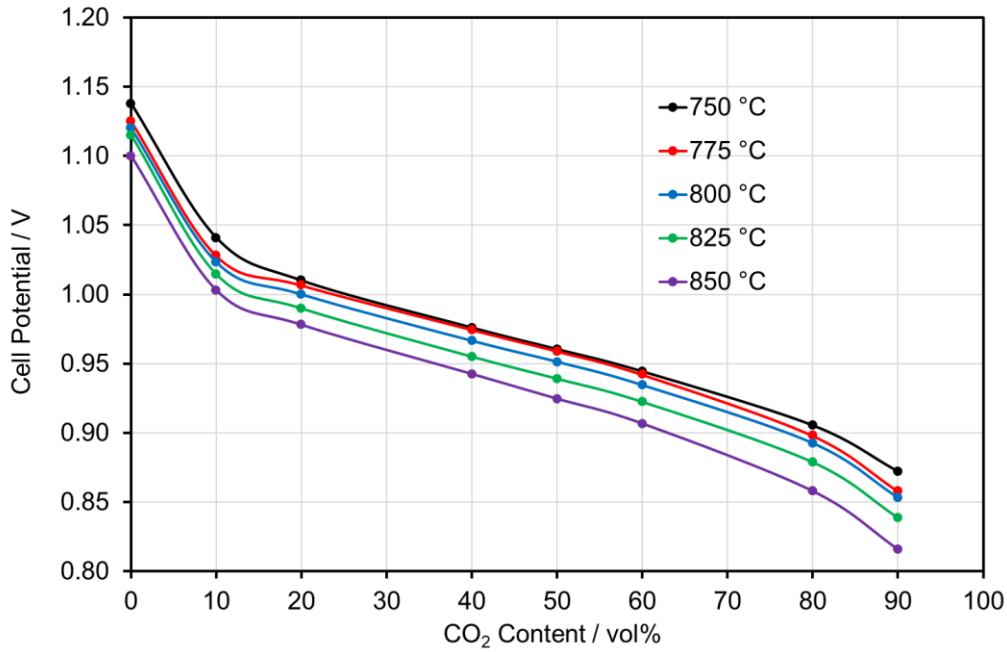

Figure 4.15: The effect of temperature on the OCP of the ASC at 750 °C – 850 °C.

4.3.2. Utilisation of 50/50 vol% H_2/CO_2

Fig. 4.16 shows the effect of temperature on the I-V and power curves of the cell when utilising 50/50 vol% H_2/CO_2 mixtures. The I-V curve at 750 °C decreased non-linearly in fuel cell mode between 1.0 V – 0.7 V indicating the presence of activation losses. However, as the temperature increased, the activation losses were alleviated due to the increased rate of the reaction taking place on the surface of the electrodes. The ohmic losses are higher at the lowest temperature 750 °C and are alleviated as the temperature increase showing the least ohmic losses at 850 °C. At low voltages, greater concentration losses were observed as the temperature increased. The maximum power output at 750 °C was 403 mW cm^{-2} and as the temperature was increased to 850 °C, the maximum power increased to 1031 mW cm^{-2}. This was expected since for biohydrogen mixtures, the main source of power production was electrochemical H_2 oxidation, which is faster at higher temperatures. Comparing the effect of temperature between ASC and ESC in fuel cell mode its apparent that increasing the temperature had a bigger effect on ASC were the activation, ohmic and concentration losses decreased as the temperature increased. The performance of the cell and the power produced by the ASC was considerably better as the temperature increased compared to the ESC.

The I-V curves in electrolysis mode show that activation losses were present in electrolysis mode, with a non-linear increase between 1.0 V – 1.2 V but as the temperature increased to 850 °C the activation losses decreased. There is also a linear increase in the mid-voltage range (1.2 V- 1.6V) has a shallower gradient at 750 °C, indicating the increased temperature increased the ohmic losses. This is also seen at high voltages (1.8 V) were the concentration losses increased with increasing temperature. Increasing the temperature in electrolysis mode did not improve the performance of the cell. In contrast this is not seen in electrolysis mode in the ESC were increasing the temperature improved the performance of the cell.

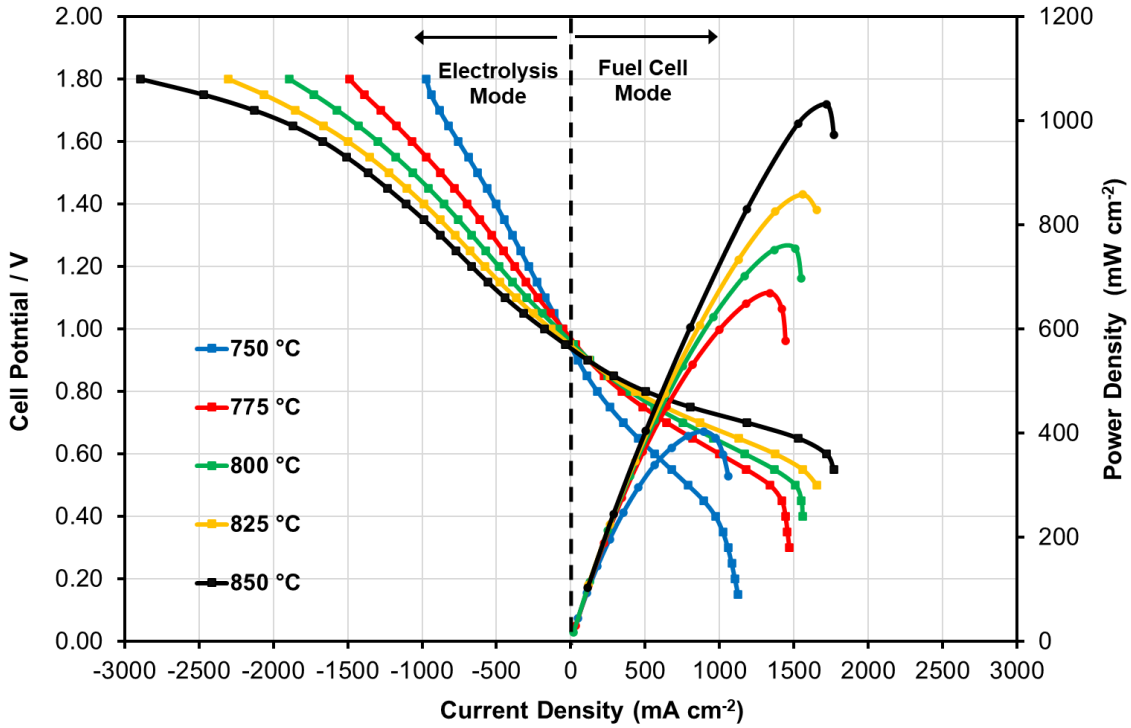

Figure 4.16: The effect of temperature on 50/50 vol% H_2/CO_2 composition on the I-V curves of the ASC running in fuel cell mode and electrolysis mode. The corresponding fuel cell power curves are plotted on the secondary axis.

4.3.2.1. Comparison of ESC and ASC performance when operating on 50/50 vol% H_2/CO_2 mixture

The I-V and power curves in Fig. 4.17 show that the current and power produced in fuel cell mode were very sensitive to changes in the MEA, with significantly more current and power produced with the ASC. The maximum power density for the ASC reached 400 mW cm^{-2},

which was almost twice compared to the ESC 230 mW cm^{-2}. This can be explained by a decreased thickness of the electrolyte and reduced anode overpotential. Both I-V curves decreased non-linearly at high voltages, in fuel cell mode in the range of 1.0 – 0.6 V indicating the presence of activation losses. Concentration losses were observed for both cells where a non-linear decrease of voltage was observed below 0.5 V.

In electrolysis mode the activation losses were present, with a non-linear increase of voltage observed at 0.9 – 1.2 V. In addition, there was no non-linear behaviour observed at voltages between 1.0 – 1.2 V. Therefore, the I-V curves clearly indicate that the efficiencies, losses and electrical power output are affected by MEA.

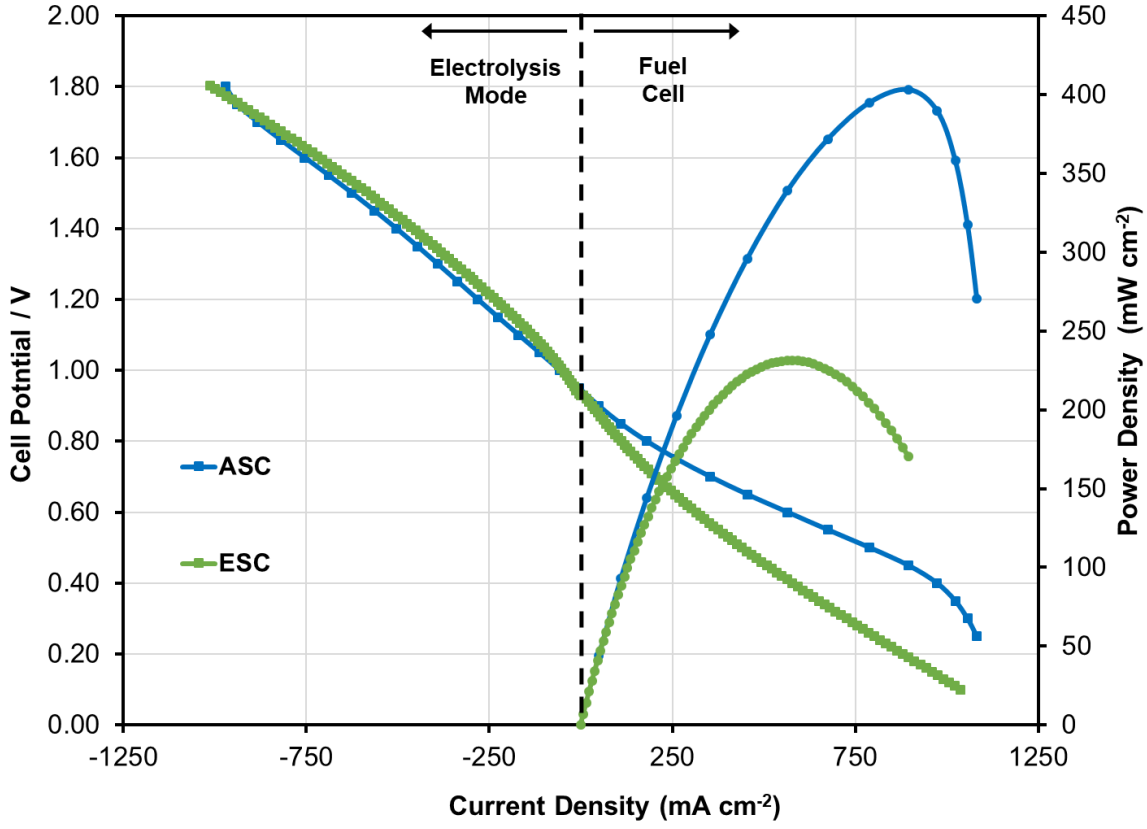

Figure 4.17: Comparison of the effect of 50/50 vol% H_2/CO_2 composition on the I-V curve of the ESC and ASC running in fuel cell mode and electrolysis mode at 800 °C. The corresponding fuel cell power curves are plotted on the secondary axis.

Fig. 4.18 shows the effect of temperature on the EIS of the cell when utilising a 50/50 vol% H_2/CO_2 mixture. The impedance data show that the activation, concentration and ohmic losses

improved as the temperature was increased (see Table 4.4). The impedance data show that there was a significant difference in performance between fuel cell and electrolysis mode as the high frequency arc in electrolysis mode is considerably wider compared to fuel cell mode.

Fig.4.18a shows the width of the high frequency arc in fuel cell mode at 750 °C decreased significantly (approx. 0.31 Ω cm^2) as the temperatures increased to 850 °C indicating the lower activation losses as temperature increase signifying less charge transfer and surface diffusion losses. The low frequency arc width was also decreased (0.05 Ω cm^2) when temperature increased from 750 °C to 850 °C indicating that gas diffusion losses had a much smaller effect on the diffusion of reactants through the anode. The ohmic losses were decreased (0.06 Ω cm^2), as the temperature increased.

Fig. 4.18b and Table.4.4 shows the width of high and low frequency arcs in electrolysis mode. The high frequency arc decreased (0.63 Ω cm^2) as the temperature increased from 750 °C to 850 °C indicating that charge transfer and surface diffusion losses in electrolysis mode are much larger than fuel cell mode. The low frequency arc decreased (0.16 Ω cm^2) and the ohmic losses decreased (0.07 Ω cm^2) as the temperature increased indicating that the concentration and ohmic losses improved as the temperature was increased. This confirms that CO_2 conversion kinetics in electrolysis mode are improved much better with increasing temperature compared to the H_2 conversion kinetics in fuel cell mode.

The temperature influenced the performance of the ASC but not as much as it influenced the performance of the ESC. For the ASC when the temperature increased from 800 °C to 850 °C during fuel cell operation the high frequency arc decreased by 0.6 Ω cm^2 whereas for the ESC the high frequency arc decreased significantly by 0.33 Ω cm^2. The low frequency arc decreased as the temperature increased for the ASC by 0.01 Ω cm^2 but increased for the ESC by 0.07 Ω cm^2. The ohmic losses also decreased for both ASC and ESC by 0.02 Ω cm^2 and 0.13 Ω cm^2 respectively as the temperature increased. The increase of temperature effect the ESC much more compared to the ASC in fuel cell operation.

When the cell was operated in electrolysis mode as the temperature was increased from 800 °C to 850 °C, the high frequency arc decreased for both ASC and ESC by 0.28 Ω $cm^2$and 0.35 Ω cm^2 respectively. The low frequency arc decreased by 0.05 Ω cm^2 for the ASC and 0.01 Ω cm^2 for the ESC. The ohmic losses also decreased by 0.2 Ω cm^2 for the ASC and 0.13 Ω cm^2 for the ESC. The increase of temperature effect the high frequency and the ohmic losses of ESC substantial compared to the ASC in electrolysis mode.

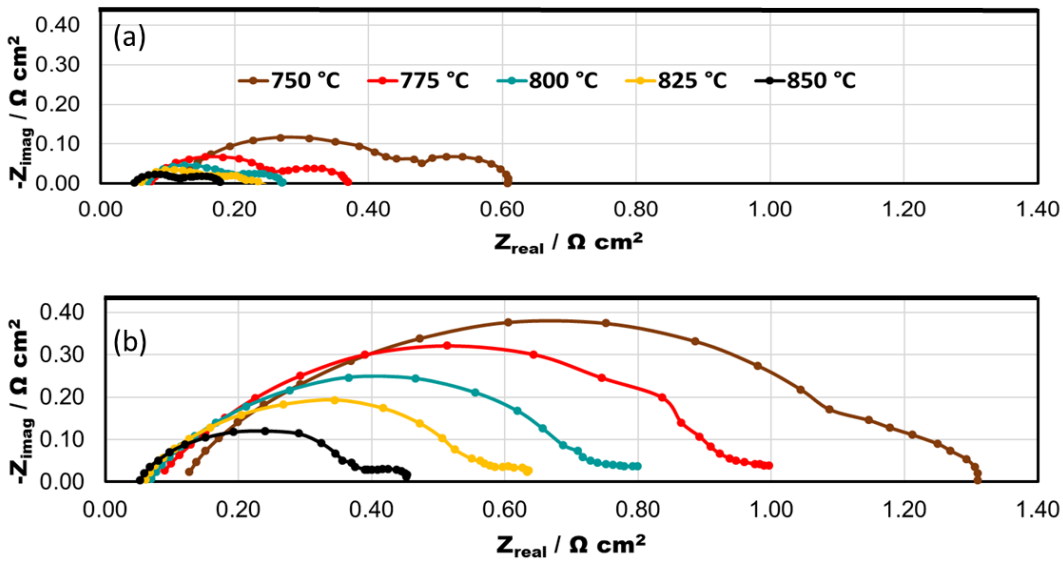

Figure 4.18: The effect of temperature on 50/50 vol% H_2/CO_2 composition on the electrochemical impedance spectra. Measurements were taken at 0.1-100000 Hz: (a) OCP - 0.1 V (fuel cell mode), and (b) OCP + 0.1 V (electrolysis mode).

Table 4.4: Widths of the ohmic losses, high and low frequency arcs in the electrochemical impedance spectra presented in Fig. 4.18.

Temperature	**OCP-0.1 V (Fuel cell mode)**			**OCP+0.1 V (Electrolysis Mode)**		
	Ohmic Losses/ Ω cm^2	High Frequency Arc Width / Ω cm^2	Low Frequency Arc Width / Ω cm^2	Ohmic Losses/ Ω cm^2	High Frequency Arc Width / Ω cm^2	Low Frequency Arc Width / Ω cm^2
750 °C	0.1144	0.3656	0.1214	0.1183	0.9687	0.2230
775 °C	0.0756	0.1806	0.1134	0.0895	0.7462	0.1603
800 °C	0.0696	0.1217	0.0805	0.0694	0.6182	0.1112
825 °C	0.0602	0.0974	0.0773	0.0601	0.4945	0.0830
850 °C	0.0502	0.0579	0.0698	0.0525	0.3377	0.0617

Fig. 4.19a shows the experimental data set and the fitting results plotted together for H_2/CO_2 50/50 vol% mixture at 750 °C of an ASC and Fig. 4.13b show the equivalent circuit model which provides the fitting values for each component and the errors associated. Although, to be brief, only one set of fitting results are shown here, all the other fittings are to the same level of precision. A very similar performance can be seen between the two curves at both frequencies.

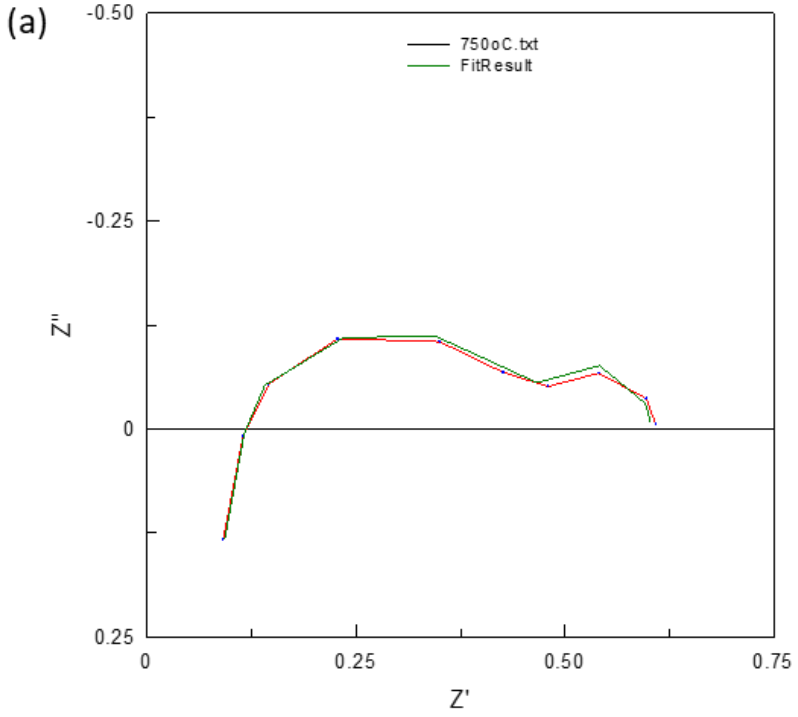

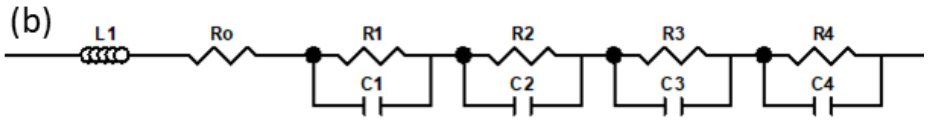

Element	Freedom	Value	Error	Error %
L1	Free(+)	3.8036E-07	1.3594E-08	3.574
Ro	Free(+)	0.086899	0.0063333	7.2881
R1	Free(+)	0.14735	0.011926	8.0937
C1	Free(+)	0.22893	0.046075	20.126
R2	Free(+)	0.16587	0.018854	11.367
C2	Free(+)	0.0007513	6.3994E-05	8.5178
R3	Free(+)	0.1639	0.019352	11.807
C3	Free(+)	0.0052155	0.0014702	28.189
R4	Free(+)	0.039001	0.0061069	15.658
C4	Free(+)	0.000163	6.3054E-05	38.683

Figure 4.19: (a) Equivalent Circuit fitting to experiment data 50/50 vol% H_2/CO_2 at 750 ℃ for an ASC and (b) equivalent circuit model and fitting results.

4.3.3. Fuel variability effects

Fig. 4.20 shows the effect of decreasing the operating voltage on the products of the ASC when running on 50/50 vol% H_2/CO_2 in fuel cell mode. Some of the initial H_2 and CO_2 were converted in the RWGS reaction to give an OCP of 0.94 V. Across all operating voltages, there was CO present in the output gases indicating that the RWGS reaction took place

simultaneously with electrochemical processes on the anode. As the cell voltage was progressively decreased, the electrical current produced increased, with a maximum current of 1278 mA cm^{-2} produced at 0.2 V. The current generated by the cell up to 0.7 V is mainly being produced from the electrochemical oxidation of H_2. When the applied voltage reached 0.7 V the H_2/CO ratio was lower than 1 and this suggests that the electrochemical oxidation of H_2 was not the predominant reaction and the reaction of electrochemical CO oxidation was also taking place (Eq. 18). Therefore, since the H_2/CO < 1 from 0.7 V – 0.2 V, the conversion of CO_2 through the direct electrochemical oxidation of CO is also taking place. As the voltage decreases (below 0.7 V) the cell reach high fuel utilisation values and the CO value in the downstream of the fuel shifts the reaction in a CO-rich direction resulting an increase in the polarization resistance (Fig 4.20a). Therefore, the concentration of H_2O produced by the electrochemical oxidation of H_2 should also increase to prevent the increase of CO if the RWGS reaction proceeds at a sufficient rate.

$$CO + O^{2-} \rightleftharpoons CO_2 + 2e^- \qquad \text{(Eq. 18)}$$

As the potential of the cell decreased from 0.7 V – 0.2 V the rate of electrochemical H_2 oxidation (Eq. 1) increased to prevent the increase of CO oxidation shifting the equilibrium of the reaction to the WGS reaction.

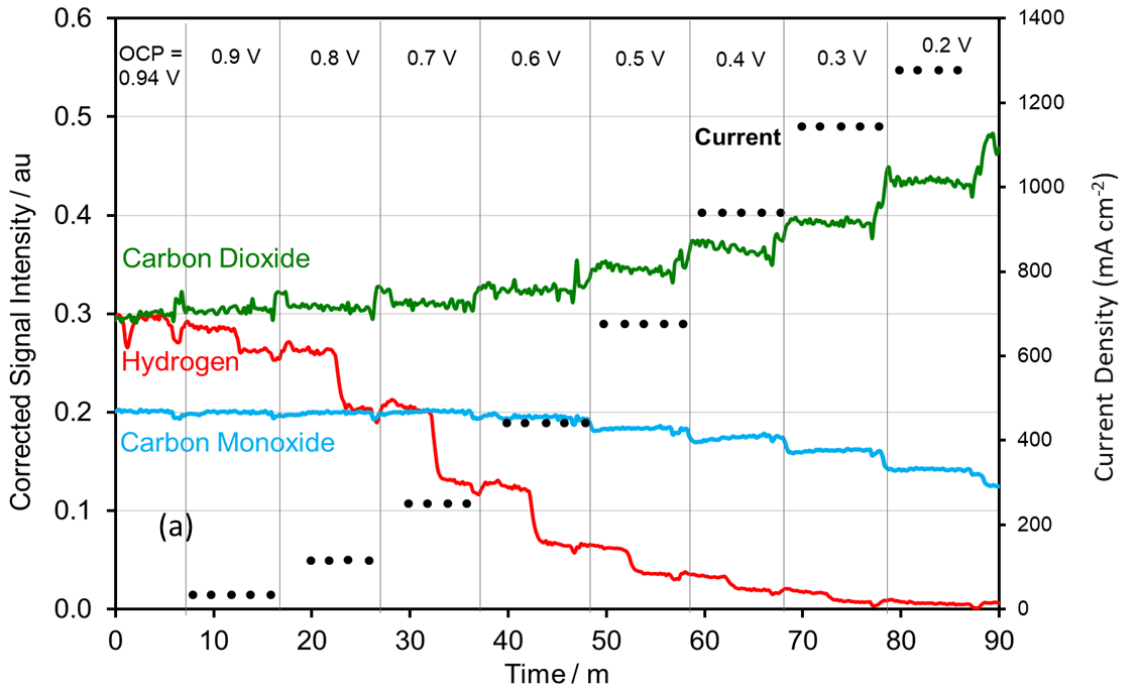

Figure 4.20: (a) The effect of operating voltage on the gaseous and current outputs of the ASC running on 50/50 vol% H_2/CO_2 in fuel cell mode at 750 °C. The figure plots the output gases on the primary vertical axis, and the corresponding current output on the secondary vertical axis.

Fig. 4.21 shows the effect of operating potential on the products of the ASC running on 50/50 vol% H_2/CO_2 in electrolysis mode. As the operating potential was increased, the partial pressure of CO_2 decreased, and the H_2 and CO increased. The synthesis gas production rate increased from approx. 12 $cm^3\ min^{-1}\ cm^{-2}$ at the OCP, to approx. 19 $cm^3\ min^{-1}\ cm^{-2}$ at 1.8 V. At the OCP, H_2-rich synthesis gas mixtures with a H_2/CO ratio of approximately 2.3 by volume were produced, whilst at the highest voltage studied (1.8 V) the H_2/CO ratio increased to approx. 2.5 by volume. The observed increase of the H_2/CO ratio which indicates the rate of CO production increased relative to H_2 production as the cell voltage was increased.

Electrochemical reduction of H_2O causes the presence of H_2O to decrease and the H_2 to increase, and is likely therefore to have shifted the equilibrium of the RWGS reaction towards the production of CO. The presence of H_2O at the OCP was likely to be the same as that of CO (they have a 1:1 stoichiometry in the RWGS reaction), with a corrected signal intensity of approximately 0.15 au. Taking into account the stoichiometries of electrochemical H_2O reduction and the RWGS reaction, the maximum possible CO production through this reaction

pathway would give a corrected signal intensity for CO of 0.30 au. At the highest voltage studied (1.8 V), the corrected signal intensity of CO was approximately 0.38 au and therefore it can be inferred that CO production must have taken place through the RWGS reaction and electrochemical reduction of CO_2 simultaneously.

This work shows that the RWGS reaction significantly influences the OCP of SOFC devices running on H_2/CO_2 mixtures and results in the in-situ production of CO and H_2O on the anode. The equilibrium of the RWGS reaction is dependent on the operating voltage of the cell; at lower voltages, the equilibrium is shifted towards the WGS direction, whilst at higher voltages the equilibrium is shifted towards the RWGS reaction.

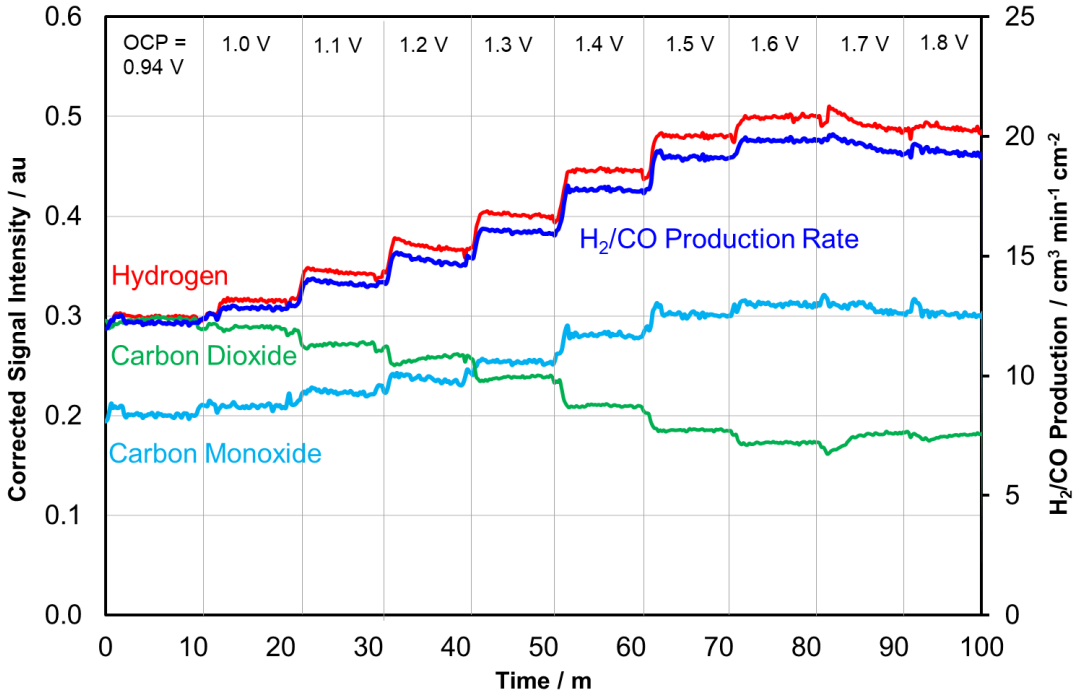

Figure 4.21: The effect of operating voltage on the gaseous products of the ASC running on 50/50 vol% H_2/CO_2 in electrolysis mode at 750 °C. The figure plots the output gases from the anode on the primary vertical axis, and the corresponding total synthesis gas production (H_2 + CO) on the secondary vertical axis.

Fig. 4.22 shows the variation in the quantity and composition of the synthesis gas produced as the voltage was changed. It is clear that voltage variability considerably influenced the composition and quantity of syngas produced by the cell in electrolysis mode. Increasing the voltage to 1.6 V increased the total production of synthesis gas from 12 cm^3 min^{-1} cm^{-2} to 20

cm^3 min^{-1} cm^{-2}. Increasing the voltage further to 1.7 V and 1.8 V caused the total production of synthesis gas to decrease marginally to 19 cm^3 min^{-1} cm^{-2}. The H_2/CO ratio of the synthesis gas increased from approximately 2.3 to 2.5 at 1.8 V. The H_2/CO ratio did not change significantly, as the voltage was changed from OCP to 1.8 V. The H_2/CO ratio continued to increase slightly due to a mixture of increased H_2 and CO production.

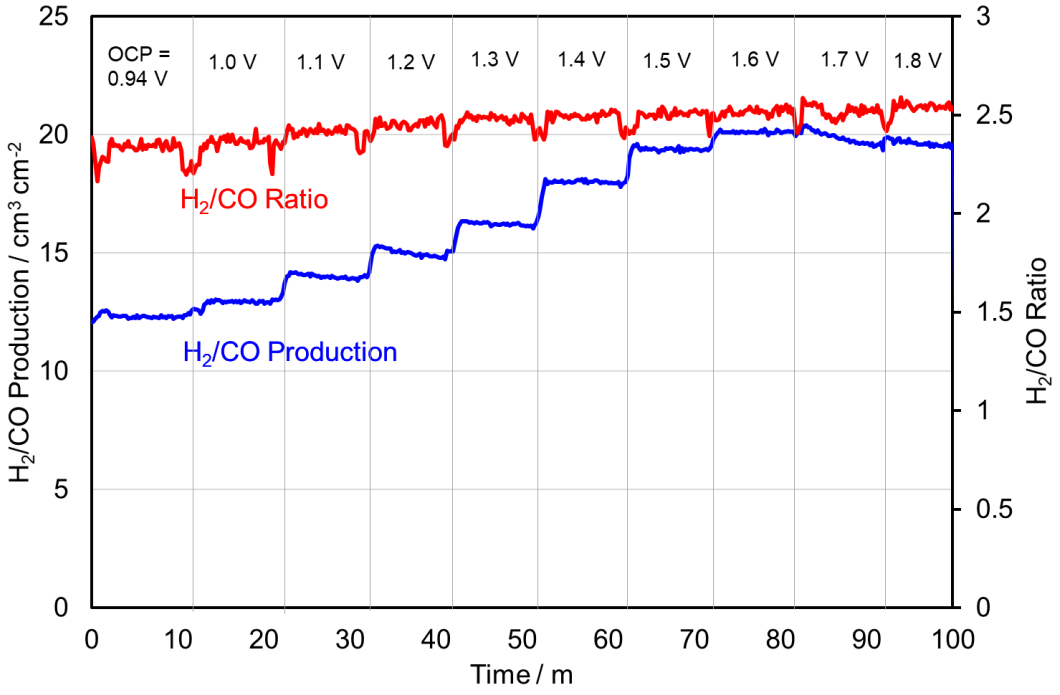

Figure 4.22: The effect of voltage on the products of the ASC running in electrolysis mode at 750 °C. The gas composition was H_2/CO 50/50 vol%. The figure shows the composition of the synthesis gas (H_2/CO ratio) on the primary vertical axis and the synthesis gas production (H_2 + CO) on the secondary vertical axis.

Fig. 4.23 shows a comparison of ESC and ASC in the quantity and composition of the synthesis gas produced in electrolysis mode at 800 °C. It is clear that MEA significantly influenced the composition and quantity of syngas produced by the cell in electrolysis mode. Fig. 4.23a shows the H_2/CO ratio of the synthesis gas decreased when operated with an ESC but increased when operated with an ASC. A sharp decrease of H_2/CO ratio from 2.33 to 1.25 observed in the ESC as the voltage was increased and an increase of H_2/CO ratio from 2.08 to 2.27 observed in the ASC as the voltage was increased. Fig. 4.23b shows the H_2/CO production rate as the voltage increases. For both ESC and ASC the syngas production rate increases as the voltage increases.

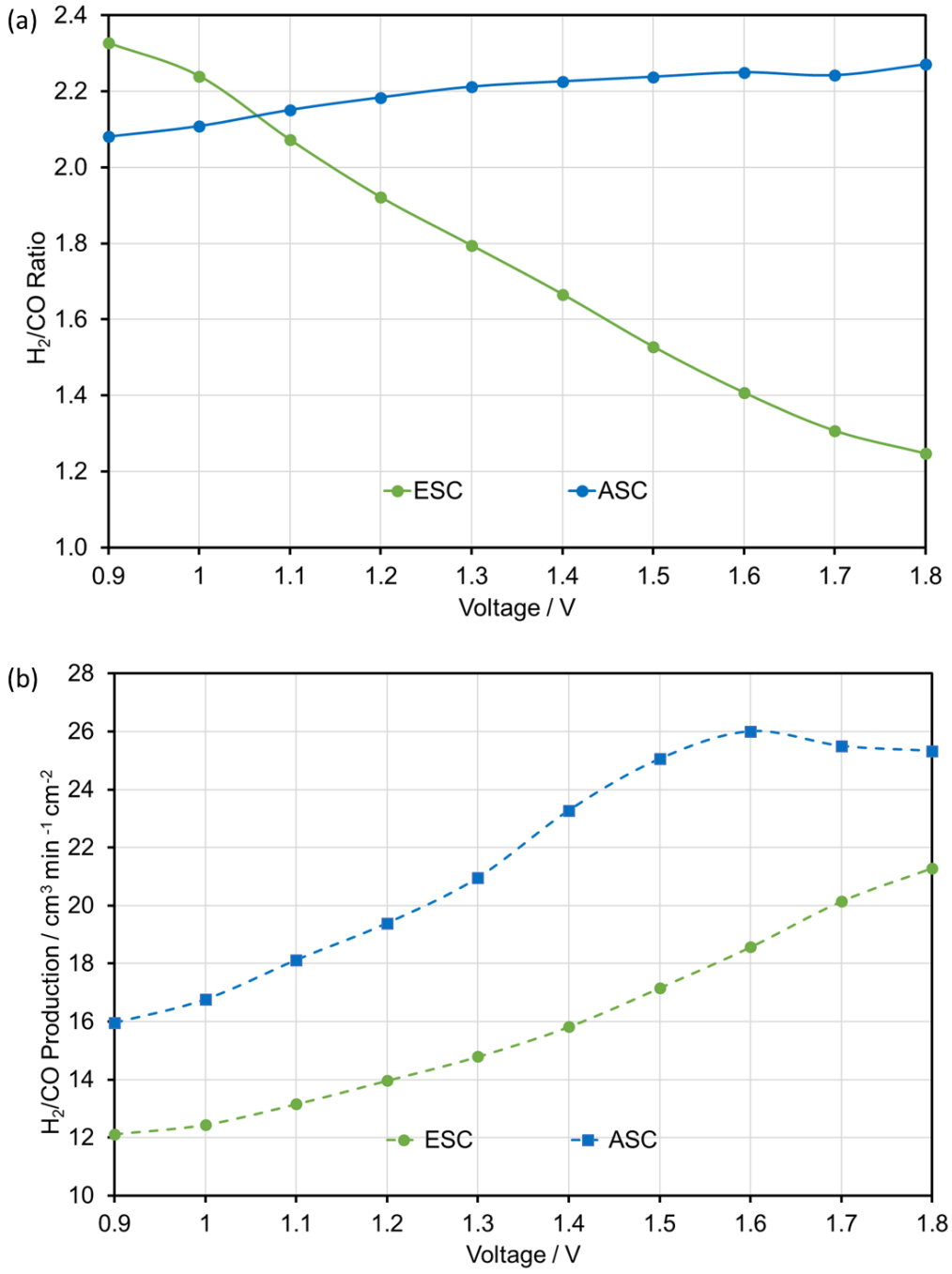

Figure 4.23: Comparison of the ESC and ASC on H_2/CO_2 50/50 vol% composition operating in electrolysis mode at 800 °C. The figure shows: (a) the composition of the synthesis gas (H_2/CO ratio) and (b) synthesis gas production (H_2 + CO).

4.3.4. Effects of fuel variability in fuel cell mode

The I-V and power curves in Fig. 4.24 show that the current and power produced in fuel cell mode were sensitive to changes in the fuel composition, with significantly more current and power produced as the H_2 content of the fuel was increased. All I-V curves decreased non-

linearly at high voltages, indicating the presence of activation losses and ohmic losses. The I-V curves were almost parallel across the fuel composition range 100 - 40 vol% H_2, suggesting similar activation losses and ohmic for each fuel composition whereas I-V curves with the fuel composition 20 – 10 vol% H_2 show higher activation losses and ohmic losses. The performance of the ASC is better compared to ESC, due to less activation and ohmic losses. Concentration losses were clearly observed for all mixtures and especially mixtures containing 60 vol% H_2 or less, where a non-linear decrease of voltage was observed below 0.6 V. This was not the case for the ESC where concentration losses were less and only observed for mixtures containing 20 – 10 vol% H_2. The power produced for the ASC was three times higher compared to the power produced from the ESC.

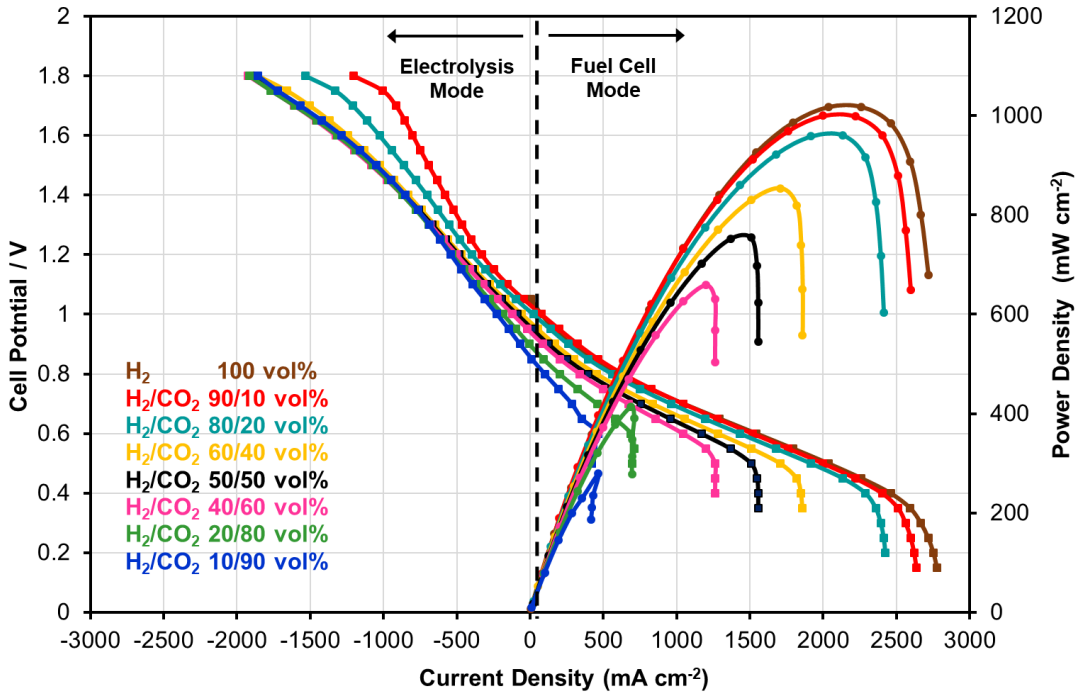

Figure 4.24: The effect of H_2/CO_2 composition on the I-V curve of the ASC running in fuel cell mode and electrolysis mode at 800 °C. The corresponding fuel cell power curves are plotted on the secondary axis.

The electrochemical impedance spectra shown in Fig. 4.25, which were collected with the cell running on different H_2/CO_2 mixtures, were composed of two polarisation arcs in fuel cell mode. The widths of the arcs were measured and are shown in Table 4.5. In fuel cell mode, the width of the high frequency arc from 90 vol% to 40 vol% of H_2 did not respond significantly to

changes in the fuel composition, indicating low charge transfer and surface diffusion losses. Although in fuel composition with 20 – 10 vol% H_2 present the high frequency arc increased signifying that charge transfer and surface diffusion losses are more apparent with at compositions with low level of H_2. This was not the case for ESC where the high frequency arc was (approx. 0.19 Ω cm^2) for all fuel compositions and was not sensitive to different fuel compositions whereas in ASC the high frequency arc is lower for H_2 compositions 90 vol% – 40 vol% (approx. 0.12 Ω cm^2) but at lower H_2 compositions the high frequency arc increases.

The low frequency arc width had similar behaviour with the ESC, where the arc increased significantly 0.05 Ω cm^2 for fuel mixtures containing 20 vol% H_2 and 0.10 Ω cm^2 for 10 vol%, indicating that gas diffusion losses were very sensitive to the fuel composition with low H_2 content. The low frequency arc for fuel compositions in the range 90 vol% - 40 vol% was much smaller (approx. 0.07 Ω cm^2) compared to (approx. 0.11 Ω cm^2) of the ESC.

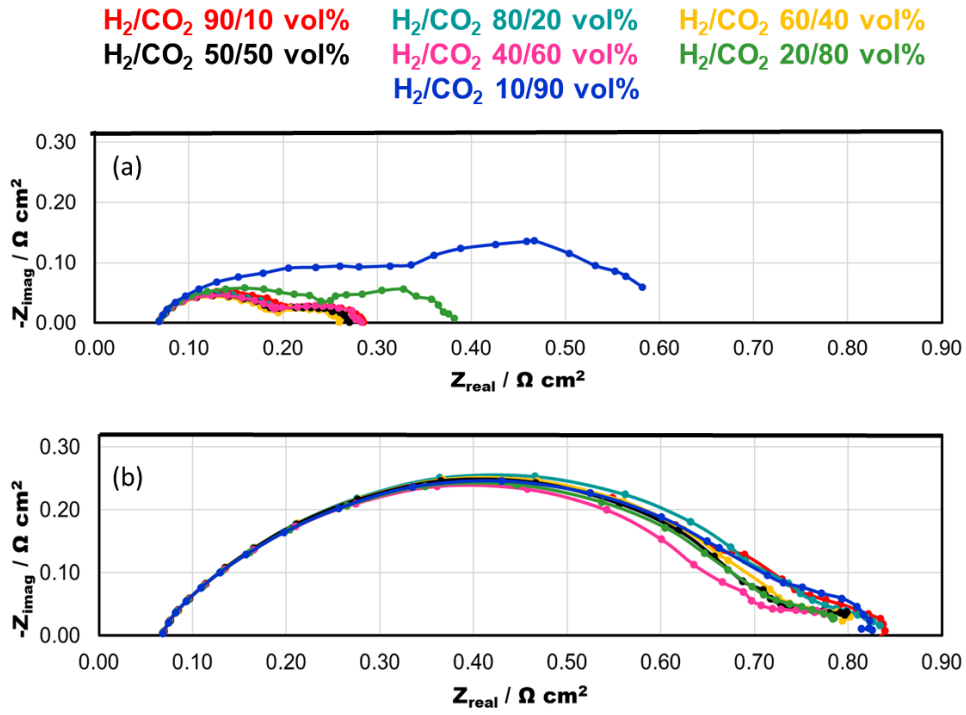

Figure 4.25: The effect of H_2/CO_2 composition on the electrochemical impedance spectra of the ASC at 800 °C. Measurements were taken at 0.1-100000 Hz: (a) OCP - 0.1 V (fuel cell mode), and (b) OCP + 0.1 V (electrolysis mode).

Table 4.5: Widths of the high and low frequency arcs in the electrochemical impedance spectra presented in Fig. 4.25.

H_2/CO_2	OCP-0.1 V (Fuel cell mode)			OCP+0.1 V (Electrolysis Mode)		
	Ohmic / Ω cm^2	High Frequency Arc Width / Ω cm^2	Low Frequency Arc Width / Ω cm^2	Ohmic / Ω cm^2	High Frequency Arc Width / Ω cm^2	Low Frequency Arc Width / Ω cm^2
90/10	0.0678	0.1324	0.0849	0.0679	0.6748	0.0967
80/20	0.0678	0.1287	0.0770	0.0679	0.6813	0.0844
60/40	0.0678	0.1253	0.0646	0.0679	0.6770	0.0572
50/50	0.0678	0.1217	0.0805	0.0679	0.6494	0.0795
40/60	0.0678	0.1219	0.0905	0.0679	0.6289	0.0772
20/80	0.0678	0.1713	0.1418	0.0679	0.6419	0.0749
10/90	0.0678	0.2629	0.2460	0.0679	0.6630	0.0950

4.3.4.1. Effect of fuel variability in electrolysis mode

The I-V curves collected in electrolysis mode (see Fig. 4.24) for the ASC show that activation losses were negligible in electrolysis mode following the same pattern of the ESC electrolysis curves. There is a non-linear increase of voltage observed between 1.2 - 1.6 V for H_2-poor (10 vol% - 20 vol%) mixtures showing ohmic losses for both ASC and ESC. The same behaviour was observed at high voltages for H_2-poor mixtures indicating that concentration losses were significant in electrolysis mode to H_2-poor mixtures for both ASC and ESC.

The electrochemical impedance spectra collected in electrolysis mode (see Fig. 4.25b) have a very wide high frequency arc, indicating that the ASC operated less efficiently in electrolysis mode. Table 4.5 shows frequency arc widths were generally greater than in fuel cell mode, indicating increased charge transfer and surface diffusion losses. In addition, the width of the frequency high frequency arc was sensitive to the fuel composition and decreased by approx. 0.05 Ω cm^2 as the H_2 content decreased from 90 vol% to 40 vol% whereas in the ESC the high frequency arc decreased significantly by 0.20 Ω cm^2 showing that the ESC is more sensitive to fuel composition. The high frequency arc increased by 0.01 Ω cm^2 for 20 vol% H_2 and by 0.02

Ω cm^2 for 10 vol% H_2 compositions for the ASC whereas the increase for the ESC was much less approx. 0.007 Ω cm^2 for 20 vol% H_2 and by 0.002 Ω cm^2 for 10 vol% H_2 compositions.

4.4. Conclusion

Fuel variability is an issue that is applicable to many gaseous renewable and waste feedstocks and this chapter has shown that the performance, fuel processing and outputs of an electrolyte and anode supported cells are very sensitive to fuel variation in the composition of feedstocks derived from biohydrogen production processes. For H_2/CO_2 mixtures, fuel variability has significantly less influence when the feedstock composition is within the range 40:60 – 60:40 vol% H_2/CO_2. The effects of fuel variability are closely related to the presence of the RWGS reaction, which was shown to take place simultaneously alongside electrochemical processes. The RWGS reaction significantly affects the OCP and results in the production of CO and H_2O. The equilibrium of the RWGS reaction is dependent on the operating voltage of the cell; at lower voltages the equilibrium is shifted towards the WGS direction, at higher voltages the equilibrium is shifted towards the RWGS reaction.

Electrolysis of H_2/CO_2 mixtures to yield synthesis gas was studied showing CO_2 production to take place through electrochemical CO_2 reduction and the RWGS reaction simultaneously. The H_2 consumed in the RWGS reaction is regenerated by subsequent electrochemical reduction of steam. Increasing the CO_2 content of the feedstock decreases activation and gas diffusion overpotentials, but results in lower synthesis gas production rates and H_2/CO ratios due to an increasing absence of the RWGS reaction. In fuel cell mode, electrical power is generated predominantly from the electrochemical oxidation of hydrogen, with minimal contribution from the electrochemical oxidation of carbon monoxide. Instead, carbon monoxide is converted through the electrochemical oxidation of hydrogen followed by the WGS reaction to subsequently regenerate the CO_2.

Operating conditions such as temperature have shown to have an effect on the performance and outputs of the cell. Increased temperature caused the OCP to decrease due to the RWGS reaction but increased the reaction rate. At high (90 vol%) and low (10-20 vol%) CO_2

compositions the activation and concentrations were increased. When the CO_2 composition was in the range of 40-60 vol% the losses were minimised and the cell performance was enhanced.

The ASC have much better performance in fuel cell mode with more power being produced compared to an ESC, although ASC was more sensitive to fuel variability. The performance of the ASC was very similar to the ESC in electrolysis mode but the ASC increased the syngas ratio as the operating voltage increased whereas the ESC decreased the syngas ratio. Comparing the effect of temperature between ASC and ESC in fuel cell mode showed that increasing the temperature had a greater effect on ASC. The performance and the power produced by the ASC was considerably better as the temperature increased compared to the ESC. However, increasing the temperature in electrolysis mode did not improve the performance of the ASC, whereas in an ESC during electrolysis mode increasing the temperature improved the performance of the cell. Therefore, the ASC is a better candidate in fuel cell mode due to better performance but in electrolysis mode, the increase in performance is not as significant and it is less sensitive to fuel variability.

Chapter 5: Utilisation of Biohythane mixtures in SOC technology

5.1. Introduction

This chapter explores the utilisation of biohythane in an anode-supported SOFC. The performance and overall energy yield of biohythane utilisation is studied and compared with conventional biogas utilisation in SOFCs. The performance of the cell is characterised using I-V curves and electrochemical impedance spectroscopy. Fuel variability effects and the optimum biohythane fuel composition for utilisation in SOFCs are established. The output gases from the anode are also characterised using QMS, giving detailed comprehensions into the fuel processing and transient behaviour of fuel conversion. The effects of fuel variability on the output gases from the anode have also been characterised and the fuel conversion pathways at the anode have been determined. In addition, the durability of an SOFC operating on a typical biohythane mixture (60/30/10 vol% $CH_4/CO_2/H_2$) over a 288-hour period is reported, demonstrating the potential to operate SOFCs on biohythane over more long-term periods. Finally, by investigating the effects of CH_4, CO_2 and H_2 variability, this work is relevant to the concept of natural gas grid decarbonisation via substitution with H_2/CO_2 mixtures (biohydrogen) and subsequent utilisation in SOFCs. The effect of changing composition as a function of temperature have been calculated with CH_4 and CO_2 being converted into product gases (H_2, CO, H_2O, CH_4 and CO_2) to predict the product gas composition at different $CH_4/CO_2/H_2$ and CO_2/H_2 mixtures at different temperatures (Appendix E).

5.2. Comparison of biohythane utilisation with other fuels

The OCP of the ASC was measured for each of the fuels and the electrochemical performance of the cell was studied in fuel cell mode when running on the fuel mixtures shown in Table 5.1. Pure H_2 gave the highest OCP of 1.126 V, indicating the sealing of the cell was very good with no gas crossover taking place. In agreement with previous work [269] into biohydrogen

utilisation in an ESC, switching to 50/50 vol% H_2/CO_2 (biohydrogen) decreased the OCP significantly to 0.982 V. This decrease was due to the lower volume of H_2 present at the anode due to dilution in CO_2 and the RWGS reaction, which catalytically consumed H_2 to produce CO. Switching to biogas improved the OCP to 1.034 V because of Nernst behaviour [84] and an increased presence of H_2 due to catalytic dry reforming of CH_4. Upon switching to biohythane, adding 10 vol% H_2 increased the OCP further to 1.049 V, again as expected from Nernst predictions and due to a further increase of H_2 present at the anode. Increasing the H_2 content to 20 vol% and 40 vol% H_2 increased the OCP to 1.052 V and 1.062 V, demonstrating the beneficial effect of blending biogas with biohydrogen on the OCP of the cell.

Table 5.1: Composition and OCP of fuel mixtures studied in this work.

Fuel	OCP	CH_4 / vol%	CO_2 / vol%	H_2 / vol%
Pure H_2	1.126 V	0	0	100
Biohydrogen (H_2/CO_2)	0.982 V	0	50	50
Biogas (CH_4/CO_2)	1.034 V	60	40	0
Biohythane ($CH_4/CO_2/H_2$)	1.049 V	60	30	10
Biohythane (20 vol% H_2)	1.052 V	53	27	20
Biohythane (40 vol% H_2)	1.062 V	40	20	40

The I-V curves in Fig. 5.1 show that H_2 gave the least kinetic losses overall, with very low OCP, activation and concentration losses observed. Biohydrogen (50/50 vol% H_2/CO_2) gave a poorer performance to that shown under pure H_2, with the I-V curve lower due to the OCP losses shown in Table 5.1. Biogas (60/40 vol% CH_4/CO_2) gave poorer performance overall than the H_2-based fuels due to the presence of CH_4 which significantly increased activation and concentration losses. Biohythane gave an increased kinetic performance compared with biogas due to improved activation losses. Concentration losses were observed but these were also less significant compared with biogas. Table 5.2 shows values from these I-V and power curves

which indicate that between 0.6-0.9 V, biohythane gave between 10-21% better kinetic performance than biogas, depending on the operating voltage of the cell. This clearly shows that it is advantageous to utilise biohythane rather than biogas in terms of cell efficiency. In addition, taking into consideration the increased energy yield of up to 46% for two-stage AD compared with single-stage AD, the utilisation of biohythane in SOFCs potentially gives a 61-77% increase in overall energy yield.

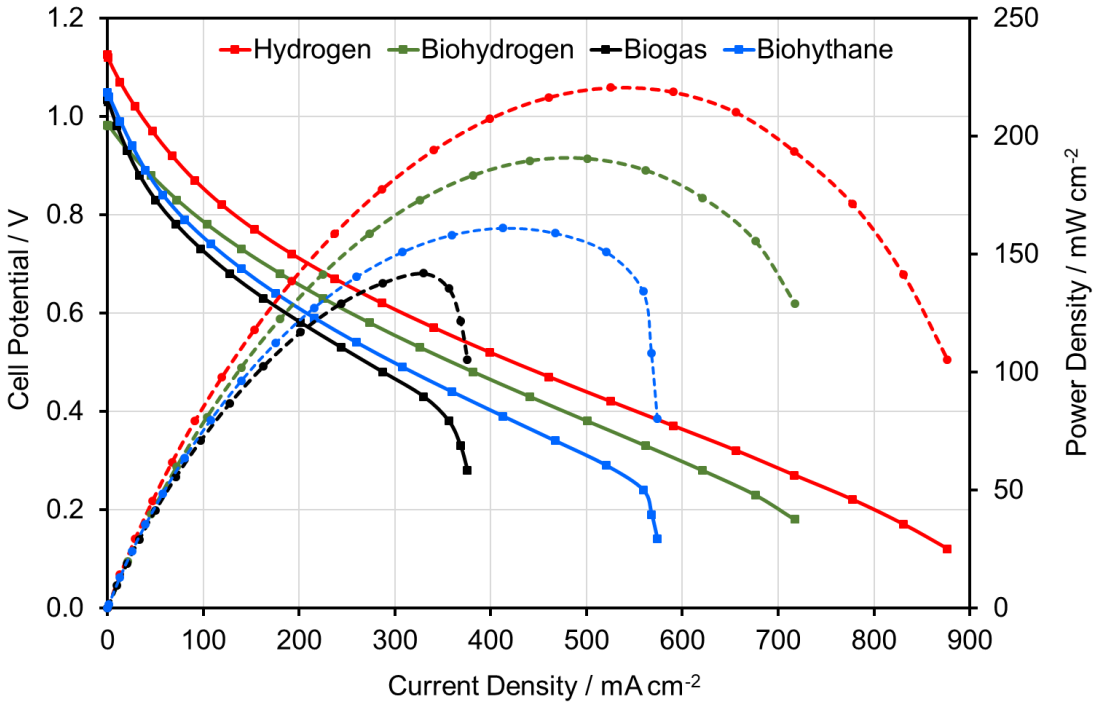

Figure 5.1: I-V curves (solid lines) and power curves (dashed lines) of an ASC operating on 100 vol% H_2, 50/50 vol% H_2/CO_2 (biohydrogen), 60/40 vol% CH_4/CO_2 (biogas) and 60/30/10 vol% (biohythane).

Table 5.2: Comparison of power density of ASC when running on biogas and biohythane over the voltage range 0.9-0.6 V. Values taken from I-V and power curves in Fig. 5.1.

Voltage / V	Biogas / mW cm^{-2}	Biohythane / mW cm^{-2}	Percentage Increase
0.9	29.1	35.3	21.3%
0.8	41.4	48.4	16.9%
0.7	71.0	79.7	12.3%
0.6	102.4	112.3	9.7%

5.3. Fuel processing of biohythane

The output gases of the fuel electrode when running on biohythane (60/30/10 vol% $CH_4/CO_2/H_2$) were measured using quadrupole mass spectrometry and are shown for biohythane in Fig. 5.2. It is clearly observed that as the voltage was decreased, the cell produced electrical power and syngas simultaneously with almost complete conversion of CH_4 achieved at 0.7 V. Decreasing the voltage further increased electrical power production at the expense of syngas production, with the syngas becoming richer in H_2 as the voltage was decreased. The figure suggests that the balance of electrical power and syngas production could be controlled by adjustment of the cell voltage.

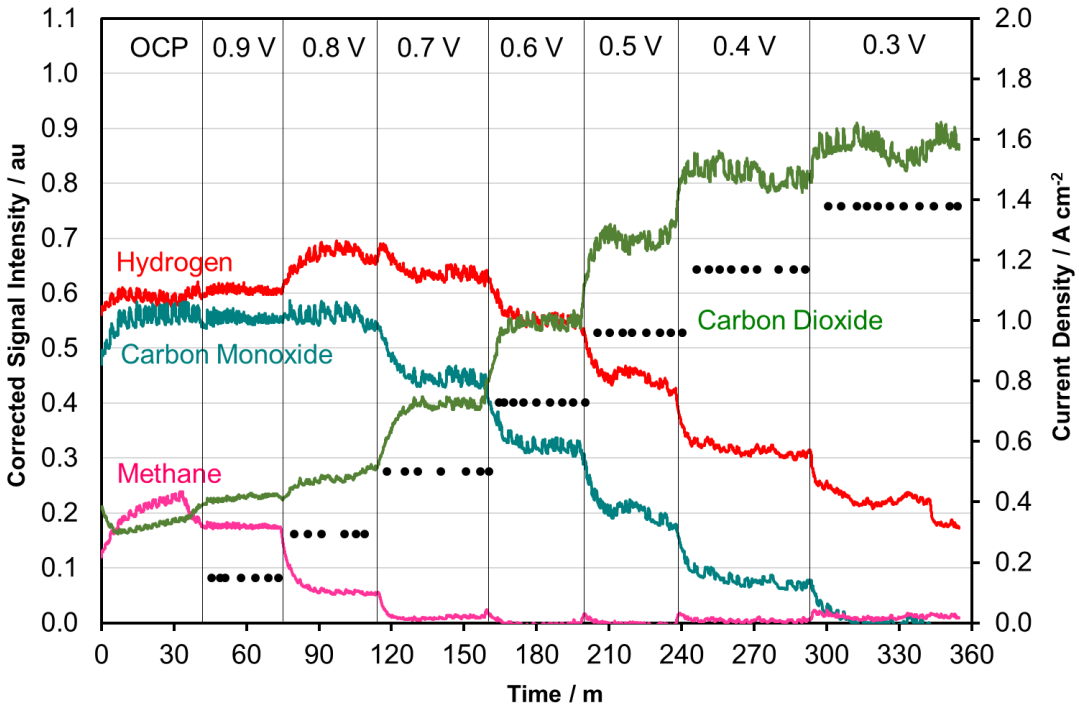

Figure 5.2: The effect of decreasing the operating voltage on the output gases and electrical power of an ASC operating on biohythane ($CH_4/CO_2/H_2$ 60/30/10 vol%).

At the OCP, CH_4 and CO_2 were converted via catalytic dry reforming of CH_4 (Eq. 17) to yield syngas with a composition of $H_2/CO = 1.08$. As the voltage was decreased to 0.8 V, CH_4 conversion and the presence of H_2 increased, indicating that power and syngas were produced simultaneously via partial electrochemical oxidation (Pox) of CH_4 (Eq. 19):

$CH_4 + CO_2 \rightleftharpoons 2H_2 + 2CO$ (Eq. 17)

$CH_4 + O^{2-} \rightleftharpoons 2H_2 + CO + 2e^-$ (Eq. 19)

This reaction was favourable because the flux of incoming O^{2-} ions from the electrolyte at high voltages was relatively low and not sufficient for total electrochemical oxidation of CH_4, which is kinetically slow [84]. Decreasing the voltage increased the flux of incoming O^{2-} ions from the electrolyte, thereby promoting total electrochemical oxidation (TOx) of CH_4 (Eq. 20) instead of POx to yield power:

$CH_4 + 4O^{2-} \rightleftharpoons 2H_2O + CO_2 + 8e^-$ (Eq. 20)

This switch from POx to TOx resulted in more electrical power and less syngas production as the voltage was decreased and was caused by the increasing concentration of O^{2-} ions at the anode. In addition, there was additional H_2 present in the initial fuel mixture and since electrochemical H_2 oxidation is fast, it is likely that electrochemical conversion of H_2 also made a contribution to power production. It has been previously reported that electrochemical CO conversion is very slow when the presence of H_2 is greater than CO [263, 265], and therefore since it is the case that H_2 > CO across all the conditions studied, electrochemical CO oxidation was not likely to have contributed significantly to power production. The observed conversion of CO to yield CO_2 was caused purely by changes in the mechanism of CH_4 conversion.

5.4. Effect of increasing the H_2 content of biohythane

Fig. 5.3 shows the performance of the cell was improved by increasing the H_2 content from 10-40 vol% (the CH_4/CO_2 ratio was kept the same). The I-V curves were increased in the high voltage region as the H_2 was increased, indicating decreased activation losses. Increasing the H_2 also improved the concentration losses as shown by the non-linear curves at low voltages, which started at a lower voltage of 0.3 V for 40/20/40 vol% $CH_4/CO_2/H_2$ compared to 0.5 V for 60/30/10 vol% $CH_4/CO_2/H_2$. This is supported by the impedance spectra, which are composed of two polarisation arcs: the width of the high frequency polarisation arc describes the magnitude of the surface diffusion and charge transfer losses (essentially the activation losses),

and the low frequency arc describes the gas phase diffusion losses (the concentration losses). The widths of these arcs were measured and are shown in Table 5.3. Increasing the H_2 content decreased the high frequency arc width, indicating reduced activation losses. Increasing the H_2 content had a lesser but clear effect on the low frequency arc width and therefore the concentration losses, both of which decreased.

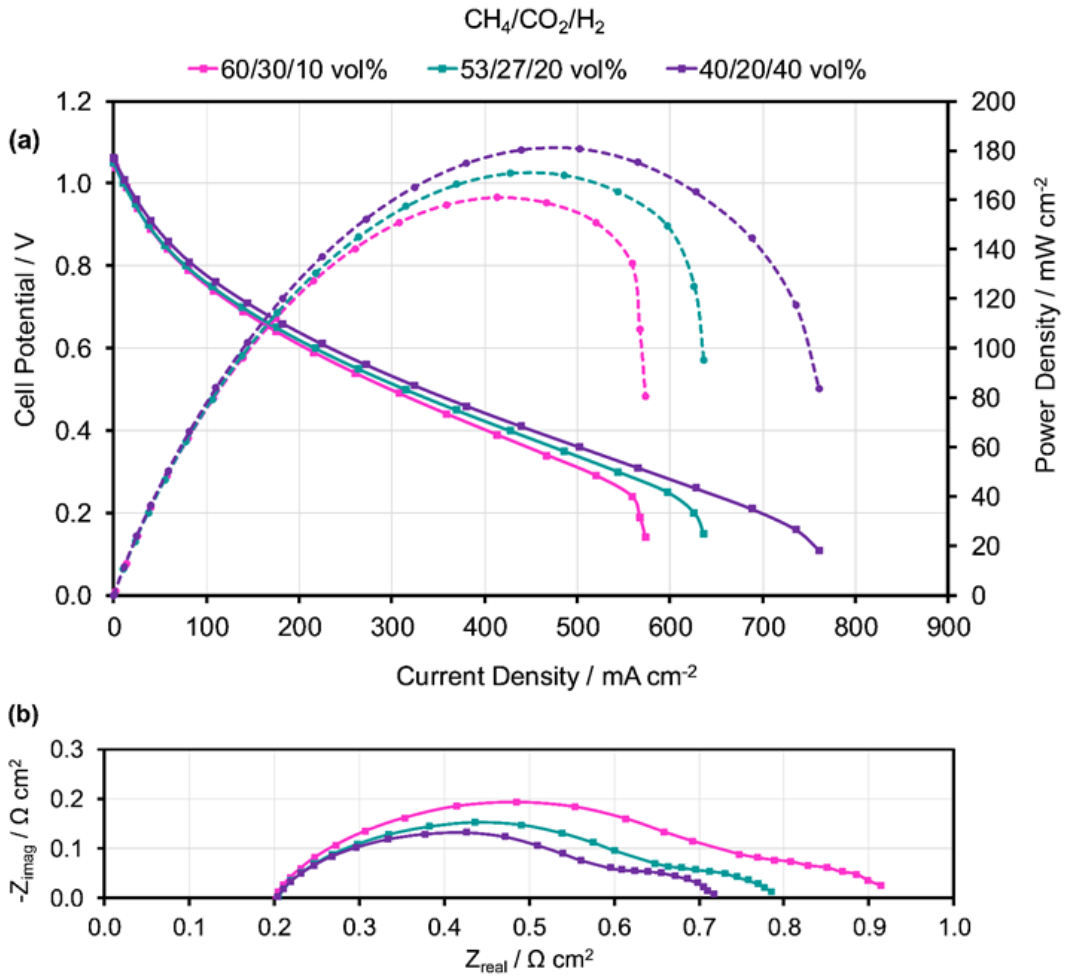

Figure 5.3: (a) I-V curves (solid lines) and power curves (dashed lines) and (b) impedance spectra at 0.1-100000 Hz: ASC operating on biohythane: 60/30/10 vol%, 53/27/20 vol% and 40/20/40 vol% $CH_4/CO_2/H_2$.

Table 5.3: Widths of the high and low frequency arcs in the electrochemical impedance spectra presented in Fig. 5.3.

Biohythane composition	High Frequency Arc Width / Ω cm^2	Low Frequency Arc Width / Ω cm^2
60/30/10 vol% $CH_4/CO_2/H_2$	0.5740	0.1672
53/27/20 vol% $CH_4/CO_2/H_2$	0.4435	0.1375
40/20/40 vol% $CH_4/CO_2/H_2$	0.4047	0.1083

Fig. 5.4 shows the overall behaviours of fuel processing and power production were similar when the H_2 content was increased to 20 vol% and 40 vol% H_2, with subtle differences. With 20 vol% H_2, there was an initial increase of H_2 observed at 0.8-0.7 V due to POx, although this effect was not as pronounced as that observed with 10 vol% H_2. This effect was not observed at all with 40 vol% H_2 present, where the H_2 remained approximately constant across the higher voltages before decreasing at voltages of 0.7 V and below. The decrease of this effect was due to the increased presence of H_2, which shifted POx in the reverse direction (Eq. 19), thereby promoting and making TOx (Eq. 20) a more favourable CH_4 conversion mechanism. Increasing the H_2 content also increased the power production of the cell, consistent with the I-V curves and impedance spectra shown in Fig. 5.3.

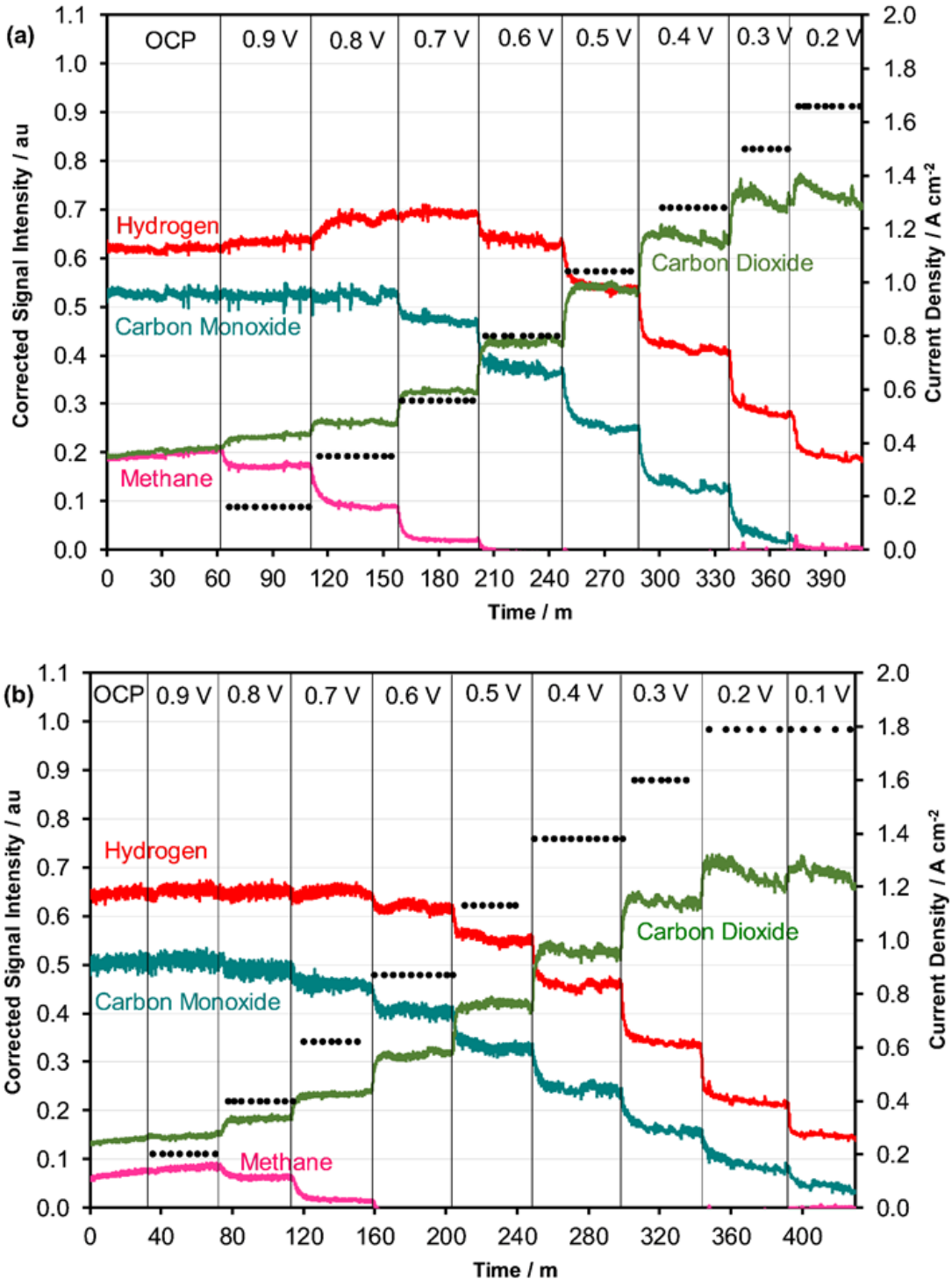

Figure 5.4: The effect of increasing the H_2 content of biohythane on output gases and electrical power of an ASC: (a) $CH_4/CO_2/H_2$ 53/27/20 vol%, (b) $CH_4/CO_2/H_2$ 40/20/40 vol%.

Fig. 5.5 shows the variation of H_2/CO ratio (Fig. 5.5a), total syngas production and electrical power production (Fig. 5.5b) for each mixture and voltage studied. Depending on the fuel composition, H_2/CO ratios in the range 1.1-4.0 were observed which, for each of the mixtures,

were dependent on the operating voltage of the cell. Fig. 5.5b also indicates that over the voltage range 0.7-0.8 V, significant quantities of both electrical power and syngas could be produced simultaneously for each of the three mixtures.

Decreasing the voltage increased the H_2/CO ratio due to the mechanism of CH_4 conversion which, upon switching from POx to TOx, caused CO production to decrease. As this effect was more pronounced for 10 vol% H_2 biohythane, the H_2/CO ratio increased the most dramatically for this mixture, with a H_2/CO ratio of 4 observed at 0.4 V, which was much higher at this voltage for this fuel mixture compared with the other fuel mixtures.

Between the OCP and 0.8 V, increasing the H_2 content of the biohythane had the expected effect of increasing the H_2/CO ratio. However, because higher H_2 contents also promoted total oxidation of CH_4, the switch from partial to total oxidation of CH_4 and therefore the increase of H_2/CO ratio, was less pronounced. The range of H_2/CO ratios observed became narrower as the H_2 content was increased, with H_2/CO ratios of 1.2-3.1 and 1.3-3.2 observed for 20 vol% H_2 and 40 vol% H_2 biohythane respectively.

In terms of total syngas production, there was very little variation between the three biohythane mixtures at higher voltages. Each fuel mixture showed slightly different behaviour for each fuel mixture, particularly between 0.6 V and 0.9 V. Over this voltage range, decreasing the voltage initially caused the total syngas production rate to increase for 10 vol% H_2 biohythane due to POx (Eq. 19). However, increasing the H_2 content decreased the presence of partial CH_4 oxidation and therefore the increase in total syngas production was less pronounced for 20 vol% H_2 biohythane, and not observed at all for 40 vol% H_2 biohythane, where partial CH_4 oxidation was absent.

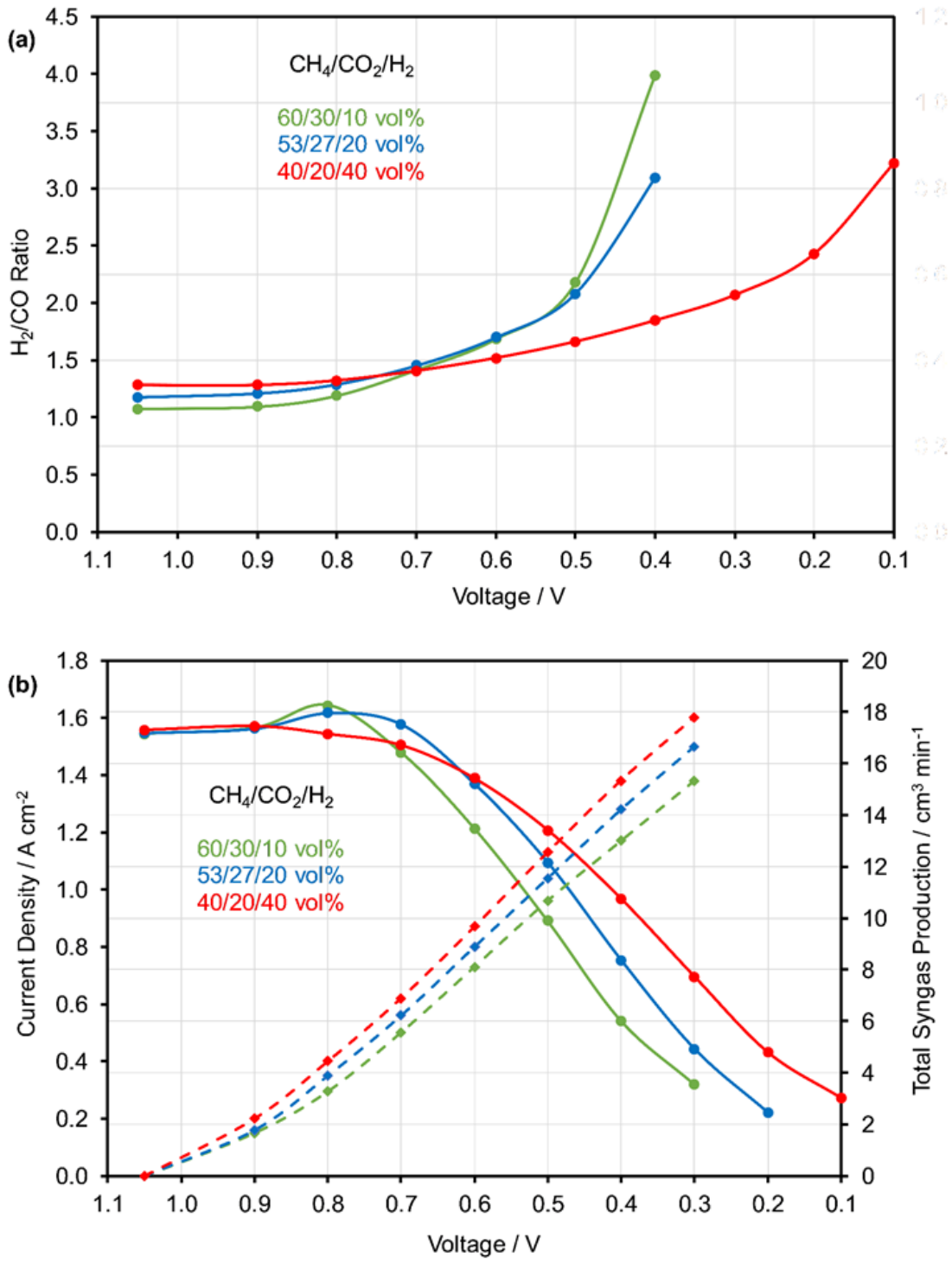

Figure 5.5: Electrical and gaseous outputs of an ASC across the voltage range 0.1-1.1 V running on various compositions of biohythane (60/30/10, 53/27/20 and 40/20/40 vol% $CH_4/CO_2/H_2$). (a) H_2/CO ratio as a function of voltage. (b) Total syngas production (solid lines) and electrical power production (dashed lines) as a function of voltage.

Following the initial increase, syngas production decreased and electrical power production increased due to the electrochemical reactions. Below 0.6 V, the increased volume of H_2

increased both the total syngas production and electrical current production of the cell at each voltage. The total syngas production increased due to poorer fuel utilisation of the cell; increasing the H_2 content of the fuel meant in effect that the cell was increasingly supplied with excess fuel. The power production also increased, with this due to improved kinetic performance of the cell, as shown by the I-V curves and impedance spectra in Fig. 5.3. Overall, therefore, increasing the H_2 content of the fuel mixture significantly improved both the kinetic performance of the cell and the quality and productivity of the gaseous products of the cell.

5.5. The effect of fuel variability on biohythane utilisation in SOFCs

The effect of increasing the H_2/CO_2 present in the gas mixture was investigated in order to understand the effects of biohythane fuel variability and to investigate the addition of H_2/CO_2 to CH_4 as a means to decarbonise the natural gas grid. The effects of substituting CH_4 with 25/75 vol% H_2/CO_2 on the I-V curve and electrochemical impedance spectrum of the cell are shown in Figs. 5.6 and 5.7 respectively, with the polarisation arc widths of the impedance spectra given in Table 5.4. The spectra are composed of two polarisation arcs: the high frequency arc described the charge transfer and surface diffusion losses, and the low frequency arc described the gas diffusion losses [268]. The effects of fuel composition on the OCP and the output gas composition from the anode at the OCP as measured by quadrupole mass spectrometry (QMS) are shown in Fig. 5.8[2].

[2] Air and He were added to each fuel mixture in order to prevent high levels of carbon deposition and to ensure the total fuel rate was consistent in between mixtures. Please see the experimental section (3.6) for details on the effects and significance of air and He additions, which the authors consider to be minimal.

Table 5.4: Composition of the gas mixtures studied.

$CH_4/CO_2/H_2$ composition / vol%	CH_4 / cm^3 min^{-1}	CO_2 / cm^3 min^{-1}	H_2 / cm^3 min^{-1}	Air / cm^3 min^{-1}	He / cm^3 min^{-1}
100 / 0 / 0	30	0.00	0.00	6.0	0.0
80 / 15 / 5	24	4.50	1.50	4.8	1.2
70 / 22.5 / 7.5	21	6.75	2.25	4.2	1.8
60 / 30 / 10	18	9.00	3.00	3.6	2.4
50 / 37.5 / 12.5	15	11.25	3.75	3.0	3.0
40 / 45 / 15	12	13.50	4.50	2.4	3.6
30 / 52.5 / 17.5	9	15.75	5.25	1.8	4.2
20 / 60 / 20	6	18.00	6.00	1.2	4.8
0 / 75 / 25	0	22.5	7.50	0.0	6.0

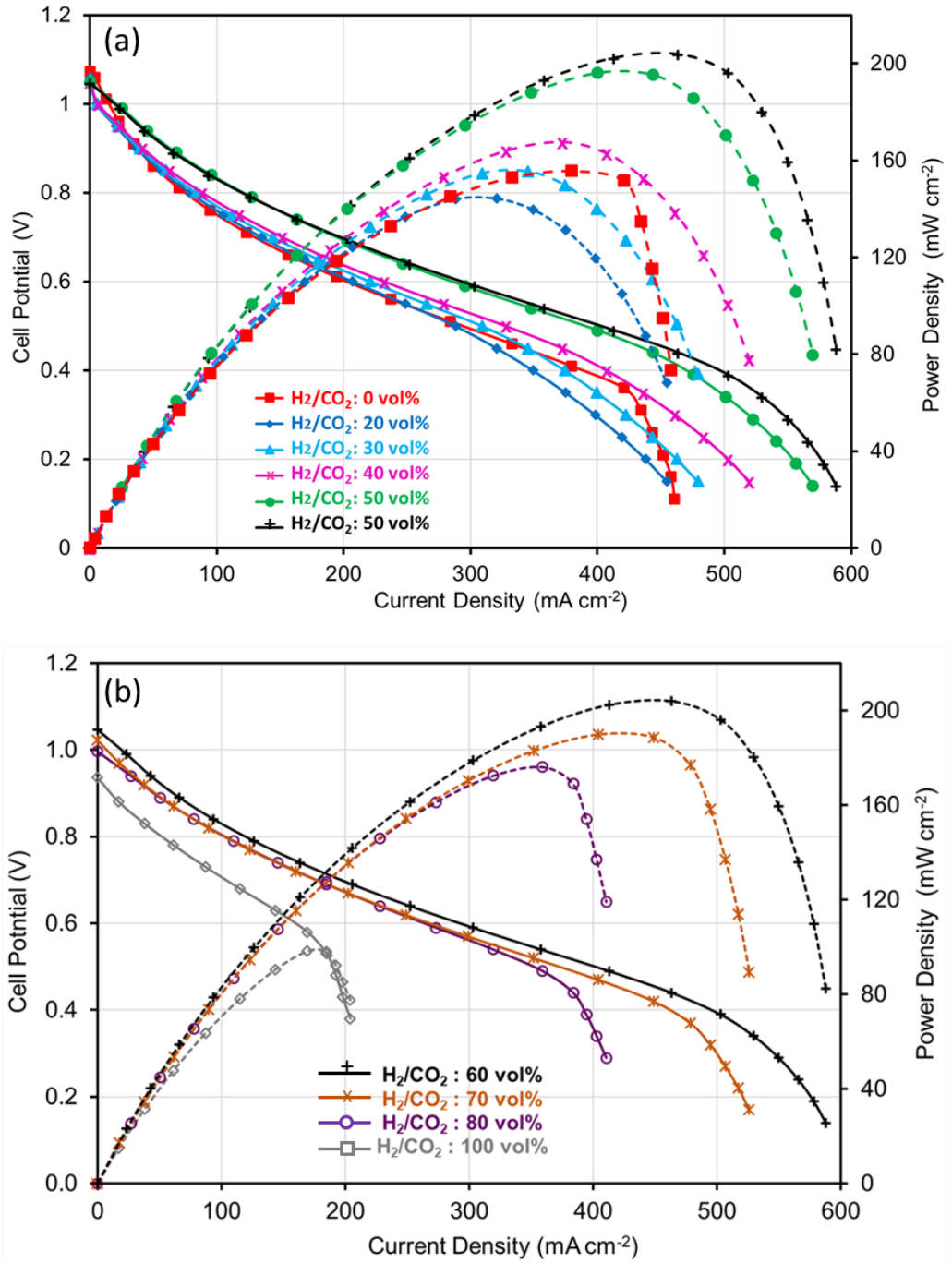

Figure 5.6: The effect of adding H_2/CO_2 to CH_4 on the I-V curve (solid line) and power curve (dashed line) of the cell at 750 °C: (a) 0-60 vol% H_2/CO_2 addition, and (b) 60-100 vol% H_2/CO_2 addition.

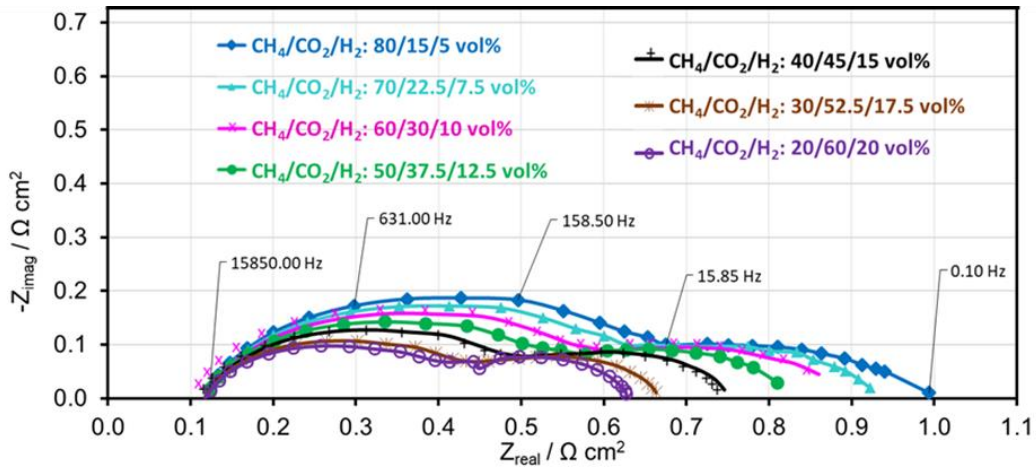

Figure 5.7: The effect of adding 20-80 vol% H_2/CO_2 to CH_4 on the electrochemical impedance spectra of the cell at 750 °C.

Table 5.5: High and low frequency polarisation arc widths of the electrochemical impedance spectra shown in Fig. 5.7.

CH_4 vol%	H_2/CO_2 vol%	High Frequency Arc Width / Ω cm^2	Low Frequency Arc Width / Ω cm^2
80	20	0.5376	0.3402
70	30	0.5121	0.2939
60	40	0.4709	0.2733
50	50	0.4316	0.2623
40	60	0.3677	0.2622
30	70	0.3343	0.2135
20	80	0.3342	0.1774

Fig. 5.8a shows the experimental data set and the fitting results plotted together for 80/15/5 vol% $CH_4/CO_2/H_2$ mixture at 750 °C and Fig. 5.8 b show the equivalent circuit model which provides the fitting values for each component and the errors associated. Only one set of fitting results are shown here, all the other fittings are to the same level of precision. A very similar

performance can be seen between the two curves at both frequencies.

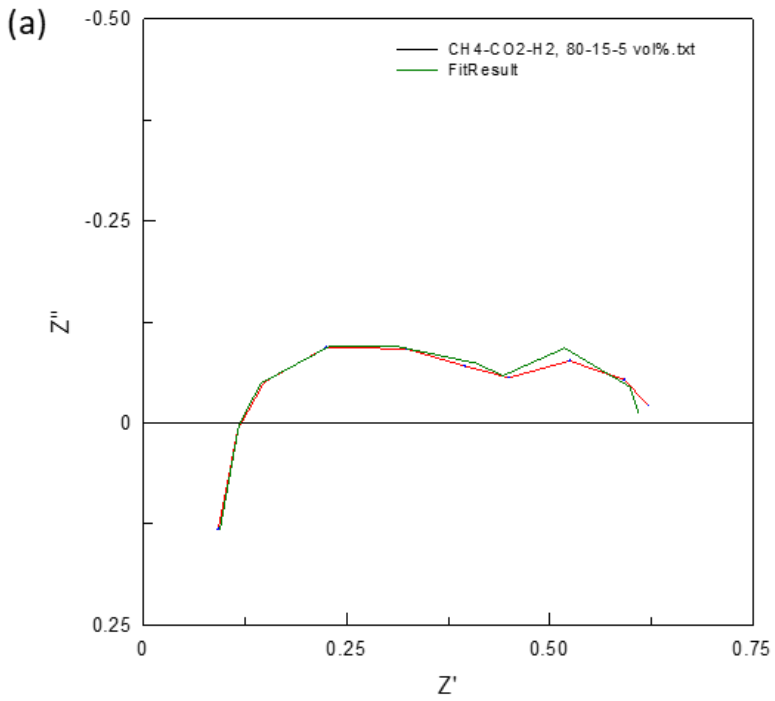

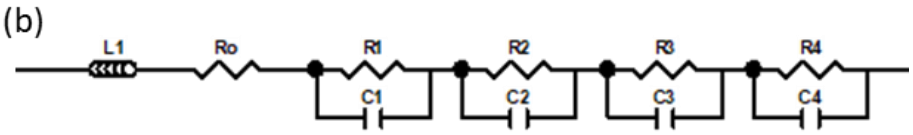

Element	Freedom	Value	Error	Error %
L1	Free(+)	3.7406E-07	1.4464E-08	3.8668
Ro	Free(+)	0.089371	0.006351	7.1063
R1	Free(+)	0.14777	0.016172	10.944
C1	Free(+)	0.0078232	0.0021264	27.181
R2	Free(+)	0.040866	0.0065018	15.91
C2	Free(+)	0.00018016	6.8011E-05	37.75
R3	Free(+)	0.15657	0.014617	9.3358
C3	Free(+)	0.00079008	8.6536E-05	10.953
R4	Free(+)	0.17607	0.013774	7.823
C4	Free(+)	0.23788	0.04501	18.921

Figure 5.8: (a) Equivalent Circuit fitting to experiment data of 80/15/5 vol% $CH_4/CO_2/H_2$ mixture at 750 ℃ and (b) equivalent circuit model and fitting results.

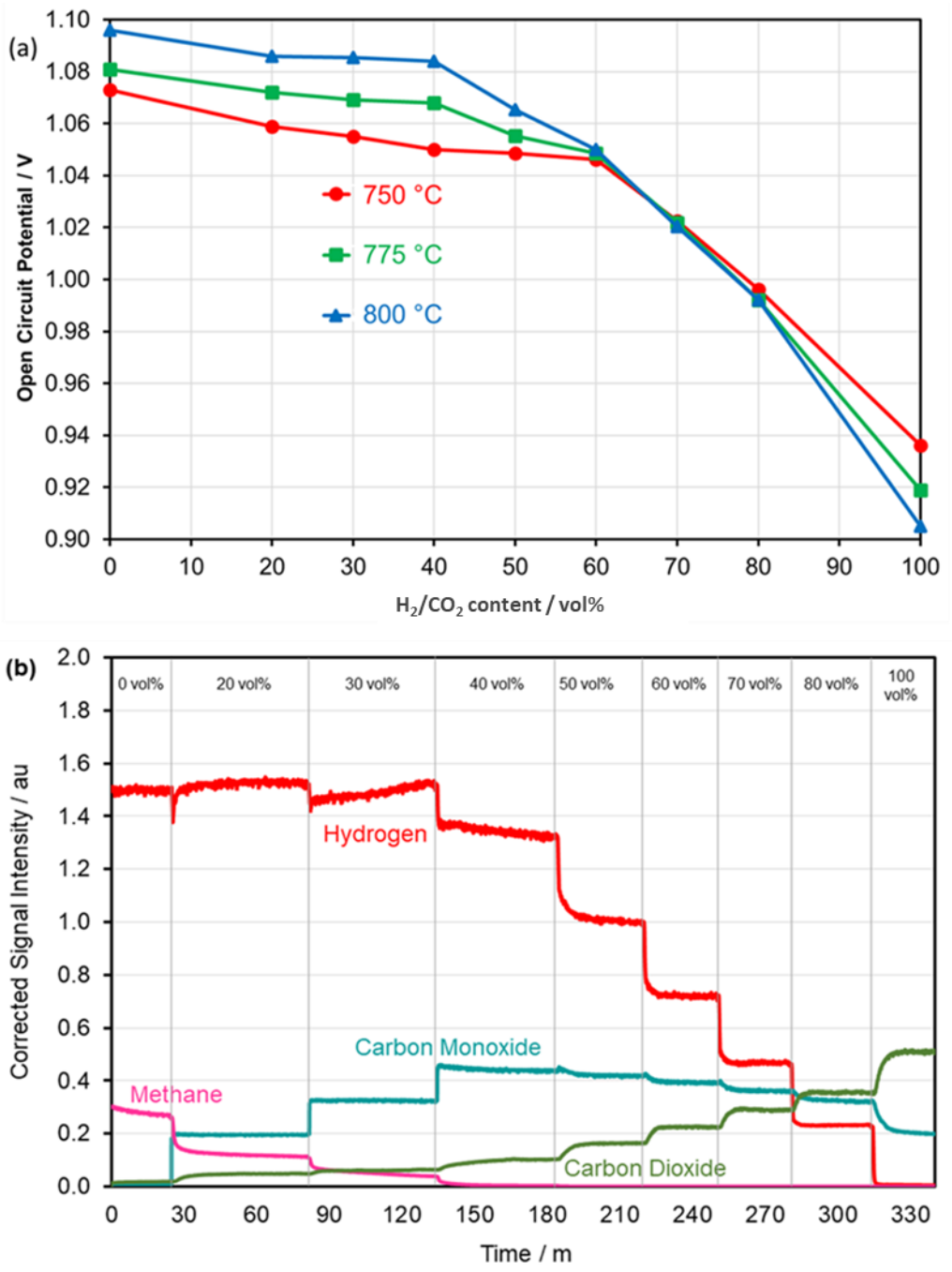

Figure 5.9: The effect of substituting 0-100 vol% CH_4 with H_2/CO_2 on: (a) the OCP, and (b) the composition of the anode output gases at OCP at 750 °C.

Under pure CH_4, the pronounced curves observed in the high voltage and low voltage regions of the I-V curve in Fig. 5.9a indicate there were significant activation and concentration losses respectively. This was expected since electrochemical conversion and gaseous diffusion of CH_4 are relatively slow processes [270-272] and there was no oxidant present to enable CH_4

reforming to take place [230, 273, 274]. The anode output gases at OCP for this mixture show a very high volume of H_2 was present, with much lower levels of CH_4 detected than expected. This indicates the presence of CH_4 cracking (Eq. 6) and therefore that carbon deposition was likely formed on the anode and probably also at the fuel electrode inlet. The carbon formed is likely to have contributed to the activation and concentration losses observed in the I-V curve and affected the production of power by electrochemical oxidation of the H_2 or CH_4 present [215, 275].

$$CH_4 \rightleftharpoons C + 2H_2 \quad \text{(Eq. 6)}$$

The I-V curves in Fig. 5.6a show that more current and power were produced by the cell as the amount of H_2/CO_2 was increased to 60 vol%. Fig. 5.9a shows the OCP was ~ 1.07 V under pure CH_4 and that this decreased slightly to ~ 1.05 V at 60 vol%. In the electrochemical impedance spectra, the overall widths of the polarisation arcs decreased by more than 25 % over this fuel composition range. Both polarisation arcs decreased as the H_2/CO_2 increased, indicating that the efficiencies of charge transfer, surface diffusion and gas diffusion processes were improved by addition of H_2/CO_2. Overall, it is clear the electrical performance of the cell was improved with substitution of up to 60 vol% CH_4 with H_2/CO_2.

Analysis of the output gases from the anode at OCP in Fig. 5.9 show that addition of H_2/CO_2 increased catalytic CH_4 conversion, with complete conversion of CH_4 observed at 40 vol% H_2/CO_2 addition. The production of CO increased as the H_2/CO_2 content was increased to 40 vol%. These observations indicate the presence of CO_2 reforming of CH_4 (Eq. 17). It is also probable that the presence of CO_2 promoted the reverse Boudouard reaction (Eq. 7), thereby helping to remove carbon from within the Ni/YSZ anode and fuel inlet [276-278].

$$CH_4 + CO_2 \rightleftharpoons 2H_2 + 2CO \quad \text{(Eq. 17)}$$

$$CO_2 + C \rightleftharpoons 2CO \quad \text{(Eq. 7)}$$

These results therefore show that the increase in electrical performance of the cell was most likely due to increased catalytic conversion of CH_4 via dry reforming and through alleviation of

carbon deposition due to inhibition of CH_4 cracking and promotion of the reverse Boudouard reaction. These effects decreased the activation and concentration losses as observed in the I-V curves and promoted electrochemical oxidation of H_2 as the primary power production pathway, thereby decreasing the charge transfer, surface diffusion and gas diffusion as observed in the impedance spectra. It is also possible that carbon deposition was alleviated due to the promotion of electrochemical H_2 oxidation, which would have increased the presence of H_2O at the anode. There is previous work that suggests the H_2O subsequently reacts with carbon deposition on the anode, increasing the durability and performance of the cell. This is discussed further in the durability work in section 5.6.

It was expected that addition of H_2/CO_2 would also increase the amount of H_2 present in the anode output gases at the OCP due to: (1) the increased volume of H_2 in the fuel input gases, and (2) the promotion of dry reforming. However, the volume of H_2 in the anode output gases remained constant with up to 40 vol% H_2/CO_2 addition, suggesting that H_2 was partly consumed via reaction with CO_2 in the reverse water-gas shift reaction.

Fig. 5.9b shows that when the H_2/CO_2 content was increased above 40 vol%, the H_2 present in the output gases decreased much more considerably. This is attributed to the decrease of CH_4 present in the initial fuel mixture and increasing conversion of H_2 in the RWGS reaction [269]. Between 40-60 vol% H_2/CO_2, the output gases show there was an increasing presence of CO_2, which further promoted the RWGS and reverse Boudouard reactions, thereby continuing to enhance the overall electrical performance of the cell up to 60 vol% H_2/CO_2 addition.

The I-V curves in Fig. 5.6b show that as the H_2/CO_2 content was increased above 60 vol%, the current and power produced by the cell decreased. Fig. 5.9a indicates this was largely due to the OCP, which decreased much more significantly from ~ 1.05 V at 60 vol% H_2/CO_2 to ~ 0.93 V under 100 vol% H_2/CO_2. The anode output gases shown in Fig. 5.9b show that the H_2 continued to decrease over this fuel composition range and became more and more diluted in CO_2 and CO. Under 100 vol% H_2/CO_2, all of the H_2 was converted in the RWGS reaction yielding a dried mixture consisting of CO_2 and CO. The RWGS reaction became the

predominant catalytic process for high H_2/CO_2 content fuel mixtures. With such a low presence of H_2, the OCP decreased according to Nernst predictions, affecting the overall electrical performance of the cell.

Despite the very low concentration of H_2 present above 60 vol% H_2/CO_2, the activation losses in the I-V curves did not appear to be affected. In addition, the overall widths of the polarisation arcs in the impedance spectra continued to decrease above 60 vol% H_2/CO_2. In order to understand this, a separate experiment was conducted in which the effect of adding CO_2 to pure H_2 on the impedance spectra was investigated and compared with adding N_2 and He to pure H_2. These spectra are shown in Fig. 5.10 with the corresponding polarisation arc widths shown in Table 5.6. It was observed that adding CO_2 (Fig. 5.10a) decreased the widths of the polarisation arcs, whereas adding N_2 (Fig. 5.10b) and He (Fig. 5.10c) increased the arc widths. In particular, the low frequency arc width decreased by up to 50 % with addition of CO_2, showing the diffusion losses were considerably reduced. It is tentatively suggested that the relatively high density of CO_2 (1.98 g dm^{-3}) compared with other gases (0.0899 g dm^{-3} for H_2, 1.14 g dm^{-3} for CO) enabled more efficient diffusion of the fuel gases through the porous structure of the anode, thereby decreasing concentration losses. In addition, the presence of the RWGS reaction provided a more balanced ratio of educt and product gases, which Ebbesen *et al*. [279] have previously shown decreases the concentration arc of an impedance measurement significantly. When N_2 and He were added, the diffusion resistance was increased [280, 281] and the RWGS reaction could not take place, causing the arc widths to increase. Therefore, whilst the overriding effect of CO_2 in high concentrations was to decrease the electrical performance of the cell due to large OCP losses, CO_2 also decreased the charge transfer, surface diffusion and gas diffusion losses associated with electrochemical H_2 oxidation. The results suggest this beneficial effect of CO_2 was likely taking place across all biohythane compositions studied.

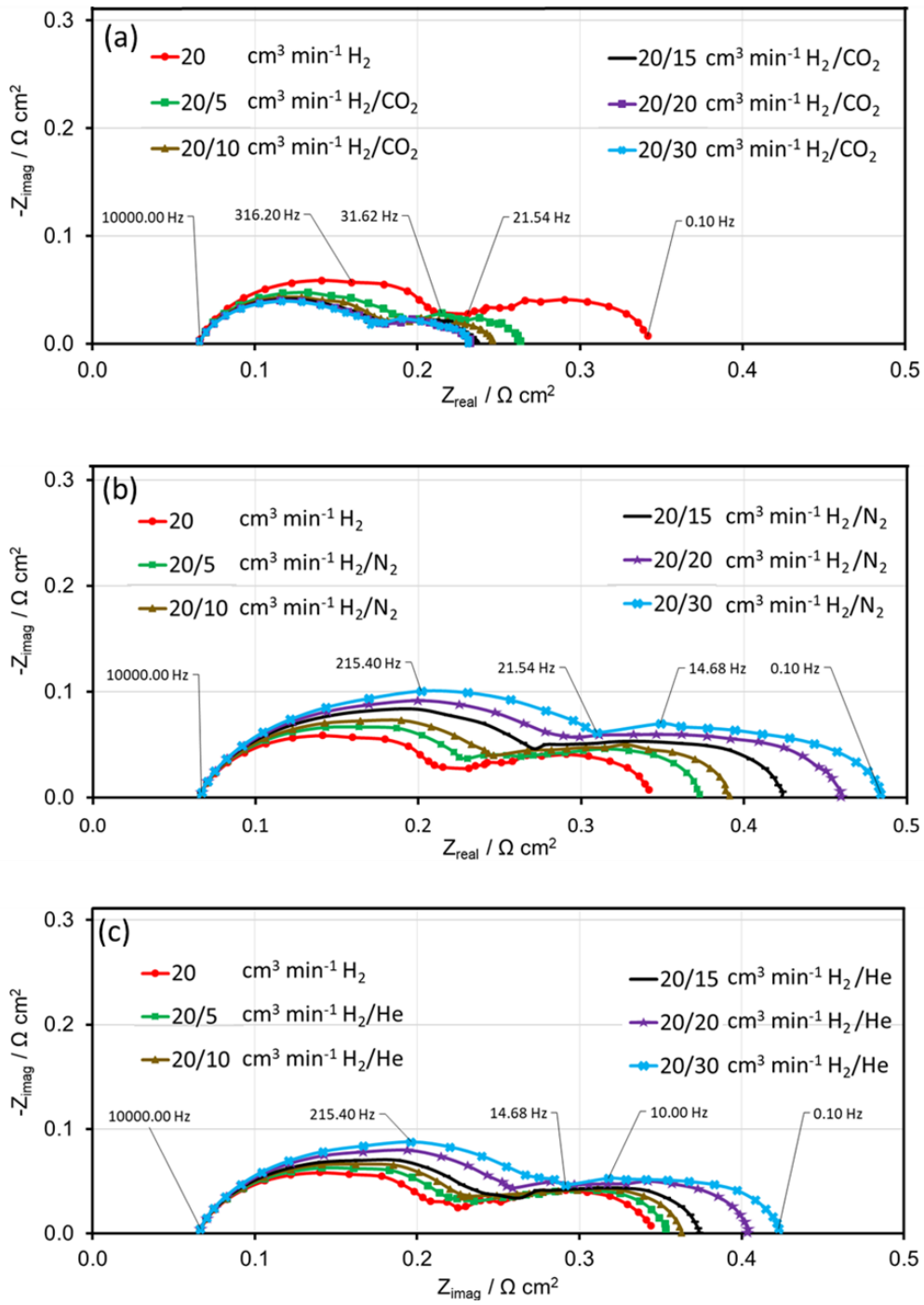

Figure 5.10: The effect of adding: (a) CO_2, (b) N_2, and (c) He to pure H_2 on the electrochemical impedance spectra of the cell at 800 °C.

Table 5.6: High frequency (HF) and low frequency (LF) polarisation arc widths of the impedance spectra in Fig. 5.10.

	CO_2		He		N_2	
H_2:balance / vol%	HF Arc Width / Ω cm^2	LF Arc Width / Ω cm^2	HF Arc Width / Ω cm^2	LF Arc Width / Ω cm^2	HF Arc Width / Ω cm^2	LF Arc Width / Ω cm^2
20:0	0.1519	0.1266	0.1519	0.1266	0.1519	0.1266
20:5	0.1258	0.0730	0.1719	0.1282	0.1669	0.1428
20:10	0.1119	0.0648	0.1651	0.1349	0.1829	0.1450
20:15	0.1076	0.0662	0.1789	0.1384	0.2085	0.1503
20:20	0.1118	0.0631	0.1892	0.1418	0.2258	0.1706
20:30	0.1116	0.0601	0.2035	0.1559	0.2465	0.1758

Fig. 5.11a shows the experimental data set and the fitting results plotted together for H_2/CO_2 20/30 vol% mixture at 800 °C and Fig. 5.11b show the equivalent circuit model which provides the fitting values for each component and the errors associated. Only one set of fitting results are shown here, all the other fittings are to the same level of precision. A very similar performance can be seen between the two curves at both frequencies.

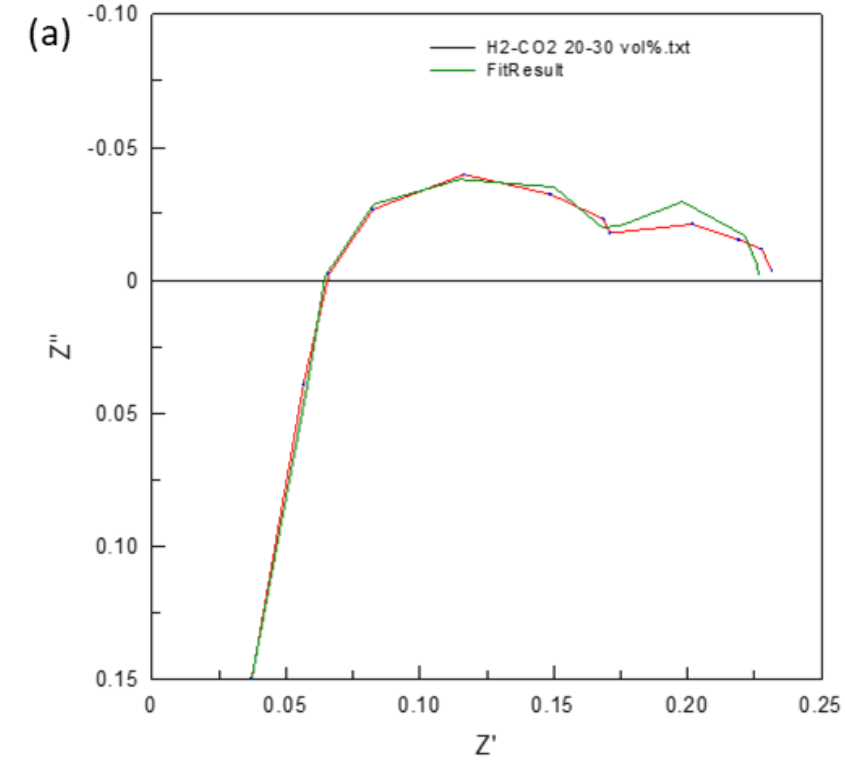

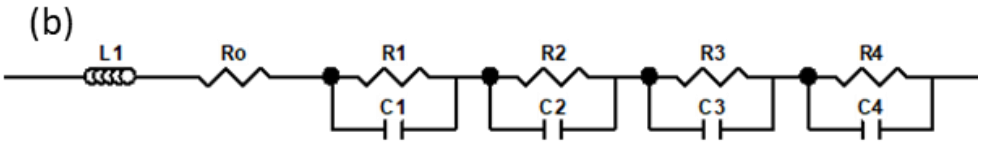

Element	Freedom	Value	Error	Error %
L1	Free(+)	4.2755E-07	8.6966E-09	2.0341
Ro	Free(+)	3.5898E-10	0.00061725	1.7195E08
R1	Free(+)	0.056047	0.0040312	7.1925
C1	Free(+)	0.4237	0.075154	17.738
R2	Free(+)	0.050352	0.0094337	18.736
C2	Free(+)	0.0018178	0.00019562	10.761
R3	Free(+)	0.058392	0.0092774	15.888
C3	Free(+)	0.0090284	0.0034024	37.686
R4	Free(+)	0.061849	0.0018316	2.9614
C4	Free(+)	3.0882E-05	3.0918E-06	10.012

Figure 5.11: (a) Equivalent Circuit fitting to experiment data of 20/30 vol% H_2CO_2 mixture at 800 °C and (b) equivalent circuit model and fitting results.

5.6. The durability of SOFCs operating on biohythane

The durability of SOFC technology operating at 750 °C on a typical biohythane mixture of 60/30/10 vol% $CH_4/CO_2/H_2$ mixture was investigated over a 288 h period (12 days) at an

operating voltage of 0.8 V. The current density and exhaust gases from the cell over this time are shown in Fig. 5.12. Fuel was supplied at 9 cm^3 min^{-1} (high fuel utilisation) for the first 260 h and 12 cm^3 min^{-1} (low fuel utilisation) for the remaining 28 h. The cell stabilised during the first 35 hours, where the current density increased from 165 to 180 mA cm^{-2}. During this time, the CO decreased slightly before stabilising. After this initial conditioning period, the output gases and current density remained very stable, with 175±5 mA cm^{-2} produced for 260 hours and only very minor changes to the composition of the output gases observed. The dried output gases were mainly composed of CO_2 with trace levels of H_2, CO and CH_4 detected.

The catalytic processes observed in Fig. 5.9b are likely to have been influenced by the H_2O produced from electrochemical H_2 oxidation [282, 283]. Steam reforming of CH_4 (Eq. 4) was likely to be present in addition to CO_2 reforming (Eq. 17), the presence of H_2O would also likely promote the water-gas shift reaction and finally, the additional presence of H_2O may have further prevented the formation of carbon via reaction to produce synthesis gas (Eq. 16). Each of these processes are known to have a beneficial effect on the durability of the cell since they limit carbon deposition and promote power production via electrochemical H_2 oxidation, which were identified in 5.5 as being key to achieving good electrical performance from the cell [264, 284, 285]. This work suggests that SOFCs could operate on biohythane for long periods with good electrical performance without deactivation due to carbon deposition. Further work is needed to determine the extent of fuel conversion due to CO_2 and that due to the H_2O produced from electrochemical H_2 oxidation. However, it is clear from section 5.5 that the presence of CO_2 makes a significant contribution to fuel conversion and power production. In particular, it is suggested the additional presence of CO_2 and H_2 enable SOFCs to operate with decreased fuel processing and steam consumption from an external reforming fuel cell subsystem.

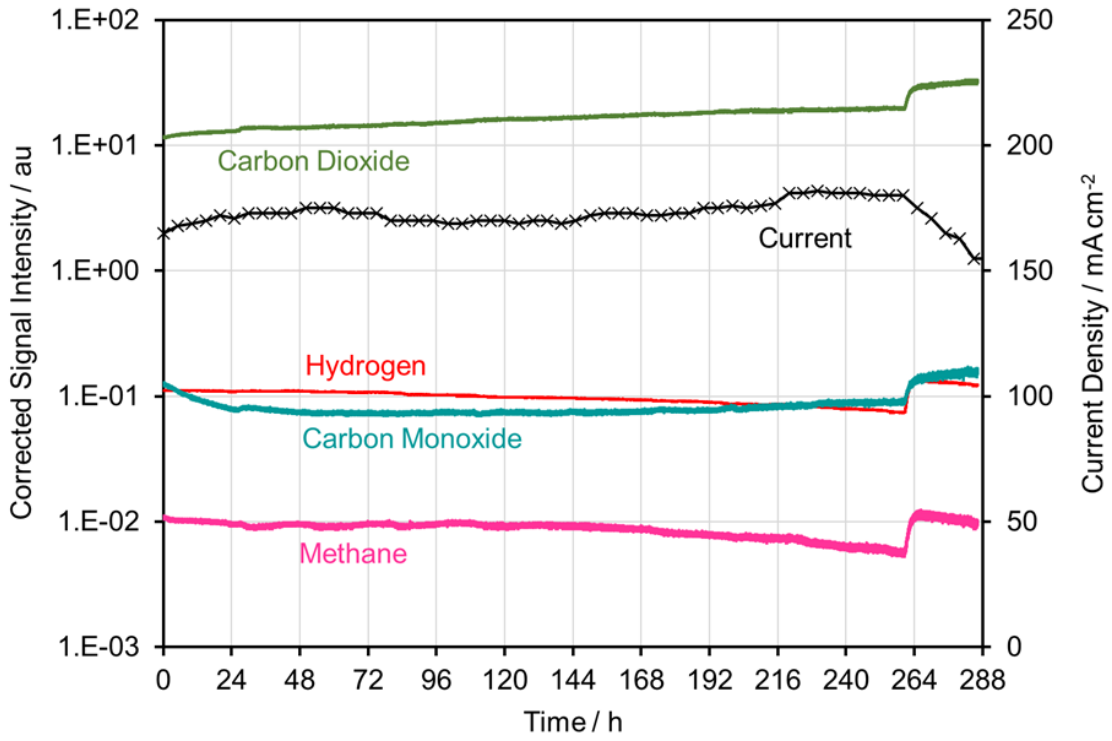

Figure 5.12: Current density and output gases of the cell operating for 288 h on a 60/30/10 vol% $CH_4/CO_2/H_2$ biohythane mixture at 750 °C with an operating voltage of 0.8 V. Fuel was supplied at 9 cm^3 min^{-1} for the first 260 h and 12 cm^3 min^{-1} for the final 28 h.

In order to accelerate and determine any mechanisms of deactivation, after 260 h of continuous operation the flow rate of fuel was increased by 33 % to 12 cm^3 min^{-1}. Initially, the volume of output gases increased, indicating there was excess fuel that the cell was unable to convert. The current and power produced by the cell instantly began to decline and after 28 hours, the current density had decreased by 17 % to 150 mA cm^{-2}.

Fig. 5.13 shows I-V curves and impedance spectra of the ASC taken at 750 °C before and after the 288 h test. The I-V curve taken before the test indicated the presence of activation (high voltage region) and concentration (low voltage region) losses, which the I-V curve analysis given in section 5.5 shows were due to the high presence of CH_4 in the fuel inlet and carbon deposition on the anode. The I-V curve taken after the test had a more prevalent curve in the high voltage region showing the activation losses had increased. The impedance spectra show that the high frequency arc width had increased considerably, indicating increased charge transfer and surface diffusion losses. No concentration losses were observed in the I-V curve

following the long-term test because the cell was unable to convert all of the fuel available. However, the impedance data show that the low frequency arc width had increased, showing diffusion of reactants through the anode had become less efficient.

All of these observations are consistent with carbon deposition on the anode and probably also at the fuel inlet. The carbon inhibited electrochemical oxidation processes and increased the diffusion resistance of the anode. In addition, the impedance data show that the high frequency arc intersected the real axis at an increased value of 0.2 Ω cm^2, showing the ohmic losses were increased. It is likely these losses had been caused by mechanical stress induced by deposits of carbon. The carbon deposition was likely due to CH_4 cracking caused by the increased presence of CH_4 and because the CH_4 and CO_2 were present in a 2:1 ratio. It is unlikely the carbon deposition was caused by the Boudouard reaction which is an exothermic process and also would be reversed by the presence of CO_2. This illustrates that complete catalytic CH_4 conversion without CH_4 cracking is key to SOFC stability and durability.

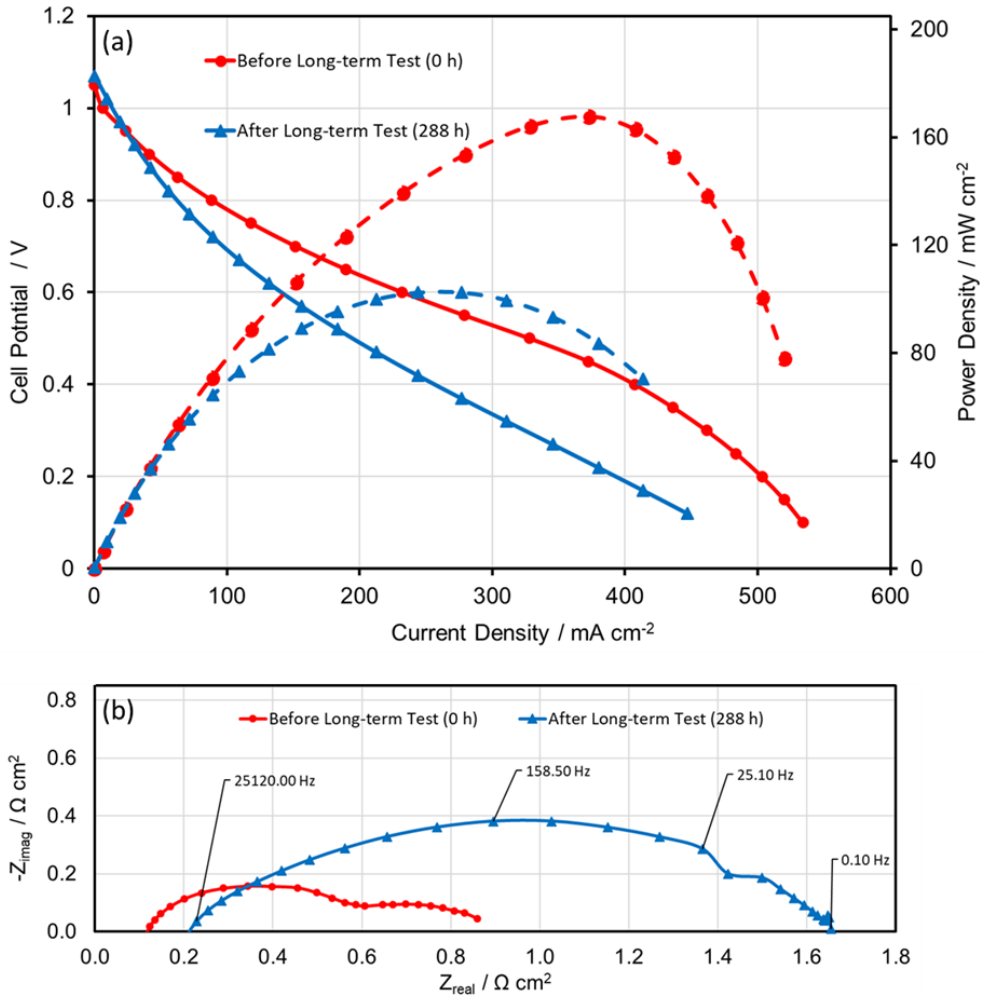

Figure 5.13. (a) I-V curves and (b) electrochemical impedance spectra of the ASC collected before and after the 288 h long-term electrical performance test at 750 ℃.

Fig. 5.14a shows the experimental data set and the fitting results plotted together for $CH_4/CO_2/H_2$ 60/30/10 vol% mixture after long term testing and Fig. 5.14b show the equivalent circuit model which provides the fitting values for each component and the errors associated. A very similar performance can be seen between the two curves at both frequencies.

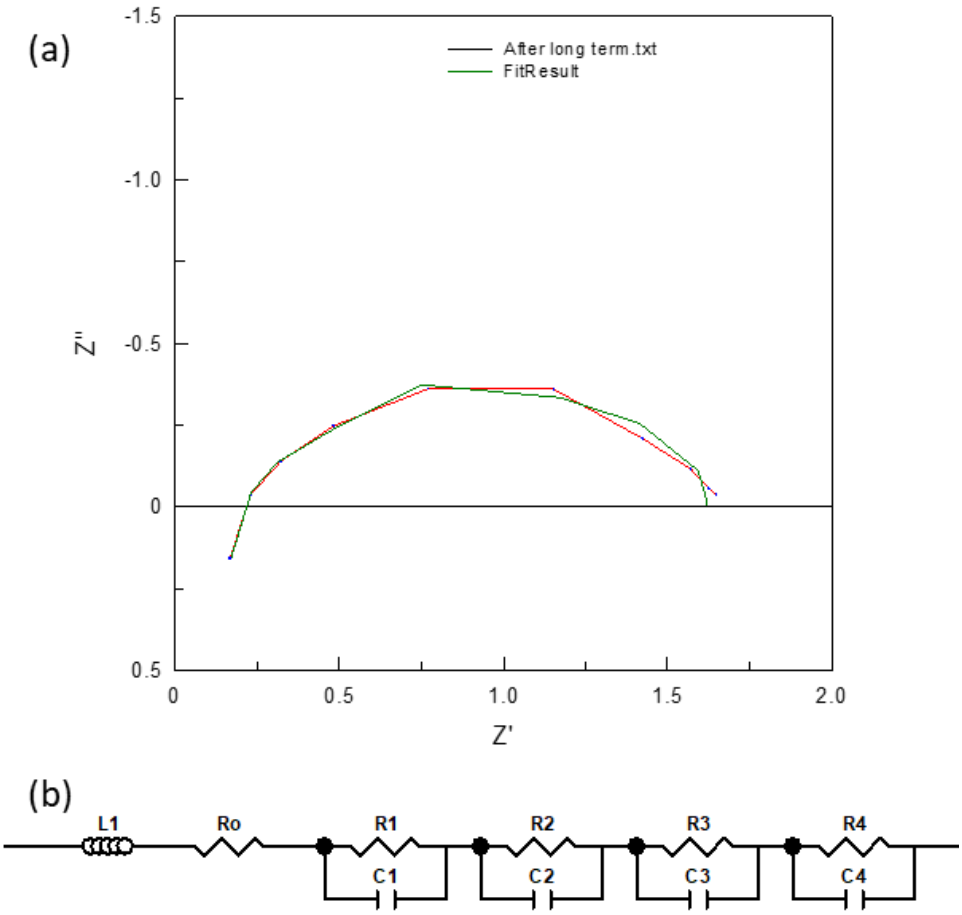

Element	Freedom	Value	Error	Error %
L1	Free(+)	5.0575E-07	1.9767E-08	3.9085
Ro	Free(+)	0.15951	0.0080791	5.0649
R1	Free(+)	0.363	0.058065	15.996
C1	Free(+)	0.029977	0.011802	39.37
R2	Free(+)	0.29469	0.033154	11.25
C2	Free(+)	0.00036685	5.0446E-05	13.751
R3	Free(+)	0.68163	0.053327	7.8235
C3	Free(+)	0.001532	0.00021776	14.214
R4	Free(+)	0.12005	0.01306	10.879
C4	Free(+)	7.3317E-05	1.3619E-05	18.576

Figure 5.14: (a) Equivalent Circuit fitting to experiment data of $CH_4/CO_2/H_2$ 60/30/10 vol% mixture after long term testing at 750 °C and (b) equivalent circuit model and fitting results.

5.7. Implications for natural gas grid decarbonisation

This work is focussed on the effects of fuel variability for SOFCs operating on biohythane but is also relevant to the decarbonisation of natural gas grids. H_2/CO_2 mixtures (biohydrogen) can be

produced very efficiently through various biomass fermentation processes and provided it is produced from renewable and low carbon biomass feedstocks, biohydrogen could potentially be blended with natural gas as a means of decarbonising natural gas grids. As this work has shown, SOFCs are not only able to utilise $CH_4/CO_2/H_2$ mixtures, but also have very high electrical performance when operating on biohythane compared with pure CH_4. Whilst the utilisation of CH_4 blended with H_2 in SOFCs has previously been studied as a means of grid decarbonisation, CH_4/H_2 (hythane) mixtures are known to have considerable issues relating to carbon deposition, particularly when more than 20 vol% H_2 is added [75, 76]. Commercially available H_2 is also an expensive commodity that is produced mainly via steam reforming of natural gas and therefore offers little improvement in terms of environmental impact [286, 287]. By substituting natural gas with renewable biohydrogen mixtures, the global warming potential (GWP) of the fuel is considerably reduced (H_2/CO_2 mixtures have a GWP of less than 1) and carbon emissions are decreased because fossil CH_4 is directly displaced with a low carbon resource.

However, in addition to displacing and therefore reducing the consumption of CH_4, a key outcome of this work is that $CH_4/CO_2/H_2$ mixtures give fundamentally better electrical performance compared with pure CH_4. It has also been shown in a previous research that biohythane gives better performance than biogas [258]. The increase in electrical performance is depicted in Fig. 5.15a, which shows the percentage increase in power output as more H_2/CO_2 was added to the fuel. The power output increased steadily as the H_2/CO_2 content was increased to 40 vol%, which is the composition of a typical biohythane mixture (60/30/10 vol% $CH_4/CO_2/H_2$), with a 22.9 % increase in power observed. Increasing the H_2/CO_2 content to 50-60 vol% gave a much more considerable increase in the power output of the cell with a 64-66 % power increased observed. Increasing the H_2/CO_2 content above 60 vol% caused the electrical performance gain of the cell to decrease. However, it was only under pure H_2/CO_2 where a worse electrical performance was observed than pure CH_4. Up to 80 vol% H_2/CO_2 addition, gains of up to 66 % in the fundamental electrical performance of the cell were observed compared with pure CH_4.

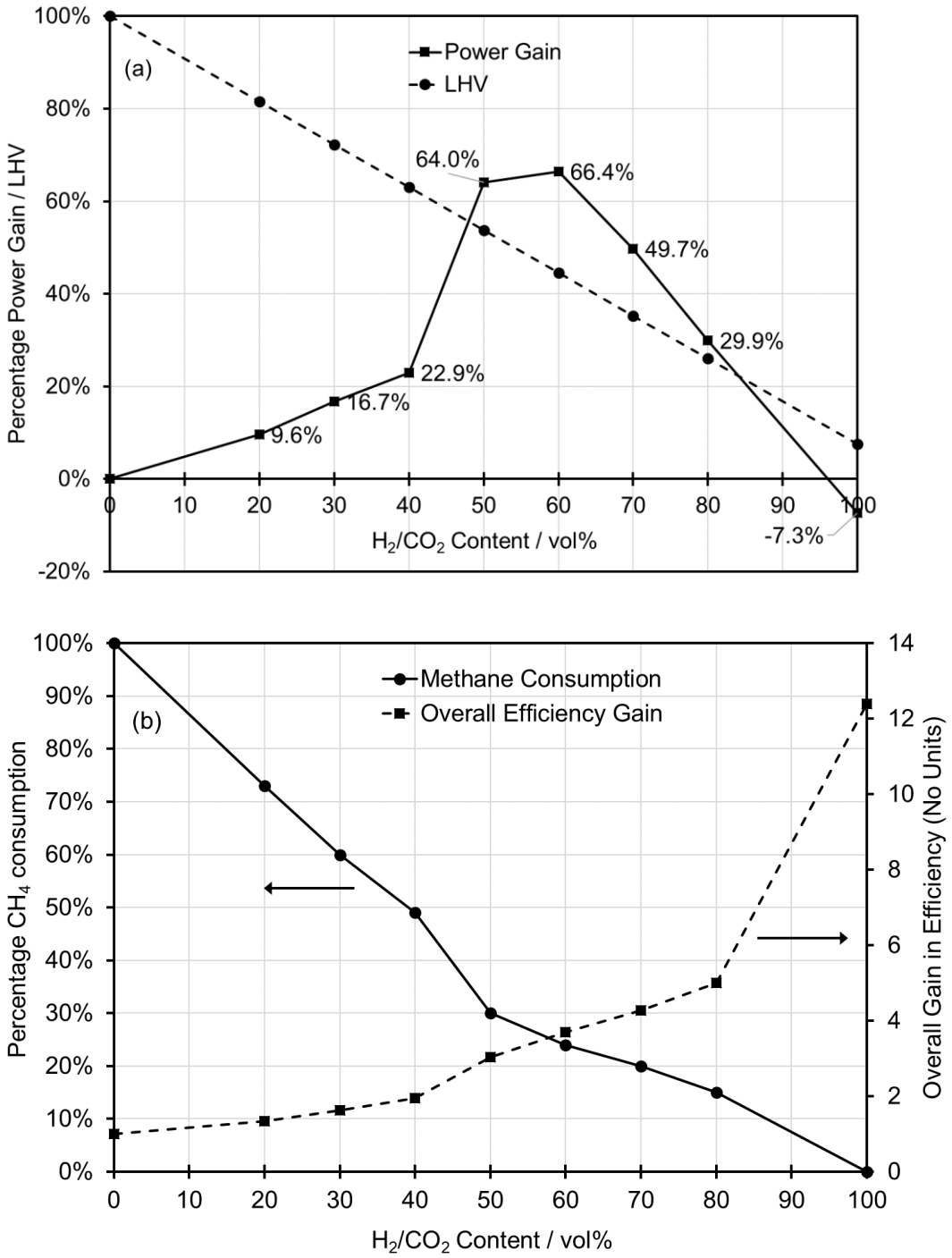

Figure 5.15: The effect of adding 0-100 vol% H_2/CO_2 to CH_4 on: (a) the gain in power from the cell and the lower heating value (LHV) of the fuel; and (b) the percentage CH_4 consumption and overall efficiency gain. The data are derived from the I-V curves in Fig. 5.6 at an operating voltage of 0.7 V and are measured relative to pure CH_4.

Fig. 5.15a also shows the effect of H_2/CO_2 addition on the lower heating value (LHV) of the fuel mixture, which decreased from 35.8 MJ m^{-3} (for pure CH_4) to 2.7 MJ m^{-3} (for 25/75 vol% H_2/CO_2). The gains in fundamental power output of the cell observed by addition of H_2/CO_2 to

CH_4 shown in Fig. 5.15a were achieved by utilisation of a fuel mixture that had a lower energy content compared with pure CH_4. The overall gain in efficiency can be described by:

Efficiency gain = Percentage cell power increase / LHV percentage of pure CH_4

This has been calculated for each of the fuel mixtures and is shown in Fig. 5.15b. Substitution of 60 vol% CH_4 with H_2/CO_2 decreased the LHV was 15.9 MJ m^{-3}, which is 45 % of the LHV of pure CH_4. When taking this into account, the percentage power increase of 66.4 % observed for this mixture is equivalent to an overall efficiency gain of 3.70[3] times that achieved under pure CH_4. Fig. 5.15b shows that adding H_2/CO_2 to CH_4 in any ratio increased the overall efficiency relative to pure CH_4. Even with pure H_2/CO_2, which gave a lower power output than pure CH_4, the overall efficiency was markedly improved compared with pure CH_4 because the LHV of the H_2/CO_2 mixture was only 8 % of pure CH_4. Therefore, addition of H_2/CO_2 to CH_4 in any quantity will always increase the overall efficiency compared with utilisation of pure CH_4 in SOFCs.

Addition of H_2/CO_2 also significantly decreased the overall CH_4 consumption. As well as direct displacement of CH_4 with H_2/CO_2, CH_4 consumption is also decreased further due to the overall efficiency gain. The overall percentage CH_4 consumption decrease can be calculated by:

Percentage CH_4 Consumption = CH_4 vol% / Power Increase

For a typical biohythane mixture of 60/30/10 vol% $CH_4/CO_2/H_2$, an CH_4 consumption of 24 %[4] that of pure CH_4 was observed, corresponding to a 76 % decrease in CH_4 consumption. Fig. 5.15b shows that addition of H_2/CO_2 to CH_4 in any ratio significantly decreased CH_4 consumption.

This work shows there are considerable advantages of substituting CH_4 with H_2/CO_2 mixtures in terms of SOFC electrical performance, overall efficiency and CH_4 consumption. Whilst the optimum electrical performance of SOFCs was observed at a 60 vol% substitution of CH_4 with

[3] Overall Efficiency Gain = Power Increase / LHV percentage of pure CH_4 = 1.664 / 0.45 = 3.7.
[4] Percentage CH_4 Consumption = CH_4 vol% / Power Increase = 40 / 1.664 = 24 %.

H_2/CO_2, in terms of overall efficiency and CH_4 consumption it is more beneficial to increase the H_2/CO_2 content of the fuel as much as possible. This work has shown that addition of H_2/CO_2 is beneficial since the H_2 and CO_2 present promote catalytic conversion of CH_4, the reverse Boudouard reaction and the RWGS reaction. In turn, these processes promote power production via electrochemical oxidation of H_2 and minimise carbon deposition, thereby increasing the electrical performance and the durability of SOFCs. These are processes that cannot take place with CH_4/H_2 blends, which unlike biohythane and biohydrogen, cannot easily be produced from non-fossil, renewable or low carbon feedstocks. In addition, the promotion of CO_2 reforming decreases the requirement to reform fuels with an external steam reforming subsystem prior to delivery into the anode, potentially decreasing the complexity and requirements of SOFC systems.

5.8. Effect of temperature on the performance of the cell

Fig. 5.9a shows the behaviour of the OCP when H_2/CO_2 was added to CH_4 from 750-800 °C. When there was less than 60 vol% H_2, increasing the temperature caused the OCP to increase because of the presence of dry reforming of CH_4 and CH_4 cracking, which are both endothermic processes. Increasing the temperature therefore promoted these reactions thermodynamically as well as kinetically, increasing the CH_4 conversion, the volume of H_2 present, and hence the OCP. For mixtures with more than 80 vol% H_2/CO_2, increasing the temperature had the opposite effect due to the dominance of the RWGS reaction, which is also endothermic but consumes H_2 to produce CO. Increasing the temperature over this fuel range therefore decreased the presence of H_2, causing the OCP to also decrease. Between 60-80 vol% H_2/CO_2, changing the temperature had little effect on the value of the OCP due to the effects of dry reforming and CH_4 cracking being cancelled by the RWGS reaction under these fuel compositions.

Fig. 5.16a shows the effect of temperature on the I-V curve when operating on 60vol% CH_4 and 40 vol% H_2/CO_2. The current output increases with temperature due an alleviation of OCP, activation, ohmic and concentration losses. In particular, the activation losses are strongly alleviated, which is further evidence that CH_4 conversion is the key limiting factor for the CH_4-

rich fuel mixtures. Increasing the temperature assisted with catalytic CH_4 conversion thermodynamically and kinetically, accelerating electrochemical CH_4 oxidation and promoting electrochemical H_2 oxidation as the main power production pathways. Fig. 5.16b shows increasing the temperature to 800 °C therefore gave a substantial increase in current output of 145-195% between 0.6-0.9 V.

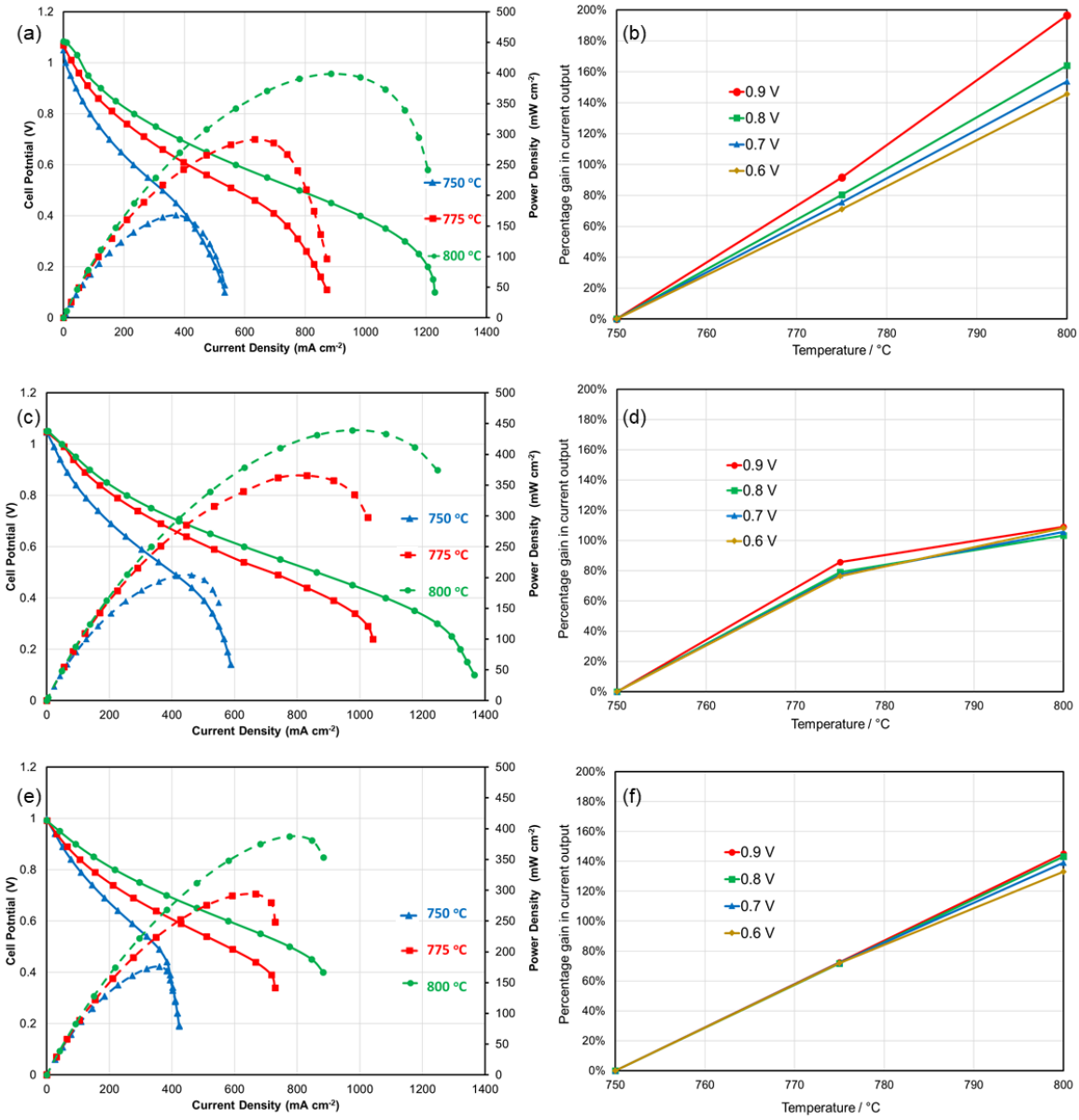

Figure 5.16: The effect of temperature on the I-V curve (left column) and percentage gain in current output (right column) at 750-800 °C with the cell operating on: (a-b) 60 vol% CH_4 and 40 vol% H_2/CO_2, (c-d) 40 vol% CH_4 and 60 vol% H_2/CO_2 and (e-f) 20 vol% CH_4 and 80 vol% H_2/CO_2.

Similar behaviour was observed for 40vol% CH_4 and 60 vol% H_2/CO_2, where the I-V curves (Fig. 5.16c) indicate that increasing the temperature improved cell performance due to a decrease of activation, ohmic and concentration losses. The OCP losses were unaffected by changes in temperature for this fuel mixture as has already been described in Fig. 5.9a. A large increase in current output of 75-90% was observed between 0.6-0.9 V when increasing the temperature to 775 ℃. This was mainly due to an increase in electrochemical H_2 oxidation kinetics, and an increase in CH_4 conversion kinetics, with the QMS data in Fig. 5.9b indicating the presence of some unconverted CH_4 at 750 °C. Increasing to 800 °C gave a more marginal increase in current output of up to 100-110% compared with 750 ℃, indicating that there was little unconverted CH_4 at 775 °C and therefore alleviation of losses was due mainly due to improved activation kinetics.

Finally, under 20 vol% CH_4 and 80 vol% H_2/CO_2, Fig. 5.16f shows that increasing the temperature to 800 ℃ increased the current output by 130-145% between 0.6-0.9 V. The I-V curves in Fig. 5.16e show the improvement in performance was due to an alleviation of activation, ohmic and concentration losses. The QMS data at 750 ℃ (Fig. 5.9b) shows that the RWGS reaction was the dominant catalytic fuel conversion process for this fuel mixture which was mainly composed of H_2 and CO_2. Increasing the temperature is therefore highly likely to have decreased the losses by increasing the rates of electrochemical H_2 and CO oxidation. The overall gain in performance was not as marked as that observed for 60 vol% CH_4 and 40vol% H_2/CO_2.

5.10. Conclusion

The utilisation of biohythane (60/30/10 vol% $CH_4/CO_2/H_2$) in solid oxide fuel cell technology has been investigated and shown to give better kinetic performance than biogas (CH_4/CO_2). A high performance method of utilising complex renewable and industrial waste gases has been demonstrated that it is possible to yield electrical power and syngas (H_2/CO) simultaneously with almost complete conversion of CH_4. Depending on the operating conditions, the balance of electrical power and syngas production, as well as the composition of syngas, were easily

controlled through adjustment of the cell voltage. H_2/CO ratios in the range 1.1-4.0 were obtained in this work. The chemistry of fuel processing at the anode was characterised by quadrupole mass spectrometry, revealing that electrical power production occurred through H_2 electrochemical oxidation and a mixture of partial (high voltages) and total (low voltages) electrochemical oxidation of CH_4. Electrochemical CO oxidation did not contribute to power production. Catalytic dry reforming of methane also contributed to fuel conversion.

The switch in fuel conversion mechanism from partial (POx) to total (TOx) electrochemical oxidation of CH_4 had complex implications for the quantity and composition of cell outputs. High voltages promoted POx and gave less electrical power, faster syngas production rates and lower H_2/CO ratios, with the reverse observed at lower voltages. Increasing the H_2 content of biohythane improved the kinetic performance of the cell to give more electrical power and, depending on the voltage, either more syngas with a lower H_2/CO ratio (at low voltages), or slightly less syngas with a higher H_2/CO ratio (at high voltages).

The effects of fuel variability on biohythane utilisation were investigated and showed that addition of 25/75 vol% H_2/CO_2 to pure CH_4 increased SOFC electrical performance due to the additional presence of H_2 and promotion of CO_2 reforming, the reverse Boudouard and RWGS reactions, each of which alleviated carbon deposition and promoted electrochemical H_2 oxidation as the primary power production pathway. In terms of electrical performance, substitution of 60 vol% CH_4 with H_2/CO_2 was found to be the optimum composition, giving an electrical power output that was 66.4 % higher than that produced from pure CH_4 at an operating voltage of 0.7 V. A 260 h durability test was conducted which demonstrated a very high stability when operating on typical 60/30/10 vol% $CH_4/CO_2/H_2$ biohythane mixture under high fuel utilisation, where high CH_4 conversion was achieved whilst preventing CH_4 cracking.

By substituting 60 vol% CH_4 with H_2/CO_2 increased the overall efficiency of energy conversion by a factor of 3.7 and decreased CH_4 consumption by 76 %. However, the overall efficiency and savings in CH_4 consumption were shown to be increased by addition of H_2/CO_2 to CH_4 in any amount. Overall, this work suggests that decarbonising gas grids by substituting natural gas with

renewably produced H_2/CO_2 mixtures (rather than pure H_2 derived from fossil fuels) and utilising in SOFC technology, gives considerable gains in energy conversion efficiency and carbon emissions savings.

In addition, the current output can be increased by another 100-110% by increasing the operating temperature to 800 °C, which further improved catalytic CH_4 conversion and accelerated electrochemical H_2 conversion. Long-test durability testing demonstrated good SOFC stability when operating on 60/30/10 vol% $CH_4/CO_2/H_2$ under high fuel utilisation, which ensured high CH_4 conversion whilst preventing CH_4 cracking.

Chapter 6: Co-electrolysis of biohythane

6.1. Introduction

This chapter reports investigations into the co-electrolysis of simulated biohydrogen, biogas and biohythane gas mixtures using an anode supported solid oxide fuel cell (SOFC). For the biohythane mixtures, the effect of co-electrolysing with H_2O, CO_2 and H_2O/CO_2 oxidant mixtures was also investigated. In addition, the effects of fuel variability on co-electrolysis were investigated for biohythane. The kinetic performance of the cell was characterised using I-V curves and electrochemical impedance spectroscopy. The performance of the cell was compared with H_2 as well as biohydrogen and biogas. The output gases from the anode were characterized in real-time using quadrupole mass spectrometry (QMS), showing the gaseous products, reaction pathways and transient behavior of fuel conversion in a high level of detail.

6.2. Co-electrolysis of fuels with steam

6.2.1. Behaviour at OCP

Firstly, the cell was studied at the OCP with H_2 and 50 vol% added steam Table 6.1 reporting the OCP for H_2/H_2O at 0.948 V. The output gases of the cell at the OCP were measured and characterized by QMS and are shown in Fig. 6.1. Switching to biohydrogen (still mixed with 50 vol% steam) decreased the OCP slightly to 0.925 V due to CO_2 dilution effects and the presence of the RWGS reaction, which as shown in Chapter 4, further decreases the presence of H_2 and generates CO at the anode. This decrease of OCP (0.02 V) was not as significant as that observed in fuel cell mode in Chapter 4 (0.12 V), indicating the additional presence of H_2O shifts the equilibrium of the RWGS alleviating the conversion of hydrogen slightly and therefore causing the OCP to decrease less. The H_2/CO ratio was 0.60 and the output gases were composed of 54.76 vol% syngas production (see Table 6.2).

Table 6.1: OCP of ASC operating on various fuels mixed with 50 vol% H_2O.

Fuel Mixture	OCP
Hydrogen (H_2)	0.948 V
Biohydrogen (50/50 vol% H_2/CO_2)	0.925 V
Biogas (60/40 vol% CH_4/CO_2)	1.016 V
Biohythane (60/30/10 vol% $CH_4/CO_2/H_2$)	1.106 V

Table 6.2: Composition and characteristics of output gases shown in Fig. 6.1. The percentage CH_4 conversion is also provided.

Fuel Composition	H_2	CO	CH_4	CO_2	Syngas (vol%)	H_2/CO Ratio	CH_4 Conv.
H_2 (100 vol%)	98.59%	0.00%	0.00%	1.41%	-	-	-
CO_2/H_2 (50/50 vol%)	20.52%	34.24%	0.00%	45.24%	54.76 vol%	0.60	-
CH_4/CO_2 (60/40 vol%)	54.10%	22.75%	3.08%	20.07%	76.86 vol%	2.38	80.78 %
$CH_4/CO_2/H_2$ (60/30/10 vol%)	60.22%	21.61%	2.89%	15.28%	81.83 vol%	2.79	81.97 %

Switching the fuel to biogas increased the OCP to 1.016 V and the output gases show a significant increase of the H_2 signal, whilst the CO signal increased slightly. This indicates the presence of steam (Eq. 4) and dry reforming of CH_4 (Eq. 17), which gave a higher H_2/CO ratio of 2.38 and a syngas content of the output gas mixture of 76.86 vol%. The level of unconverted CH_4 (19.22 vol%) was measured resulting to the remaining 80.78 vol% CH_4 being converted via steam, dry reforming of CH_4 and methane cracking. Due to the presence of CO_2 in biogas, it is likely that some CH_4 was also converted via dry reforming (Eq. 17), although the considerable presence of CO_2 detected and the high H_2/CO ratio suggests dry reforming was much less prevalent than steam reforming (Eq. 4). This agrees with previous literature where it is widely

established that H_2O reforming (Eq. 4) has faster kinetics than CO_2 reforming (Eq. 17) [288]. However, the overall the presence of dry reforming is likely to be quite significant, the steam reforming stoichiometry of the H_2/CO ratio it is 2:1, suggesting that some CH_4 was converted via dry reforming which has a H_2/CO ratio of 1:1. It is also likely that CO_2 promoted the RWGS reaction (Eq. 16), further decreasing the H_2/CO ratio. If only steam reforming was taking place, then the H_2/CO ratio would be at least 3, and probably higher due to promotion of WGS.

Switching to biohythane increased the OCP to 1.106 V. The additional H_2 in biohythane increased the OCP suggesting that the presence of H_2 suppressed catalytic reforming reactions at the anode. The amount of H_2 in the output gases was increased by 6.12 % compared with biogas, giving an increased syngas ratio and syngas production of 2.79 and 81.83 vol% respectively. Steam and dry reforming of CH_4 were likely to be present as was the case for biogas, with a slightly higher percentage CH_4 conversion of 81.97 % was achieved with biohythane. This indicate that the decreased presence of CO_2 decreased the dry reforming of methane reaction (Eq. 17) and steam reforming is the prenominal reaction (Eq. 4) taking place due to the H_2/CO ratio being 3:1. Therefore switching to biohythane resulted in more CH_4 to be converted (1.19 % more compared with biogas) due to the increased presence of steam reforming of methane resulting in higher syngas production (4.97 vol% compared with biogas).

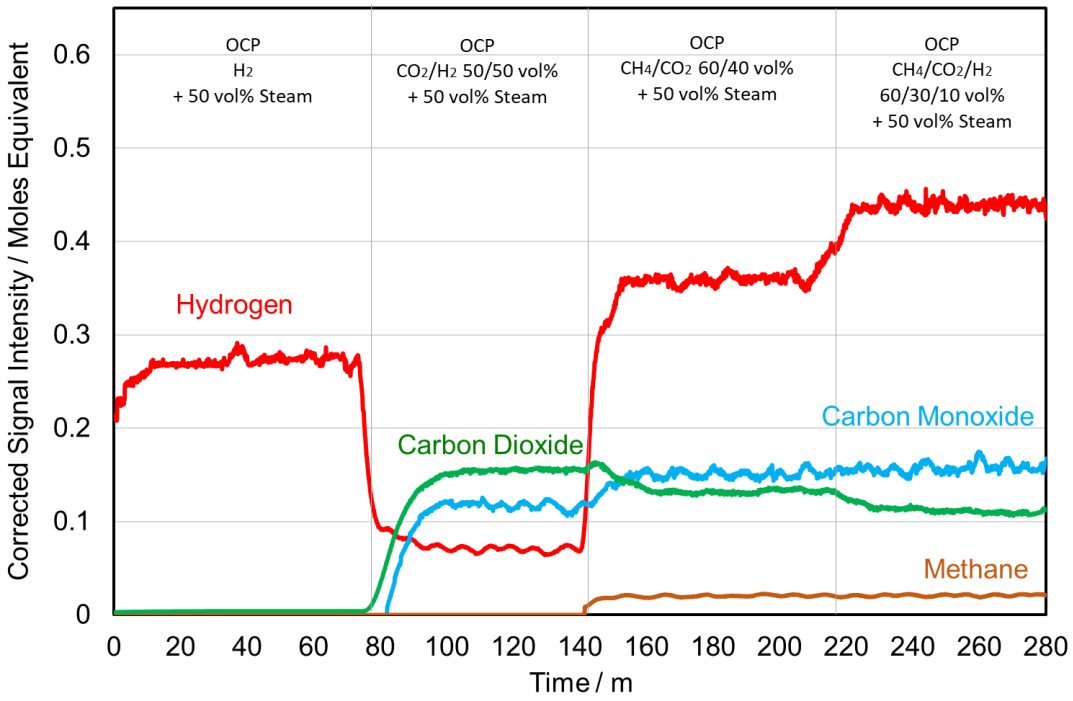

Figure 6.1: The effect of fuel composition on the output gases of an ASC operating at OCP at 750 °C. The fuels studied were hydrogen (H_2 100 vol%), biohydrogen (CO_2/H_2 50/50 vol%), biogas (CH_4/CO_2 60/40 vol%) and biohythane ($CH_4/CO_2/H_2$ 60/30/10 vol) mixed with 50 vol% H_2O.

6.2.2. Co-electrolysis mode

Fig. 6.2a shows the effect of fuel composition on the I-V curve of the cell in electrolysis mode. With pure H_2, the I-V curve was very linear up to approximately 1.2 V, indicating the activation and concentration losses were very low. For biohydrogen, the I-V curve was very similar to that measured for pure H_2, showing the presence of CO_2 had very little effect on the activation and concentration losses of the cell under these conditions. Switching to biogas caused the cell performance to decrease markedly. The OCP increased in agreement with previous work, and this was due to the presence of steam (Eq. 4) and dry reforming of CH_4 (Eq. 17), which increased the volume of H_2 at the anode. In addition, the overall kinetic performance decreased due to a considerable increase in the activation losses as indicated by the pronounced non-linear curve across the full voltage range. These losses were alleviated slightly by switching to biohythane, which gave a similar I-V curve but with decreased activation losses compared with biogas, showing that even adding only 10 vol% H_2 to the fuel mixture improved the kinetic

performance of the cell considerably. For example, a voltage of approximately 17% lower was required to achieve 400 mA cm^{-2}. The enhanced performance overall compared with biogas was most likely due to improved reduction of the anode surface and suppression of methane cracking [84, 230, 231].

The corresponding impedance spectra are shown in Fig. 6.2b, with the widths of the polarisation arcs given in Table 6.3. The fuel mixture did not have an effect on ohmic losses but both high and low frequency arcs responded to changes in fuel mixtures indicating that fuel mixtures influenced activation and diffusion losses. In electrolysis mode, H_2 and H_2/CO_2 mixtures had the lowest arc widths indicating the fewer activation and diffusion losses in agreement with the I-V curves. Switching the mixture to biogas increased considerably the low frequency arc width indicating increased diffusion losses. The high frequency arc width also increased displaying greater surface diffusion and charge transfer losses for biogas. Switching to biohythane mixture decreased the high (≈ 0.01 Ω cm^2) and low (≈ 0.55 Ω cm^2) frequency arc widths. This indicate that biohythane had a better performance with lower losses compared with biogas with diffusion losses decreasing considerably compared with biogas.

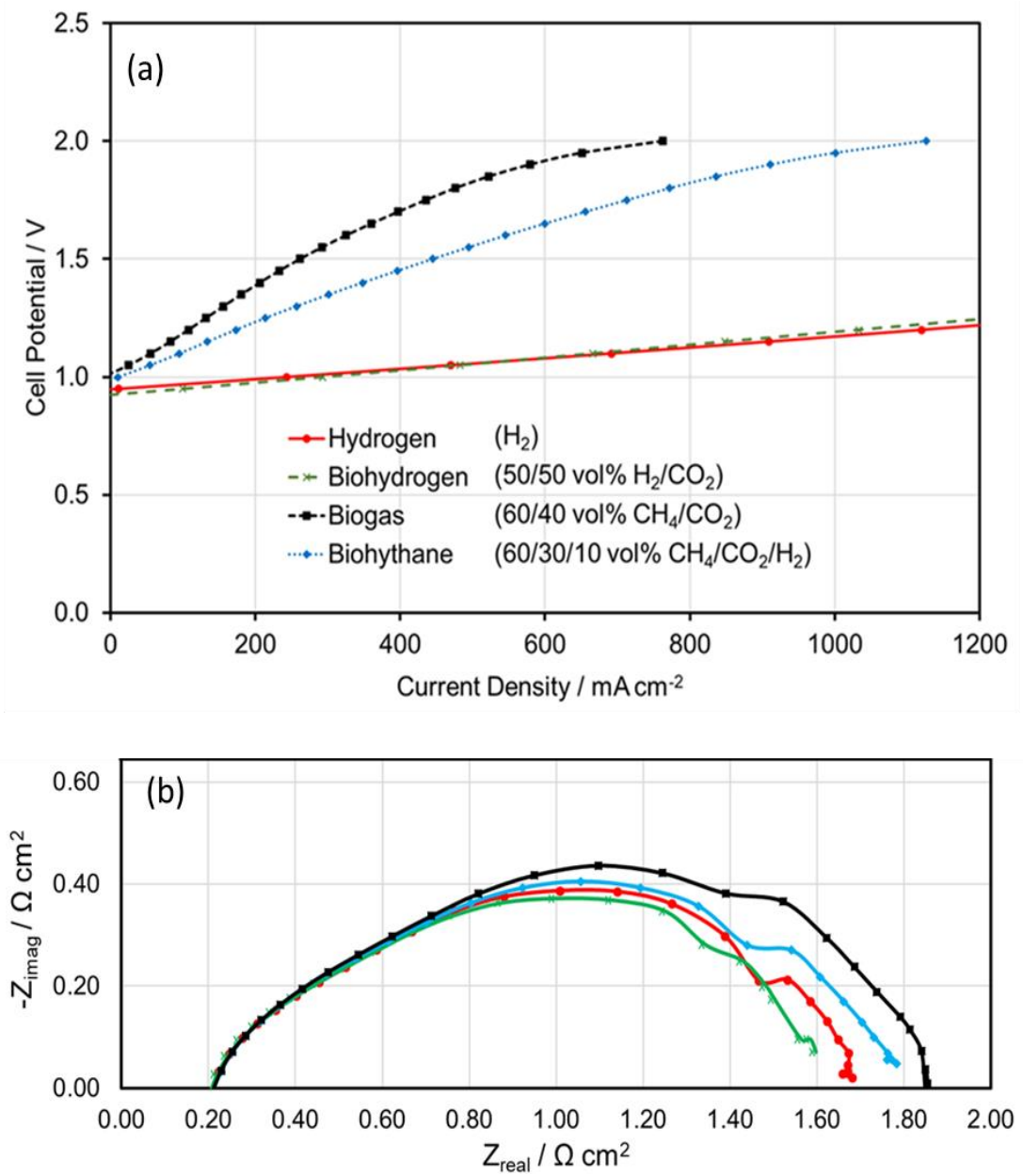

Figure 6.2: The effect of fuel composition on (a) the I-V curves and (b) the impedance of an ASC operating in electrolysis mode at 0.1-100000 Hz. The fuels studied were hydrogen (H_2 100 vol%), biohydrogen (CO_2/H_2 50/50 vol%), biogas (CH_4/CO_2 60/40 vol%) and biohythane ($CH_4/CO_2/H_2$ 60/30/10 vol%. In each case, the fuels are mixed with 50 vol% H_2O.

Table 6.3: Widths of the high and low frequency arcs in the electrochemical impedance spectra presented in Fig. 6.2b.

Fuel Mixture + Steam 50/50 vol%	Ohmic / Ω cm^2	High Frequency Arc Width / Ω cm^2	Low Frequency Arc Width / Ω cm^2
H_2	0.2028	1.2642	0.2140
H_2/CO_2	0.2009	1.1410	0.2530
CH_4/CO_2	0.2082	1.2478	0.3990
$CH_4/CO_2/H_2$	0.2081	1.2390	0.3440

The output gases of the cell were measured during under electrolysis mode with a voltage of 1.4 V applied to the cell, as shown in Fig. 6.3 and Table 6.4. Initially, with H_2 and 50 vol% steam (as a dried gases) the measurements show that 98.60 % H_2 (with the rest being CO_2 impurities) was produced and the production of H_2 was mainly through electrolysis of steam (Eq. 21):

$$H_2O + 2e^- \rightleftharpoons H_2 + O^{2-} \qquad \text{(Eq. 21)}$$

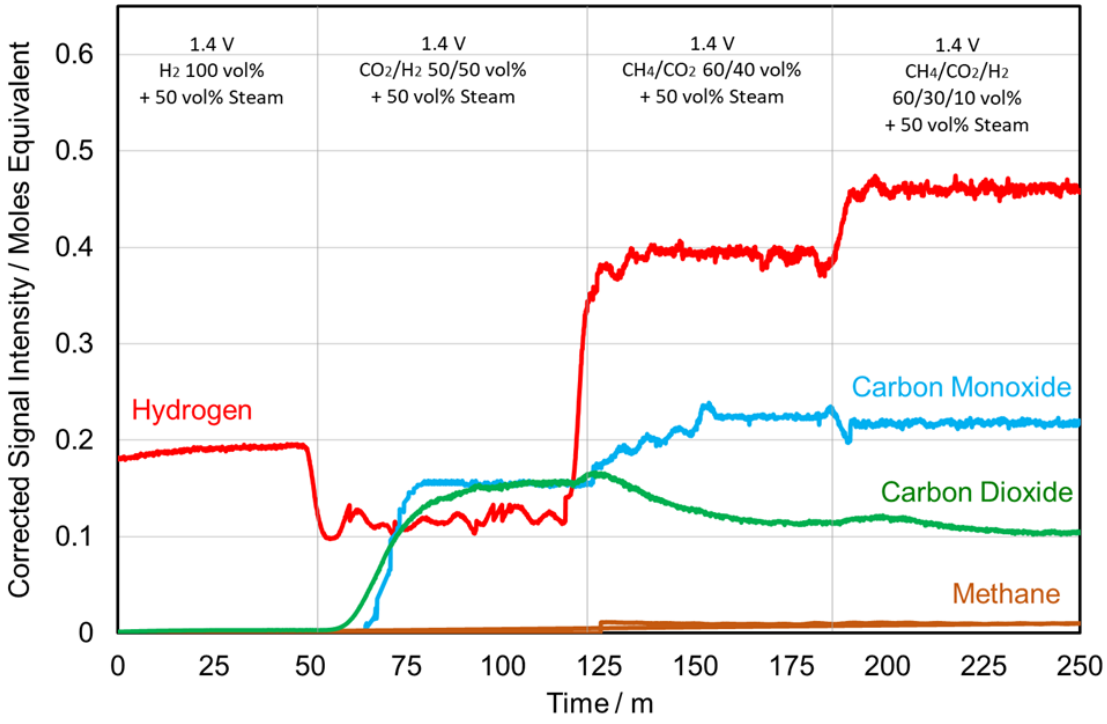

Figure 6.3: The effect of fuel composition on the output gases of an ASC operating in electrolysis mode (1.4 V) at 750 °C. The fuels studied were hydrogen (H_2 100 vol%), biohydrogen (CO_2/H_2 50/50 vol%), biogas (CH_4/CO_2 60/40 vol%) and biohythane ($CH_4/CO_2/H_2$ 60/30/10 vol) mixed with 50 vol% H_2O.

Table 6.4: Composition and characteristics of output gases shown in Fig. 6.3. The percentage CH_4 conversion is also provided.

Fuel Composition	H_2	CO	CH_4	CO_2	Syngas (Vol%)	H_2/CO Ratio	CH_4 Conv.
H_2 (100 vol%)	98.60%	0.00%	0.00%	1.40%	-	-	-
CO_2/H_2 (50/50 vol%)	28.26 %	36.52%	0.00%	35.22%	64.78 vol%	0.77	-
CH_4/CO_2 (60/40 vol%)	52.81%	30.26%	1.29%	15.64%	83.07 vol%	1.75	91.93%
$CH_4/CO_2/H_2$ (60/30/10 vol%)	57.73%	27.33%	1.25%	13.68%	85.06 vol%	2.11	92.16%

Upon switching to the biohydrogen mixture, the H_2 decreased to 28.26 vol%. A gas composition of 64.78 % syngas was produced with a H_2/CO ratio of 0.77, which is higher compared to the H_2/CO ratio at OCP. The increased presence of CO (2.28 %) indicates electrochemical reduction of CO_2 (Eq. 22) and H_2O (Eq. 21) representing the presence of the RWGS reaction. Therefore, the product gases increased when the cell was operated under 1.4 V compared to OCP. Overall, applying a voltage to the cell increased the syngas produced by ≈10 vol% compared with OCP due to a combination of electrochemical H_2O (Eq. 21) and CO_2 reduction reactions (Eq. 22)

$$CO_2 + 6e^- \rightleftharpoons CO + 3O^{2-} \quad \text{(Eq. 22)}$$

When the fuel was switched to biogas, the presence of H_2 and CO increased to produce output gases composed of 83.07 vol% syngas with the H_2/CO ratio decreased to 1.75. The fact that the presence of CO_2 in the output gases decreased to 15.64 % confirm the existence of the methane reforming reactions (Eqs. 4 and 17) and the RWGS reaction (Eq. 16). Applying a voltage increased the syngas produced compared with OCP by ≈6 %, also the methane conversion was increased by ≈11 % compared with OCP operation. Applying a voltage has an increase in the flow rate of H_2 and CO produced due to electrochemical reduction of H_2O (Eq. 21) and CO_2 (Eq. 22) due to the increased presence steam and dry reforming reactions.

When switching to biohythane, the initial presence of H_2 resulted in higher levels of H_2 present in the output gases, with the H_2/CO ratio increased to 2.11. The CO decreased slightly due to the decreased presence of CO_2 in the initial mixture but syngas presence in the output gases overall increased to 85.06 %. The CH_4 conversion increased to 92.16% and it is suggested this was due to enhanced reduction of the nickel anode through the additional presence of hydrogen and decreased presence of carbon dioxide, improving the catalytic activity towards reforming. The methane conversion increased by ≈10 % when a voltage was applied compared to OCP due to the increased presence of CH_4 electrochemical and dry reforming reactions.

6.3. Effect of the oxidant composition on co-electrolysis of biohythane

A significant advantage of co-electrolysis is the flexibility of adjusting the outlet syngas composition by varying the operating conditions, including the inlet gas composition and applied operating voltage. In this work, the effect of the oxidant composition on the electrochemical performance and outputs of the cell were investigated when operating on biohythane.

Fig. 6.4 shows the output gases of the cell operating on biohythane with H_2O, H_2/CO_2 and CO_2 as the oxidant mixtures. With pure H_2O as the oxidant, the H_2 production was highest due to the electrolysis of H_2O. A H_2/CO ratio of 1.99 (see Table 6.5) with 88.14 vol% of syngas produced due to increased electrochemical conversion of H_2O. The CH_4 conversion was the highest 93.25 %, suggesting that catalytic H_2O reforming was also enhanced by with the increased presence of H_2O.

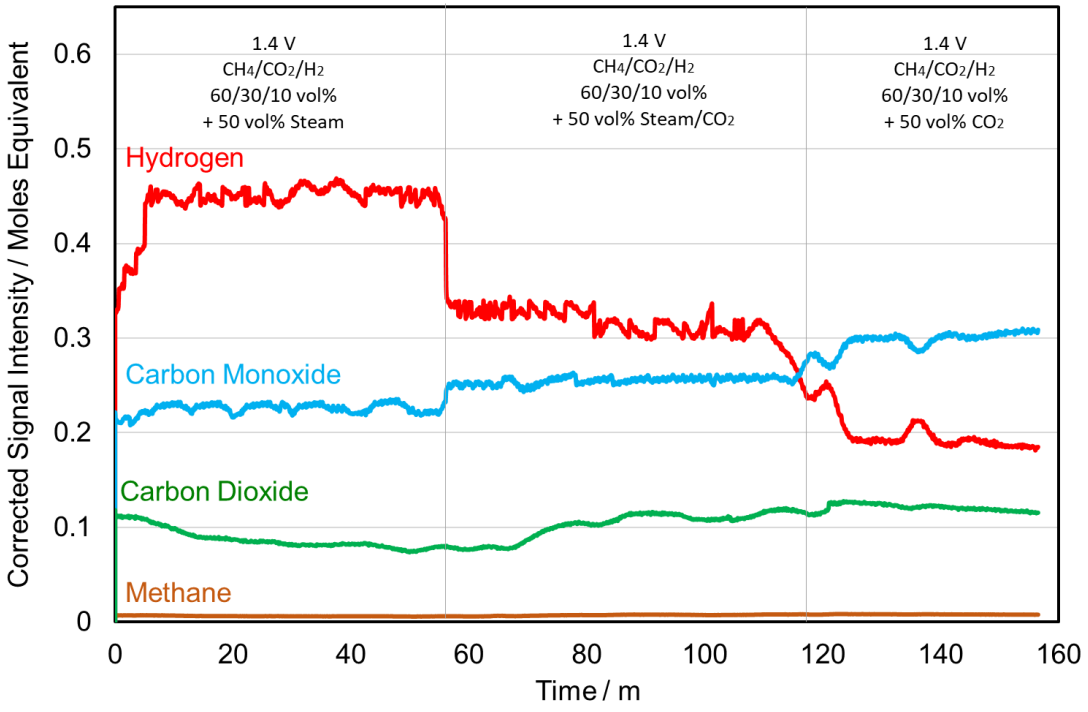

Figure 6.4: The effect of oxidant composition on the output gases of an ASC operating on biohythane ($CH_4/CO_2/H_2$ 60/30/10 vol%) in electrolysis mode. In each case, biohythane was mixed with 50 vol% of oxidant. The oxidants studied were steam (H_2O), carbon dioxide (CO_2) and a 50/50 vol% H_2O/CO_2 mixture.

Table 6.5: Composition and characteristics of output gases shown in Fig. 6.4. The percentage CH_4 conversion is also provided.

Oxidant Composition	H_2	CO	CH_4	CO_2	Syngas (vol%)	H_2/CO Ratio	CH_4 Conv.
H_2O (100 vol%)	58.70%	29.44%	0.81%	11.05%	88.14 vol%	1.99	93.25 %
H_2O/CO_2 (50/50 vol%)	46.65%	37.41%	1.06%	14.89%	84.05 vol%	1.25	91.17 %
CO_2 (100 vol%)	30.87%	48.37%	1.30%	19.46%	79.24 vol%	0.64	89.16 %

Switching the oxidant to 50/50 vol% H_2O/CO_2 decreased the H_2 content (by ≈ 11 %) and H_2/CO ratio of the mixture to 1.25. This was due to increased electrochemical CO_2 reduction (Eq. 22) and decreased electrochemical H_2O reduction (Eq. 21). The CO volume increased slightly but the total volume of syngas decreased to 84.05%, which is an indication of slower CO production due to slower electrochemical CO_2 reduction kinetics. The CH_4 conversion decreased by ≈ 2 % compared with H_2O (100 vol% as an oxidant), demonstrating slower kinetics of CO_2 reforming compared with steam reforming.

These effects were observed more strongly when using CO_2 (100 vol%) as a co-oxidant, which produced only 79.24% syngas and a H_2/CO ratio below 1. In addition, CH_4 conversion was decreased by ≈4 % with H_2O (100 vol%) and ≈ 2 % with H_2O/CO_2 (50/50 vol%) as oxidants. This is due to the kinetics of CO_2 conversion catalytically via dry and steam reforming and electrochemical CO_2 reduction are much slower than H_2O conversion [288].

I-V curves and electrochemical impedance spectra were measured to investigate the effect of the oxidant mixtures studied on the performance of the cell. These are shown in Fig. 6.5 along with the impedance spectra. For each of the oxidant mixtures, the high frequency arc was 3-5 times larger, indicating the surface diffusion and charge transfer losses dominated. The low frequency arc stayed approximately constant as the co-oxidant was changed, suggesting gas diffusion losses were not greatly influenced by the co-oxidant. The width of the high frequency increased as follows: $H_2O < H_2O/CO_2 < CO_2$, showing that with increasing CO_2 as a co-oxidant increased the charge transfer and surface diffusion losses. The OCP also increased in this order. The data

show the performance of the cell was highest when the co-oxidant was H_2O: the OCP was the lowest (0.990 V) and the I-V curve was linear and the impedance arc widths were the narrowest, indicating low activation losses for H_2O. In addition to enhancing catalytic conversion of CH_4, H_2O increased the electrochemical conversion of reactants, since electrochemical conversion and diffusion of H_2O is faster compared with CO_2. This increased H_2 production and therefore led to increased syngas production which was subsequently more H_2-rich. Increasing the use of CO_2 as co-oxidant increased activation losses because CO_2 is more stable and slower to convert than H_2O. Upon switching to H_2O/CO_2 and CO_2, CO_2 did not appear to have a pronounced effect on the gas diffusion losses, but did increase the OCP and the activation losses, reducing the overall kinetic performance of the cell. As well as reducing the H_2/CO ratio and catalytic conversion of CH_4 therefore, using more CO_2 as co-oxidant decreased the overall yield of syngas through electrochemical processes.

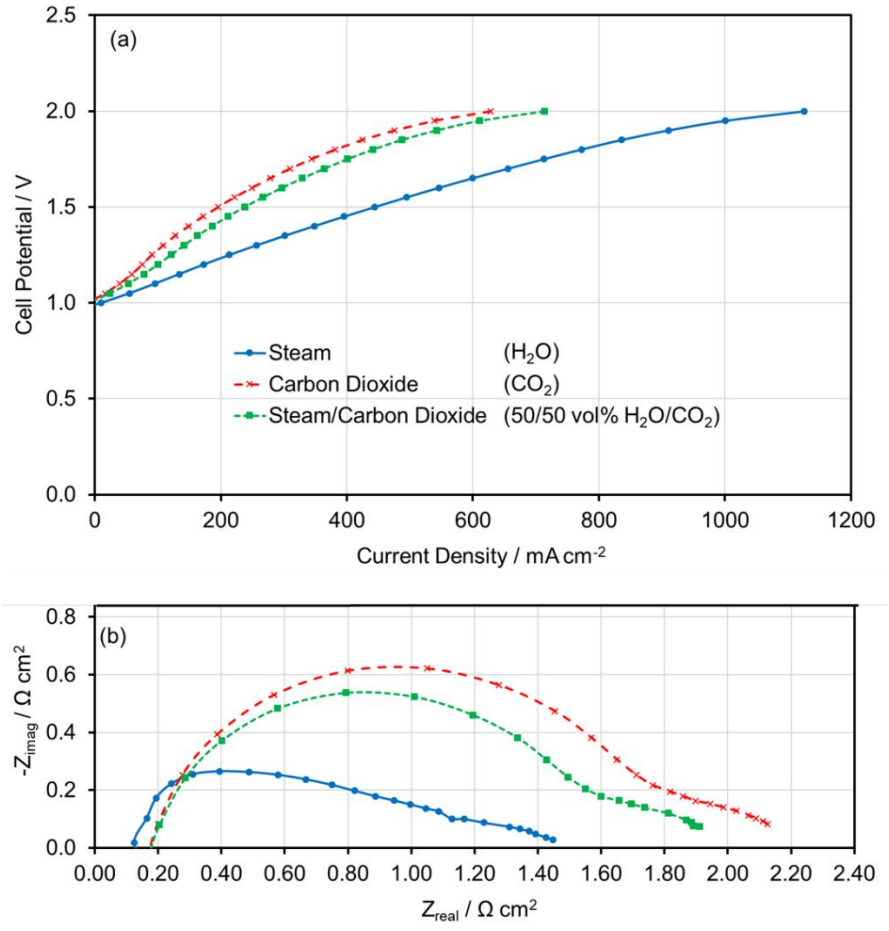

Figure 6.5: The effect of oxidant composition on the: (a) I-V curve, and (b) electrochemical impedance spectrum at 0.1-100000 Hz, of an ASC operating on biohythane in electrolysis mode.

6.4. The effect of fuel composition on the co-electrolysis of biohythane with steam

Fig. 6.6a shows the effect of substituting CH_4 with H_2/CO_2 on the performance of the cell using H_2O (100 vol%) as the co-oxidant. Under 80 vol% of CH_4, the I-V curve have the highest OCP (approx. 1.00 V) but the cell displayed increased activation losses due to the high presence CH_4. It is also possible that there was increased carbon deposition as the methane content was increased. As the H_2-content was increased to 7.5 vol% and the CH_4 was decreased to 70 vol%, the OCP and the activation losses decreased, showing a better overall kinetic performance. As the CH_4 was substituted further with H_2/CO_2 the OCP decreased further due to fuel dilution effects. There was a much larger decrease in the activation losses and the OCP (0.930 V), with a more linear I-V curve observed at 20 vol% H_2 indicating enhanced performance of the cell when the H_2-content was increased. The activation losses decreased due to the greater presence of CO_2 and increasing the concentration of the reactants increased the kinetics of a chemical conversion process. As the CH_4 content was decreased, there was likely to be less carbon deposition, which would improve the activation and concentration kinetics.

The EIS spectra Fig. 6.6b show the widths of the polarisation arcs (see Table 6.6) showing that both arcs responded to changes in the fuel composition. As the H_2/CO_2 content of biohythane was increased from 5 vol% - 20 vol% both the high and low frequency arc widths decreased indicating that surface diffusion, charge transfer and gas diffusion decrease as the CH_4 content of biohythane was substituted with H_2/CO_2.

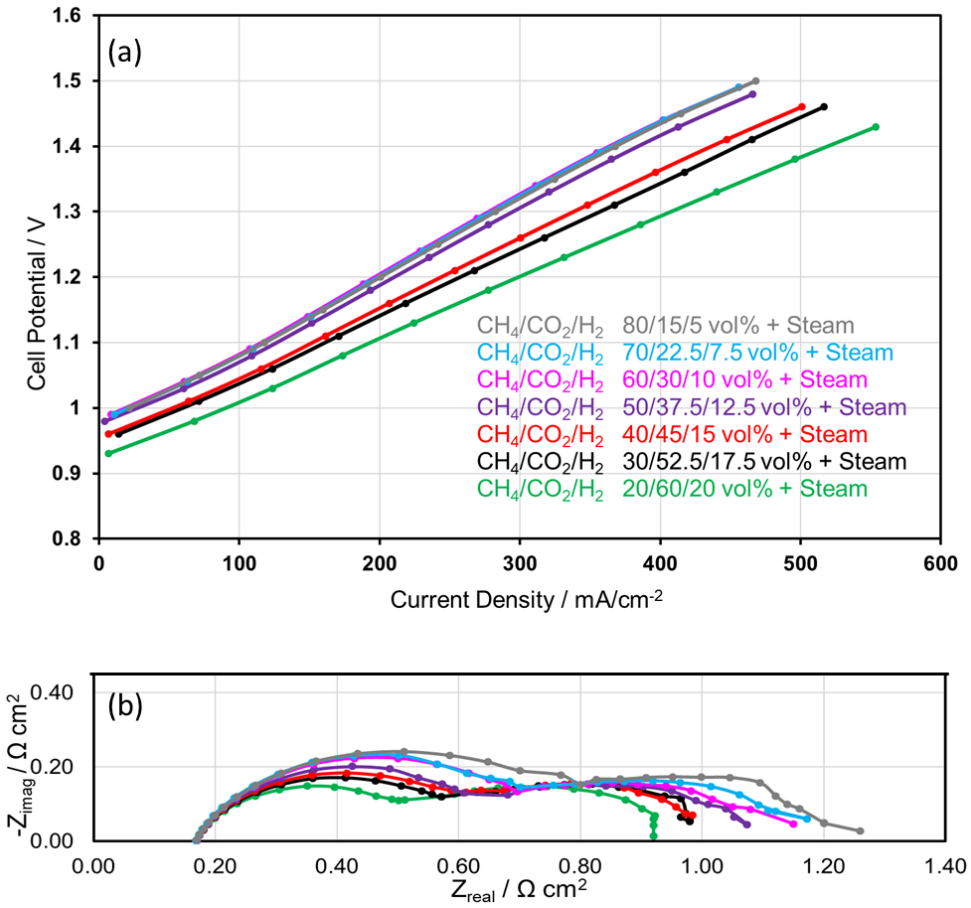

Figure 6.6: The effect of fuel composition on the: (a) I-V curve, and (b) electrochemical impedance spectrum at 0.1-100000 Hz.

Table 6.6: High frequency and low frequency polarisation arc widths of the impedance spectra in Fig. 6.6b.

H_2 Composition (Vol %)	**EIS High Frequency Arc Width / Ω cm^2**	**EIS Low Frequency Arc Width / Ω cm^2**
5	0.6307	0.4705
7.5	0.5377	0.4700
10	0.5272	0.4537
12.5	0.4900	0.4147
15	0.4230	0.3965
17.5	0.4079	0.3960
20	0.3465	0.3912

6.5. Conclusion

This chapter examined the co-electrolysis of simulated biohydrogen, biogas and biohythane gas mixtures using an anode supported SOFC. For the biohythane mixtures, the effect of co-

electrolysing with H_2O, CO_2 and H_2O/CO_2 oxidant mixtures and the effects of fuel variability were investigated. The kinetic performance of the cell was characterised using I-V curves and electrochemical impedance spectroscopy. The experimental work has shown that addition of 10 vol% H_2 to CH_4/CO_2 feedstocks markedly improves the overall performance of the cell in co-electrolysis mode. Co-electrolyzing biohythane with H_2O gave the highest performance with the highest syngas yield and highest H_2/CO ratio whereas co-electrolysis with CO_2 decreased the catalytic and electrochemical conversion of reactants, giving lower performance, lower syngas yields and lower H_2/CO ratios. Syngas production with high conversation rate of CH_4 and CO_2 and in addition desired H_2/CO molar ratio can be achieved by adjusting the operating conditions with H_2O enhancing the performance of the cell due to a mixture of increased catalytic and electrochemical conversion of reactants. Using H_2O gave the highest performance, highest syngas yield and highest H_2/CO ratio of all the oxidants. The performance decreased in the order $H_2O > H_2O/CO_2 > CO_2$. Increasing the CO_2 decreased both catalytic and electrochemical conversion of reactants and therefore gave lower performance, lower syngas yields and lower H_2/CO ratios.

Chapter 7: Conclusions

7.1. Summary of work

The aims of the research to investigate the performance of SOFC with biomass-derived fuels were successfully achieved. The research indicates that the performance of SOFC technology operating on biomass derived fuels can be markedly enhanced and used to decarbonise the natural gas grids by substituting CH_4 with H_2/CO_2. A successful investigation for the utilisation of biohydrogen and biohythane in SOFC has been investigated using ESC and ASC technology, with fuel conversion mechanisms being studied, the implications for gas grid decarbonisation have been explored and the effect of fuel variability and temperature in fuel cell mode and electrolysis mode have been investigated. Consequently, the aims outlined in 1.8 have been achieved.

7.2. Utilisation of biohydrogen in SOFCs

7.2.1. Fuel variability and conversion mechanisms

The performance, fuel processing, electrical power production and output gas composition of SOFC devices running on H_2/CO_2 mixtures are very sensitive to variation in the inlet feedstock composition, demonstrating the need for SOFC anode materials and designs that minimise the effects of fuel variability on SOC performance and stability. However, the cell performance of the cell is not significantly affected by fuel variability when the biohydrogen composition stays within the range 40-60 vol% H_2. Solid oxide electrolysis of H_2/CO_2 mixtures to yield synthesis gas was demonstrated. Syngas production rates and composition are dependent on the initial fuel composition and cell operating voltage. H_2O and CO production takes place in-situ on the anode via the reverse water-gas shift (RWGS) reaction and had a significant effect on the mechanism of reactant conversion and the OCP of the cell. In fuel cell mode, electrical power is produced predominantly via the electrochemical oxidation of H_2. CO does not contribute to power production and is instead converted via the WGS reaction to regenerate CO_2. In

electrolysis mode, CO production takes place through electrochemical CO_2 reduction and the RWGS reaction simultaneously. H_2 is regenerated through electrochemical reduction of H_2O. Increasing the H_2 content of the inlet fuel composition generally decreases the overpotentials when running in fuel cell mode, giving increased power production. The electrical power output of the cell is not significantly affected by fuel variability provided the biohydrogen composition stays within the range 40-60 vol% H_2. In electrolysis mode, overpotentials are decreased by increasing the CO_2 of the fuel; however, this does not necessarily yield increased synthesis gas production rates or a consistent H_2/CO ratio, since CO is produced through the RWGS reaction as well as electrochemical CO_2 reduction. Increasing the temperature have a major effect on the performance and outputs of the cell. Increased temperature caused the OCP to decrease due to the RWGS reaction but increased the reaction rate. At high (90 vol%) and low (10-20 vol%) CO_2 compositions the activation and concentrations were increased. When the CO_2 composition was in the range of 40-60 vol% the losses were minimised and the cell performance was enhanced.

7.2.2. ESC and ASC comparison

Both ESC Both ESC and ASC were able to utilise successfully biomass derived fuels in fuel cell and in electrolysis mode. ESCs were more durable and not affected as greatly by changes in fuel variability as ASCs. According to the results, ESCs are more suitable for utilizing hydrogen-based mixtures. ASC had overall a better performance and produced a significantly higher power density, making this type of cells more suitable to utilize more complex fuels (methane-based fuels) despite their higher cost compared to ESC.

7.3. Utilisation of biohythane in SOFCs

A novel and highly efficient method of utilising renewable and industrial waste gases using SOFCs for coproduction of energy and useful chemicals was demonstrated

experimentally through investigations into the utilisation of biohythane produced from an optimised two-stage AD process. The gain in energy yield from two-stage AD is shown to be

supplemented with additional gains in SOFC efficiency due to the presence of H_2 in biohythane, giving up to 77% increased electrical energy yields from biomass overall compared with utilisation of biogas from single-stage AD in SOFCs. The results therefore show that biohythane production rather than biogas is a highly advantageous route to energy production from biomass.

The effects of fuel variability on biohythane utilisation were investigated and showed that the addition of H_2/CO_2 to pure CH_4 increased SOFC electrical performance. The results demonstrated that dry reforming of CH_4 and the RWGS reaction had key roles in fuel conversion at the anode, with electrical power production occurring primarily through H_2 electrochemical oxidation and a mixture of partial and total electrochemical oxidation of CH_4. Addition of 25/75 vol% H_2/CO_2 to pure CH_4 increased SOFC electrical performance due to the additional presence of H_2 and promotion of CO_2 reforming, the reverse Boudouard and RWGS reactions, each of which alleviated carbon deposition and promoted electrochemical H_2 oxidation as the primary power production pathway. Substitution of 60 vol% CH_4 with H_2/CO_2 was found to be the optimum composition, which increased the overall efficiency of energy conversion by a factor of 3.7 and decreased CH_4 consumption by 76 %. Increased performance was due to the presence of H_2, greater catalytic conversion of CH_4 via dry reforming, and the presence of CO_2, which was shown to promote the activation and diffusion of H_2 through the anode. Also increasing the H_2/CO_2 suppressed CH_4 cracking and promoted the reverse water-gas shift reaction. Blending H_2/CO_2 with CH_4 is a potential way to decarbonise the natural gas grid. Substituting between 50-60 vol% CH_4 with bio-H_2 substantially improves SOFC current output by 56-90% compared with pure CH_4, depending on the operating voltage of the cell. The increase was due to greater catalytic conversion of CH_4 via dry reforming and a switch to electrochemical H_2 oxidation as the primary power production pathway. Substituting anywhere between 20-80 vol% CH_4 with H_2/CO_2 improved SOFC performance to some degree compared with pure CH_4; only under pure H_2/CO_2 was the performance worse due to the very low calorific value of the fuel.

This work has also shown that addition of CO_2 considerably decreases the activation and concentration losses associated with electrochemical H_2 oxidation, although SOFC performance is affected overall due to deterioration of the OCP.

7.4. Gas grid decarbonisation

SOFCs present a great potential for efficient and clean energy production, especially for CHP applications. Their capability to work directly on a large range of fuels and exploiting the heat by-product, offering high system efficiencies and their tolerance to impurities in the fuel, signify important advantages of the SOFC in the future. SOFCs are likely to become a commercial reality with the intriguing possibility to utilise renewable fuels, generated from biomass and directly fed in SOFCs. Future challenges involve the development of more advanced, robust and cheaper materials for SOFCs and fuel cell systems. A safe and efficient infrastructure for hydrogen-based fuels delivery and distribution for the transition to a hydrogen based economy from carbon based energy system, implicates many scientific and technological barriers for decarbonisation of gas grids and use fuel cells as a clean energy technology.

Alleviation of greenhouse gas emissions and air pollutants will require innovative deployment of efficient and clean energy technologies combined with optimal management of waste and renewable resources. Biohythane production rather than biogas is a highly advantageous route to energy production from biomass. This work has shown the utilisation of biohythane for coproduction of electrical power and synthesis gas in SOFCs. The effects of fuel variability on biohythane utilisation were investigated showing that the addition of H_2/CO_2 to pure CH_4 increased SOFC electrical performance showing an alternative and effective way of decarbonising gas grids. Overall, this work suggests that decarbonising gas grids by substituting natural gas with renewably produced H_2/CO_2 mixtures (rather than pure H_2 derived from fossil fuels) and utilising in SOFC technology, gives considerable gains in energy conversion efficiency and carbon emissions savings.

7.5. Future work

Future work to extend this research can include utilisation of real gas mixtures from bio-reactors establishing the effects of impurities in biohydrogen and biohythane mixtures including H_2S, NH_3 and hydrocarbons and how to effectively eliminate impurities. In addition, trials with 5x5 stacks of ASCs can be conducted to learn more about cell efficiency and deactivation mechanisms with both simulated and real gas mixtures in fuel cell and electrolysis modes.

Many novel materials have been studied and displayed improved cell performance [289, 290] therefore; further testing with cells made with novel materials can be studied. Anodes with nickel based materials suffer from carbon deposition and can be modified with Al_2O_3 [291, 292] which increases the electrical conductivity and chemical stability, Ag [293] which decreases the carbon deposition. For cathodes, LSM materials can enhance cell performance by the addition of GDC [294-296].

Long-term testing of biohydrogen and biohythane mixtures can be examined further to investigate cell durability in detail.

References

1. M. Allen, Dube OP, Solecki W, Aragón-Durand F, Cramer W, Humphreys S, Kainuma M, Kala J, Mahowald N, Mulugetta Y, Perez R, Wairiu M, Zickfeld K. Framing and Context. In: Masson-Delmotte V, Zhai P, Pörtner H-O, Roberts D, Skea J, Shukla PR, Pirani A, Moufouma-Okia W, Péan C, Pidcock R, Connors S, Matthews JBR, Chen Y, Zhou X, Gomis MI, Lonnoy E, Maycock T, Tignor M, Waterfield T, *Global Warming of 1.5°C*, in *In Press*. 2018.
2. I.R. Orimoloye, S.P. Mazinyo, A.M. Kalumba, O.Y. Ekundayo, and W. Nel, *Implications of climate variability and change on urban and human health: A review.* Cities, 2019. **91**: p. 213-223. https://doi.org/10.1016/j.cities.2019.01.009.
3. D. Papurello, R. Borchiellini, P. Bareschino, V. Chiodo, S. Freni, A. Lanzini, F. Pepe, G.A. Ortigoza, and M. Santarelli, *Performance of a Solid Oxide Fuel Cell short-stack with biogas feeding.* Applied Energy, 2014. **125**: p. 254-263. https://doi.org/10.1016/j.apenergy.2014.03.040.
4. Z. Shao and M.O. Tadé, *Application of SOFC Technology*, in *Intermediate-Temperature Solid Oxide Fuel Cells: Materials and Applications*. 2016, Springer Berlin Heidelberg: Berlin, Heidelberg. p. 247-266. https://doi.org/10.1007/978-3-662-52936-2_8.
5. M.D. Gross, J.M. Vohs, and R.J. Gorte, *Recent progress in SOFC anodes for direct utilization of hydrocarbons.* Journal of Materials Chemistry, 2007. **17**(30): p. 3071-3077. https://doi.org/10.1039/B702633A.
6. R. O'Hayre, *Fuel Cell Fundamentals*. 3 ed. Fuel Cell Fundamentals, ed. 3. 2016: Wiley
7. A.B. Stambouli and E. Traversa, *Solid oxide fuel cells (SOFCs): a review of an environmentally clean and efficient source of energy.* Renewable and Sustainable Energy Reviews, 2002. **6**(5): p. 433-455. https://doi.org/10.1016/S1364-0321(02)00014-X.
8. H.E. Vollmar, C.U. Maier, C. Nölscher, T. Merklein, and M. Poppinger, *Innovative concepts for the coproduction of electricity and syngas with solid oxide fuel cells.* Journal of Power Sources, 2000. **86**(1): p. 90-97. https://doi.org/10.1016/S0378-7753(99)00421-8.
9. R.S. Amado, L.F.B. Malta, F.M.S. Garrido, and M.E. Medeiros, *Solid oxide fuel cells: Materials, components and configurations.* Quimica Nova, 2007. **30**(1): p. 189-197. https://doi.org/10.1590/s0100-40422007000100031.
10. P. Piela and A. Czerwinski, *Review of fuel cell technology. Part II. Types of fuel cells.* Przemysl Chemiczny, 2006. **85**(3): p. 164-170.
11. R.M. Ormerod, *Solid oxide fuel cells.* Chemical Society Reviews, 2003. **32**(1): p. 17-28. https://doi.org/10.1039/b105764m.
12. M.C. Williams, *Chapter 2 - Fuel Cells*, in *Fuel Cells: Technologies for Fuel Processing*, D. Shekhawat, J.J. Spivey, and D.A. Berry, Editors. 2011, Elsevier: Amsterdam. p. 11-27. https://doi.org/10.1016/B978-0-444-53563-4.10002-1.
13. U. Hennings, M. Brune, M. Wolf, and R. Reimert, *Fuels and fuel cells: The "right way" from fuels to fuel gas.* Chemical Engineering & Technology, 2008. **31**(5): p. 782-787. https://doi.org/10.1002/ceat.200800054.
14. P.P. Edwards, V.L. Kuznetsov, W.I.F. David, and N.P. Brandon, *Hydrogen and fuel cells: Towards a sustainable energy future.* Energy Policy, 2008. **36**(12): p. 4356-4362. https://doi.org/10.1016/j.enpol.2008.09.036.
15. W. Shi, J. Zhu, M. Han, Z. Sun, and Y. Guo, *Operating limitation and degradation modeling of micro solid oxide fuel cell-combined heat and power system.* Applied Energy, 2019. **252**: p. 113444. https://doi.org/10.1016/j.apenergy.2019.113444.
16. S. Giarola, O. Forte, A. Lanzini, M. Gandiglio, M. Santarelli, and A. Hawkes, *Techno-economic assessment of biogas-fed solid oxide fuel cell combined heat and power*

system at industrial scale. Applied Energy, 2018. **211**: p. 689-704. https://doi.org/10.1016/j.apenergy.2017.11.029.
17. X. Xing, J. Lin, N. Brandon, A. Banerjee, and Y. Song, *Time-Varying Model Predictive Control of a Reversible-SOC Energy-Storage Plant Based on the Linear Parameter-Varying Method.* IEEE Transactions on Sustainable Energy, 2020. **11**(3): p. 1589-1600. https://doi.org/10.1109/TSTE.2019.2932103.
18. E.J. Naimaster and A.K. Sleiti, *Potential of SOFC CHP systems for energy-efficient commercial buildings.* Energy and Buildings, 2013. **61**: p. 153-160. https://doi.org/10.1016/j.enbuild.2012.09.045.
19. K. Brinkman and K. Huang, *Solid Oxide Fuel Cells and Membranes.* Chemical Engineering Progress, 2016. **112**(7): p. 44-49.
20. N. Briguglio, M. Ferraro, G. Brunaccini, and V. Antonucci, *Evaluation of a low temperature fuel cell system for residential CHP.* International Journal of Hydrogen Energy, 2011. **36**(13): p. 8023-8029. https://doi.org/10.1016/j.ijhydene.2011.01.050.
21. G. Gigliucci, L. Petruzzi, E. Cerelli, A. Garzisi, and A. La Mendola, *Demonstration of a residential CHP system based on PEM fuel cells.* Journal of Power Sources, 2004. **131**(1): p. 62-68. https://doi.org/10.1016/j.jpowsour.2004.01.010.
22. P. Kazempoor, V. Dorer, and A. Weber, *Modelling and evaluation of building integrated SOFC systems.* International Journal of Hydrogen Energy, 2011. **36**(20): p. 13241-13249. https://doi.org/10.1016/j.ijhydene.2010.11.003.
23. F. Barbir, *Chapter Ten - Fuel Cell Applications*, in *PEM Fuel Cells (Second Edition)*, F. Barbir, Editor. 2013, Academic Press: Boston. p. 373-434. https://doi.org/10.1016/B978-0-12-387710-9.00010-2.
24. P. Boldrin and N.P. Brandon, *Progress and outlook for solid oxide fuel cells for transportation applications.* Nature Catalysis, 2019. **2**(7): p. 571-577. https://doi.org/10.1038/s41929-019-0310-y.
25. C. Bernay, M. Marchand, and M. Cassir, *Prospects of different fuel cell technologies for vehicle applications.* Journal of Power Sources, 2002. **108**(1): p. 139-152. https://doi.org/10.1016/S0378-7753(02)00029-0.
26. G. Hoogers, *Fuel Cell Technology Handbook*. 2003, RCR Press: Boca Raton. https://doi.org/10.1201/9781420041552.
27. G.J. Offer, D. Howey, M. Contestabile, R. Clague, and N.P. Brandon, *Comparative analysis of battery electric, hydrogen fuel cell and hybrid vehicles in a future sustainable road transport system.* Energy Policy, 2010. **38**(1): p. 24-29. https://doi.org/10.1016/j.enpol.2009.08.040.
28. T. Wilberforce, A. Alaswad, A. Palumbo, M. Dassisti, and A.G. Olabi, *Advances in stationary and portable fuel cell applications.* International Journal of Hydrogen Energy, 2016. **41**(37): p. 16509-16522. https://doi.org/10.1016/j.ijhydene.2016.02.057.
29. K. Cowey, K.J. Green, G.O. Mepsted, and R. Reeve, *Portable and military fuel cells.* Current Opinion in Solid State and Materials Science, 2004. **8**(5): p. 367-371. https://doi.org/10.1016/j.cossms.2004.12.004.
30. H. Voss and J. Huff, *Portable fuel cell power generator.* Journal of Power Sources, 1997. **65**(1-2): p. 155-158. https://doi.org/10.1016/s0378-7753(97)02484-1.
31. A.S. Patil, T.G. Dubois, N. Sifer, E. Bostic, K. Gardner, M. Quah, and C. Bolton, *Portable fuel cell systems for America's army: technology transition to the field.* Journal of Power Sources, 2004. **136**(2): p. 220-225. https://doi.org/10.1016/j.jpowsour.2004.03.009.
32. J. Ramkumar and S. Chandramouleeswaran, *A Basic Overview of Fuel Cells: Materials and Applications*, in *Smart Polymers and Composites*, A. Nasar, Editor. 2018, Materials Research Forum Llc: Millersville. p. 133-147.
33. L. Carrette, K.A. Friedrich, and U. Stimming, *Fuel cells: Principles, types, fuels, and applications.* Chemphyschem, 2000. **1**(4): p. 162-193.
34. J.C. Yang, Y.S. Park, S.H. Seo, H.J. Lee, and J.S. Noh, *Development of a 50 kW PAFC power generation system.* Journal of Power Sources, 2002. **106**(1): p. 68-75. https://doi.org/10.1016/S0378-7753(01)01052-7.

35. T. Brenscheidt, K. Janowitz, H.J. Salge, H. Wendt, and F. Brammer, *Performance of ONSI PC25 PAFC cogeneration plant.* International Journal of Hydrogen Energy, 1998. **23**(1): p. 53-56. https://doi.org/10.1016/S0360-3199(97)00029-3.
36. A. Dicks and A. Siddle, *Assessment of commercial prospects of molten carbonate fuel cells.* Journal of Power Sources, 2000. **86**(1): p. 316-323. https://doi.org/10.1016/S0378-7753(99)00449-8.
37. A. Torazza, A. Dufour, A. Perfumo, A. Ricerche, J. Gegundez, F. Sanson, and A. Moreno, *MOLCARE development towards MCFC commercial power plants based on 500 kW standard modules*. 1998, United States: PennWell Conferences and Exhibitions.
38. T. Ishikawa and H. Yasue, *Start-up, testing and operation of 1000 kW class MCFC power plant.* Journal of Power Sources, 2000. **86**(1): p. 145-150. https://doi.org/10.1016/S0378-7753(99)00446-2.
39. O.Z. Sharaf and M.F. Orhan, *An overview of fuel cell technology: Fundamentals and applications.* Renewable & Sustainable Energy Reviews, 2014. **32**: p. 810-853. https://doi.org/10.1016/j.rser.2014.01.012.
40. S. Mekhilef, R. Saidur, and A. Safari, *Comparative study of different fuel cell technologies.* Renewable and Sustainable Energy Reviews, 2012. **16**(1): p. 981-989. https://doi.org/10.1016/j.rser.2011.09.020.
41. P. Zegers, *Fuel cell commercialization: The key to a hydrogen economy.* Journal of Power Sources, 2006. **154**(2): p. 497-502. https://doi.org/10.1016/j.jpowsour.2005.10.051.
42. J.H.J.S. Thijssen and W.P. Teagan, *Long-Term Prospects for PEMFC and SOFC in Vehicle Applications.* SAE Transactions, 2002. **111**: p. 840-853.
43. A. Alaswad, A. Palumbo, M. Dassisti, and A.G. Olabi, *Fuel Cell Technologies, Applications, and State of the Art. A Reference Guide*, in *Reference Module in Materials Science and Materials Engineering*. 2016, Elsevier. https://doi.org/10.1016/B978-0-12-803581-8.04009-1.
44. N.H. Behling, *Chapter 2 - Fuel Cells and the Challenges Ahead*, in *Fuel Cells*, N.H. Behling, Editor. 2013, Elsevier. p. 7-36. https://doi.org/10.1016/B978-0-444-56325-5.00002-8.
45. K. Huang, *8 - Solid oxide fuel cells*, in *Materials for Fuel Cells*, M. Gasik, Editor. 2008, Woodhead Publishing. p. 280-343. https://doi.org/10.1533/9781845694838.280.
46. B. Timurkutluk, C. Timurkutluk, M.D. Mat, and Y. Kaplan, *A review on cell/stack designs for high performance solid oxide fuel cells.* Renewable & Sustainable Energy Reviews, 2016. **56**: p. 1101-1121. https://doi.org/10.1016/j.rser.2015.12.034.
47. P. Kofstad and R. Bredesen, *High temperature corrosion in SOFC environments.* Solid State Ionics, 1992. **52**(1): p. 69-75. https://doi.org/10.1016/0167-2738(92)90092-4.
48. K. Ke, A. Gunji, H. Mori, S. Tsuchida, H. Takahashi, K. Ukai, Y. Mizutani, H. Sumi, M. Yokoyama, and K. Waki, *Effect of oxide on carbon deposition behavior of CH4 fuel on Ni/ScSZ cermet anode in high temperature SOFCs.* Solid State Ionics, 2006. **177**(5): p. 541-547. https://doi.org/10.1016/j.ssi.2005.12.009.
49. A. Musa and M. De Paepe, *Performance of combined internally reformed intermediate/high temperature SOFC cycle compared to internally reformed two-staged intermediate temperature SOFC cycle.* International Journal of Hydrogen Energy, 2008. **33**(17): p. 4665-4672. https://doi.org/10.1016/j.ijhydene.2008.05.093.
50. D.J.L. Brett, A. Atkinson, N.P. Brandon, and S.J. Skinner, *Intermediate temperature solid oxide fuel cells.* Chemical Society Reviews, 2008. **37**(8): p. 1568-1578. https://doi.org/10.1039/b612060c.
51. H.J. Hwang, J.-W. Moon, S. Lee, and E.A. Lee, *Electrochemical performance of LSCF-based composite cathodes for intermediate temperature SOFCs.* Journal of Power Sources, 2005. **145**(2): p. 243-248. https://doi.org/10.1016/j.jpowsour.2005.02.063.
52. T. Papadam, G. Goula, and I.V. Yentekakis, *Long-term operation stability tests of intermediate and high temperature Ni-based anodes' SOFCs directly fueled with simulated biogas mixtures.* International Journal of Hydrogen Energy, 2012. **37**(21): p. 16680-16685. https://doi.org/10.1016/j.ijhydene.2012.02.147.

53. J.P.P. Huijsmans, F.P.F. van Berkel, and G.M. Christie, *Intermediate temperature SOFC – a promise for the 21st century.* Journal of Power Sources, 1998. **71**(1): p. 107-110. https://doi.org/10.1016/S0378-7753(97)02789-4.
54. J. Huang, F. Xie, C. Wang, and Z. Mao, *Development of solid oxide fuel cell materials for intermediate-to-low temperature operation.* International Journal of Hydrogen Energy, 2012. **37**(1): p. 877-883. https://doi.org/10.1016/j.ijhydene.2011.04.030.
55. D. Penchini, G. Cinti, G. Discepoli, E. Sisani, and U. Desideri, *Characterization of a 100 W SOFC stack fed by carbon monoxide rich fuels.* International Journal of Hydrogen Energy, 2013. **38**(1): p. 525-531. https://doi.org/10.1016/j.ijhydene.2012.09.060.
56. Y. Inui, A. Urata, N. Ito, T. Nakajima, and T. Tanaka, *Performance simulation of planar SOFC using mixed hydrogen and carbon monoxide gases as fuel.* Energy Conversion and Management, 2006. **47**(13): p. 1738-1747. https://doi.org/10.1016/j.enconman.2005.10.014.
57. B. Stoeckl, V. Subotić, M. Preininger, H. Schroettner, and C. Hochenauer, *SOFC operation with carbon oxides: Experimental analysis of performance and degradation.* Electrochimica Acta, 2018. **275**: p. 256-264. https://doi.org/10.1016/j.electacta.2018.04.036.
58. C. Lu, W.L. Worrell, R.J. Gorte, and J.M. Vohs, *SOFCs for Direct Oxidation of Hydrocarbon Fuels with Samaria-Doped Ceria Electrolyte.* Journal of the Electrochemical Society, 2003. **150**(3): p. A354. https://doi.org/10.1149/1.1553765.
59. F. Dogan, *Solid-Oxide Fuel Cells Operating with Direct-Alcohol and Hydrocarbon Fuels*. Alcoholic Fuels, ed. S. Minteer. Vol. 112. 2006, Boca Raton: Crc Press-Taylor & Francis Group. 203-214.
60. S. Park, J.M. Vohs, and R.J. Gorte, *Direct oxidation of hydrocarbons in a solid-oxide fuel cell.* Nature, 2000. **404**(6775): p. 265-7. https://doi.org/10.1038/35005040.
61. S. McIntosh and R.J. Gorte, *Direct hydrocarbon solid oxide fuel cells.* Chemical Reviews, 2004. **104**(10): p. 4845-4865. https://doi.org/10.1021/cr020725g.
62. A. Fuerte, R.X. Valenzuela, M.J. Escudero, and L. Daza, *Ammonia as efficient fuel for SOFC.* Journal of Power Sources, 2009. **192**(1): p. 170-174. https://doi.org/10.1016/j.jpowsour.2008.11.037.
63. A. Afif, N. Radenahmad, Q. Cheok, S. Shams, J.H. Kim, and A.K. Azad, *Ammonia-fed fuel cells: a comprehensive review.* Renewable and Sustainable Energy Reviews, 2016. **60**: p. 822-835. https://doi.org/10.1016/j.rser.2016.01.120.
64. Q. Ma, J. Ma, S. Zhou, R. Yan, J. Gao, and G. Meng, *A high-performance ammonia-fueled SOFC based on a YSZ thin-film electrolyte.* Journal of Power Sources, 2007. **164**(1): p. 86-89. https://doi.org/10.1016/j.jpowsour.2006.09.093.
65. Q. Ma, R. Peng, Y. Lin, J. Gao, and G. Meng, *A high-performance ammonia-fueled solid oxide fuel cell.* Journal of Power Sources, 2006. **161**(1): p. 95-98. https://doi.org/10.1016/j.jpowsour.2006.04.099.
66. J. Liu and S.A. Barnett, *Operation of anode-supported solid oxide fuel cells on methane and natural gas.* Solid State Ionics, 2003. **158**(1): p. 11-16. https://doi.org/10.1016/S0167-2738(02)00769-5.
67. T.A. Adams and P.I. Barton, *High-efficiency power production from natural gas with carbon capture.* Journal of Power Sources, 2010. **195**(7): p. 1971-1983. https://doi.org/10.1016/j.jpowsour.2009.10.046.
68. M. Noponen, M. Halinen, J. Kiviaho, and J. Saarinen, *Feasibility of autothermally reformed natural gas on anode supported solid oxide fuel cells.* Journal of Fuel Cell Science and Technology, 2006. **3**(4): p. 438-444. https://doi.org/10.1115/1.2349526.
69. Y. Shiratori, T. Ijichi, T. Oshima, and K. Sasaki, *Internal reforming SOFC running on biogas.* International Journal of Hydrogen Energy, 2010. **35**(15): p. 7905-7912. https://doi.org/10.1016/j.ijhydene.2010.05.064.
70. J. Staniforth and K. Kendall, *Biogas powering a small tubular solid oxide fuel cell.* Journal of Power Sources, 1998. **71**(1-2): p. 275-277. https://doi.org/10.1016/s0378-7753(97)02762-6.

71. J. Staniforth and R.M. Ormerod, *Implications for Using Biogas as a Fuel Source for Solid Oxide Fuel Cells: Internal Dry Reforming in a Small Tubular Solid Oxide Fuel Cell.* Catalysis Letters, 2002. **81**(1): p. 19-23. https://doi.org/10.1023/a:1016000519280.
72. J. Staniforth and R.M. Ormerod, *Running solid oxide fuel cells on biogas.* Ionics, 2003. **9**(5): p. 336-341. https://doi.org/10.1007/bf02376583.
73. G. D'Andrea, M. Gandiglio, A. Lanzini, and M. Santarelli, *Dynamic model with experimental validation of a biogas-fed SOFC plant.* Energy Conversion and Management, 2017. **135**: p. 21-34. https://doi.org/10.1016/j.enconman.2016.12.063.
74. K. Nikooyeh, R. Clemmer, V. Alzate-Restrepo, and J.M. Hill, *Effect of hydrogen on carbon formation on Ni/YSZ composites exposed to methane.* Applied Catalysis A: General, 2008. **347**(1): p. 106-111. https://doi.org/10.1016/j.apcata.2008.06.005.
75. M.J. Escudero, I. Gómez de Parada, A. Fuerte, and J.L. Serrano, *Analysis of the electrochemical performance of MoNi–CeO2 cermet as anode material for solid oxide fuel cell. Part I. H2, CH4 and H2/CH4 mixtures as fuels.* Journal of Power Sources, 2014. **253**: p. 64-73. https://doi.org/10.1016/j.jpowsour.2013.12.027.
76. G. Almutairi, A. Dhir, and W. Bujalski, *Direct Operation of IP-Solid Oxide Fuel Cell with Hydrogen and Methane Fuel Mixtures under Current Load Cycle Operating Condition.* Fuel Cells, 2014. **14**(2): p. 231-238. https://doi.org/10.1002/fuce.201300096.
77. Z. Chen, L. Bian, L. Wang, N. Chen, H. Zhao, F. Li, and K. Chou, *Effect of hydrogen and carbon dioxide on the performance of methane fueled solid oxide fuel cell.* International Journal of Hydrogen Energy, 2016. **41**(18): p. 7453-7463. https://doi.org/10.1016/j.ijhydene.2016.03.090.
78. G. Cinti, G. Bidini, and K. Hemmes, *Comparison of the solid oxide fuel cell system for micro CHP using natural gas with a system using a mixture of natural gas and hydrogen.* Applied Energy, 2019. **238**: p. 69-77. https://doi.org/10.1016/j.apenergy.2019.01.039.
79. O. Razbani and M. Assadi, *Performance of a biohydrogen solid oxide fuel cell.* International Journal of Hydrogen Energy, 2013. **38**(31): p. 13781-13791. https://doi.org/10.1016/j.ijhydene.2013.08.061.
80. P. Leone, A. Lanzini, M. Santarelli, M. Cali, F. Sagnelli, A. Boulanger, A. Scaletta, and P. Zitella, *Methane-free biogas for direct feeding of solid oxide fuel cells.* Journal of Power Sources, 2010. **195**(1): p. 239-248. https://doi.org/10.1016/j.jpowsour.2009.06.108.
81. P. Leone, A. Lanzini, M. Santarelli, P. Zitella, and M. Calì Quaglia, *Feasibility of SOFC Operation with Bio-Methane and Bio-Hydrogen from Anaerobic Digestion.* ECS Transactions, 2009. **17**(1): p. 185-195. https://doi.org/10.1149/1.3142748.
82. E.P. Reznicek and R.J. Braun, *Reversible solid oxide cell systems for integration with natural gas pipeline and carbon capture infrastructure for grid energy management.* Applied Energy, 2020. **259**: p. 114118. https://doi.org/10.1016/j.apenergy.2019.114118.
83. S. Sengodan, R. Lan, J. Humphreys, D. Du, W. Xu, H. Wang, and S. Tao, *Advances in reforming and partial oxidation of hydrocarbons for hydrogen production and fuel cell applications.* Renewable and Sustainable Energy Reviews, 2018. **82**: p. 761-780. https://doi.org/10.1016/j.rser.2017.09.071.
84. K. Kendall, C.M. Finnerty, G. Saunders, and J.T. Chung, *Effects of dilution on methane entering an SOFC anode.* Journal of Power Sources, 2002. **106**(1-2): p. 323-327. https://doi.org/10.1016/s0378-7753(01)01066-7.
85. K. Sasaki, K. Haga, T. Yoshizumi, D. Minematsu, E. Yuki, R.-R. Liu, C. Uryu, T. Oshima, S. Taniguchi, Y. Shiratori, and K. Ito, *Impurity Poisoning of SOFCs.* ECS Transactions, 2019. **35**(1): p. 2805-2814. https://doi.org/10.1149/1.3570280.
86. Y. Matsuzaki and I. Yasuda, *The poisoning effect of sulfur-containing impurity gas on a SOFC anode: Part I. Dependence on temperature, time, and impurity concentration.* Solid State Ionics, 2000. **132**(3–4): p. 261-269. https://doi.org/10.1016/S0167-2738(00)00653-6.
87. S.A. Saadabadi, A. Thallam Thattai, L. Fan, R.E.F. Lindeboom, H. Spanjers, and P.V. Aravind, *Solid Oxide Fuel Cells fuelled with biogas: Potential and constraints.*

Renewable Energy, 2019. **134**: p. 194-214. https://doi.org/10.1016/j.renene.2018.11.028.
88. A. Lanzini and P. Leone, *Experimental investigation of direct internal reforming of biogas in solid oxide fuel cells.* International Journal of Hydrogen Energy, 2010. **35**(6): p. 2463-2476. https://doi.org/10.1016/j.ijhydene.2009.12.146.
89. A. Hauch, S.D. Ebbesen, S.H. Jensen, and M. Mogensen, *Highly efficient high temperature electrolysis.* Journal of Materials Chemistry, 2008. **18**(20): p. 2331-2340. https://doi.org/10.1039/B718822F.
90. L. Bi, S. Boulfrad, and E. Traversa, *Steam electrolysis by solid oxide electrolysis cells (SOECs) with proton-conducting oxides.* Chem Soc Rev, 2014. **43**(24): p. 8255-70. https://doi.org/10.1039/c4cs00194j.
91. A. Brisse, J. Schefold, and M. Zahid, *High temperature water electrolysis in solid oxide cells.* International Journal of Hydrogen Energy, 2008. **33**(20): p. 5375-5382. https://doi.org/10.1016/j.ijhydene.2008.07.120.
92. C.M. Stoots, J.E. O'Brien, K. Condie, L. Moore-McAteer, G. Housley, J.J. Hartvigsen, and J.S. Herring, *The High-Temperature Electrolysis Integrated Laboratory-Scale Experiment.* Nuclear Technology, 2009. **166**(1): p. 32-42. https://doi.org/10.13182/NT09-A6966.
93. J.B. Hansen, *Solid oxide electrolysis – a key enabling technology for sustainable energy scenarios.* Faraday Discussions, 2015. **182**(0): p. 9-48. https://doi.org/10.1039/C5FD90071A.
94. L. Ye and K. Xie, *High-temperature electrocatalysis and key materials in solid oxide electrolysis cells.* Journal of Energy Chemistry, 2021. **54**: p. 736-745. https://doi.org/10.1016/j.jechem.2020.06.050.
95. X. Chen, C. Guan, G. Xiao, X. Du, and J.-Q. Wang, *Syngas production by high temperature steam/CO2 coelectrolysis using solid oxide electrolysis cells.* Faraday Discussions, 2015. **182**(0): p. 341-351. https://doi.org/10.1039/C5FD00017C.
96. V.N. Nguyen and L. Blum, *Syngas and Synfuels from H2O and CO2: Current Status.* Chemie Ingenieur Technik, 2015. **87**(4): p. 354-375. https://doi.org/10.1002/cite.201400090.
97. S.H. Jensen, P.H. Larsen, and M. Mogensen, *Hydrogen and synthetic fuel production from renewable energy sources.* International Journal of Hydrogen Energy, 2007. **32**(15): p. 3253-3257. https://doi.org/10.1016/j.ijhydene.2007.04.042.
98. R.D. Green, C.-C. Liu, and S.B. Adler, *Carbon dioxide reduction on gadolinia-doped ceria cathodes.* Solid State Ionics, 2008. **179**(17): p. 647-660. https://doi.org/10.1016/j.ssi.2008.04.024.
99. F. Bidrawn, G. Kim, G. Corre, J.T.S. Irvine, J.M. Vohs, and R.J. Gorte, *Efficient Reduction of CO2 in a Solid Oxide Electrolyzer.* Electrochemical and Solid-State Letters, 2008. **11**(9): p. B167-B170. https://doi.org/10.1149/1.2943664.
100. S.D. Ebbesen and M. Mogensen, *Electrolysis of carbon dioxide in Solid Oxide Electrolysis Cells.* Journal of Power Sources, 2009. **193**(1): p. 349-358. https://doi.org/10.1016/j.jpowsour.2009.02.093.
101. C. Graves, S.D. Ebbesen, and M. Mogensen, *Co-electrolysis of CO2 and H2O in solid oxide cells: Performance and durability.* Solid State Ionics, 2011. **192**(1): p. 398-403. https://doi.org/10.1016/j.ssi.2010.06.014.
102. R. Xing, Y. Wang, Y. Zhu, S. Liu, and C. Jin, *Co-electrolysis of steam and CO2 in a solid oxide electrolysis cell with La0.75Sr0.25Cr0.5Mn0.5O3−δ –Cu ceramic composite electrode.* Journal of Power Sources, 2015. **274**: p. 260-264. https://doi.org/10.1016/j.jpowsour.2014.10.066.
103. M.T. Mehran, S.-B. Yu, D.-Y. Lee, J.-E. Hong, S.-B. Lee, S.-J. Park, R.-H. Song, and T.-H. Lim, *Production of syngas from H2O/CO2 by high-pressure coelectrolysis in tubular solid oxide cells.* Applied Energy, 2018. **212**: p. 759-770. https://doi.org/10.1016/j.apenergy.2017.12.078.
104. Z. Zhan, *Syngas Production By Coelectrolysis of CO2-H2O The Basis for a reneable cycle.* Energy & Fuels, 2009. **23**: p. 3089-3096.

105. S.D. Ebbesen, C. Graves, and M. Mogensen, *Production of Synthetic Fuels by Co-Electrolysis of Steam and Carbon Dioxide.* International Journal of Green Energy, 2009. **6**(6): p. 646-660. https://doi.org/10.1080/15435070903372577.
106. A.O. Isenberg, *Energy conversion via solid oxide electrolyte electrochemical cells at high temperatures.* Solid State Ionics, 1981. **3-4**: p. 431-437. https://doi.org/10.1016/0167-2738(81)90127-2.
107. R. Küngas, P. Blennow, T. Heiredal-Clausen, T. Holt Nørby, J. Rass-Hansen, J.B. Hansen, and P.G. Moses, *Progress in SOEC Development Activities at Haldor Topsøe.* ECS Transactions, 2019. **91**(1): p. 215-223. https://doi.org/10.1149/09101.0215ecst.
108. J.P. Stempien, O.L. Ding, Q. Sun, and S.H. Chan, *Energy and exergy analysis of Solid Oxide Electrolyser Cell (SOEC) working as a CO2 mitigation device.* International Journal of Hydrogen Energy, 2012. **37**(19): p. 14518-14527. https://doi.org/10.1016/j.ijhydene.2012.07.065.
109. C. Schlitzberger, N.O. Brinkmeier, and R. Leithner, *CO2 Capture in SOFC by Vapor Condensation and CH4 Production in SOEC Storing Excess Electricity.* Chemical Engineering & Technology, 2012. **35**(3): p. 440-444. https://doi.org/10.1002/ceat.201100464.
110. O. Posdziech, K. Schwarze, and J. Brabandt, *Efficient hydrogen production for industry and electricity storage via high-temperature electrolysis.* International Journal of Hydrogen Energy, 2019. **44**(35): p. 19089-19101. https://doi.org/10.1016/j.ijhydene.2018.05.169.
111. J.E. O'Brien, J.L. Hartvigsen, R.D. Boardman, J.J. Hartvigsen, D. Larsen, and S. Elangovan, *A 25 kW high temperature electrolysis facility for flexible hydrogen production and system integration studies.* International Journal of Hydrogen Energy, 2020. **45**(32): p. 15796-15804. https://doi.org/10.1016/j.ijhydene.2020.04.074.
112. H.F. Zhang, L.G. Wang, F. Marechal, and U. Desideri, *Solid-oxide electrolyzer coupled biomass-to-methanol systems*, in *Innovative Solutions for Energy Transitions*, J. Yan, *et al.*, Editors. 2019, Elsevier Science Bv: Amsterdam. p. 4548-4553. https://doi.org/10.1016/j.egypro.2019.01.755.
113. P. Kim-Lohsoontorn and J. Bae, *Electrochemical performance of solid oxide electrolysis cell electrodes under high-temperature coelectrolysis of steam and carbon dioxide.* Journal of Power Sources, 2011. **196**(17): p. 7161-7168. https://doi.org/10.1016/j.jpowsour.2010.09.018.
114. C. Stoots, J. O'Brien, and J. Hartvigsen, *Results of recent high temperature coelectrolysis studies at the Idaho National Laboratory.* International Journal of Hydrogen Energy, 2009. **34**(9): p. 4208-4215. https://doi.org/10.1016/j.ijhydene.2008.08.029.
115. Y. Shi, Y. Luo, N. Cai, J. Qian, S. Wang, W. Li, and H. Wang, *Experimental characterization and modeling of the electrochemical reduction of CO2 in solid oxide electrolysis cells.* Electrochimica Acta, 2013. **88**: p. 644-653. https://doi.org/10.1016/j.electacta.2012.10.107.
116. Y. Zheng, J. Wang, B. Yu, W. Zhang, J. Chen, J. Qiao, and J. Zhang, *A review of high temperature co-electrolysis of H2O and CO2 to produce sustainable fuels using solid oxide electrolysis cells (SOECs): advanced materials and technology.* Chem Soc Rev, 2017. **46**(5): p. 1427-1463. https://doi.org/10.1039/c6cs00403b.
117. A. Hankin and N. Shah, *Process exploration and assessment for the production of methanol and dimethyl ether from carbon dioxide and water.* Sustainable Energy & Fuels, 2017. **1**(7): p. 1541-1556. https://doi.org/10.1039/C7SE00206H.
118. L. Kleiminger, T. Li, K. Li, and G.H. Kelsall, *Syngas (CO-H2) production using high temperature micro-tubular solid oxide electrolysers.* Electrochimica Acta, 2015. **179**: p. 565-577. https://doi.org/10.1016/j.electacta.2015.07.062.
119. C.M. Stoots, J.E. O'Brien, J.S. Herring, and J.J. Hartvigsen, *Syngas Production via High-Temperature Coelectrolysis of Steam and Carbon Dioxide.* Journal of Fuel Cell Science and Technology, 2008. **6**(1): p. 011014-011014-12. https://doi.org/10.1115/1.2971061.

120. A. Nikitin, A. Ozersky, V. Savchenko, I. Sedov, V. Shmelev, and V. Arutyunov, *Matrix conversion of natural gas to syngas: The main parameters of the process and possible applications.* Chemical Engineering Journal, 2019. **377**: p. 7. https://doi.org/10.1016/j.cej.2019.01.162.
121. R.S. Haszeldine, *Carbon Capture and Storage: How Green Can Black Be?* Science, 2009. **325**(5948): p. 1647-1652. https://doi.org/10.1126/science.1172246.
122. D.Y.C. Leung, G. Caramanna, and M.M. Maroto-Valer, *An overview of current status of carbon dioxide capture and storage technologies.* Renewable and Sustainable Energy Reviews, 2014. **39**: p. 426-443. https://doi.org/10.1016/j.rser.2014.07.093.
123. Y.Y. Ren, M. Yu, C.F. Wu, Q.H. Wang, M. Gao, Q.Q. Huang, and Y. Liu, *A comprehensive review on food waste anaerobic digestion: Research updates and tendencies.* Bioresource Technology, 2018. **247**: p. 1069-1076. https://doi.org/10.1016/j.biortech.2017.09.109.
124. J. Massanet-Nicolau, R. Dinsdale, A. Guwy, and G. Shipley, *Utilising biohydrogen to increase methane production, energy yields and process efficiency via two stage anaerobic digestion of grass.* Bioresource Technology, 2015. **189**: p. 379-383. https://doi.org/10.1016/j.biortech.2015.03.116.
125. D.W. Liu, D.P. Liu, R.J. Zeng, and I. Angelidaki, *Hydrogen and methane production from household solid waste in the two-stage fermentation process.* Water Research, 2006. **40**(11): p. 2230-2236. https://doi.org/10.1016/j.watres.2006.03.029.
126. Y. Luo, Y. Shi, W. Li, M. Ni, and N. Cai, *Elementary reaction modeling and experimental characterization of solid oxide fuel-assisted steam electrolysis cells.* International Journal of Hydrogen Energy, 2014. **39**(20): p. 10359-10373. https://doi.org/10.1016/j.ijhydene.2014.05.018.
127. H.R. Xu, B. Chen, J. Irvine, and M. Ni, *Modeling of CH4-assisted SOEC for H2O/CO2 co-electrolysis.* International Journal of Hydrogen Energy, 2016. **41**(47): p. 21839-21849. https://doi.org/10.1016/j.ijhydene.2016.10.026.
128. Y. Wang, T. Liu, L.B. Lei, and F.L. Chen, *Methane assisted solid oxide co-electrolysis process for syngas production.* Journal of Power Sources, 2017. **344**: p. 119-127. https://doi.org/10.1016/j.jpowsour.2017.01.096.
129. J. Martinez-Frias, A.-Q. Pham, and S. M. Aceves, *A natural gas-assisted steam electrolyzer for high-efficiency production of hydrogen.* International Journal of Hydrogen Energy, 2003. **28**(5): p. 483-490. https://doi.org/10.1016/S0360-3199(02)00135-0.
130. W. Wang, J.M. Vohs, and R.J. Gorte, *Hydrogen Production Via CH4 and CO Assisted Steam Electrolysis.* Topics in Catalysis, 2007. **46**(3): p. 380-385. https://doi.org/10.1007/s11244-007-9005-8.
131. W. Wang, R.J. Gorte, and J.M. Vohs, *Analysis of the performance of the electrodes in a natural gas assisted steam electrolysis cell.* Chemical Engineering Science, 2008. **63**(3): p. 765-769. https://doi.org/10.1016/j.ces.2007.10.026.
132. A.D. James Larminie, *Operational Fuel Cell Voltages*, in *Fuel Cell Systems Explained*. 2003. p. 45-66. https://doi.org/10.1002/9781118878330.ch3.
133. R.P. Iczkowski and M.B. Cutlip, *Voltage Losses in Fuel Cell Cathodes.* Journal of the Electrochemical Society, 1980. **127**(7): p. 1433-1440. https://doi.org/10.1149/1.2129925.
134. H. Huang, M. Nakamura, P. Su, R. Fasching, Y. Saito, and F.B. Prinz, *High-Performance Ultrathin Solid Oxide Fuel Cells for Low-Temperature Operation.* Journal of the Electrochemical Society, 2007. **154**(1): p. B20. https://doi.org/10.1149/1.2372592.
135. S.H. Chan and Z.T. Xia, *Polarization effects in electrolyte/electrode-supported solid oxide fuel cells.* Journal of Applied Electrochemistry, 2002. **32**(3): p. 339-347. https://doi.org/10.1023/A:1015593326549.
136. E.D. Wachsman and K.T. Lee, *Lowering the Temperature of Solid Oxide Fuel Cells.* Science, 2011. **334**(6058): p. 935. https://doi.org/10.1126/science.1204090.
137. J.W. Fergus, *Electrolytes for solid oxide fuel cells.* Journal of Power Sources, 2006. **162**(1): p. 30-40. https://doi.org/10.1016/j.jpowsour.2006.06.062.

138. T. Tsai and S.A. Barnett, *Increased solid-oxide fuel cell power density using interfacial ceria layers.* Solid State Ionics, 1997. **98**(3): p. 191-196. https://doi.org/10.1016/S0167-2738(97)00113-6.
139. S.A. Inc. *Scribner*. 2017 [cited 2021 01/05/2021]; Available from: https://www.scribner.com/.
140. M.A. Laguna-Bercero, *Recent advances in high temperature electrolysis using solid oxide fuel cells: A review.* Journal of Power Sources, 2012. **203**: p. 4-16. https://doi.org/10.1016/j.jpowsour.2011.12.019.
141. A.J. Jacobson, *Materials for Solid Oxide Fuel Cells.* Chemistry of Materials, 2010. **22**(3): p. 660-674. https://doi.org/10.1021/cm902640j.
142. X.J. Chen, K.A. Khor, S.H. Chan, and L.G. Yu, *Influence of microstructure on the ionic conductivity of yttria-stabilized zirconia electrolyte.* Materials Science and Engineering: A, 2002. **335**(1): p. 246-252. https://doi.org/10.1016/S0921-5093(01)01935-9.
143. Q. Zhu and B. Fan, *Low temperature sintering of 8YSZ electrolyte film for intermediate temperature solid oxide fuel cells.* Solid State Ionics, 2005. **176**(9): p. 889-894. https://doi.org/10.1016/j.ssi.2004.12.010.
144. M. Gaudon, E. Djurado, and N.H. Menzler, *Morphology and sintering behaviour of yttria stabilised zirconia (8-YSZ) powders synthesised by spray pyrolysis.* Ceramics International, 2004. **30**(8): p. 2295-2303. https://doi.org/10.1016/j.ceramint.2004.01.010.
145. D. Fray. *Fuel Cells*. 2006; Available from: https://www.doitpoms.ac.uk/tlplib/fuel-cells/printall.php.
146. Y.-M. Yin, M.-W. Xiong, N.-T. Yang, Z. Tong, Y.-Q. Guo, Z.-F. Ma, E. Sun, J. Yamanis, and B.-Y. Jing, *Investigation on thermal, electrical, and electrochemical properties of scandium-doped Pr0.6Sr0.4(Co0.2Fe0.8)(1−x)ScxO3−δ as cathode for IT-SOFC.* International Journal of Hydrogen Energy, 2011. **36**(6): p. 3989-3996. https://doi.org/10.1016/j.ijhydene.2010.12.113.
147. R. Pornprasertsuk, P. Ramanarayanan, C.B. Musgrave, and F.B. Prinz, *Predicting ionic conductivity of solid oxide fuel cell electrolyte from first principles.* Journal of Applied Physics, 2005. **98**(10): p. 103513. https://doi.org/10.1063/1.2135889.
148. J.T.S. Irvine, J.W.L. Dobson, T. Politova, S. García Martín, and A. Shenouda, *Co-doping of scandia–zirconia electrolytes for SOFCs.* Faraday Discuss., 2007. **134**: p. 41-49. https://doi.org/10.1039/b604441g.
149. D. Lee, I. Lee, Y. Jeon, and R. Song, *Characterization of scandia stabilized zirconia prepared by glycine nitrate process and its performance as the electrolyte for IT-SOFC.* Solid State Ionics, 2005. **176**(11): p. 1021-1025. https://doi.org/10.1016/j.ssi.2005.01.004.
150. T.I. Politova and J.T.S. Irvine, *Investigation of scandia–yttria–zirconia system as an electrolyte material for intermediate temperature fuel cells—influence of yttria content in system (Y2O3)x(Sc2O3)(11−x)(ZrO2)89.* Solid State Ionics, 2004. **168**(1): p. 153-165. https://doi.org/10.1016/j.ssi.2004.02.007.
151. C. Haering, A. Roosen, H. Schichl, and M. Schnöller, *Degradation of the electrical conductivity in stabilised zirconia system: Part II: Scandia-stabilised zirconia.* Solid State Ionics, 2005. **176**(3): p. 261-268. https://doi.org/10.1016/j.ssi.2004.07.039.
152. C. Varanasi, C. Juneja, C. Chen, and B. Kumar, *Electrical conductivity enhancement in heterogeneously doped scandia-stabilized zirconia.* Journal of Power Sources, 2005. **147**(1): p. 128-135. https://doi.org/10.1016/j.jpowsour.2005.01.028.
153. Z. Lei and Q. Zhu, *Low temperature processing of dense nanocrystalline scandia-doped zirconia (ScSZ) ceramics.* Solid State Ionics, 2005. **176**(37): p. 2791-2797. https://doi.org/10.1016/j.ssi.2005.09.005.
154. M. Irshad, K. Siraj, R. Raza, F. Javed, M. Ahsan, I. Shakir, and M.S. Rafique, *High performance of SDC and GDC core shell type composite electrolytes using methane as a fuel for low temperature SOFC.* AIP Advances, 2016. **6**(2): p. 025202. https://doi.org/10.1063/1.4941676.
155. R. Maric, S. Seward, P.W. Faguy, and M. Oljaca, *Electrolyte Materials for Intermediate Temperature Fuel Cells Produced via Combustion Chemical Vapor Condensation.*

Electrochemical and Solid-State Letters, 2003. **6**(5): p. A91. https://doi.org/10.1149/1.1562071.
156. J. Huang, Z. Mao, Z. Liu, and C. Wang, *Performance of fuel cells with proton-conducting ceria-based composite electrolyte and nickel-based electrodes.* Journal of Power Sources, 2008. **175**(1): p. 238-243. https://doi.org/10.1016/j.jpowsour.2007.09.018.
157. S. Wang, T. Kato, S. Nagata, T. Kaneko, N. Iwashita, T. Honda, and M. Dokiya, *Electrodes and performance analysis of a ceria electrolyte SOFC.* Solid State Ionics, 2002. **152-153**: p. 477-484. https://doi.org/10.1016/S0167-2738(02)00376-4.
158. K. Huang and J.B. Goodenough, *A solid oxide fuel cell based on Sr- and Mg-doped LaGaO3 electrolyte: the role of a rare-earth oxide buffer.* Journal of Alloys and Compounds, 2000. **303-304**: p. 454-464. https://doi.org/10.1016/S0925-8388(00)00626-5.
159. S. Kim, M.C. Chun, K.T. Lee, and H.L. Lee, *Oxygen-ion conductivity of BaO- and MgO-doped LaGaO3 electrolytes.* Journal of Power Sources, 2001. **93**(1): p. 279-284. https://doi.org/10.1016/S0378-7753(00)00567-X.
160. Sigma-Aldrich. *Solid Oxide Fuel Cell Materials*. [cited 2018 20/01/2018]; Available from: https://www.sigmaaldrich.com/materials-science/material-science-products.html?TablePage=105700873.
161. T.S. Zhang, J. Ma, L.B. Kong, P. Hing, and J.A. Kilner, *Preparation and mechanical properties of dense Ce0.8Gd0.2O2−δ ceramics.* Solid State Ionics, 2004. **167**(1): p. 191-196. https://doi.org/10.1016/j.ssi.2003.11.025.
162. N.P. Brandon, S. Skinner, and B.C.H. Steele, *Recent advances in materials for fuel cells.* Annual Review of Materials Research, 2003. **33**: p. 183-213. https://doi.org/10.1146/annurev.matsci.33.022802.094122.
163. P. Tanasini, M. Cannarozzo, P. Costamagna, A. Faes, J. Van Herle, A. Hessler-Wyser, and C. Comninellis, *Experimental and Theoretical Investigation of Degradation Mechanisms by Particle Coarsening in SOFC Electrodes.* Fuel Cells, 2009. **9**(5): p. 740-752. https://doi.org/10.1002/fuce.200800192.
164. H.-Y. Chen, H.-C. Yu, J. Scott Cronin, J.R. Wilson, S.A. Barnett, and K. Thornton, *Simulation of coarsening in three-phase solid oxide fuel cell anodes.* Journal of Power Sources, 2011. **196**(3): p. 1333-1337. https://doi.org/10.1016/j.jpowsour.2010.08.010.
165. F. Abdeljawad and M. Haataja, *Microstructural coarsening effects on redox instability and mechanical damage in solid oxide fuel cell anodes.* Journal of Applied Physics, 2013. **114**(18): p. 183519. https://doi.org/10.1063/1.4830015.
166. R.J. Gorte, J.M. Vohs, and S. McIntosh, *Recent developments on anodes for direct fuel utilization in SOFC.* Solid State Ionics, 2004. **175**(1): p. 1-6. https://doi.org/10.1016/j.ssi.2004.09.036.
167. M. Gong, X. Liu, J. Trembly, and C. Johnson, *Sulfur-tolerant anode materials for solid oxide fuel cell application.* Journal of Power Sources, 2007. **168**(2): p. 289-298. https://doi.org/10.1016/j.jpowsour.2007.03.026.
168. J.-S. Kim, V.V. Nair, J.M. Vohs, and R.J. Gorte, *A study of the methane tolerance of LSCM–YSZ composite anodes with Pt, Ni, Pd and ceria catalysts.* Scripta Materialia, 2011. **65**(2): p. 90-95. https://doi.org/10.1016/j.scriptamat.2010.06.016.
169. A. Atkinson, S. Barnett, R.J. Gorte, J.T.S. Irvine, A.J. McEvoy, M. Mogensen, S.C. Singhal, and J. Vohs, *Advanced anodes for high-temperature fuel cells.* Nature Materials, 2004. **3**(1): p. 17-27. https://doi.org/10.1038/nmat1040.
170. T. Kim, G. Liu, M. Boaro, S.I. Lee, J.M. Vohs, R.J. Gorte, O.H. Al-Madhi, and B.O. Dabbousi, *A study of carbon formation and prevention in hydrocarbon-fueled SOFC.* Journal of Power Sources, 2006. **155**(2): p. 231-238. https://doi.org/10.1016/j.jpowsour.2005.05.001.
171. B.C.H. Steele, I. Kelly, H. Middleton, and R. Rudkin, *Oxidation of methane in solid state electrochemical reactors.* Solid State Ionics, 1988. **28-30**: p. 1547-1552. https://doi.org/10.1016/0167-2738(88)90417-1.
172. E.P. Murray, T. Tsai, and S.A. Barnett, *A direct-methane fuel cell with a ceria-based anode.* Nature, 1999. **400**(6745): p. 649-651. https://doi.org/10.1038/23220.

173. B.C.H. Steele, *Appraisal of Ce1−yGdyO2−y/2 electrolytes for IT-SOFC operation at 500°C.* Solid State Ionics, 2000. **129**(1): p. 95-110. https://doi.org/10.1016/S0167-2738(99)00319-7.
174. A. Fuerte, R.X. Valenzuela, M.J. Escudero, and L. Daza, *Effect of cobalt incorporation in copper-ceria based anodes for hydrocarbon utilisation in Intermediate Temperature Solid Oxide Fuel Cells.* Journal of Power Sources, 2011. **196**(9): p. 4324-4331. https://doi.org/10.1016/j.jpowsour.2010.12.053.
175. V.V. Kharton, F.M. Figueiredo, L. Navarro, E.N. Naumovich, A.V. Kovalevsky, A.A. Yaremchenko, A.P. Viskup, A. Carneiro, F.M.B. Marques, and J.R. Frade, *Ceria-based materials for solid oxide fuel cells.* Journal of Materials Science, 2001. **36**(5): p. 1105-1117. https://doi.org/10.1023/a:1004817506146.
176. W.Z. Zhu and S.C. Deevi, *A review on the status of anode materials for solid oxide fuel cells.* Materials Science and Engineering: A, 2003. **362**(1): p. 228-239. https://doi.org/10.1016/S0921-5093(03)00620-8.
177. J.Y. Chen, M.Z. Ouyang, P. Boldrin, A. Atkinson, and N.P. Brandon, *Understanding the Coarsening and Degradation in a Nanoscale Nickel Gadolinia-Doped-Ceria Electrode for High-Temperature Applications.* Acs Applied Materials & Interfaces, 2020. **12**(42): p. 47564-47573. https://doi.org/10.1021/acsami.0c13784.
178. J. Chen, X. Wang, P. Boldrin, N.P. Brandon, and A. Atkinson, *Hierarchical dual-porosity nanoscale nickel cermet electrode with high performance and stability.* Nanoscale, 2019. **11**(38): p. 17746-17758. https://doi.org/10.1039/C9NR06740J.
179. R.D. Cortright, R.R. Davda, and J.A. Dumesic, *Hydrogen from catalytic reforming of biomass-derived hydrocarbons in liquid water.* Nature, 2002. **418**(6901): p. 964-967. https://doi.org/10.1038/nature01009.
180. T.M. Mata, A.A. Martins, and N.S. Caetano, *Microalgae for biodiesel production and other applications: A review.* Renewable & Sustainable Energy Reviews, 2010. **14**(1): p. 217-232. https://doi.org/10.1016/j.rser.2009.07.020.
181. D.M. Alonso, J.Q. Bond, and J.A. Dumesic, *Catalytic conversion of biomass to biofuels.* Green Chemistry, 2010. **12**(9): p. 1493-1513. https://doi.org/10.1039/c004654j.
182. N.L. Panwar, S.C. Kaushik, and S. Kothari, *Role of renewable energy sources in environmental protection: A review.* Renewable & Sustainable Energy Reviews, 2011. **15**(3): p. 1513-1524. https://doi.org/10.1016/j.rser.2010.11.037.
183. P. McKendry, *Energy production from biomass (part 1): overview of biomass.* Bioresource Technology, 2002. **83**(1): p. 37-46. https://doi.org/10.1016/s0960-8524(01)00118-3.
184. P. McKendry, *Energy production from biomass (part 2): conversion technologies.* Bioresource Technology, 2002. **83**(1): p. 47-54. https://doi.org/10.1016/s0960-8524(01)00119-5.
185. C.L. Mao, Y.Z. Feng, X.J. Wang, and G.X. Ren, *Review on research achievements of biogas from anaerobic digestion.* Renewable & Sustainable Energy Reviews, 2015. **45**: p. 540-555. https://doi.org/10.1016/j.rser.2015.02.032.
186. J.X. Zhang, L.W. Mao, K. Nithya, K.C. Loh, Y.J. Dai, Y.L. He, and Y.W. Tong, *Optimizing mixing strategy to improve the performance of an anaerobic digestion waste-to-energy system for energy recovery from food waste.* Applied Energy, 2019. **249**: p. 28-36. https://doi.org/10.1016/j.apenergy.2019.04.142.
187. K. Srirangan, L. Akawi, M. Moo-Young, and C.P. Chou, *Towards sustainable production of clean energy carriers from biomass resources.* Applied Energy, 2012. **100**: p. 172-186. https://doi.org/10.1016/j.apenergy.2012.05.012.
188. S. Achinas, V. Achinas, and G.J.W. Euverink, *A Technological Overview of Biogas Production from Biowaste.* Engineering, 2017. **3**(3): p. 299-307. https://doi.org/10.1016/j.eng.2017.03.002.
189. Y. Li, Y.G. Chen, and J. Wu, *Enhancement of methane production in anaerobic digestion process: A review.* Applied Energy, 2019. **240**: p. 120-137. https://doi.org/10.1016/j.apenergy.2019.01.243.

190. A.S. Dieter Deublein, *Biogas from Waste and Renewable Resources: An Introduction, 2nd, Revised and Expanded Edition*. 2010: Wiley-VCH 578.
191. S. Shilpi, D. Lamb, N. Bolan, B. Seshadri, G. Choppala, and R. Naidu, *Waste to watt: Anaerobic digestion of wastewater irrigated biomass for energy and fertiliser production.* Journal of Environmental Management, 2019. **239**: p. 73-83. https://doi.org/10.1016/j.jenvman.2019.02.122.
192. D. Wu, L. Li, X.F. Zhao, Y. Peng, P.J. Yang, and X.Y. Peng, *Anaerobic digestion: A review on process monitoring.* Renewable & Sustainable Energy Reviews, 2019. **103**: p. 1-12. https://doi.org/10.1016/j.rser.2018.12.039.
193. J. Kainthola, A.S. Kalamdhad, and V.V. Goud, *A review on enhanced biogas production from anaerobic digestion of lignocellulosic biomass by different enhancement techniques.* Process Biochemistry, 2019. **84**: p. 81-90. https://doi.org/10.1016/j.procbio.2019.05.023.
194. R. Cozzolino, L. Lombardi, and L. Tribioli, *Use of biogas from biowaste in a solid oxide fuel cell stack: Application to an off-grid power plant.* Renewable Energy, 2017. **111**: p. 781-791. https://doi.org/10.1016/j.renene.2017.04.027.
195. J.B. Curtis, *Natural Gas*, in *World Scientific Handbook of Energy*, G.M. Crawley, Editor. 2013, World Scientific Publ Co Pte Ltd: Singapore. p. 59-81. https://doi.org/10.1142/9789814343527-0005.
196. T. Horschig, P.W.R. Adams, E. Gawel, and D. Thrän, *How to decarbonize the natural gas sector: A dynamic simulation approach for the market development estimation of renewable gas in Germany.* Applied Energy, 2018. **213**: p. 555-572. https://doi.org/10.1016/j.apenergy.2017.11.016.
197. Y.S. Gao and A.H. Wang, *Energy Consumption and Emissions Analysis of Natural Gas Exploitation*, in *Advanced Materials and Structures, Pts 1 and 2*, Y.H. Kim, Editor. 2011, Trans Tech Publications Ltd: Stafa-Zurich. p. 1525-1529. https://doi.org/10.4028/www.scientific.net/AMR.335-336.1525.
198. R.W. Howarth, *A bridge to nowhere: methane emissions and the greenhouse gas footprint of natural gas.* Energy Science & Engineering, 2014. **2**(2): p. 47-60. https://doi.org/10.1002/ese3.35.
199. I. Angelidaki, L. Treu, P. Tsapekos, G. Luo, S. Campanaro, H. Wenzel, and P.G. Kougias, *Biogas upgrading and utilization: Current status and perspectives.* Biotechnology Advances, 2018. **36**(2): p. 452-466. https://doi.org/10.1016/j.biotechadv.2018.01.011.
200. B. Bharathiraja, T. Sudharsanaa, A. Bharghavi, J. Jayamuthunagai, and R. Praveenkumar, *Biohydrogen and Biogas – An overview on feedstocks and enhancement process.* Fuel, 2016. **185**: p. 810-828. https://doi.org/10.1016/j.fuel.2016.08.030.
201. I. Ullah Khan, M. Hafiz Dzarfan Othman, H. Hashim, T. Matsuura, A.F. Ismail, M. Rezaei-DashtArzhandi, and I. Wan Azelee, *Biogas as a renewable energy fuel – A review of biogas upgrading, utilisation and storage.* Energy Conversion and Management, 2017. **150**: p. 277-294. https://doi.org/10.1016/j.enconman.2017.08.035.
202. I.N. Mohamad, R. Rohani, M.T.M. Nor, P. Claassen, M.S. Abd. Rahaman, M.S. Mastar Masdar, and M.I. Rosli, *An overview of gas-upgrading technologies for biohydrogen produced from treatment of palm oil mill effluent.* Journal of Engineering Science and Technology, 2017. **12**(3): p. 725-755.
203. S. Rasi, J. Lantela, and J. Rintala, *Trace compounds affecting biogas energy utilisation - A review*. Energy Conversion and Management, 2011. **52**(12): p. 3369-3375. https://doi.org/10.1016/j.enconman.2011.07.005.
204. E. Ryckebosch, M. Drouillon, and H. Veruaeren, *Techniques for transformation of biogas to biomethane.* Biomass & Bioenergy, 2011. **35**(5): p. 1633-1645. https://doi.org/10.1016/j.biombioe.2011.02.033.
205. D. Papurello, C. Iafrate, A. Lanzini, and M. Santarelli, *Trace compounds impact on SOFC performance: Experimental and modelling approach.* Applied Energy, 2017. **208**: p. 637-654. https://doi.org/10.1016/j.apenergy.2017.09.090.
206. J. Van herle, F. Maréchal, S. Leuenberger, Y. Membrez, O. Bucheli, and D. Favrat, *Process flow model of solid oxide fuel cell system supplied with sewage biogas.* Journal

of Power Sources, 2004. **131**(1–2): p. 127-141. https://doi.org/10.1016/j.jpowsour.2004.01.013.
207. P. Piroonlerkgul, S. Assabumrungrat, N. Laosiripojana, and A.A. Adesina, *Selection of appropriate fuel processor for biogas-fuelled SOFC system.* Chemical Engineering Journal, 2008. **140**(1): p. 341-351. https://doi.org/10.1016/j.cej.2007.10.007.
208. J. Xuan, M.K.H. Leung, D.Y.C. Leung, and M. Ni, *A review of biomass-derived fuel processors for fuel cell systems.* Renewable and Sustainable Energy Reviews, 2009. **13**(6): p. 1301-1313. https://doi.org/10.1016/j.rser.2008.09.027.
209. Y. Shiratori, T. Oshima, and K. Sasaki, *Feasibility of direct-biogas SOFC.* International Journal of Hydrogen Energy, 2008. **33**(21): p. 6316-6321. https://doi.org/10.1016/j.ijhydene.2008.07.101.
210. A. Hagen, A. Winiwarter, H. Langnickel, and G. Johnson, *SOFC Operation with Real Biogas.* Fuel Cells, 2017. **17**(6): p. 854-861. https://doi.org/10.1002/fuce.201700031.
211. J. Staniforth and K. Kendall, *Biogas powering a small tubular solid oxide fuel cell.* Journal of Power Sources, 1998. **71**(1): p. 275-277. https://doi.org/10.1016/S0378-7753(97)02762-6.
212. G.N. Prodromidis and F.A. Coutelieris, *Thermodynamic analysis of biogas fed solid oxide fuel cell power plants.* Renewable Energy, 2017. **108**: p. 1-10. https://doi.org/10.1016/j.renene.2017.02.043.
213. N. Laosiripojana and S. Assabumrungrat, *Catalytic dry reforming of methane over high surface area ceria.* Applied Catalysis B: Environmental, 2005. **60**(1): p. 107-116. https://doi.org/10.1016/j.apcatb.2005.03.001.
214. J. Kuhn and O. Kesler, *Carbon deposition thresholds on nickel-based solid oxide fuel cell anodes II. Steam:carbon ratio and current density.* Journal of Power Sources, 2015. **277**: p. 455-463. https://doi.org/10.1016/j.jpowsour.2014.07.084.
215. J.-H. Koh, Y.-S. Yoo, J.-W. Park, and H.C. Lim, *Carbon deposition and cell performance of Ni-YSZ anode support SOFC with methane fuel.* Solid State Ionics, 2002. **149**(3): p. 157-166. https://doi.org/10.1016/S0167-2738(02)00243-6.
216. L. Zhang, S.P. Jiang, H.Q. He, X.B. Chen, J. Ma, and X.C. Song, *A comparative study of H2S poisoning on electrode behavior of Ni/YSZ and Ni/GDC anodes of solid oxide fuel cells.* International Journal of Hydrogen Energy, 2010. **35**(22): p. 12359-12368. https://doi.org/10.1016/j.ijhydene.2010.08.067.
217. J.F.B. Rasmussen and A. Hagen, *The effect of H2S on the performance of Ni-YSZ anodes in solid oxide fuel cells.* Journal of Power Sources, 2009. **191**(2): p. 534-541. https://doi.org/10.1016/j.jpowsour.2009.02.001.
218. T.R. Smith, A. Wood, and V.I. Birss, *Effect of hydrogen sulfide on the direct internal reforming of methane in solid oxide fuel cells.* Applied Catalysis A: General, 2009. **354**(1): p. 1-7. https://doi.org/10.1016/j.apcata.2008.10.055.
219. K. Sasaki, K. Haga, T. Yoshizumi, D. Minematsu, E. Yuki, R. Liu, C. Uryu, T. Oshima, T. Ogura, Y. Shiratori, K. Ito, M. Koyama, and K. Yokomoto, *Chemical durability of Solid Oxide Fuel Cells: Influence of impurities on long-term performance.* Journal of Power Sources, 2011. **196**(22): p. 9130-9140. https://doi.org/10.1016/j.jpowsour.2010.09.122.
220. K. Haga, S. Adachi, Y. Shiratori, K. Itoh, and K. Sasaki, *Poisoning of SOFC anodes by various fuel impurities.* Solid State Ionics, 2008. **179**(27-32): p. 1427-1431. https://doi.org/10.1016/j.ssi.2008.02.062.
221. J.F.B. Rasmussen and A. Hagen, *The effect of H2S on the performance of Ni–YSZ anodes in solid oxide fuel cells.* Journal of Power Sources, 2009. **191**(2): p. 534-541. https://doi.org/10.1016/j.jpowsour.2009.02.001.
222. S. Park, J.M. Vohs, and R.J. Gorte, *Direct oxidation of hydrocarbons in a solid-oxide fuel cell.* Nature, 2000. **404**(6775): p. 265-267. https://doi.org/10.1038/35005040.
223. H. Madi, S. Diethelm, C. Ludwig, and J. Van Herle, *Organic-sulfur poisoning of solid oxide fuel cell operated on bio-syngas.* International Journal of Hydrogen Energy, 2016. **41**(28): p. 12231-12241. https://doi.org/10.1016/j.ijhydene.2016.06.014.

224. M. Ni, *Is steam addition necessary for the landfill gas fueled solid oxide fuel cells?* International Journal of Hydrogen Energy, 2013. **38**(36): p. 16373-16386. https://doi.org/10.1016/j.ijhydene.2013.10.006.
225. X. Zhu, P. Huo, Y.-p. Zhang, D.-g. Cheng, and C.-j. Liu, *Structure and reactivity of plasma treated Ni/Al2O3 catalyst for CO2 reforming of methane.* Applied Catalysis B: Environmental, 2008. **81**(1): p. 132-140. https://doi.org/10.1016/j.apcatb.2007.11.042.
226. F. Gallucci, S. Tosti, and A. Basile, *Pd–Ag tubular membrane reactors for methane dry reforming: A reactive method for CO2 consumption and H2 production.* Journal of Membrane Science, 2008. **317**(1): p. 96-105. https://doi.org/10.1016/j.memsci.2007.03.058.
227. C. Guerra, A. Lanzini, P. Leone, M. Santarelli, and D. Beretta, *Experimental study of dry reforming of biogas in a tubular anode-supported solid oxide fuel cell.* International Journal of Hydrogen Energy, 2013. **38**(25): p. 10559-10566. https://doi.org/10.1016/j.ijhydene.2013.06.074.
228. A. Lanzini, P. Leone, C. Guerra, F. Smeacetto, N.P. Brandon, and M. Santarelli, *Durability of anode supported Solid Oxides Fuel Cells (SOFC) under direct dry-reforming of methane.* Chemical Engineering Journal, 2013. **220**: p. 254-263. https://doi.org/10.1016/j.cej.2013.01.003.
229. G.B. Johnson, P. Hjalmarsson, K. Norrman, U.S. Ozkan, and A. Hagen, *Biogas Catalytic Reforming Studies on Nickel-Based Solid Oxide Fuel Cell Anodes.* Fuel Cells, 2016. **16**(2): p. 219-234. https://doi.org/10.1002/fuce.201500179.
230. C.J. Laycock, J.Z. Staniforth, and R.M. Ormerod, *Biogas as a fuel for solid oxide fuel cells and synthesis gas production: effects of ceria-doping and hydrogen sulfide on the performance of nickel-based anode materials.* Dalton Transactions, 2011. **40**(20): p. 5494-5504. https://doi.org/10.1039/c0dt01373k.
231. J. Staniforth and R.M. Ormerod, *Implications for using biogas as a fuel source for solid oxide fuel cells: internal dry reforming in a small tubular solid oxide fuel cell.* Catalysis Letters, 2002. **81**(1-2): p. 19-23. https://doi.org/10.1023/a:1016000519280.
232. A.J. Guwy, R.M. Dinsdale, J.R. Kim, J. Massanet-Nicolau, and G. Premier, *Fermentative biohydrogen production systems integration.* Bioresource Technology, 2011. **102**(18): p. 8534-8542. https://doi.org/10.1016/j.biortech.2011.04.051.
233. C. Cavinato, D. Bolzonella, F. Fatone, F. Cecchi, and P. Pavan, *Optimization of two-phase thermophilic anaerobic digestion of biowaste for hydrogen and methane production through reject water recirculation.* Bioresource Technology, 2011. **102**(18): p. 8605-8611. https://doi.org/10.1016/j.biortech.2011.03.084.
234. S. Manish and R. Banerjee, *Comparison of biohydrogen production processes.* International Journal of Hydrogen Energy, 2008. **33**(1): p. 279-286. https://doi.org/10.1016/j.ijhydene.2007.07.026.
235. Y. Kalinci, A. Hepbasli, and I. Dincer, *Biomass-based hydrogen production: A review and analysis.* International Journal of Hydrogen Energy, 2009. **34**(21): p. 8799-8817. https://doi.org/10.1016/j.ijhydene.2009.08.078.
236. H. Paradis, M. Andersson, J. Yuan, and B. Sundén, *Simulation of alternative fuels for potential utilization in solid oxide fuel cells.* International Journal of Energy Research, 2011. **35**(12): p. 1107-1117. https://doi.org/10.1002/er.1862.
237. O. Razbani, M. Assadi, and M. Andersson, *Three dimensional CFD modeling and experimental validation of an electrolyte supported solid oxide fuel cell fed with methane-free biogas.* International Journal of Hydrogen Energy, 2013. **38**(24): p. 10068-10080. https://doi.org/10.1016/j.ijhydene.2013.05.153.
238. B. La Licata, F. Sagnelli, A. Boulanger, A. Lanzini, P. Leone, P. Zitella, and M. Santarelli, *Bio-hydrogen production from organic wastes in a pilot plant reactor and its use in a SOFC.* International Journal of Hydrogen Energy, 2011. **36**(13): p. 7861-7865. https://doi.org/10.1016/j.ijhydene.2011.01.096.
239. T. Patterson, S. Esteves, R. Dinsdale, A. Guwy, and J. Maddy, *Life cycle assessment of biohydrogen and biomethane production and utilisation as a vehicle fuel.* Bioresource Technology, 2013. **131**: p. 235-245. https://doi.org/10.1016/j.biortech.2012.12.109.

240. A. Lima da Silva and N.C. Heck, *Oxide incorporation into Ni-based solid oxide fuel cell anodes for enhanced sulfur tolerance during operation on hydrogen or biogas fuels: A comprehensive thermodynamic study.* International Journal of Hydrogen Energy, 2015. **40**(5): p. 2334-2353. https://doi.org/10.1016/j.ijhydene.2014.12.037.
241. A. Galvagno, V. Chiodo, F. Urbani, and F. Freni, *Biogas as hydrogen source for fuel cell applications.* International Journal of Hydrogen Energy, 2013. **38**(10): p. 3913-3920. https://doi.org/10.1016/j.ijhydene.2013.01.083.
242. J.J. Ma, C.R. Jiang, P.A. Connor, M. Cassidy, and J.T.S. Irvine, *Highly efficient, coking-resistant SOFCs for energy conversion using biogas fuels.* Journal of Materials Chemistry A, 2015. **3**(37): p. 19068-19076. https://doi.org/10.1039/c5ta06421j.
243. J. Van Herle, A. Schuler, L. Dammann, M. Bosco, T.-B. Truong, E. De Boni, F. Hajbolouri, F. Vogel, and G.G. Scherer, *Fuels for Fuel Cells: Requirements and Fuel Processing.* CHIMIA International Journal for Chemistry, 2004. **58**(12): p. 887-895. https://doi.org/10.2533/000942904777677092.
244. H.R. Ellamla, I. Staffell, P. Bujlo, B.G. Pollet, and S. Pasupathi, *Current status of fuel cell based combined heat and power systems for residential sector.* Journal of Power Sources, 2015. **293**: p. 312-328. https://doi.org/10.1016/j.jpowsour.2015.05.050.
245. M. Ni, M.K.H. Leung, and D.Y.C. Leung, *Technological development of hydrogen production by solid oxide electrolyzer cell (SOEC).* International Journal of Hydrogen Energy, 2008. **33**(9): p. 2337-2354. https://doi.org/10.1016/j.ijhydene.2008.02.048.
246. P. Kazempoor and R.J. Braun, *Hydrogen and synthetic fuel production using high temperature solid oxide electrolysis cells (SOECs).* International Journal of Hydrogen Energy, 2015. **40**(9): p. 3599-3612. https://doi.org/10.1016/j.ijhydene.2014.12.126.
247. S.Y. Gómez and D. Hotza, *Current developments in reversible solid oxide fuel cells.* Renewable and Sustainable Energy Reviews, 2016. **61**: p. 155-174. https://doi.org/10.1016/j.rser.2016.03.005.
248. D. Ferrero, A. Lanzini, M. Santarelli, and P. Leone, *A comparative assessment on hydrogen production from low- and high-temperature electrolysis.* International Journal of Hydrogen Energy, 2013. **38**(9): p. 3523-3536. https://doi.org/10.1016/j.ijhydene.2013.01.065.
249. A. Wolf, A. Jess, and C. Kern, *Syngas Production via Reverse Water-Gas Shift Reaction over a Ni-Al2O3 Catalyst: Catalyst Stability, Reaction Kinetics, and Modeling.* Chemical Engineering & Technology, 2016. **39**(6): p. 1040-1048. https://doi.org/10.1002/ceat.201500548.
250. L. Wang, H. Liu, Y. Liu, Y. Chen, and S. Yang, *Influence of preparation method on performance of Ni-CeO2 catalysts for reverse water-gas shift reaction.* Journal of Rare Earths, 2013. **31**(6): p. 559-564. https://doi.org/10.1016/S1002-0721(12)60320-2.
251. J.Y. Lim, J. McGregor, A.J. Sederman, and J.S. Dennis, *The role of the Boudouard and water–gas shift reactions in the methanation of CO or CO2 over Ni/γ-Al2O3 catalyst.* Chemical Engineering Science, 2016. **152**: p. 754-766. https://doi.org/10.1016/j.ces.2016.06.042.
252. B. Lu and K. Kawamoto, *Preparation of mesoporous CeO2 and monodispersed NiO particles in CeO2, and enhanced selectivity of NiO/CeO2 for reverse water gas shift reaction.* Materials Research Bulletin, 2014. **53**: p. 70-78. https://doi.org/10.1016/j.materresbull.2014.01.043.
253. J. Bacenetti, C. Sala, A. Fusi, and M. Fiala, *Agricultural anaerobic digestion plants: What LCA studies pointed out and what can be done to make them more environmentally sustainable.* Applied Energy, 2016. **179**: p. 669-686. https://doi.org/10.1016/j.apenergy.2016.07.029.
254. J. Massanet-Nicolau, R. Dinsdale, A. Guwy, and G. Shipley, *Use of real time gas production data for more accurate comparison of continuous single-stage and two-stage fermentation.* Bioresource Technology, 2013. **129**: p. 561-567. https://doi.org/10.1016/j.biortech.2012.11.102.
255. G. Luo, L. Xie, Q. Zhou, and I. Angelidaki, *Enhancement of bioenergy production from organic wastes by two-stage anaerobic hydrogen and methane production process.*

Bioresource Technology, 2011. **102**(18): p. 8700-8706. https://doi.org/10.1016/j.biortech.2011.02.012.
256. C. Nathao, U. Sirisukpoka, and N. Pisutpaisal, *Production of hydrogen and methane by one and two stage fermentation of food waste.* International Journal of Hydrogen Energy, 2013. **38**(35): p. 15764-15769. https://doi.org/10.1016/j.ijhydene.2013.05.047.
257. M. Hans and S. Kumar, *Biohythane production in two-stage anaerobic digestion system.* International Journal of Hydrogen Energy, 2019. **44**(32): p. 17363-17380. https://doi.org/10.1016/j.ijhydene.2018.10.022.
258. K. Panagi, C.J. Laycock, J.P. Reed, and A.J. Guwy, *Highly efficient coproduction of electrical power and synthesis gas from biohythane using solid oxide fuel cell technology.* Applied Energy, 2019. **255**: p. 113854. https://doi.org/10.1016/j.apenergy.2019.113854.
259. C.H. Sun, A. Xia, Q. Liao, Q. Fu, Y. Huang, and X. Zhu, *Life-cycle assessment of biohythane production via two-stage anaerobic fermentation from microalgae and food waste.* Renewable & Sustainable Energy Reviews, 2019. **112**: p. 395-410. https://doi.org/10.1016/j.rser.2019.05.061.
260. F.C. Materials. *Cells*. 2018 20/01/2018]; Available from: https://fuelcellmaterials.com/.
261. Fiaxell. *Fiaxell SOFC Technologies™*. 15/1/2020]; Available from: http://www.fiaxell.com/.
262. P. Holtappels, L.G.J. De Haart, U. Stimming, I.C. Vinke, and M. Mogensen, *Reaction of CO/CO2 gas mixtures on Ni-YSZ cermet electrodes.* Journal of Applied Electrochemistry, 1999. **29**(5): p. 561-568. https://doi.org/10.1023/a:1003446721350.
263. Y. Matsuzaki and I. Yasuda, *Electrochemical Oxidation of H 2 and CO in a H 2 - H 2 O - CO - CO 2 System at the Interface of a Ni-YSZ Cermet Electrode and YSZ Electrolyte.* Journal of the Electrochemical Society, 2000. **147**(5): p. 1630-1635. https://doi.org/10.1149/1.1393409.
264. A. Weber, B. Sauer, A.C. Müller, D. Herbstritt, and E. Ivers-Tiffée, *Oxidation of H2, CO and methane in SOFCs with Ni/YSZ-cermet anodes.* Solid State Ionics, 2002. **152-153**(Supplement C): p. 543-550. https://doi.org/10.1016/S0167-2738(02)00359-4.
265. Y. Jiang and A.V. Virkar, *Fuel Composition and Diluent Effect on Gas Transport and Performance of Anode-Supported SOFCs.* Journal of the Electrochemical Society, 2003. **150**(7): p. A942-A951. https://doi.org/10.1149/1.1579480.
266. M. Andersson, J. Yuan, and B. Sundén, *SOFC modeling considering hydrogen and carbon monoxide as electrochemical reactants.* Journal of Power Sources, 2013. **232**: p. 42-54. https://doi.org/10.1016/j.jpowsour.2012.12.122.
267. A.P. Kulkarni, S. Giddey, and S.P.S. Badwal, *Efficient conversion of CO2 in solid oxide electrolytic cells with Pd doped perovskite cathode on ceria nanofilm interlayer.* Journal of CO2 Utilization, 2017. **17**: p. 180-187. https://doi.org/10.1016/j.jcou.2016.11.014.
268. Z. Zhan, W. Kobsiriphat, J.R. Wilson, M. Pillai, I. Kim, and S.A. Barnett, *Syngas Production By Coelectrolysis of CO2/H2O: The Basis for a Renewable Energy Cycle.* Energy & Fuels, 2009. **23**(6): p. 3089-3096. https://doi.org/10.1021/ef900111f.
269. C.J. Laycock, K. Panagi, J.P. Reed, and A.J. Guwy, *The importance of fuel variability on the performance of solid oxide cells operating on H-2/CO2 mixtures from biohydrogen processes.* International Journal of Hydrogen Energy, 2018. **43**(18): p. 8972-8982. https://doi.org/10.1016/j.ijhydene.2018.03.169.
270. H. Timmermann, D. Fouquet, A. Weber, E. Ivers-Tiffée, U. Hennings, and R. Reimert, *Internal Reforming of Methane at Ni/YSZ and Ni/CGO SOFC Cermet Anodes.* Fuel Cells, 2006. **6**(3-4): p. 307-313. https://doi.org/10.1002/fuce.200600002.
271. T. Takeguchi, Y. Kani, T. Yano, R. Kikuchi, K. Eguchi, K. Tsujimoto, Y. Uchida, A. Ueno, K. Omoshiki, and M. Aizawa, *Study on steam reforming of CH4 and C2 hydrocarbons and carbon deposition on Ni-YSZ cermets.* Journal of Power Sources, 2002. **112**(2): p. 588-595. https://doi.org/10.1016/S0378-7753(02)00471-8.
272. E. Ivers-Tiffée, Timmermann, H., Leonide, A., Menzler, N.H. and Malzbender, J., *Methane reforming kinetics, carbon deposition, and redox durability of Ni/8 yttria-stabilized zirconia (YSZ) anodes*, in *Handbook of Fuel Cells*. 2010. https://doi.org/10.1002/9780470974001.f500063.

273. E.S. Hecht, G.K. Gupta, H. Zhu, A.M. Dean, R.J. Kee, L. Maier, and O. Deutschmann, *Methane reforming kinetics within a Ni–YSZ SOFC anode support.* Applied Catalysis A: General, 2005. **295**(1): p. 40-51. https://doi.org/10.1016/j.apcata.2005.08.003.
274. A. Baldinelli, L. Barelli, G. Bidini, A. Di Michele, and R. Vivani, *SOFC direct fuelling with high-methane gases: Optimal strategies for fuel dilution and upgrade to avoid quick degradation.* Energy Conversion and Management, 2016. **124**: p. 492-503. https://doi.org/10.1016/j.enconman.2016.07.051.
275. H. He and J.M. Hill, *Carbon deposition on Ni/YSZ composites exposed to humidified methane.* Applied Catalysis A: General, 2007. **317**(2): p. 284-292. https://doi.org/10.1016/j.apcata.2006.10.040.
276. Y. Wu, C. Su, C. Zhang, R. Ran, and Z. Shao, *A new carbon fuel cell with high power output by integrating with in situ catalytic reverse Boudouard reaction.* Electrochemistry Communications, 2009. **11**(6): p. 1265-1268. https://doi.org/10.1016/j.elecom.2009.04.016.
277. S.-K. Kim, M.T. Mehran, U. Mushtaq, T.-H. Lim, J.-W. Lee, S.-B. Lee, S.-J. Park, and R.-H. Song, *Effect of reverse Boudouard reaction catalyst on the performance of solid oxide carbon fuel cells integrated with a dry gasifier.* Energy Conversion and Management, 2016. **130**: p. 119-129. https://doi.org/10.1016/j.enconman.2016.10.047.
278. J.-Y. Lee, R.-H. Song, S.-B. Lee, T.-H. Lim, S.-J. Park, Y.G. Shul, and J.-W. Lee, *A performance study of hybrid direct carbon fuel cells: Impact of anode microstructure.* International Journal of Hydrogen Energy, 2014. **39**(22): p. 11749-11755. https://doi.org/10.1016/j.ijhydene.2014.05.145.
279. S.D. Ebbesen, R. Knibbe, and M. Mogensen, *Co-Electrolysis of Steam and Carbon Dioxide in Solid Oxide Cells.* Journal of the Electrochemical Society, 2012. **159**(8): p. F482-F489. https://doi.org/10.1149/2.076208jes.
280. S.P. Yoon, J. Han, S.W. Nam, T.-H. Lim, I.-H. Oh, S.-A. Hong, Y.-S. Yoo, and H.C. Lim, *Performance of anode-supported solid oxide fuel cell with La0.85Sr0.15MnO3 cathode modified by sol–gel coating technique.* Journal of Power Sources, 2002. **106**(1): p. 160-166. https://doi.org/10.1016/S0378-7753(01)01037-0.
281. S. Bebelis, N. Kotsionopoulos, A. Mai, D. Rutenbeck, and F. Tietz, *Electrochemical characterization of mixed conducting and composite SOFC cathodes.* Solid State Ionics, 2006. **177**(19): p. 1843-1848. https://doi.org/10.1016/j.ssi.2006.05.041.
282. G. De Lorenzo, O. Corigliano, M. Lo Faro, P. Frontera, P. Antonucci, S.C. Zignani, S. Trocino, F.A. Mirandola, A.S. Arico, and P. Fragiacomo, *Thermoelectric characterization of an intermediate temperature solid oxide fuel cell system directly fed by dry biogas.* Energy Conversion and Management, 2016. **127**: p. 90-102. https://doi.org/10.1016/j.enconman.2016.08.079.
283. V. Chiodo, A. Galvagno, A. Lanzini, D. Papurello, F. Urbani, M. Santarelli, and S. Freni, *Biogas reforming process investigation for SOFC application.* Energy Conversion and Management, 2015. **98**: p. 252-258. https://doi.org/10.1016/j.enconman.2015.03.113.
284. X. Wu, Y. Tian, X. Zhou, X. Kong, J. Zhang, W. Zuo, D. Wang, and X. Ye, *Performance and long-term stability of nickel/yttria-stabilized zirconia anode-supported solid oxide fuel cell in simulated biosyngas.* Energy, 2016. **114**: p. 1-9. https://doi.org/10.1016/j.energy.2016.07.160.
285. T. Chen, W.G. Wang, H. Miao, T. Li, and C. Xu, *Evaluation of carbon deposition behavior on the nickel/yttrium-stabilized zirconia anode-supported fuel cell fueled with simulated syngas.* Journal of Power Sources, 2011. **196**(5): p. 2461-2468. https://doi.org/10.1016/j.jpowsour.2010.11.095.
286. S.C.J. Van Acht, C. Laycock, S.J.W. Carr, J. Maddy, A.J. Guwy, G. Lloyd, and L. Raymakers, *Simulation of integrated novel PSA/EHP/C process for high-pressure hydrogen recovery from Coke Oven Gas.* International Journal of Hydrogen Energy, 2020. **45**(30): p. 15196-15212. https://doi.org/10.1016/j.ijhydene.2020.03.211.
287. C. Coutanceau, S. Baranton, T. Audichon, C. Coutanceau, S. Baranton, and T. Audichon, *Hydrogen Electrochemical Production*. Hydrogen Electrochemical

Production. 2018, London: Academic Press Ltd-Elsevier Science Ltd. 1-+. https://doi.org/10.1016/b978-0-12-811250-2.00001-7.
288. S.-W. Kim, H. Kim, K.J. Yoon, J.-H. Lee, B.-K. Kim, W. Choi, J.-H. Lee, and J. Hong, *Reactions and mass transport in high temperature co-electrolysis of steam/CO2 mixtures for syngas production.* Journal of Power Sources, 2015. **280**: p. 630-639. https://doi.org/10.1016/j.jpowsour.2015.01.083.
289. F.S. da Silva and T.M. de Souza, *Novel materials for solid oxide fuel cell technologies: A literature review.* International Journal of Hydrogen Energy, 2017. **42**(41): p. 26020-26036. https://doi.org/10.1016/j.ijhydene.2017.08.105.
290. V.A. Sadykov, E.M. Sadovskaya, N.F. Eremeev, E. Yu. Pikalova, N.M. Bogdanovich, E.A. Filonova, T.A. Krieger, Y.E. Fedorova, A.V. Krasnov, P.I. Skriabin, A.I. Lukashevich, R. Steinberger-Wilckens, and I.C. Vinke, *Novel materials for solid oxide fuel cells cathodes and oxygen separation membranes: Fundamentals of oxygen transport and performance.* Carbon Resources Conversion, 2020. **3**: p. 112-121. https://doi.org/10.1016/j.crcon.2020.08.002.
291. X. Song, X. Dong, M. Li, and H. Wang, *Effects of adding alumina to the nickel-zirconia anode materials for solid oxide fuel cells and a two-step sintering method for half-cells.* Journal of Power Sources, 2016. **308**: p. 58-64. https://doi.org/10.1016/j.jpowsour.2016.01.070.
292. F. Wang, W. Wang, R. Ran, M.O. Tade, and Z. Shao, *Aluminum oxide as a dual-functional modifier of Ni-based anodes of solid oxide fuel cells for operation on simulated biogas.* Journal of Power Sources, 2014. **268**: p. 787-793. https://doi.org/10.1016/j.jpowsour.2014.06.087.
293. X. Wu, Y. Tian, J. Zhang, W. Zuo, X. Kong, J. Wang, K. Sun, and X. Zhou, *Enhanced electrochemical performance and carbon anti-coking ability of solid oxide fuel cells with silver modified nickel-yttrium stabilized zirconia anode by electroless plating.* Journal of Power Sources, 2016. **301**: p. 143-150. https://doi.org/10.1016/j.jpowsour.2015.10.006.
294. S.U. Rehman, R.-H. Song, J.-W. Lee, T.-H. Lim, S.-J. Park, and S.-B. Lee, *Effect of GDC addition method on the properties of LSM–YSZ composite cathode support for solid oxide fuel cells.* Ceramics International, 2016. **42**(10): p. 11772-11779. https://doi.org/10.1016/j.ceramint.2016.04.098.
295. Y. Liu, F. Wang, B. Chi, J. Pu, L. Jian, and S.P. Jiang, *A stability study of impregnated LSCF–GDC composite cathodes of solid oxide fuel cells.* Journal of Alloys and Compounds, 2013. **578**: p. 37-43. https://doi.org/10.1016/j.jallcom.2013.05.021.
296. M. Ferkhi and H.A. Yahia, *Electrochemical and morphological characterizations of La2□xNiO4±d (x=0.01, 0.02, 0.03 and 0.05) as new cathodes materials for IT-SOFC.* Materials Research Bulletin, 2016. **83**: p. 268-274. https://doi.org/10.1016/j.materresbull.2016.06.009.

Publications

C.J. Laycock, Panagi, K., J.P. Reed, and A.J. Guwy, The importance of fuel variability on the performance of solid oxide cells operating on H-$_2$/CO_2 mixtures from biohydrogen processes. International Journal of Hydrogen Energy, 2018. 43(18): p. 8972-8982. https://doi.org/10.1016/j.ijhydene.2018.03.169.

Panagi, K., C.J. Laycock, J.P. Reed, and A.J. Guwy, Highly efficient coproduction of electrical power and synthesis gas from biohythane using solid oxide fuel cell technology. Applied Energy, 2019. 255: p. 113854. https://doi.org/10.1016/j.apenergy.2019.113854.

Panagi, K., C.J. Laycock, J.P. Reed, and A.J. Guwy, Co-Electrolysis of Biohythane Using Solid Oxide Fuel Cell Technology. ECS Transactions, 2019. 91(1): p. 2333-2342. https://doi.org/10.1149/09101.2333ecst.

Panagi, K., C.J. Laycock, J.P. Reed, and A.J. Guwy, The effects of fuel variability on the electrical performance and durability of a solid oxide fuel cell operating on biohythane. International Journal of Hydrogen Energy, 2021. 46(2): p. 2630-2645. https://doi.org/10.1016/j.ijhydene.2020.10.151.

Appendices

A. Nernst plot calculations

For H_2-based mixtures:

ΔG of H_2 = -157.582 kJ/mol

ΔG of O_2 = -238.584 kJ/mol

ΔG of steam = -465.44 kJ/mol

Fuel composition (CO_2:H_2 0:100 vol% = 1 H_2 coefficient)

ΔG of H_2-O2 = -465.44 - (-157.582) - (0.5* -238.584) = -188.565 kJ/mol

Ideal Potential (E^o) = Δg_{rxn} / nF = (-188.565*1000) / (2*96485) = 0.977 V

Nernst Potential (E_{rev}) = E^o - (RT / nF) ln (Πa^{vi}products / Πa^{vi}reactants)

E_{rev} = 0.977 - (((8.314*1073.15) / (2*96485)) ln (0.025/(1*0.21^0.5))) = 1.112 V

Fuel composition (CO_2:H_2 10:90 vol% = 0.9 H_2 coefficient)

E_{rev} = 0.977 - (((8.314*1073.15) / (2*96485)) *ln ((0.025^(0.9)) / ((1^(0.9)) * (0.21^0.5)))) = 1.095 V

Fuel composition (CO_2:H_2 20:80 vol% = 0.8 H_2 coefficient)

E_{rev} = 0.977 - (((8.314*1073.15) / (2*96485)) *ln ((0.025^(0.8)) / ((1^(0.8)) * (0.21^0.5)))) = 1.078 V

Fuel composition (CO_2:H_2 30:70 vol% = 0.7 H_2 coefficient)

E_{rev} = 0.977 - (((8.314*1073.15) / (2*96485)) *ln ((0.025^(0.7)) / ((1^(0.7)) * (0.21^0.5)))) = 1.060 V

Fuel composition (CO_2:H_2 40:60 vol% = 0.6 H_2 coefficient)

E_{rev} = 0.977 - (((8.314*1073.15) / (2*96485)) *ln ((0.025^(0.6)) / ((1^(0.6)) * (0.21^0.5)))) = 1.043 V

Fuel composition (CO_2:H_2 50:50 vol% = 0.5 H_2 coefficient)

E_{rev} = 0.977 - (((8.314*1073.15) / (2*96485)) *ln ((0.025^(0.5)) / ((1^(0.5)) * (0.21^0.5)))) = 1.026 V

Fuel composition (CO_2:H_2 60:40 vol% = 0.4 H_2 coefficient)

E_{rev} = 0.977 - (((8.314*1073.15) / (2*96485)) *ln ((0.025^(0.4)) / ((1^(0.4)) * (0.21^0.5)))) = 1.009 V

Fuel composition (CO_2:H_2 70:30 vol% = 0.3 H_2 coefficient)

E_{rev} = 0.977 - (((8.314*1073.15) / (2*96485)) *ln ((0.025^(0.3)) / ((1^(0.3)) * (0.21^0.5)))) = 0.992 V

Fuel composition (CO_2:H_2 80:20 vol% = 0.2 H_2 coefficient)

E_{rev} = 0.977 - (((8.314*1073.15) / (2*96485)) *ln ((0.025^(0.2)) / ((1^(0.2)) * (0.21^0.5)))) = 0.975 V

Fuel composition (CO_2:H_2 90:10 vol% = 0.1 H_2 coefficient)

E_{rev} = 0.977 - (((8.314*1073.15) / (2*96485)) *ln ((0.025^(0.1)) / ((1^(0.1)) * (0.21^0.5)))) = 0.958 V

For CH_4-based mixtures:

ΔG of O_2 = -238.584 kJ/mol

ΔG of steam = -465.44 kJ/mol

ΔG of CO_2 = -648.868 kJ/mol

ΔG of CH_4 = -301.961 kJ/mol

Fuel composition (CO_2:CH_4 0:100 vol% = 1 CH_4 coefficient)

ΔG of CH_4-O2 = (-648.868 + (2*-465.44)) – (-301.961 + (2*-238.584)) = -800.619

Ideal Potential (E^o) = Δg_{rxn} / nF = (-800.6195*1000) / (8*96485) = 1.038 V

Nernst Potential (E_{rev}) = E^o - (*R*T / n*F*) ln (Πa^{vi}products / Πa^{vi}reactants)

E_{rev} = 1.038 - (((8.314*1073.15) / (8*96485)) *ln (((0.025^2)*1) / (1*0.21^2))) = 1.038 V

Fuel composition (CO_2:CH_4 10:90 vol% = 0.9 CH_4 coefficient)

E_{rev} = 1.038 - (((8.314*1073.15) / (8*96485)) *ln (((0.2^ (2*0.9)) * (1^(0.9+1))) / ((1^(0.9)) * (0.21^2)))) = 1.035 V

Fuel composition (CO_2:CH_4 20:80 vol% = 0.8 CH_4 coefficient)

E_{rev} = 1.038 - (((8.314*1073.15) / (8*96485)) *ln (((0.2^ (2*0.8)) * (1^(0.8+1))) / ((1^(0.8)) * (0.21^2)))) = 1.031 V

Fuel composition (CO_2:CH_4 30:70 vol% = 0.7 CH_4 coefficient)

E_{rev} = 1.038 - (((8.314*1073.15) / (8*96485)) *ln (((0.2^ (2*0.7)) * (1^(0.7+1))) / ((1^(0.7)) * (0.21^2)))) = 1.027 V

Fuel composition (CO_2:CH_4 40:40 vol% = 0.6 CH_4 coefficient)

E_{rev} = 1.038 - (((8.314*1073.15) / (8*96485)) *ln (((0.2^ (2*0.6)) * (1^(0.6+1))) / ((1^(0.6)) * (0.21^2)))) = 1.023 V

Fuel composition (CO_2:CH_4 50:50 vol% = 0.5 CH_4 coefficient)

E_{rev} = 1.038 - (((8.314*1073.15) / (8*96485)) *ln (((0.2^ (2*0.5)) * (1^(0.5+1))) / ((1^(0.5)) * (0.21^2)))) = 1.020 V

Fuel composition (CO_2:CH_4 60:40 vol% = 0.4 CH_4 coefficient)

E_{rev} = 1.038 - (((8.314*1073.15) / (8*96485)) *ln (((0.2^ (2*0.4)) * (1^(0.4+1))) / ((1^(0.4)) * (0.21^2)))) = 1.016 V

Fuel composition (CO_2:CH_4 70:30 vol% = 0.3 CH_4 coefficient)

E_{rev} = 1.038 - (((8.314*1073.15) / (8*96485)) *ln (((0.2^ (2*0.3)) * (1^(0.3+1))) / ((1^(0.3)) * (0.21^2)))) = 1.012 V

Fuel composition (CO_2:CH_4 80:20 vol% = 0.2 CH_4 coefficient)

E_{rev} = 1.038 - (((8.314*1073.15) / (8*96485)) *ln (((0.2^ (2*0.2)) * (1^(0.2+1))) / ((1^(0.2)) * (0.21^2)))) = 1.009 V

Fuel composition (CO_2:CH_4 90:10 vol% = 0.1 CH_4 coefficient)

E_{rev} = 1.038 - (((8.314*1073.15) / (8*96485)) *ln (((0.2^ (2*0.1)) * (1^(0.1+1))) / ((1^(0.1)) * (0.21^2)))) = 1.005 V

B. Mass flow controllers operation and calibration

Bronkhorst EL-Flow mass flow controllers connected in series and controlled through the computer.

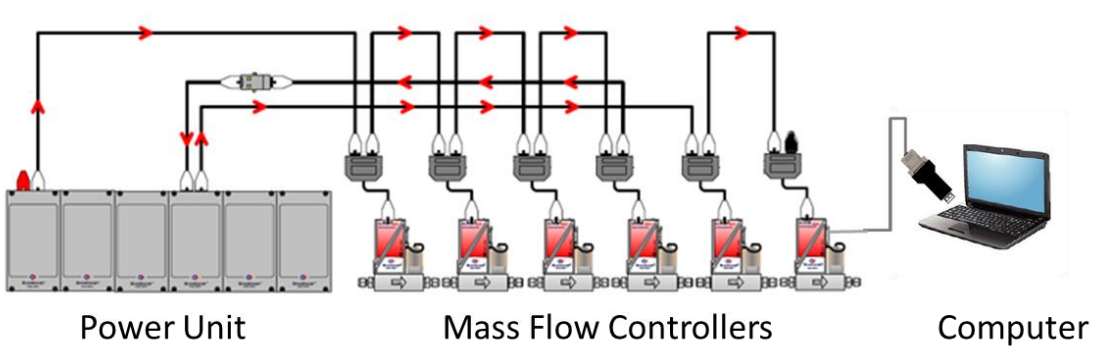

Figure B1: 6-channel Flow-Mass System

The mass flow controllers were calibrated by the manufacturer under different conditions (ambient temperature and pressure) to those under which they were used in the laboratory. Therefore, it was necessary to calibrate the mass flow controller set-point against the actual flow of gas the mass flow controllers produced. For each gas, the mass flow controllers were set to the following set-points: (5, 10, 15, 20 and 30). The actual flow rate was then measured using a bubble-flow meter by measuring the time taken for bubbles to travel through a volume of 25 mL. These measurements were repeated, averaged and used to calculate the actual flow rate at each set-point measured.

For example: if a bubble takes 50 seconds to travel 25 mL, the flow rate is:

$$\frac{25\ milliliters\ traversed}{50\ seconds\ travel\ time} \times \frac{60\ sec.}{} = 30\ \text{ml min}^{-1}$$

This calibration procedure was repeated every year. A linear relationship was observed between flow rate and set-point and this was used to calculate the set-point required to generate the desired flow rate of gas. Example measurements are shown in Table A1.

Table B1: Example mass flow calibration of flow rate against set-point for gases used in this work.

Flow Rate	H_2	CH_4	CO_2	N_2	He	Air
1	0.93	0.90	0.90	0.90	0.91	0.91
2	1.86	1.79	1.81	1.81	1.82	1.82
3	2.79	2.69	2.72	2.71	2.73	2.73
4	3.72	3.58	3.61	3.61	3.64	3.64
5	4.65	4.48	4.53	4.51	4.55	4.55
6	5.58	5.38	5.43	5.42	5.46	5.46
7	6.51	6.27	6.34	6.32	6.37	6.37
8	7.44	7.17	7.25	7.22	7.28	7.29
9	8.37	8.06	8.15	8.12	8.19	8.20
10	9.30	8.96	9.06	9.03	9.10	9.11
11	10.23	9.86	9.96	9.93	10.01	10.02
12	11.16	10.75	10.87	10.83	10.92	10.93
13	12.09	11.65	11.77	11.73	11.83	11.84
14	13.02	12.54	12.68	12.64	12.74	12.75
15	13.95	13.44	13.59	13.54	13.65	13.66
16	14.88	14.34	14.49	14.44	14.56	14.57
17	15.81	15.23	15.40	15.34	15.47	15.48
18	16.74	16.13	16.30	16.25	16.38	16.39

19	17.67	17.03	17.21	17.15	17.29	17.30
20	18.60	17.92	18.11	18.05	18.20	18.21
21	19.53	18.82	19.02	18.95	19.10	19.12
22	20.46	19.71	19.93	19.86	20.01	20.03
23	21.39	20.61	20.83	20.76	20.92	20.95
24	22.32	21.51	21.74	21.66	21.83	21.86
25	23.25	22.40	22.64	22.57	22.74	22.77
26	24.18	23.30	23.55	23.47	23.65	23.68
27	25.11	24.19	24.45	24.37	24.56	24.59
28	26.04	25.09	25.36	25.27	25.47	25.50
29	26.97	25.99	26.27	26.18	26.38	26.41
30	27.90	26.88	27.17	27.08	27.29	27.32
31	28.83	27.78	28.08	27.98	28.20	28.23
32	29.76	28.67	28.98	28.88	29.11	29.14
33	30.69	29.57	29.89	29.79	30.02	30.05
34	31.62	30.47	30.79	30.69	30.93	30.96
35	32.55	31.36	31.70	31.59	31.84	31.87
36	33.48	32.26	32.61	32.49	32.75	32.78
37	34.41	33.15	33.51	33.40	33.66	33.69
38	35.34	34.05	34.42	34.30	34.57	34.61
39	36.27	34.95	35.32	35.20	35.48	35.52

40	37.20	35.84	36.23	36.10	36.39	36.43
41	38.13	36.74	37.13	37.01	37.30	37.34
42	39.06	37.63	38.04	37.91	38.21	38.25
43	39.99	38.53	38.95	38.81	39.12	39.16
44	40.92	39.43	39.85	39.71	40.03	40.07
45	41.85	40.32	40.76	40.62	40.94	40.98
46	42.78	41.22	41.66	41.52	41.85	41.89
47	43.71	42.11	42.57	42.42	42.76	42.80
48	44.64	43.01	43.47	43.33	43.67	43.71
49	45.57	43.91	44.38	44.23	44.58	44.62
50	46.50	44.80	45.29	45.13	45.49	45.53

C. QMS gas sensitivity corrections

The sensitivity of the QMS towards each of the gases was measured and used for data correction so that the data presented represent the relative partial pressures of the output gases leaving the cell. CO_2 was used as a baseline to normalise the peak intensities and was assigned a sensitivity of 1.00. Each gas (H_2, CH_4, N_2 and He) sensitivity factor was calculated against CO_2. To determine the sensitivity value of each gas, mixtures of 5/5 vol%, 7.5/7.5 vol%, 5/15 vol% and 10/20 vol% of CO_2/gas (gas: H_2, CH_4, N_2 and He) were fed directly to the QMS via the bypass line. The signal intensity of each gas and CO_2 were measured and averaged. The sensitivity was measured as follows:

$$\text{Sensitivity of gas} = \frac{Peak\ Intensity\ of\ gas}{Peak\ Intensity\ of\ Carbon\ Dioxide}$$

For example, the sensitivity of H_2 was calculated:

$$\text{Sensitivity of } H_2 = \frac{426.02}{33.09} = 12.87$$

For best results, each mixture sensitivity was repeated four times at different ratios. Table B1 shows the calculated signal sensitivities for each gas. Before plotting the QMS data, the sensitivity of each gas was normalized by dividing the peak intensity of each gas with the corresponding sensitivity value of the gas.

Table C1: Example calculated gas sensitivities used in this work.

Gases	Sensitivity
CO_2	1.00
H_2	12.87
CH_4	1.07
He	1.04
CO	20.89

D. Generation of laminar steam flows

To create laminar flows of steam, deionized water was delivered through a cartridge using a peristaltic pump at the required flow rate. The cartridge was resistively heated from the chamber furnace, enabling a constant steam flux to be delivered to the anode as required. Because the pump controlled the flow rate of water in the liquid phase, it was necessary to calculate the corresponding flow rate of steam that was generated. To calculate the conversion of water to steam the ideal gas equation was used:

$Pv = nRT$

where,

P = pressure = 101325 Pa
V = volume of flow per minute in m^3
n = number of moles = 0.000179 mol
R = gas constant = 8.31441 $J K^{-1} mol^{-1}$
T = temperature = 1023.15 K

Re-arranging the equation to: $V = nRT / P$

E. Thermodynamic equilibrium at different compositions

The effect of changing composition as a function of temperature have been calculated with CH_4 and CO_2 being converted into product gases (H_2, CO, H_2O, CH_4 and CO_2). A chemical equilibrium model was used (Aspen Plus) to predict the product gas composition at different $CH_4/CO_2/H_2$ and CO_2/H_2 mixtures at different temperatures.

Fig. E1 show the predicted equilibrium results for mixtures containing 90/10 vol%, 60/40 vol%, 50/50 vol%, 40/60 vol% and 10/90 vol% H_2/CO_2. Fig. E1a. shows 90/10 vol% H_2/CO_2 mixture and the product gases at equilibrium 750 °C and above contain 80 vol% H_2, 9 vol% H_2O, 9 vol% CO and 1 vol% CO_2. Switching the fuel mixture to 60/40 vol% H_2/CO_2 (Fig. E1b) the product gases at equilibrium contain 36 vol% H_2, 23 vol% H_2O, 23 vol% CO and 17 vol% CO_2. Switching the fuel mixture to 50/50 vol% H_2/CO_2 (Fig. E1c) the product gases at equilibrium contain 26 vol% H_2, 24 vol% H_2O, 24 vol% CO and 26 vol% CO_2. Switching the fuel mixture to 40/60 vol% H_2/CO_2 (Fig. E1d) the product gases at equilibrium contain 17 vol% H_2, 23 vol% H_2O, 23 vol% CO and 37 vol% CO_2. Switching the fuel mixture to 10/90 vol% H_2/CO_2 (Fig. E1e) the product gases reach equilibrium at 750 °C and contain 1 vol% H_2, 9 vol% H_2O, 9 vol% CO and 81 vol% CO_2. Therefore, the calculated thermodynamic equilibrium doesn't impact the conclusions made for how the cell is utilising the gases. The fuel conversion mechanisms suggested will be the same.

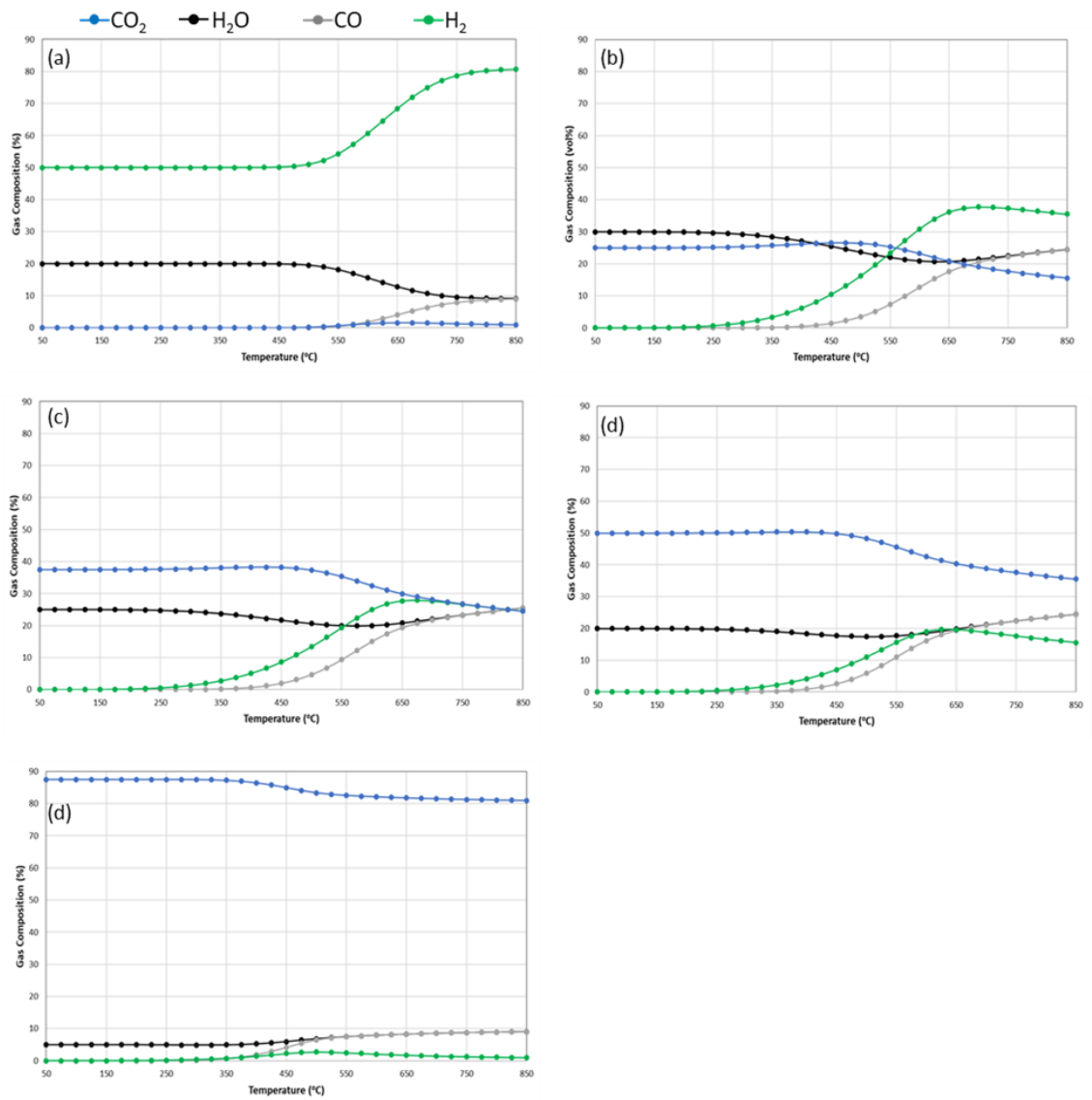

Figure E1: Predicted thermodynamic equilibrium using Aspen plus for H_2/CO_2 compositions: (a) 90/10 vol%, (b) 60/40 vol%, (c) 50/50 vol%, (d) 40/60 vol% and (e) 10/90 vol%.

Fig.E2 show the predicted equilibrium results for mixtures containing 60/30/10, 53:27:20 and 40/20/40 vol% $CH_4/CO_2/H_2$. Equilibrium is achieved for all mixtures from 750 °C. Fig. E2a shows the 60/30/10 vol% $CH_4/CO_2/H_2$ mixture with the product gases at equilibrium containing 69 vol% H_2, 59 vol% CO and 30 vol% CH_4. Switching the fuel mixture to 53:27:20 vol% of $CH_4/CO_2/H_2$ (Fig. E2b) the equilibrium is reached at 750°C and the product gases at equilibrium contain 73 vol% H_2, 53 vol% CO and 26 vol% CH_4. Switching the fuel mixture to 40:20:40

vol% of $CH_4/CO_2/H_2$ (Fig. E2c) the equilibrium is reached at 750°C and the product gases at equilibrium contain 79 vol% H_2, 40 vol% CO and 20 vol% CH_4.

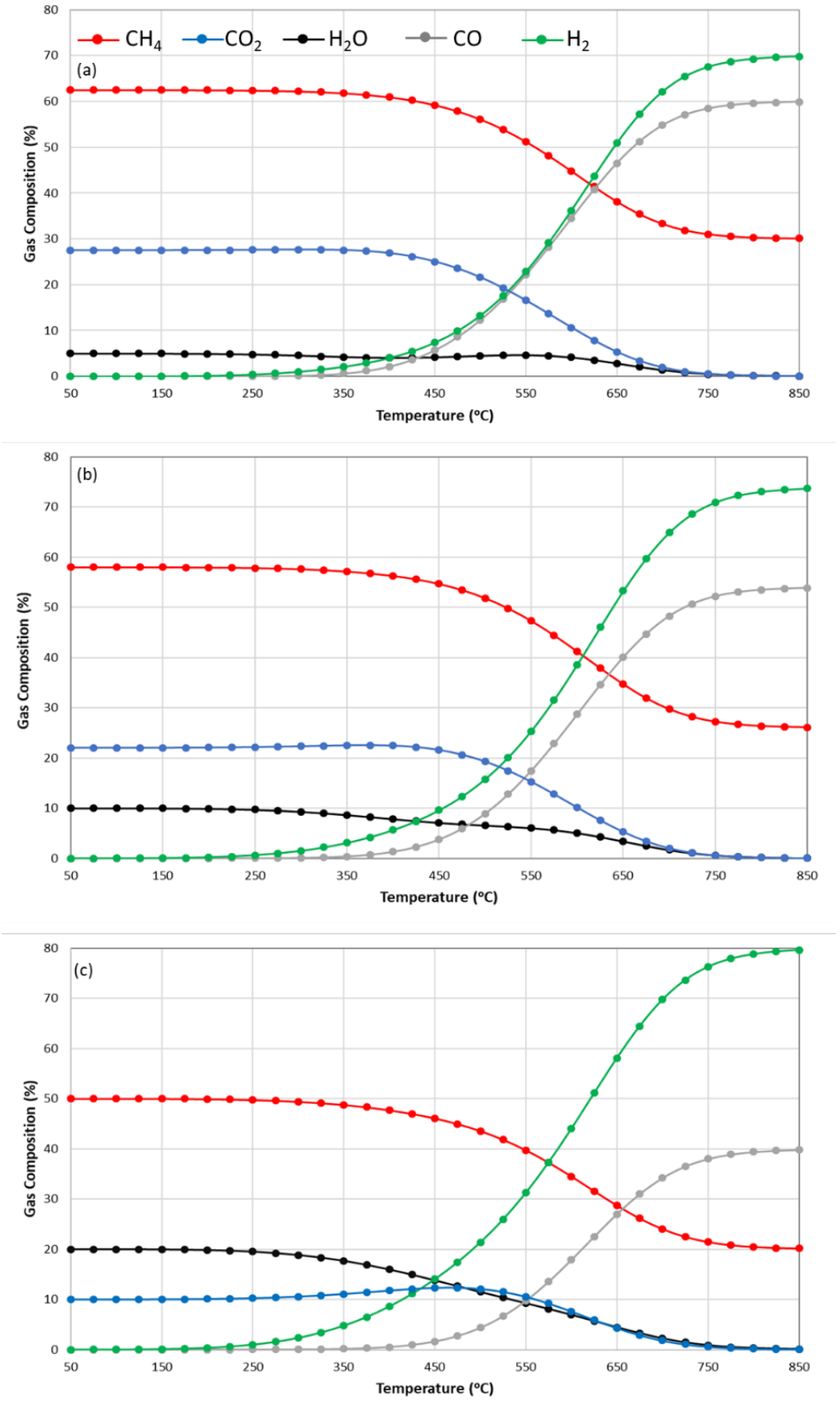

***Figure E2:** Predicted thermodynamic equilibrium using Aspen plus for $CH_4/CO_2/H_2$ compositions: (a) 60/30/10 vol%, (b) 53/27/20 vol% and (c) 40/20/40 vol%.*